Università degli Studi di Trieste

Department of Physics
Doctoral School of Physics

Dust across galaxies

PhD candidate:
Lorenzo Gioannini

Supervisor:
Prof.ssa Francesca Matteucci

Co-supervisor:
Dott. Giovanni Vladilo

Cycle XXX

Contents

Summary of the thesis

In this thesis, we investigate the evolution of dust mass and chemical composition in different galaxies by means of detailed chemical evolution models which account for the presence of dust. We present a new model (Gioannini et al., 2017a), in which we adopt updated prescriptions for dust formation in Asymptotic Giant Branch (AGB) stars and Type II SNe (Piovan et al., 2011; Dell'Agli et al., 2017), as well as for dust processes in the interstellar medium (ISM), i.e. dust accretion and destruction (Asano et al., 2013). We relax the instantaneous recycling approximation and therefore we take into account stellar lifetimes. In this way, we can predict in detail the evolution of the abundances of single elements both in the dust and in gas phase of the ISM, and distinguish the contributions from different sources during the galactic time.

We study the dust evolution in galaxies of different morphological type, i.e. dwarf irregulars, spirals, Milky Way-type and ellipticals: our model has proven to be very useful to study various dust properties in these galaxies, such as dust mass, dust-to-gas (DG) ratio and chemical composition. In our approach, the main difference between galaxies is the star formation history: in ellipticals it is assumed a very fast and intense star formation rate, and this rate decreases going towards spirals, irregulars and smaller galaxies.

First, we compare our model predictions for a typical dwarf irregular galaxy with chemical abundances measured in Damped Lyman Alpha (DLA) systems (Wolfe et al., 1986, 2005). After having reproduced the abundances of volatile elements S and Zn (unaffected by the presence of dust), we study the depletion patterns of refractory elements (Si and Fe), which tend to be incorporated in the dust phase. Our study suggests that Fe and Si undergo a different history of dust formation and evolution. We show evidences that Fe is mainly incorporated into iron-rich solid nano-particles, which may form by dust growth in the ISM. This dust component has never been taken into account in previous models. We also provide a new method, based on DLA column density measurements and the ratio between volatile and refractory elements, to give for the first time an estimate of the chemical abundance ratios inside dust grains. In this way, we try to disentangle the main dust constituents and predict their evolution: in particular, we focus on the fraction between silicates and metallic particles and between pyroxenes and olivines.

Concerning the Milky Way, we present the evolution (in space and time) of the DG ratio in the context of the galactic habitable zone (GHZ), defined as the region with highly enough metallicity to form planetary systems capable of sustaining life (Gonzalez et al., 2001). In this study, we provide theoretical prescriptions of the DG ratio and metallicity for models of planetary systems formation (Spitoni et al., 2017).

Then we focus our study on high redshift elliptical galaxies, and we try to disentangle the responsible processes for the sudden appearance of metals and dust observed in those objects. The first metals and dust appear very early since they are both produced by short living massive stars (core-collapse SNe), on the time-scales of few tenths of million years. In their initial burst of star formation, the metallicity can attain almost a solar value after one hundred million years and the same is true for dust, to which also AGB stars contribute on time-scales equal or larger than 30 million years.

Finally, we study the cosmic dust rate (CDR) across the Universe by assuming that the cosmic dust abundance results from the contribution of galaxies of different morphological type averaged in a unitary volume of the Universe (Gioannini et al., 2017b). These galaxies are assumed to evolve in number density according to their weight in the luminosity function at different redshifts and different cosmological scenarios (Vincoletto et al., 2012; Pozzi et al., 2015). Parallel to the CDR we compute the cosmic star formation rate (CSFR) as well as the cosmic rate of metallicity. Our predictions are extreme important to understand the roles of dust production, accretion and destruction in the CDR evolution. Our best scenario predicts a dust rate peak between $2 < z < 3$ and reproduce the observed CSFR. Eventually, we estimate the comoving dust density parameter Ω_{dust} and we find a good agreement with data for z<0.5.

Chapter 1

Introduction

Light is the most important source in Astrophysics and it is the only mediator we have to obtain information about astronomical objects outside the Solar System (except for the recent detections of gravitational waves, e.g. Abbott et al. 2016; The LIGO Scientific Collaboration et al. 2017; The LIGO Scientific Collaboration & The Virgo Collaboration 2017). In the interstellar and intergalactic medium, dust always modifies the light coming from background sources, and therefore we constantly must correct observations to perform a truthful interpretation of the Universe. In this way, the best we know dust the most accurate information of the Universe we can have.

The first evidence for the presence of interstellar dust was performed by Struve (1847), when he noticed that star counts appear to decrease with increasing distance from the Earth. Kapteyn (1909) suggested that this effect could arise from the light absorption of the intervening material located between stars. It was Robert Trumpler who first discovered the wavelength dependent absorption of the light, called "extinction", and concluded that it was caused by the scattering and absorption by material made of solid grains in the interstellar medium (ISM) (Trumpler, 1930).

When Astronomy was mainly conducted at optical wavelength, dust was considered as an annoying component, an obstacle to our understanding of the Universe. However, in the last decades this field of study has become extremely important, as dust it is involved in a great variety of physical processes. In fact, dust absorbs the ultraviolet (UV) stellar light and re-emits in the infrared (IR) band (Draine & Lee, 1984; Desert et al., 1990; Witt & Gordon, 2000; Calzetti, 2001) and it deeply affects the spectral energy distribution (SED) of galaxies (Silva et al., 1998; Granato et al., 2000); dust depletes metals from the gas phase of the ISM and therefore modifies its chemical composition (Vladilo, 2004; Jenkins, 2009); furthermore, dust grains are the catalysts for the formation of molecular hydrogen and on their surfaces many chemical reactions increase the chemical complexity of the ISM (Hollenbach & Salpeter, 1971; Mathis, 1990; Petitjean et al., 2000; Hirashita, Hunt & Ferrara, 2002); dust is involved in the star formation process: in fact, the emission of vibrational-rotational lines by molecules leads to the formation of molecular clouds, the densest and the coldest regions of the ISM, where the physical conditions lead to the formation of new stars (e.g. Abel et al., 2002; Matsuda et al., 1969; Nakamura & Umemura, 2002; Hirashita & Ferrara, 2002); dust grains are also involved in the formation of planetary systems: in fact, according to the accretion theory, dust grains in a proto-planetary disc coagulate into clumps that eventually collide forming larger bodies (planetesimals) and then planets (e.g. Safronov & Zvjagina, 1969; Pollack et al., 1996; Dullemond & Dominik, 2005). To conclude, dust grains could potentially be the precursor of life on Earth: based on the theory of panspermia, dust grains might act as the carriers of microbiological life in the ISM (Wickramasinghe, 2011), because of their ability in shielding complex molecules from the ionizing effect of ultraviolet radiation emitted by stars (Brown et al., 1995).

The study of interstellar dust represents an exiting and challenging area of current Astronomy. In the next Sections we provide an overview on the general properties of dust particles.

1.1 Dust in the Interstellar medium

The presence of dust is associated to different scales in our Universe and it has been detected in different astronomical objects. The zodiacal light witnesses the presence of dust particles in our Solar system, and a direct collection of dust grains have been performed by space missions, such as by *Ulysses*, *Galileo* and *Stardust* spacecrafts (Grun et al., 1993; Baguhl et al., 1996; Landgraf et al., 1999; Altobelli et al., 2005). Beyond the Solar system, thermal emission of light has been detected in the different stellar cold envelopes, indicating that dust can be efficiently produced by stars. At Galactic scales, the presence of dust in the Galactic plane is responsible for the high disk extinction when observing towards the Galactic center, whereas this effect decreases for observations at higher latitudes. Despite high-resolution observations achievable in the local galactic environment, our location in the Milky Way complicates the global study of interstellar and circumstellar dust, because of several uncertainties about distances (Zhukovska & Henning, 2013). Therefore, the study of dust properties in local galaxies such as Andromeda galaxy (see Fig. 1.2) or the Magellanic Clouds avoid these complications (e.g. Meixner et al., 2006, 2013; Schneider et al., 2014; Dell'Agli et al., 2015) and allows to study how dust distributes inside galaxies (e.g. Bocchio et al., 2016; Casasola et al., 2017). Far from the Local Universe, high quality observations carried out using satellites and ground based telescopes have shed light on the nature and composition of the dust in high-redshift galaxies, between $5 < z < 9$ (e.g. Carilli et al., 2001; Draine, 2003; Cooray et al., 2014; Maiolino et al., 2015; Watson et al., 2015). The detection of dust masses in these objects has raised a fundamental question on the origin of dust (Dunne et al., 2003; Santini et al., 2014; Valiante et al., 2014; Popping et al., 2016; Calura et al., 2017). In fact, at such high redshifts, the Universe is relatively young, suggesting that dust formation has to occur on short time-scales (e.g. Morgan & Edmunds, 2003; Maiolino et al., 2004; Santini et al., 2010; Galliano et al., 2011; Valiante et al., 2011; Rowlands et al., 2014).

In summary, dust has been detected in various environments both in the local and in high redshift Universe and it is widely studied both in the local framework as well as in the cosmological context (Bekki, 2013; McKinnon et al., 2016; Popping et al., 2016). Grain properties have been determined from many kinds of observations such as infrared continuum emission, depletion patterns in the ISM (Jenkins, 2009), isotopic anomalies in meteorites (Gail et al., 2009) and extinction curves (Aguirre, 1999). In the next Paragraph, we summarize the main properties of interstellar dust and we discuss some of the main studies adopted to cast light on the nature of dust grains.

1.1.1 A picture of interstellar dust

Since its discovery in the first decades of the XX century, interstellar dust has been a major topic in observational studies, and many models has been advanced to explain its properties. One of the first attempts in dust modeling suggests that metallic particles might be the responsible for the diffusion of starlight by interstellar matter (Schoenberg & Jung, 1934). Then, a "dirty ice" model for dust was proposed by Oort & van de Hulst (1946) by studying the physical processes occurring in the cold ISM. In the following decades, an alternative model for dust material has been advanced to explain the near-IR extinction: in this model, silicate and graphite grains with or without ice mantles were suggested (Hoyle & Wickramasinghe, 1962; Wickramasinghe, 1963, 1970). The presence of carbon in form of graphite grains was strengthened by the UV bump extinction observed at 2175 Å (Stecher & Donn, 1965), even its nature is still under debate.

The model suggesting graphite grains along silicates has been the most successful one and it has put the basis for all the subsequent theories and experiments. Mathis et al. (1977), advanced a more detailed description of silicate grains, preferentially made of olivine-type material (Mg-rich), to fit the extinction curve of the ISM. All the following models have been fine tuned in order to explain observations (Draine & Lee, 1984), and other dust components were added such as Polycyclic Aromatic Hydrocarbon (PAH) molecules (Desert et al., 1990; Draine & Li, 2007; Siebenmorgen et al., 2014) and amorphous carbon grains (Zubko et al., 2004; Galliano et al., 2011).

In this way, we inherited a general picture of interstellar dust which is composed by a mixture of "astronomical" silicates, graphite/amorphous carbons and polycyclic aromatic hydrocarbons separated in the ISM. This idea of interstellar dust is the most widely and accepted one in the Astronomical community (Hoyle & Wickramasinghe, 1969; Mathis et al., 1977; Draine & Lee, 1984; Desert et al., 1990; Li & Draine, 2001; Draine & Li, 2007).

However, this picture is far away to give a complete explanation of the real composition of interstellar dust. First of all, it is unlikely that such three different dust species are separated in the ISM. In fact, given the turbulent nature of the ISM and the evidence that depletions of the dust-forming elements vary significantly and differentially (e.g. Routly & Spitzer, 1952; Crinklaw et al., 1994; Savage & Sembach, 1996; Jones, 2000; Welty et al., 2001; Jenkins, 2009; Parvathi et al., 2012), it is difficult to justify how the different dust materials could remain distinct. The cycling of gas and dust through different ISM phases naturally requires that the dust materials become mixed into inhomogeneous assemblages. The mixing grains could be in the form of a dusty core made up of silicates and graphite with a mantle of ice (Wickramasinghe, 1963). Secondly, this composition strongly depends on the physical conditions of the ISM and the properties of dust may be different from one region to another. For example, the dust in the diffuse interstellar medium, molecular clouds, photo-dissociation regions and HII regions is not exactly the same but exhibits important evolution within and between these regions (e.g. Fanciullo et al., 2013; Jones, 2013, 2014). An understanding of these evolutionary and regional variations exhibited by dust is now critical.

For this reason interstellar dust should be considered as a variable component of the ISM rather than “static”. The circumstellar environments of evolved stars represent the sites where cosmic dust comes from, producing materials of silicate and carbonaceous type, i.e. the most important populations of dust species in the Universe. A wide range of stars is believed to contribute to dust production. In particular, low and intermediate mass stars ($1.0M_\odot \leq M_* \leq 8.0M_\odot$) produce significant amount of dust during the Asymptotic Giant Branch (AGB) phases (Ferrarotti & Gail, 2006; Gail et al., 2009; Ventura et al., 2012; Dell’Agli et al., 2017). On the other hand, massive stars ($M_* \geq 8.0M_\odot$), exploding as core-collapse supernovae (SNe) are responsible for the production of dust, even it is not yet clear how much of the formed dust can survive to the destruction process during the passage of the reverse shock after the explosion (Todini & Ferrara, 2001; Bianchi & Schneider, 2007; Bianchi et al., 2009; Hirashita et al., 2014; Bocchio et al., 2014; Schneider et al., 2014). Stellar winds eject these dust particles in the ISM, and then, dust experiences lots of processes, which can decrease or increase its mass (Ferrarotti & Gail, 2006; Zhukovska et al., 2008). Thermal sputtering, evaporation in grain-grain collision, thermal sublimation or desorption are some examples of destruction processes, but the most important mechanism for cycling dust back to the gas phase resides in supernova shocks (Dwek & Scalo, 1980; McKee, 1989; Jones et al., 1994). On the other hand, grain growth by dust coagulation and metals accretion onto preexisting grains increases either the dust mass or size and preferably occur in molecular clouds (Liffman & Clayton, 1989; Hirashita, 2000; Asano et al., 2013). These clouds are the sites where stars form and where new production of dust occurs. All these processes together give rise to the so called “dust cycle” (see Fig. 1.1). Unfortunately, in spite of much observational and theoretical effort, large uncertainties are still present in the exhaustive comprehension of dust production, accretion and destruction.

The accretion and destruction processes in the ISM can also modify the grain dimension or even change the chemical composition. The typical life-time of a dust grain is assumed to be $\sim 10^8 yr$, similar to the life-time of a molecular cloud (Oort & van de Hulst, 1946; Dwek, 1998), even if the destruction time-scales may vary for grains of different sizes (e.g. Hirashita et al., 2016).

The size distribution of the grains is another fundamental characteristic of dust and depends on various processes. In fact, dust destruction in the ISM by shocks or shattering (grain disruption due to grain-grain collision) decreases the grain size, whereas the condensation of gas-phase metals onto pre-existing dust grains or coagulation (sticking of grains) enhances the ISM of larger grains. The size of interstellar grains is usually inferred by models to match the observed extinction curve, independent from the assumed chemical composition. A first semi-empirical power law for the distribution was performed by Mathis et al. (1977), in a grain radius (a) range between 0.001-0.25 μm. Hirashita (2015) calculate the evolution of this distribution in the context of a theoretical study. In that study, the approximation of the grain distribution in two population, one of large grains ($a > 0.03\mu$m) and one of small grains ($a < 0.03\mu$m), is useful both in predicting observational properties of the extinction curve and in the understanding of the chemical reaction rate in the grain surface.

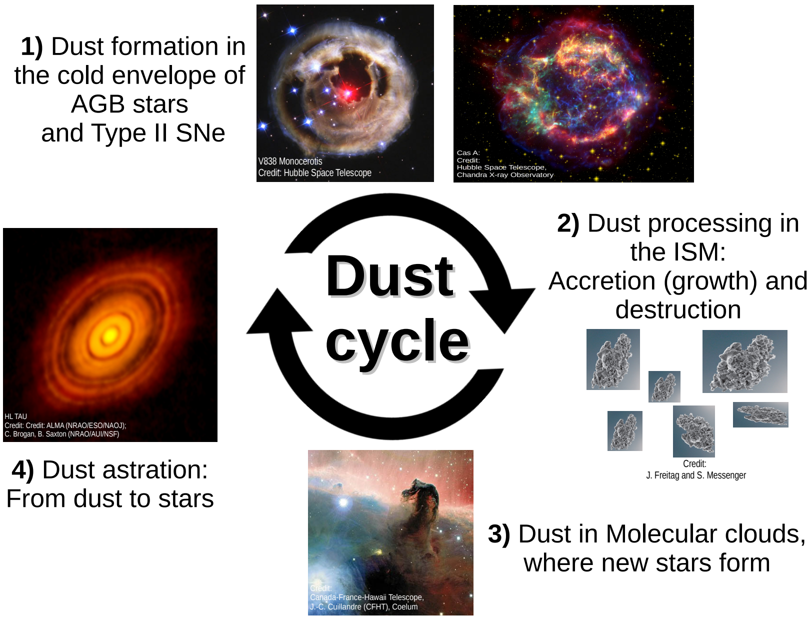

Figure 1.1: A cartoon representing the cycle of the dust in the interstellar medium.

All the studies in the last Century have led to the discovery of large properties and constraints of interstellar dust grains. However, the number of open questions is more than the answers, and a lot of work is still necessary to increase our understanding of cosmic dust.

1.1.2 Dust observations and properties

Dust is composed by particles ranging sizes from $\sim 10\mu m$ down to molecules containing tens of atoms $\sim 10nm$. The dust extinction consists in the light obscuration of background objects. The light attenuation is wavelength-dependent and it is determined by the grain size distribution: the extinction tends to be larger in the blue than in the red wavebands, and therefore dusty environments appear redder than dust-poor ones (reddening phenomenon). Dust extinction therefore plays a crucial role in the observation of the Universe.

Our understanding of dust composition comes from the analysis of the spectral features observed in extinction curves, scattering and thermal emission by interstellar grains. Direct analysis of dust grains is accessible from meteorites (Kissel et al., 1986; Clayton & Nittler, 2004; Messenger et al., 2013) or by the collection of incoming grains in the atmosphere of the Earth by stratospheric-flying airplanes (Sandford, 1987), even if these grains are subject to severe selection effects and cannot be considered representative grains of the ISM (Draine, 2003). However, despite the huge amount of data we have collected, we are far away to have a model able to explain the real composition of dust (Jones, 2013)

The study of the extinction curve is one of the most important to con-

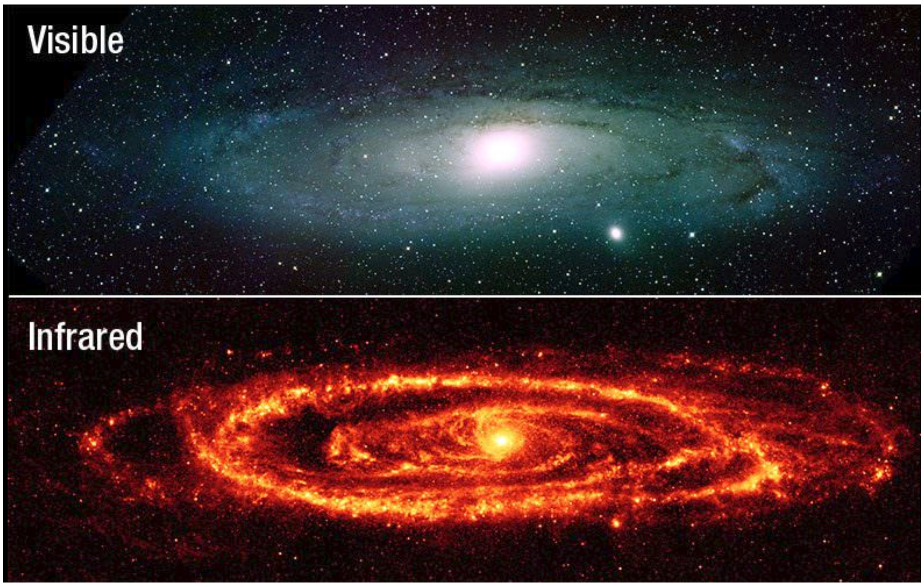

Figure 1.2: The Andromeda Galaxy, as it appears in the optical (upper panel) and in the sub-millimeter wavelengths (bottom panel). Credit: Kitt Peak National Observatory

strain the properties of the interstellar dust. In fact, the features in the extinction curve change with the composition and the size distribution of the grains. The extinction depends on the wavelength λ and it is defined as $A_\lambda = 2.5\log_{10}(F^0_{\imath ambda}/F_\lambda)$, where F_λ is the observed flux and F^0_λ is the flux in the absence of extinction (Draine, 2003). Usually, the reference flux is constrained by the observation of a star (or a general astronomical object) that has a negligible foreground dust (the pair method). As we have already pointed out, the net effect of extinction is to decrease (obscure) the luminosity of background sources in the UV/optical band and increase the emission in the infrared and sub-millimeter wavelengths. In this way, one of the most simple evidences of the presence of dust is the observation of the reddening of an astronomical object. For instance, in Fig 1.2, we show an image of Andromeda galaxy, as seen in the optical and in the sub-millimeter wavelengths. The contribution to the optical light is mainly provided by stars in the galaxy, whereas the sub-millimeter one is mainly caused by dust emission. The black features observable in the optical match with the presence of dust: in fact, these observed regions correspond to the emission in the sub-millimeter image, and this effect is caused by the absorption and re-emission of the stellar light by dust.

The extinction curve does not shape in an only-one way and it varies depending on the line of sight and in different astronomical objects. This suggests that dust may vary depending on the physical conditions of the ISM. As an example, in Fig 1.3 we show the extinction curves of the Milky Way and the Magellanic clouds. The Milky Way curve shows a broad peak corresponding to the wavelength of 2175 Å, where it reaches a local maximum and then it decreases: the nature of this “2175 extinction bump“ it is not completely understood, but it has been associated to the presence of grains of carbonaceous

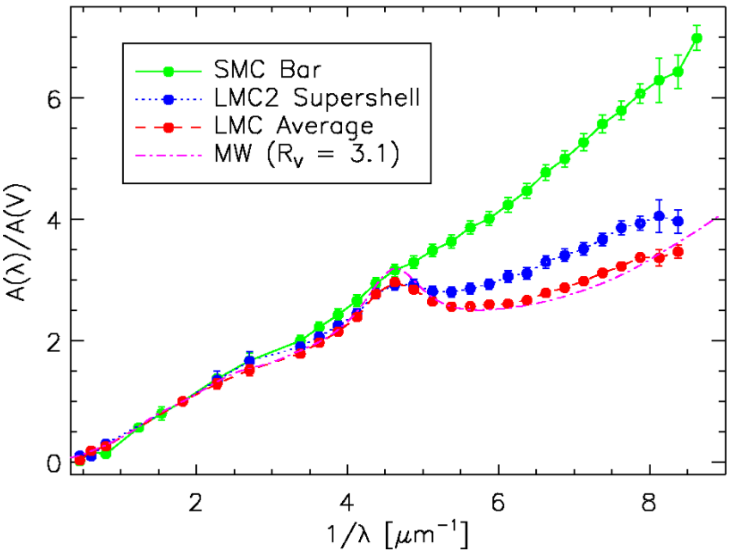

Figure 1.3: Extinction A(λ) normalized to the extinction in the V-band A(V) as a function of λ^{-1}. The extinction curves represent the ones of the Milky Way (MW) and the Magellanic Clouds (SMC and LMC). R_V is defined as $R_V = A_V/E(B-V)$, namely ratio between the extinction in the V-band and the color index (B-V). Credit: Gordon et al. (2003)

type, i.e. carbonaceous grains (graphite or large Polycyclic Aromatic Hydrocarbon molecules, PAHs). On the other hand, the extinction curve of the Small Magellanic cloud is smoother than the previous one and linearly increases with $\sim \lambda^{-1}$. In the case of the SMC, the extinction bump is not visible and the visible trend can be reproduced by models which lack of small carbonaceous grains (Weingartner & Draine, 2001).

The observations in the IR or in the far-infrared (FIR) wavebands directly allow one to detect the dust thermal emission. By approximating the emitting dust energy with a blackbody, is possible to estimate the mass of the dust by the observed SED of a galaxy. This technique is one of the most adopted to constrain dust masses in galaxies, even if it is affected by several uncertainties (Jones, 2014; Galliano et al., 2011). In fact, the constraints on dust properties strongly depend on the adopted model and assumptions to fit a SED: the microscopic properties of the grains are still poorly known and Zubko et al. (2004) demonstrated an important degeneracy by presenting complete fits of the same data set, with five different dust compositions; the UV to millimeter (mm) opacities are sensitive to the grain composition, which is derived from sparse constraints including astrophysical features, laboratory spectra of analogs of interstellar dust materials, and theoretical solid state physics (e.g. Weingartner & Draine, 2001); furthermore there may be variations in the grain properties as functions of the physical condition of the environment, i.e. the effect of dust destruction in HII regions (e.g. Madden et al., 2006), the coagulation of dust grains in dense regions (e.g. Stepnik et al., 2003; Berné et al., 2007), the evolution of dust abundances with the metallicity of the ISM (e.g. Galliano et al., 2005) and the transition from amorphous to crystalline dust (silicates) observed in protostars (e.g. Hallenbeck et al., 2000; Poteet et al., 2011). These uncertainties can be misleading and may lead to inaccurate constraints on the properties of dust, especially when considering the whole integrated SED of a galaxy (Galliano et al., 2011). For instance, Rémy-Ruyer et al. (2014) adopted two dust models which assume two different compositions of carbon-rich dust, one with graphite and another one with amorphous carbonaceous grains: both models are able to fit the observations, but provide estimated dust masses which differ by a factor of 2.5. Furthermore, the dust emissivity in dense clouds is different from that in the diffuse interstellar medium (Martin et al., 2012; Ysard et al., 2012). In this way, different regions would have different SEDs, and therefore is essential to consider each peculiar environment in these analysis (Fanciullo et al., 2013; Jones, 2013).

The study of the Universe in the IR-window has made a breakthrough thanks to *Herschel Space Observatory* satellite, launched in 2009 (Pilbratt et al., 2010). It was the largest telescope ever sent into space and it was designed primarily to observe in the FIR ($50\mu m \geq \lambda \geq 200\mu m$) and sub-millimeter wavelengths ($200\mu m \geq \lambda \geq 1000\mu m$). Herschel stopped its operations in 2013, but its data remain of fundamental importance in the study of dust when combined to other surveys. In fact, in order to study dust properties from the SED of galaxies, data in a wide waveband of the electromagnetic spectrum are needed. In this way, it is possible to estimate the amount of emission absorbed by dust at UV wavelengths and the re-emitted in the FIR and sub-millimeter (e.g. Silva et al., 1998). DustPedia group[1] (Davies et al., 2017) is now actively in this kind of study: they take advantage of various surveys that operate at different wavelengths such as the *Wide-field Infrared Survey Explorer* (WISE Wright et al., 2010), the Herschel Space Observatory, the *Plank* mission or the *Galaxy Evolution Explorer* (GALEX), and started an ambitious project which aims at measure the complete UV-mm spectral energy distribution of a large sample of galaxies (> 1000) of different morphological type.

Beyond orbiting satellites, the *Atacama Large Millimeter/sub-millimeter* Array (ALMA) is a very important instrument able to provide ground based high resolution millimeter and sub-millimeter measurements. The array is composed by 66 antennas and achieves interferometric measurements on a maximum baseline of 16 Km. The high spatial resolution and sensitivity of ALMA is unachievable by current orbiting telescopes and it has proved to be very useful for the study of the molecular complexity in the ISM and for the detection of dust in high redshift galaxies.

Dust properties are influenced by the physical condition of the ISM and therefore is extremely important to know the best we can the environment in which dust is located. A study of the chemical composition of the ISM can be useful to constrain the composition of dust grains. The chemical composition of the ISM is inferred from spectroscopic measurements in the UV/optical: light coming from a background source is absorbed by atoms that reside in the intervening medium and provokes an absorption feature in the spectrum. However, this physical phenomenon only reveal the composition of the gas phase of the

---

[1] http://www.dustpedia.com/

ISM, leaving undetected the elemental particles embedded in the dust phase. Because the atoms locked into dust are not detected, the measured abundances appear to be depleted. Jenkins (2009) presented the systematic patterns for the depletion of 17 elements along 243 different sightlines. He defined the logarithmic depletion of an element as the difference between the reference abundance and the observed one:

$$(X_{gas}/H)_{dep} = log\left(\frac{N(X)}{N(H)}\right)_{obs} - log\left(\frac{X}{H}\right)_{ref}, \tag{1.1}$$

where N(X) is the column density of an element X, N(H) is the total hydrogen abundance and the last term on the right side of the equation represents the reference abundance ratio. The reference value can be associated to the Solar elemental abundances (e.g. Anders & Grevesse, 1989; Lodders, 2003; Asplund et al., 2005, 2009), even in this case it is implicitly assumed that the observed abundances should reflect the ones of the Solar neighborhood. However, different galaxies have different metallicities and chemical composition, and therefore the elemental depletion can be calculated using as reference abundances the ones predicted by chemical evolution models, rather than the Solar values (Vladilo et al., 2011).

It is not simple to assert what does cause elemental depletion, but there are some evidences that prove its connection with dust. One is that high depletions are observed in high density environments, where dust is self-shielded and can more easily grow (Snow et al., 2002; Jenkins, 2009). Another one is that some elements are more depleted than others, as expected on the basis of their condensation temperature (Field, 1974; Savage & Sembach, 1996). The condensation temperature T_c of a chemical compound is defined as the temperature at which 50% of the element has been removed from the gas phase because of condensation (e.g. Lodders, 2003). An element with a relative high T_c is called "refractory" (such as Si, Mg and Fe), whereas one with a lower T_c is called "volatile" (such as Zn, S or P). Refractory elements are the ones with larger depletions and therefore associated to the elements that compose dust grains. In this way, depletion studies are fundamental because can constrain the elemental composition of interstellar dust (stoichiometry); from these studies emerge that dust composition is dominated by C, O, Si, Mg and Fe elements.

Si and Mg elements represent two of the major constituents of silicates, and their depletion can give an idea of the total fraction of silicate-type dust (e.g. Kemper et al., 2004; Ueda et al., 2005; Voshchinnikov & Henning, 2010). Fe is another fundamental element locked up in silicates, even though its high depletion factor suggests that it may be incorporated in other dust species, composed by metallic particles (e.g., Wickramasinghe & Wickramasinghe, 1993; Dwek, 2004; Sofia et al., 2006; Voshchinnikov & Henning, 2010; Draine & Hensley, 2012, 2013; Dwek, 2016). Unfortunately, elemental depletions do not provide any information about the chemistry and grain mineralogy (Jones, 2014).

A way to probe the reliability of grain models is to compare laboratory measurements with astronomical observation. Measurements on laboratory analogues of interstellar silicates have been performed at the FIR and sub-millimeter wavelengths, which enable us to better constrain the properties of interstellar dust (e.g. Agladze et al., 1996; Mennella et al., 1998; Boudet et al., 2005; Coupeaud et al., 2011).

Nowadays, new development on the X-rays facilities can improve even more our understanding of dust composition. Astronomical observations in the X-rays wavebands (>600 eV or <2 nm) are very important to constrain the composition of dust grains. If an X-ray emitter is located behind a layer of dust, its radiation will be absorbed and at the same time scattered at small angles, into the direction of the observer (Overbeck, 1965). Through the analysis of the absorbed spectrum, many informations are achievable such as the chemistry of dust, the depletion in the ISM, the distribution and the abundances of the dust grains along the line of sight (Costantini et al., 2005). The ESA *XMM-Newton* and NASA *Chandra* missions marked the beginning of a new investigation in X-ray astronomy in the study of interstellar dust (e.g. Yao et al., 2003; Smith et al., 2006; Tiengo et al., 2010). Furthermore, future X-ray missions (e.g. *Athena*) will enhance the sensitivity at harder X-rays (E>1keV) and will be able to study in detail the dense environment through the Galactic center.

Historically, X-rays observations has been used to provide quantitative tests on the interstellar grain models (Draine, 2003). However current laboratory measurements are compared with astronomical data by using synchrotron emission on material samples of similar composition of interstellar dust, helping in the determination of the real composition of these grains (Zeegers et al., 2017).

1.2 Computing dust evolution in the ISM through chemical evolution models

The evolution of chemical abundances is fundamental to understand the evolution and the formation of galaxies.

The chemical composition of stars indicates the composition of ISM at the time of their birth. These chemical signatures can be seen as “astronomical fossils”, which inform us on how the chemical composition has changed during the history of a galaxy. In the field of Astroarcheology, chemical evolution models study the evolution of galaxies from these observables. In fact, the abundances of the main chemical species in stars and diffuse gas represent a key tool to reconstruct the evolution of galaxies. The abundance ratios of different elements, the radial distribution of the metallicity or the different chemical composition in galaxies of different morphological type can be explained by different star formation histories (SFHs) (Matteucci, 2001; Pagel, 2009; Matteucci, 2012).

The primordial chemical composition is defined as the composition of the ISM during the Big Bang, before the formation of stars and galaxies. Following the Big Bang, the physical conditions of the Universe did not allow the formation of all the elements we observe at the present time. In the Big Bang only light elements formed (such as hydrogen, deuterium, helium and a very tiny fraction of lithium), because the temperature rapidly decreased as a consequence of the expansion of the Universe, making the formation of heavier elements impossible. All the elements with $A \geq 12$ starting from carbon to uranium and beyond have been synthesized inside the stars and their sum in Astronomy is called *metallicity* and indicated with capital Z.

After the formation of a star in the ISM, nuclear reactions in its internal regions of the star modify the chemical composition of the gas. Furthermore, during their life, stars expel in the ISM part of their mass, containing new and old elements. Depending on stellar properties (mass and metallicity), different type of stars eject different quantities of masses (from a small fraction to almost their total mass) with different chemical features and on different time-scales (Woosley & Weaver, 1995; van den Hoek & Groenewegen, 1997; Kobayashi et al., 2006; Karakas, 2010; Nomoto et al., 2013). For instance, low and intermediate stars ($0.8 \leq M/M_{\odot} \leq 8.0$) have typical life-times >30 Myr and mainly produce He, C and N (plus some CNO isotopes and s-process elements, A>90), whereas massive stars ($8 \leq M/M_{\odot} \leq 40$), which have shorter time-scales $\leq$ 30Myr mainly produce α-elements (O, Ne, Mg, Si, S, Ca) and some Fe-peak elements. As time passes by, more and more stellar generations succeed to one another and the new ones form out of gas enriched in heavy elements by the previous generations. In this way, stars transform the chemical composition of the ISM and play the most important role in the chemical evolution of galaxies. This is what we intend for "chemical evolution".

The history of star formation is one of the main drivers of chemical evolution since the number of stars formed (the star formation rate) and the distribution of stars as a function of their mass (the initial mass function) are regulating the rate of chemical enrichment at any cosmic time. Models of chemical evolution of galaxies aim at reproducing the abundance patterns in stars and gas and since they strongly depend on stellar nucleosynthesis, SFH and possible gas flows inwards and outwards, we can reconstruct the history of formation and evolution of galaxies by studying their chemical abundances. The well-known diagram abundance ratios vs. metallicity ([Fe/H]) depends on stellar nucleosynthesis but also on the star formation history of the peculiar galaxy (e.g Matteucci & Brocato, 1990; Ballero et al., 2007; Lanfranchi & Matteucci, 2010; Romano et al., 2010; Matteucci, 2012; Vincenzo et al., 2014): this allows us to identify a galaxy type by its abundance pattern and also to reconstruct the star formation rate and the formation time-scale (Matteucci, 2012).

Chemical evolution models have been widely adopted to study the properties of dust in the ISM. In fact, these models study the evolution of the metal content in a galaxy, which represents the main constituent of dust grains.

To compute the evolution of dust in galaxies one needs to compute first the evolution of metals in the ISM. It is of great importance to follow the evolution of the abundances of the main metals (C, N, O, Mg, Si, S, Ca, Fe, Ni, Zn) in galaxies and in parallel to compute the evolution of dust which is composed of the refractory elements such as Si, Mg, Fe and to a lesser extent C and O. An advantage of this approach is that it naturally includes constraints on the elemental abundance of the interstellar dust mixture, which is necessary to study the variation of its amount and chemical composition. In this way, chemical evolution models are not only important to constrain the formation and evolution of galaxies, but they also play a key role in the study of the interstellar dust.

Dwek & Scalo (1980) developed a model of the life cycle of refractory grains in the solar neighborhood, by including the main processes of the dust cycle, i.e. dust destruction and dust growth in the ISM. This model, based on the chemical evolution of the Milky Way, has been the first one that accounted for global processes such as the star formation and galactic inflows and outflows to study the dust content. Later on, Dwek (1998) adopted the same approach of Dwek & Scalo (1980) and studied the evolution of dust at Galactic scale. He presented the elemental abundances both in the gas and the dust phase of the ISM of the Galaxy and compared them with the observed elemental depletion in the solar neighborhood. Since these pioneering works, significant progress has been made concerning dust properties, both in theory and in observations, and nowadays new theoretical prescriptions about dust processing have appeared in more recent papers (Inoue, 2011; Piovan et al., 2011; Asano et al., 2013; Hirashita, 2013; Mattsson, 2015). Beyond the Milky Way, other works focused on the study of other objects, such as the dust evolution in late-type dwarf galaxies and the Large Magellanic Cloud (Zhukovska, 2014; Zhukovska & Henning, 2013). Calura et al. (2008) studied the dust evolution in galaxies of different morphological type: they made the same assumptions of Dwek (1998) about the processes producing and destroying dust, and investigated how different SFHs influence the evolution of some dust properties such as the total mass, the elemental depletion, the dust-to-gas ratio and the dust-to-metal ratio. Zhukovska et al. (2008) developed a model for calculating the chemical evolution of the Milky Way disk and the dust content of the interstellar medium. At variance with Dwek (1998) and Calura et al. (2008) they adopted different dust prescriptions concerning the dust formation by stars: concerning AGB stars they used Ferrarotti & Gail (2006) prescriptions, who combine synthetic AGB evolution models with models for circumstellar dust shells that include dust formation in the stellar wind; for Type II SNe, they provide new dust yields by the study of the observed abundances of pre-solar dust grains.

In these models, the evolution of interstellar dust is incorporated in one-zone model of the chemical evolution of galaxies, and consider dust properties averaged over the whole galaxy. Zhukovska et al. (2016) developed a new model with the inclusion of hydrodynamical simulations and able to follow the dust evolution in galaxies in a multi-phase inhomogeneous ISM. Hydrodynamical simulations are often used beside chemical evolution models to include the complex physical processes occurring in the different phases of the ISM (e.g. Bekki, 2013; Zhukovska et al., 2016; Aoyama et al., 2017).

Chemical evolution models have become more and more important in the study of the elemental depletions in the ISM. At variance with stellar abundances, the chemical composition of the ISM only reflects part of the total elemental abundance. In fact, the gas abundances of some specific metals (the refractory ones, defined before) are depleted into dust grains, leaving them undetectable from optical/UV spectroscopic measurements. In this way, it is extremely important to take into account the presence of dust, as it can affect our interpretation of observational data. This is particularly important in the observations of high redshift Universe, where the only chemical abundances we derive are from the gas. Damped Lyman Alpha systems (DLAs) represent very useful tools to study these abundances. These systems are QSO-absorbers characterized by a neutral hydrogen column density $\log N(H_I) > 20.3$ (Wolfe et al., 1986, 2005) and lie in a redshift range between $1.6 \leq< z \leq 5$. They are the best observables available of the ISM in the high redshift Universe and, thanks to high resolution spectroscopy in the optical/UV wavebands, it is possible to measure high precision column densities from their spectra. Observations show a variation in metallicity during the cosmic time, revealing that they can be seen in different stages of their evolution (e.g. Prochaska et al., 2003; Cooke et al., 2015, 2017; Rafelski et al., 2012). In this way, for chemical evolution models, DLAs represent an extremely important class of objects to study the evolution of the metallicity and the properties of dust (e.g. Matteucci et al., 1997; Calura et al., 2003; Vladilo et al., 2011).

The study of dust evolution at high redshifts has been studied by many authors in a cosmological framework (e.g. Dayal et al., 2010; Valiante et al., 2011; de Bennassuti et al., 2014; Bekki, 2013, 2015). Cosmological simulations can study how dusty systems can from at high redshift and how their dust content evolves in time, both in the ISM and in the intergalactic medium (IGM) (e.g. Zu et al., 2011; Kimm & Cen, 2013; McKinnon et al., 2016; Aoyama et al., 2017).

During the past years, several studies tried to assess the total amount of dust in the Universe at different scales and redshifts (Fukugita, 2011; Ménard & Fukugita, 2012; De Bernardis & Cooray, 2012; Clark et al., 2015). Recently, Popping et al. (2016) used a semi-analytical model of galaxy formation to study the dust content in cosmological volumes: their study confirmed that dust accretion is a necessary ingredient to reproduce the buildup of dust in galaxies. McKinnon et al. (2016) studied the distribution of dust in a cosmological hydrodynamical simulation: their model fails in reproducing dust-rich galaxies at high redshift, even when a top heavy IMF is adopted, but they obtained a good agreement with the low redshift observations of the comoving dust density Ω_{dust} (defined as the ratio between the density of the total dust mass in the Universe and the critical metallicity).

However, even in a cosmological context, chemical evolution models are very promising: Grieco et al. (2014) used chemical evolution models with dust to compute the cosmic dust rate (CDR) as the result of the contribution of galaxies of different morphology. For this purpose, they assumed two different scenarios of galaxy formation, which mimic the monolithic and hierarchical formation theories. Their estimate of the dust comoving density was larger than observed and the two different scenarios led to a very different behavior of the dust rate as a function of redshift.

1.2.1 Plan of the thesis

In this thesis we present a new chemical evolution model which takes into account the presence of dust, according to the most updated prescriptions for its formation and ISM processing, and we investigate many issues related to dust in galaxies of different type and at different redshifts. In particular, we intend to study the evolution of dust and gas chemical composition in different galaxies. We adopt updated prescriptions relative to Dwek (1998) and Calura et al. (2008) for dust formation in AGB stars and Type II SNe (as suggested in Piovan et al. 2011), as well as for dust processes in the ISM, i.e. dust accretion and destruction (Asano et al., 2013). Our model can follow the evolution of 30 chemical elements during the galactic time both in the gas and in the dust phase of the ISM.

We study the chemical evolution and dust properties in galaxies of different morphological type, i.e. ellipticals, spirals, and irregulars. The main difference between galaxies is the star formation history: in particular, in spheroids (ellipticals and bulges) it is assumed a very fast star formation rate, and this rate decreases going towards spirals, irregulars and smaller galaxies. Our models reproduce the main chemical features of ellipticals (Pipino & Matteucci, 2004; Pipino et al., 2011), spirals (Chiappini et al., 1997; Spitoni & Matteucci, 2011; Micali et al., 2013) and irregulars (Bradamante et al., 1998; Vladilo et al., 2011). We relax the instantaneous recycling approximation and stellar life-times are taken into account. In this way, we can predict in detail the evolution of the abundances of single elements and easily compare the dust contribution from various sources (AGB, Type II SNe and dust accretion), as well as their metal enrichment.

Our work investigates many dust-related issues at various scales: Chapter by Chapter we present many different studies and results, from the dust grain composition in low-mass and low-luminosity galaxies to the total amount of dust in the starburst of elliptical galaxies, until the estimate of the cosmic dust rate and budget in the Universe.

In Chapter 2 we present a detailed description of our new chemical evolution models and the adopted prescriptions for the inclusion of dust processes, i.e. dust stellar formation, dust accretion and dust destruction.

In Chapter 3 we study the evolution of dust rates (formation, accretion and destruction) predicted by our model for a typical dwarf irregular galaxy and compare our results with previous works. Then, we study the depletion patterns of refractory elements (Si, Mg and Fe), by comparing our model with chemical abundances of DLAs, which are associated to dwarf irregular galaxies (Møller & Warren, 1998; Matteucci et al., 1997; Molaro et al., 2000; Fynbo et al., 2010; Cooke et al., 2015). In this context, we investigate both the element-to-element abundance ratios in the gas phase and in dust grains, by means of a new method based on DLA column density measurements and the ratio between volatile and refractory elements.

In Chapter 4 we study the dust evolution in the Milky Way in the context of the Galactic Habitable Zone, defined as the region in the Galaxy with high enough metallicity to form planetary systems capable of sustaining life (Gonzalez et al., 2001). Dust plays a very important role in the study of planet formation: in fact, it represents the necessary building block to form more massive and extended objects (planetesimals) that can grow to form planets. In particular, the dust-to-gas ratio is a fundamental parameter, adopted in models of planetary systems formation. By means of our model, we intend to connect the dust-to-gas ratio (a fundamental parameter used in models of planetary systems formation) to the metallicity [Fe/H] (an observable of the host star).

In Chapter 5 we focus on the evolution of the mass of dust in elliptical galaxies. We investigate the main process responsible for the presence of large dust masses observed in the high redshift Universe. Furthermore, we cast light on the time-scale formation for dust in such high redshift systems and we quantify the amount of dust formed by different kind of stellar sources, i.e. AGB stars, Type II SNe and Type Ia SNe.

In Chapter 6 we first study the relation between the dust-to-gas ratio and the metallicity observed in irregulars and spiral galaxies to perform a fine-tuning of the dust parameters in our model. Then, we study the cosmic dust rate (CDR) as the result of the contribution to dust, during the cosmic time, from galaxies of different morphological type. For this purpose, we assume different scenarios for the evolution of the number density of galaxies of each morphological type: a pure luminosity scenario (PLE) in which the number density of spirals, ellipticals and irregulars is constant in time, a number density evolution scenario (DE), as suggested by the classical hierarchical clustering scenario in the framework of the ΛCDM paradigm and an alternative scenario, where the number densities of ellipticals and spirals evolve as suggested by observations. Moreover, always in the framework of these scenarios we study the cosmic evolution of other quantities which are strictly related to the CDR, namely the cosmic star formation rate and the mean metallicity of the Universe.

Finally, in Chapter 7 we summarize the main results of this thesis.

Chapter 2

A new model of galactic chemical evolution with dust

2.1 Chemical evolution model

To study the evolution of chemical abundances we use self-consistent chemical evolution models, in which the instantaneous recycling approximation (IRA) is relaxed and the stellar lifetimes are taken into account.

The birthrate function represents the number of stars formed in the mass interval m and $m + dm$ in the time range between t and $t + dt$. It depends on two physical quantities, the star formation rate ($SFR = \psi(t)$) and the stellar initial mass function (IMF=$\phi(m)$):

$$B(m, t) = \psi(t)\phi(m) \tag{2.1}$$

The star formation rate determines the rate at which the stars form and it is usually expressed in solar masses per year. We adopt a simple Schmidt law for the SFR:

$$\psi(t) = \nu G(t)^k, \tag{2.2}$$

where ν is the *star formation efficiency* $[Gyr^{-1}]$ and the parameter k is set equal to 1. $G(t)$ is the mass fraction of the ISM relative to the total mass accumulated up to the present time, $G(t) = M_{ISM}(t)/M_{tot}(t_G)$. The star formation efficiency, defined as the SFR per unit mass of gas, can assume very different values depending on the morphological type of the modeled galaxy. Its inverse represents the time scale at which the total amount of gas is converted into stars. In this work, the initial mass function is assumed to be constant in space and time and normalized to unity in the mass interval between 0.1 and 100 $M_\odot$. In this work, we will adopt the Salpeter (1955) IMF:

$$\phi_{Salp}(m) \propto m^{-(1+1.35)} \tag{2.3}$$

and the Scalo (1986) IMF, characterized by a two slope power law:

$$\phi_{Scalo}(m) = \begin{cases} 0.19 \cdot m^{-(1+1.35)}, & for \;\; m < 2M_\odot \\ \\ 0.24 \cdot m^{-(1+1.70)}, & for \;\; m > 2M_\odot \end{cases} \tag{2.4}$$

In the next section we will show and discuss the basic equations used in the chemical evolution code which take into account the evolution of stars, SNe feedback, galactic winds and the infall of primordial gas.

2.1.1 Basic equations

Let us define $G_i(t) = G(t)X_i(t)$ as the fractional mass of the element i at the time t in the ISM, where $X_i(t)$ represents the abundance of the element i in the gas at the time t. The temporal evolution of $G_i(t)$ is described by the following expression:

$$\dot{G}_i(t) = -\psi(t)X_i(t) + R_i(t) + \dot{G}_{i,inf}(t) - \dot{G}_{i,w}(t), \tag{2.5}$$

1. The first term represents the rate at which the fraction of the element i is removed by the ISM due to the SFR.

2. $R_i(t)$ is the returned mass fraction of the element i injected into the ISM from stars thanks to stellar winds and SN explosions. This term takes into account nucleosynthesis prescriptions concerning stellar yields and supernova progenitor models. $R_i(t)$ can be described as in Matteucci & Greggio (1986):

$$\begin{aligned} R_i(t) = &+ \int_{M_L}^{M_{B_m}} \psi(t-\tau_m)Q_{mi}(t-\tau_m)\phi(m)dm + \\ &A \int_{M_{B_m}}^{M_{B_M}} \phi(m) \cdot \left[\int_{\mu_{min}}^{0.5} f(\mu)\psi(t-\tau_{m2})Q_{mi}(t-\tau_{m2})d\mu \right] dm \\ &+ (1-A) \int_{M_{B_m}}^{M_{B_M}} \psi(t-\tau_m)Q_{mi}(t-\tau_m)\phi(m)dm \\ &+ \int_{M_{B_M}}^{M_U} \psi(t-\tau_m)Q_{mi}(t-\tau_m)\phi(m)dm \end{aligned} \tag{2.6}$$

The first term on the right side of eq. 2.6 takes into account the enrichment of the element i restored in the ISM by individual stars with a mass range between M_L and M_{B_m}, which are respectively the minimum mass of a star contributing to the chemical enrichment of the ISM ($M_L = 0.8M_\odot$) and the minimum mass of a binary system that can give rise to Type Ia SNe ($M_{B_m} = 3M_\odot$). $Q_{mi}(t-\tau_m)$, where τ_m is the lifetime of a star of mass m, contains all the information about stellar nucleosynthesis for elements produced or destroyed by nuclear reactions inside each single star and injected into the ISM (Talbot & Arnett, 1971). The second term gives the enrichment due to binary systems originating Type Ia SNe. For this type of SNe the single degenerate scenario is assumed, where a single C-O white dwarf explodes by the C-deflagration mechanism, (Whelan & Iben, 1973) after having exceeded the Chandrasekhar mass ($1.44 M_{\odot}$). A is a parameter representing the unknown fraction of binary stars giving rise to Type Ia SNe and it is fixed by reproducing the observed present time SN Ia rate. $\mu = M_2/M_B$ is defined as the ratio between the secondary component of the system over the total mass, and $f(\mu)$ represents the distribution of this ratio. M_{B_M} is the mass limit of the system and it is set to $16 M_{\odot}$: in fact, if one of the two stars in the system exceeds the mass of $8 M_{\odot}$, a Type II SN would result. Finally, τ_{m2} is the lifetime of the secondary star of the binary system, or rather the explosion timescale. The third term of Eq.(2.6) represents the enrichment due to stars in the mass range $M_{B_m} - M_{B_M}$, which are single, or if in binaries, do not produce an explosion of SN Ia. In this mass range, stars with $m > 8 M_{\odot}$ explode as Type II SNe. The fourth term of Eq.(2.6) concerns the stars with masses above M_{B_M} and lower than $100 M_{\odot}$: all these stars explode as core-collapse SNe.

3. The third term of Eq.(2.5) represents the rate of the infall of the element i. The infalling gas is not pre-enriched and consists in a pure primordial composition. The infall rate follows a decaying exponential law characterized by the *infall time-scale* τ:

$$\dot{G}_{i,inf}(t) = \frac{\Gamma X_{i,inf} e^{-t/\tau}}{M_{tot}(t_G)} \tag{2.7}$$

   where Γ is the normalization constant constrained to reproduce the total mass at the present time. The time-scale of the infall τ is a free parameter which is fixed by reproducing the observed infall rate of the studied galaxy.

4. The last term of Eq.(2.5) concerns the outflow of the element i due to galactic wind which occurs when the thermal energy of the gas heated by SN explosions exceeds its binding energy. The rate of the gas lost via galactic wind is proportional to the SFR and it is described as follows:

$$\dot{G}_{i,w}(t) = \omega_i \psi(t), \tag{2.8}$$

   where ω_i is a parameter which can be fixed or can variate depending on the elements in the case of differential wind.

Nucleosynthetic prescriptions

Stars reprocess the ISM and contribute to the chemical enrichment of a galaxy. The stellar yields represent the amount of both newly formed and pre-existing elements injected into the ISM by the stars when they die. In our model we adopt different stellar yields for the contribution of low mass stars, Type Ia and Type II SNe:

1. For low and intermediate mass stars (*LIMS* with masses $0.8 M_{\odot} < m < 8 M_{\odot}$) we use the metallicity-dependent yields of van den Hoek & Groenewegen (1997).

2. We assume that massive stars ($m > 8M_{\odot}$) explode as core collapse SNe adopting the yields suggested by François et al. (2004), who performed an empirical modification to the ones of Woosley & Weaver (1995). In the case of sulfur we adopted the yields suggested in Vladilo et al. (2011).

3. For Type Ia SNe we assume the yields of Iwamoto et al. (1999).

2.2 Dust chemical evolution model

The evolution of dust is one of the most critical issues in Astrophysics. It is first produced by different types of stars, but during the galactic evolution, several physical phenomena critically modify the ISM and therefore the interstellar dust. In particular, astronomical observations and pre-solar grains analysis from meteorites indicate that physical processes responsible for the evolution of dust can be divided in two groups. The first takes into account all the mechanisms which change the total dust mass (destruction processes and grain growth by accretion), while the second group includes processes, like shattering and coagulation (Asano et al., 2013), which affect the grain size distribution. This work considers the evolution of the total amount of dust and its chemical composition during the cosmic time, so all the processes affecting the grain-size distribution are not taken into account.

We use the same approach first used by Dwek (1998) later adopted in C08 (hereafter D98 and C08, respectively) and more recently by Grieco et al. (2014). The equation for the dust evolution is similar to Eq.(2.5), but it includes all the physical processes which change the mass distribution of dust in the ISM, beside dust production by stars. Defining $G_{i,dust} = X_{i,dust} \cdot G(t)$ as the normalized mass of the element i at the time t in the dust phase, we can write:

$$\begin{aligned}\dot{G}_{i,dust}(t) = -\psi(t)X_{i,dust}(t) + R_{i,dust}(t) + \left(\frac{G_{i,dust}(t)}{\tau_{accr}}\right) \\ - \left(\frac{G_{i,dust}(t)}{\tau_{destr}}\right) - \dot{G}_{i,dust}(t)_w,\end{aligned} \tag{2.9}$$

This equation takes into account all the processes which govern the so called dust cycle: the first term on the right side of the equation represents the rate at which the dust is removed from the ISM and utilized to form new stars (astration), whereas the second one gives the dust production rate of stars; the third and the fourth terms represent the processes which occur in the ISM and are dust accretion and destruction, respectively; the last term indicates the rate of dust expelled by galactic winds assuming dust and ISM to be coupled. In the next paragraphs we will discuss these terms in more details.

2.2.1 Dust formation

Asymptotic Giant Branch (AGB) stars and SNe represent the first environments where dust form: depending on the physical structure of the progenitor, various dust species can originate.

The second term in the right side of Eq.(2.9) deals with the dust production by stars and can be described by the following expression:

$$
\begin{aligned}
R_{i,dust}(t) = \\
&+ \int_{M_L}^{M_{B_m}} \psi(t-\tau_m)\delta_i^{AGB} Q_{mi}(t-\tau_m)\phi(m)dm \\
&+ A \int_{M_{B_m}}^{M_{B_M}} \phi(m) \cdot \left[\int_{\mu_{min}}^{0.5} f(\mu)\psi(t-\tau_{m2})\delta_i^{Ia} Q_{mi}(t-\tau_{m2})d\mu \right] dm \\
&+ (1-A) \int_{M_{B_m}}^{8M_\odot} \psi(t-\tau_m)\delta_i^{AGB} Q_{mi}(t-\tau_m)\phi(m)dm \\
&+ (1-A) \int_{8M_\odot}^{M_{B_M}} \psi(t-\tau_m)\delta_i^{II} Q_{mi}(t-\tau_m)\phi(m)dm \\
&+ \int_{M_{B_M}}^{M_U} \psi(t-\tau_m)\delta_i^{II} Q_{mi}(t-\tau_m)\phi(m)dm
\end{aligned}
\tag{2.10}
$$

This equation is the same as Eq.(2.6) with the addition of $\delta_i^{AGB}, \delta_i^{Ia}, \delta_i^{II}$: these terms are the so called dust condensation efficiencies and represent the fractions of an element i expelled from AGB stars, Type Ia and II SNe respectively, which goes into the dust phase of the ISM. In Eq.(2.10) we divided the third term of Eq.(2.6) into two integrals in order to separate the contribution between massive and low mass stars.

D98 and C08, in their works adopted arbitrary values for δ_i, based on simple assumptions: for low and intermediate mass stars ($0.8 - 8M_\odot$), δ_i^{AGB} were assumed equal to 1: it means that all the amount of carbon (C) and *silicate-elements* (O, Mg, Si, Ca, and Fe) produced by a single star condensate into the dust phase when the C/O ratio in the star ejecta is higher or lower than 1, respectively. For Type II and Type Ia SNe, δ_i^{II} and δ_i^{Ia} were set equal to 0.8 for both carbon and silicates.

In this work we adopt more recent and improved δ_i calculated by Piovan et al. (2011) (hereafter P11) for AGB stars and Type II SNe: these values depend on the mass and the metallicity of progenitor stars and have been derived from the comparison between theoretical studies and observational data. In the next paragraphs we will discuss the yields of dust by AGB stars and Type II SNe adopting these prescriptions and compare them with others widely employed in literature.

Dust from AGB stars

The cold envelope of AGB stars is a good environment in which nucleation and formation of the first dust-seeds can occur. The total amount of dust produced in the previous phases of these stars is negligible because of the low amount of material in their ejecta and because the physical conditions of their winds do not favor its formation (Gail et al., 2009). The dust species formed during the AGB-phase of low and intermediate mass stars (LIMS) strongly depend on their surface composition (Ferrarotti & Gail, 2006). The stellar mass and metallicity play a key role in the number of thermal pulses that occur in the

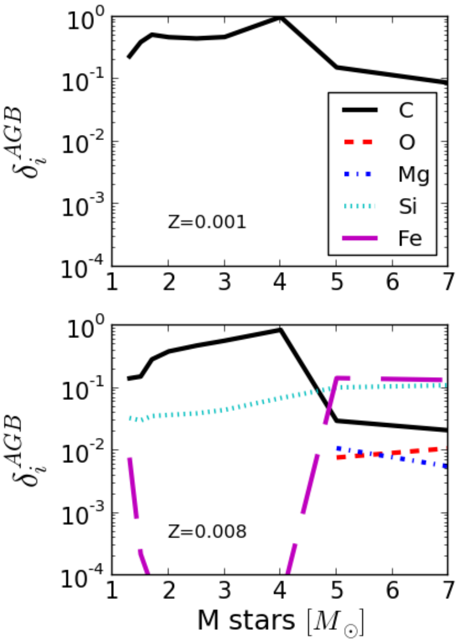

Figure 2.1: Condensation efficiencies of C, O, Mg, Si and Fe for AGB stars as reported in Piovan et al. (2011) for different metallicities. Black solid line for C, red dashed line for O, blue dash-dot line for Mg, cyan dotted line for Si and magenta long-dashed line for Fe. When condensation efficiencies are equal to zero, no lines are shown.

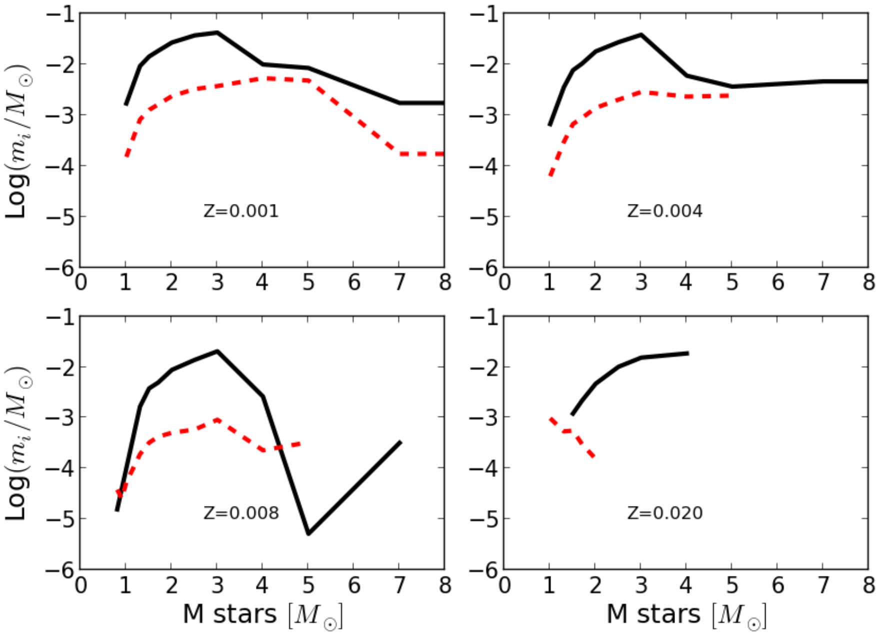

Figure 2.2: Newly produced carbon (black solid lines) and oxygen (red dashed lines) mass of dust for AGB stars as a function of the initial stellar mass for four different metallicities. The dust yields have been reproduced taking into account condensation efficiencies by Piovan et al. (2011) and stellar yields from van den van den Hoek & Groenewegen (1997).

AGB phase and determine the surface composition, and therefore, the formation of particular dust species (Ferrarotti & Gail, 2006; Gail et al., 2009; Nanni et al., 2013; Ventura et al., 2012; Dell'Agli et al., 2017).

In Fig. 2.1 we show the condensation efficiencies of AGB stars as predicted in P11 for carbon, silicon, magnesium, oxygen and iron, which are the elements we consider in this work. The δ_i^{AGB} values depend on the stellar mass and metallicity, thus accounting for the dependence of the C/O ratio in their surfaces. The δ_C^{AGB} dominates on δ_O^{AGB} at low metallicities and then decreases towards higher ones favoring the condensation of heavier elements (O, Mg, Si and Fe). This is in agreement with AGB models of Nanni et al. (2013), where C/O in the stellar surfaces decreases with the metallicity. In Fig. 2.2 we show the carbon and oxygen dust mass produced by AGB stars in the mass range $1 - 8M_\odot$: the yields peak at mass values between 2 and $3M_\odot$. Carbon is the only element with a non-negligible dust yield for two main reasons: it has a relatively high condensation efficiency and AGB stars are strong carbon producers. Carbon dust yields are comparable with the D98, Zhukovska et al. (2008) and Valiante et al. (2009) prescriptions. On the other hand, elements heavier than carbon have lower condensation efficiencies and yields (Romano et al., 2010), which cause the net separation between the carbon and silicate dust production. From Fig. 2.2, it seems that AGB stars are not able to form silicates. However, these dust yields reflect only the newly produced element abundance. Actually, our chemical evolution model also considers the fraction of the initial stellar mass that has not been processed in the inner region of the star and that during AGB-phases is expelled into the ISM: this returned mass composition reflects that of the star when it was formed, and could be chemically enriched by heavy elements. According to the differential condensation efficiencies, part of this mass can condensate, forming silicates in a non negligible mass fraction.

Dust from Type II SNe

Type II SNe are believed to cover an important role in dust production as witnessed by observations. Thanks to infrared and sub-millimeter studies, evidence of the presence of dust in the environment of historical supernova remnants like SN1987A (Danziger et al., 1991), Cas A and the Crab Nebula has been observed (Gomez (2013) and reference therein). Core collapse SNe are believed to be prolific dust factories: for instance, the origin of dust in QSO hosts at high redshift, can be only explained by a particular source able to reproduce a consistent amount of dust mass in less than 1 Gyr of cosmic evolution, in agreement with the typical time-scales of SNe.

However, we are far away to have a clear picture on the exact mass of dust ejected from SNe. In Fig. 2.3, we show the detected dust mass in SNe as a function of the mass of the progenitor, as provided by Schneider et al. (2014). The range of dust masses is wide and it varies between $\sim 0.01M_\odot$ and $\sim 0.7M_\odot$. In this way, it is difficult to predict, through models, an estimate of the real amount of dust formed in these objects. In particular, one of the fundamental uncertainty concerns how the mass of dust changes after the SN explosion (see later in the text).

Stars with masses higher than $8M_\odot$ can explode as Type II SNe in less than 30 million years (Matteucci & Greggio, 1986): for this reason, they are believed to be the main sources of dust in early epochs of galactic evolution

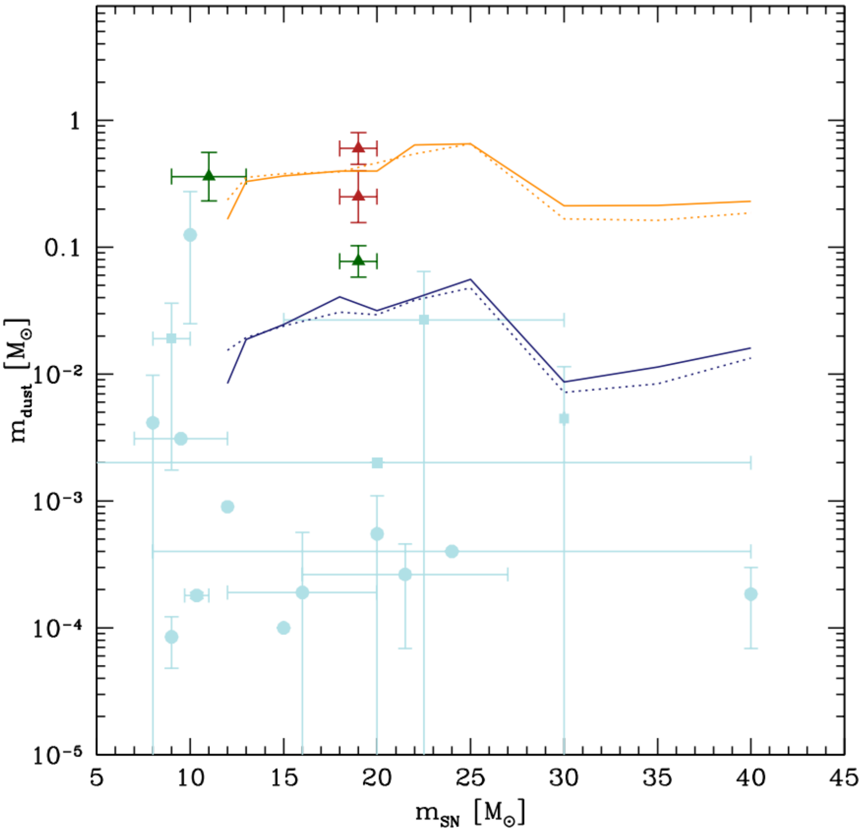

Figure 2.3: Mass of dust produced by SNe as a function of the mass of the progenitor star. The Figure is taken from Schneider et al. (2014) and it shows the data sample collected in Gall et al. (2011) and Otsuka et al. (2012). Green and red triangles indicate sources detected with Herschel in the Milky Way and in the Large Magellanic Cloud, respectively. The two lines represent the theoretical dust yields provided by Bianchi & Schneider (2007) for $Z = Z_\odot$, in solid, and $Z = 0.1Z_\odot$, in dashed. The upper and the lower lines represent the dust mass predicted before and after the passage of the reverse shock, respectively.

(e.g. Maiolino et al. 2006), although some other studies consider that either AGB stars (Valiante et al., 2009; Dwek & Cherchneff, 2011) or dust accretion (Piovan et al., 2011; Calura et al., 2014; Mancini et al., 2015, 2016; Ginolfi et al., 2017) might play a significant role in the dust enrichment of such high redshift objects. Even if Herschel, SCUBA and more recently ALMA are acquiring a great deal of data, it is not easy to give a satisfactory estimate of the total amount of dust produced from Type II SNe. In particular, it is unknown what is the real effect of the reverse shock which has a typical time scale of $10^3 - 10^4$yr, longer than the actual lifetime of historical SNe (Bianchi & Schneider, 2007; Bianchi et al., 2009; Hirashita et al., 2014).

In Fig. 2.4, dust yields from various authors are compared with the ones used in this work. Bianchi & Schneider (2007) revisited the previous work of Todini & Ferrara (2001) on Type II SNe dust yields predicting the formation of $0.1 - 0.6 M_\odot$ of dust in the ejecta of $12 - 40 M_\odot$ stellar progenitors. Considering also the presence of the reverse shock, they concluded that only between 2 and 20% of the initial dust mass can survive. In an independent work, Zhukovska et al. (2008) predict a similar amount of dust for such objects: their prescriptions come both from theoretical studies and observational data which include IR dust emission in SNRs, the amount of dust in historical SNe and studies on pre-solar grains in meteorites. Another important role is played by the environment surrounding the explosion of Type II SNe: the higher the density, the more resistance the shock will encounter and more dust will be destroyed (Piovan et al., 2011; Nozawa et al., 2007). On the other hand, in a lower density environment, dust can easily resist to the passage of the shock, causing a more efficient dust formation.

Also for Type II SNe we adopt the dust $\delta_i II$ predicted by P11, which are calculated by taking into account the above-mentioned studies on dust formation, destruction as well as the density of the environment in which the SNe explode. Black lines in Fig. 2.4 show the total dust production considering three different conditions for the density of neutral hydrogen, i.e. $\mathrm{n}_H = 0.1 - 1 - 10\,\mathrm{cm}^{-3}$. In low density environments the amount of dust produced is similar to the prescription of Todini & Ferrara (2001) and Bianchi & Schneider (2007), whereas in high density regions dust production becomes similar to the models where the reverse shock is included. In this work we adopt the yields of P11 corresponding to a neutral hydrogen density of $\mathrm{n}_H = 1\,\mathrm{cm}^{-3}$: with this selection we do not overestimate nor underestimate previous prescriptions for high mass progenitors.

Dust from Type Ia SNe

A separate discussion must be reserved to Type Ia SNe for which observational data and theoretical studies progressively changed their role concerning dust production. During the last decade, the search for newly-formed dust in Type Ia SN remnants has been performed by Spitzer and Herschel satellites: most of the results attribute the IR emission to the shocked interstellar dust, with no detection of the newly formed one (Blair et al., 2007; Williams et al., 2012; Gomez et al., 2012). From a theoretical point of view, Nozawa et al. (2011) predicted that dust formed in Type Ia SN explosions is destroyed before it can be injected into the ISM. The condensation efficiency δ_i^{Ia} was decreased by a factor 10 by Pipino et al. (2011) with respect to D98 and C08. Here, as starting

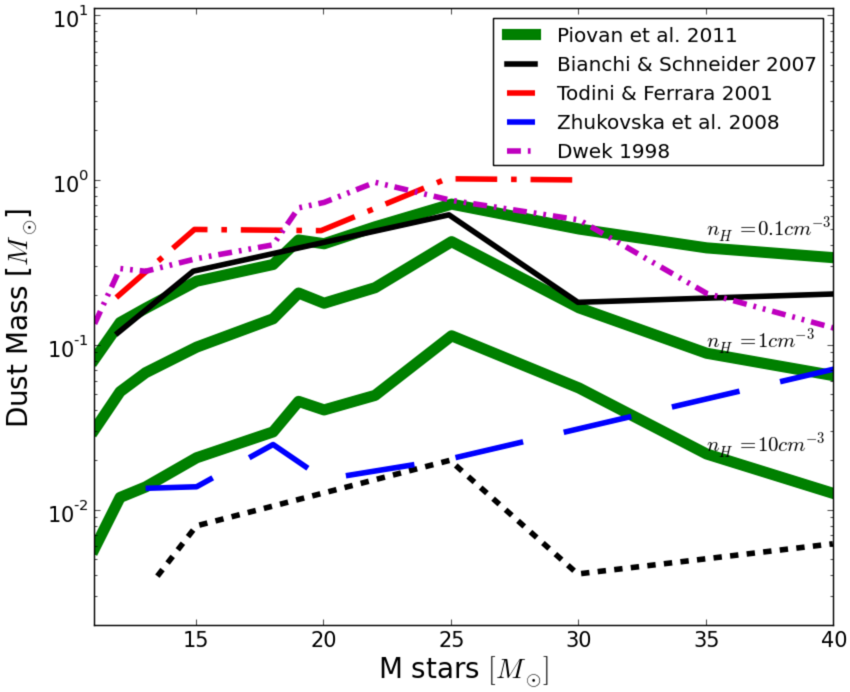

Figure 2.4: Total dust amount $[M_\odot]$ produced by Type II SNe as function of the initial stellar mass for different prescriptions. In green thick lines are presented the yields using δ_i^{II} of Piovan et al. (2011) for three different hydrogen densities: as the ambient density increase, the destruction process becomes more efficient, leading to lower dust yields. In our work we adopt the yields which correspond to $n_H = 1cm^{-3}$. Todini & Ferrara (2001) prescriptions are shown in dash-dot red line, Bianchi & Schneider (2007) with and without considering the presence of the reverse shock in black solid and short-dashed line respectively, Zhukovska et al. (2008) with the contribution of all dust species in long-dashed blue line and Dwek (1998) in magenta dash-dot-dot line.

hypothesis, we set to zero the condensation efficiencies for each element as far as the contribution of Type Ia SNe is concerned ($\delta_i^{Ia} = 0$).

2.2.2 Dust destruction

In literature it is possible to find various prescription describing dust destruction in the ISM. The main process for dust destruction is the sputtering in the ISM in high velocity SN shocks. The timescale of dust destruction is independent from the dust mass and it can be expressed as reported by C08:

$$T_{destr} = \frac{M_{ISM}}{(\epsilon \cdot M_{Swept})SN_{rate}} = \frac{M_{ISM}}{1360 \cdot SN_{rate}} \tag{2.11}$$

where M_{ISM} is the mass of the ISM in the galaxy, SN_{rate} represents the supernova rate and M_{Swept} is the amount of mass swept up by the remnant. McKee

(1989) suggested $M_{Swept} = 6800M_{\odot}$ with an efficiency $\epsilon = 0.2$. Zhukovska et al. (2008) predicted that the position of SNe in the galaxy influences the swept up mass. Furthermore, they adopted differential destruction time-scales depending on the dust species. Mancini et al. (2015) used prescriptions of de Bennassuti et al. (2014), where different parameters are adopted for core-collapse SNe and Pair-Instability ones ($M > 100M_{\odot}$).

Another interesting study was made by Asano et al. (2013) (Hereafter A13), in which some differences can be highlighted with respect to Eq.(2.11). They suggest an efficiency $\epsilon = 0.1$ and predict that M_{swept} becomes smaller either when the density of the ISM is higher or when the metallicity increases (the line cooling of metals is more efficient, leading to a lower temperature and higher density). Their prescription gives:

$$M_{Swept} = 1535 \cdot n^{-0.202} \cdot [Z/Z_{\odot} + 0.039]^{-0.289} [M_{\odot}] \tag{2.12}$$

where $n = 1.0\, cm^{-3}$ is the ISM density surrounding the SN environment. The swept mass in this case, assuming $Z/Z_{\odot} < 1$ is always above the value of $1300M_{\odot}$, as used in C08.

In this work we will use the updated metallicity-dependent prescriptions written in Eq.(2.12), whereas the destruction time-scale in Eq.(2.11) will be only used for comparison to the C08 model.

2.2.3 Dust accretion

Some processes, like coagulation, increase the dust size favoring the formation of larger grain particles. As already pointed out, in this work we only follow the mass evolution of the dust and therefore we only consider as dust accretion the condensation of metals onto the surface of pre-existing dust grains. This process takes place efficiently in cold dense regions and, for this reason, it preferably occurs in molecular clouds rather than in the diffuse ISM. Since the pioneering work of D98, it was pointed out that grain growth is one of the fundamental ingredients in studying the dust mass evolution and, more recently, other studies support this thesis (Asano et al., 2013; Hirashita, 2013; Valiante et al., 2011; Mancini et al., 2015).

In C08 the time-scale for the accretion is expressed as:

$$\tau_{C08} = \tau_{0,i}/(1 - f_i) \tag{2.13}$$

where f_i represents the ratio between the dust and the gas phase of the element i. $\tau_{0,i}$ represents the typical lifetime of a molecular cloud which in C08 was kept constant for all elements at the value of 5×10^7 yr.

Dust accretion depends on many other parameters such as the fraction of molecular clouds in the whole galaxy and the metallicity of the ISM. For this reasons, Hirashita (2000) expressed the rate of dust accretion as follows:

$$\left[\frac{dM_{dust}}{dt}\right] = \frac{M_{dust} X_{cl}\, \chi_i}{\tau_g} = \frac{M_{dust}}{\tau_{acc}} \tag{2.14}$$

where, $\chi_i = (1 - f_i)$, X_{cl} represents the fraction of the cool component in the ISM, with τ_g the characteristic dust growth time-scale and:

$$\tau_{acc} = \tau_g/(X_{cl}\chi_i) \tag{2.15}$$

Even if some elements (refractories) tend to be more depleted in dust grains with respect to others (volatiles), the dust composition consists substantially of metals. This justifies the relation given by A13 between the growth time-scale and the metallicity:

$$\tau_g = 2.0 \times 10^7 yr \times \left[\frac{a}{0.1 \mu m} \cdot \left(\frac{n_H}{100 cm^{-3}} \right)^{-1} \cdot \left(\frac{T}{50K} \right)^{-\frac{1}{2}} \cdot \left(\frac{Z}{0.02} \right)^{-1} \right] \tag{2.16}$$

where the parameters reproduce the physical structure of a molecular cloud as well properties of dust grains. The typical time-scale $\tau_g = 2\,Myr$ is reached when physical parameters are set on $T = 50K$ for temperature, $n = 100cm^{-3}$ for density and $\bar{a} = 0.1\mu m$ for the typical size of grains.

In this work we use the prescription of Eq.(2.14) with the inclusion of the metallicity-dependent time-scale of Eq.(2.16).

Chapter 3

Dust properties in Damped Lyman Alpha systems

3.1 Introduction

In this Chapter, we aim at studying the chemical evolution and composition of the dust in Damped Lyman Alpha systems (DLAs), which represent a class of high-redshift galaxies observed in absorption, by comparing abundance measurements of DLAs with model predictions of dwarf irregular galaxies. Here, we give a general description of DLAs and their dust properties.

The ISM of galaxies is composed of gas, dust and cosmic rays. Depending on the temperature and density, the gas component can be made of ions, atoms or molecules. These conditions divide the ISM in different phases (Ferrière, 2001):

- The hot ionized medium. The high temperatures ($T \sim 10^5 - 10^6\,K$) characterize this phase, which is made of low density ($\sim 10^{-3} cm^{-3}$) and ionized gas.
- The warm medium, characterized by lower temperatures ($T \sim 10^4\,K$) and densities of $\sim 10^{-2} cm^{-3}$ (ionized medium) and $\sim 10^{-1} cm^{-3}$ (neutral medium).
- The cold neutral medium, where $T \sim 100\,K$ and densities are of the order of tens atoms per cm^3.
- Molecular clouds, where $T \geq 10\,K$, density $\geq 100 cm^{-3}$ and almost all the hydrogen is in molecular form.

The ISM chemical composition is mainly made up of hydrogen and helium, with a low fraction of heavier elements ($\sim 0.1\%$). Nevertheless, the ISM plays a crucial role in the chemical evolution process, because it acts as an intermediary between stars at the galactic scale. Stars form in the core of molecular clouds and, during their evolution, pollute the surrounding ISM with metals (in different ways depending on the stellar properties, see Chap. 1). The new, metal-enriched ISM becomes a new site for the birth of chemical enriched stars.

In this way, stars that formed in different places and/or different times in a galaxy have different chemical composition. In this context, chemical evolution models predict the evolution of the abundances of the ISM with time in galaxies.

Damped Lyman Alpha Systems

The chemical abundances in the ISM are usually constrained by the analysis of absorption spectral lines. However, to measures the column densities of various elements in these lines, a luminous background source is required. In particular, the chemical composition of the ISM can be studied at different distances and ages of the Universe when quasars (QSOs) are used as background sources. In fact, QSOs are very luminous objects and have been found in the high redshift Universe, up to z>6 (the current most distant QSO discovered until now is ULAS J1120+0641 at redshift 7.1 by Mortlock et al. (2011), which correspond to a look back time of $\sim 12.9 Gyr$). Before reaching telescopes on Earth, the light from QSOs travels a long distance and for each intervening cloud several absorption features are detected in their spectra. This is very important for studying the chemical evolution of galaxies, because with QSO absorption spectroscopy it is possible to measure the chemical composition of faint objects at cosmological distances, otherwise impossible to detect.

QSO absorbers can be classified on the basis of the measured column density of neutral hydrogen $N(HI)$. Lyman limit system are characterized by $2 \times 10^{17} cm^{-2} < N(HI) < 10^{19} cm^{-2}$ (e.g. Tytler, 1982; Prochaska et al., 2010; Songaila & Cowie, 2010; Fumagalli et al., 2016), sub-DLAs by $10^{19} cm^{-2} < N(HI) < 2 \times 10^{20} cm^{-2}$ (e.g. Péroux et al., 2003; Dessauges-Zavadsky et al., 2003) and Damped Lyman Alpha (DLAs) systems by $N(H_I) > 2 \times 10^{20} cm^{-2}$ (Wolfe et al., 1986, 2005).

In this work, we focus on DLAs, the QSO-absorbers with the highest value of hydrogen column density. Since they discovery it was proposed that they are associated with galaxies (see Wolfe et al. 2005), at variance with QSO absorbers of low HI column density, which originate in the intergalactic medium. The gas neutrality suggests that they descend from cold neutral clouds, which are the precursor of molecular clouds (the star forming regions). They seem to contain most of the neutral hydrogen in the Universe between redshift 1.6 and 5 (Lanzetta et al., 1991, 1995; Storrie-Lombardi & Wolfe, 2000; Zwaan et al., 2005; Sánchez-Ramírez et al., 2016).

Among QSO-absorbers, DLAs have particular properties that make them interesting from the point of view of chemical evolution. In fact, they are the best observables we have of the ISM of high redshift galaxies. By means of high resolution spectroscopy, it is possible to measure absorption lines of various elements with a precision not achievable for other high redshift objects (Wolfe et al., 2005). Thanks to their low degree of ionization it is possible to derive column densities almost unaffected by the ionization state of different elements (Vladilo et al., 2001). For this reason DLA systems offer a great opportunity to study the composition of the ISM at different cosmic epochs and evolutionary stages. In particular, observations show a variation in metallicity from $10^{-1} Z_{\odot}$ in the Local Universe down to $10^{-3} Z_{\odot}$ at higher redshifts (e.g. Prochaska et al., 2003; Cooke et al., 2015, 2017; Rafelski et al., 2012).

The nature and the morphological type of DLA-host galaxies have been the subject of a long debate. Initially, they have been associated with massive disks progenitors of present-day spirals (e.g. Wolfe et al., 1986). Nowadays, a general agreement links them to the progenitors of low-mass galaxies (Møller & Warren, 1998; Fynbo et al., 2010; Salvadori & Ferrara, 2012; Noterdaeme et al., 2012; Krogager et al., 2013; Christensen et al., 2014; Cooke et al., 2015). From the pattern of chemical abundances, using chemical evolution models, it is possible to cast light on the morphological type of such galaxies. A comparison between model predictions and data suggests a star formation history made of short but intense bursts of star formation, as predicted for dwarf irregulars (Matteucci et al., 1997; Molaro et al., 2000; Centurión et al., 2000; Calura et al., 2003, 2009a; Vladilo et al., 2011; Salvadori & Ferrara, 2012). The chemical composition of DLA systems has been also compared with stellar abundances: even in these studies, DLAs are preferably associated to local dwarf galaxies than to the stellar abundances measured in the Milky Way Disk (e.g. Salvadori & Ferrara, 2012; Cooke et al., 2015).

Dust in DLA systems

The metallicity is defined as the mass fraction of all the elements from C to heavier ones. In DLAs, the metallicity is inferred from the sum of the observed metal absorption features. However, a perfect determination of the column density is not necessarily enough to constrain their ”real” metallicity, because of the presence of dust (e.g. Pei et al., 1991; Pettini et al., 1994; Junkkarinen et al., 2004; Vladilo & Péroux, 2005; Vladilo et al., 2006; De Cia et al., 2016). In fact, column density taken from absorption lines in optical/UV spectra can only measure the amount of atoms present in the gas phase. The fraction of the elemental abundances incorporated in the dust phase is therefore undetectable with the large optical telescopes equipped with high resolution spectrographs. Because the atoms locked into dust grains are not detected, the measured abundances appear to be depleted. Due to this fact, dust depletion, defined as the fraction of an element included in the dust phase with respect to its total abundance, affects the measured chemical abundances and therefore complicate the interpretation of the galactic chemical evolution (Savage & Sembach, 1996; Calura et al., 2003; Jenkins, 2009; Vladilo et al., 2011; Jenkins, 2014).

Depletions are fundamental because they can constrain the elemental composition (stoichiometry) of interstellar dust. In particular, depletion studies reveal that dust composition is dominated by C, O, Si, Mg and Fe elements, which are the basic components of the most successful dust model, consisting in carbonaceous-species and silicates grains (Hoyle & Wickramasinghe, 1969; Mathis et al., 1977; Draine & Lee, 1984; Desert et al., 1990; Li & Draine, 2001; Draine & Li, 2007). Carbonaceous components are usually formed in the densest molecular phases of the ISM, where organic compounds can grow. The molecular phase is very hard to detect in DLAs, suggesting that in most cases the observation sample gas with low or negligible content of carbonaceous dust.

Si and Mg atoms represent the major constituents of silicates, which is generally assumed made of a mixture of pyroxenes and olivines, even though the chemical structure and the proportion of the mixture is not completely clear. In fact, it is important to notice that elemental depletions do not provide any information about the grain mineralogy (Jones, 2014) and, to have a more precise picture, a comparison between astronomical observations and laboratory measurements is necessary (e.g. Agladze et al., 1996; Mennella et al., 1998;

Coupeaud et al., 2011; Lee, 2010). Fe is another fundamental building block of silicates, even though its high depletion factor suggests that it may also be incorporated in other dust forms such as metallic particles (e.g., Wickramasinghe & Wickramasinghe, 1993; Dwek, 2004a; Sofia et al., 2006; Voshchinnikov & Henning, 2010; Draine & Hensley, 2012, 2013; Dwek, 2016).

In this Chapter, we study the ISM chemical composition of DLA systems by means of galactic chemical evolution models. First, in Section 3.2 we present our model and a prescription for dust formation in a typical irregular galaxy. In Section 3.3 we study the depletion patterns of Si and Fe in the ISM of DLA systems, and we try to explain their origins through our chemical evolution model. Then, in Section 3.4 we show a new method based on DLA column density measurements and the ratio between volatile and refractory elements, to give for the first time an estimate of the chemical abundance ratios inside dust grains. In this way, we try to disentangle the main dust constituents and predict their evolution: in particular, we focus on the fraction between silicates and metallic particles and between pyroxenes and olivines. Finally, we resume our conclusions in Section 3.5.

3.2 Dust predictions for dwarf irregular galaxies

Dwarf irregular galaxies have been suggested as the host galaxies of DLAs (e.g. Matteucci et al., 1997; Møller & Warren, 1998; Centurión et al., 2000; Salvadori & Ferrara, 2012). In this Section we present the predictions for the evolution of dust in dwarf irregular galaxies for a set of chosen models in order to study the dust in DLAs. Dwarf irregulars are low-mass and low-luminosity galaxies which are characterized by ongoing star formation. They are assumed to form by means of a continuous infall of pristine gas with a continuous and low star formation. Based on previous works, we adopt a Salpeter IMF (eq. 2.3) which is able to reproduce the chemical abundances, observational features and the local metallicity of dwarf irregulars (Bradamante et al., 1998; Calura & Matteucci, 2003, 2006).

In this work, we want to optimize the parameters of our model to reproduce a typical dwarf irregular galaxy. In particular, we are interested in the evolution of dust properties such as the dust-to-gas mass ratio. For this reason we keep constant the parameters of galaxy evolution of our reference model and we only vary the parameters that describe the production of dust in the galaxy.

Our chemical evolution model with dust works in a similar way to the one of C08, which was based on the work of D98. We set the parameters concerning the chemical evolution model of a typical irregular as in C08, where also the evolution of dust was studied: in this way, we can directly compare the results obtained by old and more recent prescriptions of dust production. In Table 3.1 we summarize the adopted dust prescriptions and model parameters. We show the model name in the first column, the star formation efficiency in the second column, the infalling mass in the third column, the time-scale of the infall in the fourth column, the wind efficiency in the fifth column, the assumed IMF in the sixth column and the references to the assumed dust condensation efficiencies in the seventh column. Finally, in column eight and nine we indicate the references for the dust destruction and accretion time-scales, respectively. Our typical irregular galaxy model is represented by the I0, I1 and I3 models, which only

name	$\nu[Gyr^{-1}]$	$M_{infall}[M_{\odot}]$	$T_{infall}[Gyr]$	ω	IMF	δ_i	$T_{destruction}$	$T_{accretion}$
Dwarf irregular galaxy model								
I0	1.00	10^9	10	1.00	Salpeter	D98	D98	—
I1	1.00	10^9	10	1.00	Salpeter	P11	A13	—
I2	1.00	10^9	10	1.00	Salpeter	D98	D98	D98
I3	1.00	10^9	10	1.00	Salpeter	P11	A13	A13
I4	1.00	10^9	10	6.50	Salpeter	P11	A13	A13

Table 3.1: Parameters adopted for different models of dwarf irregular galaxies. In columns from left to right we show the name of the model, the star formation efficiency (expressed in Gyr^{-1}), the mass of the galaxy (in $M_{\odot}$), the infall time-scale (in Gyr), the wind parameter (dimensionless) and the adopted IMF. In the seventh, eighth and ninth columns we show the different prescriptions used for condensation efficiencies (δ_i), destruction and accretion time-scales, respectively. D98, P11 and A13 refer to prescriptions of Dwek (1998), Piovan et al. (2011), Asano et al. (2013), respectively.

differ for dust prescriptions. In particular, model I3 represents our best model, as it includes the most updated dust prescriptions.

For the sake of completeness, we have investigated how results change with varying the model parameters. In more detail, we found that acceptable values for the star formation efficiency, ν, lie in the range 0.4-1.0 Gyr^{-1}, the time scale of the infall has a modest effect on the abundances and it lies in the range 5-10 Gyr. Finally, the wind parameter has to vary between 1 and 2.5 in order to obtain acceptable results concerning the abundance patterns. In Fig. 3.1 we present the effects on the SFR by varying such parameters. In the top panel we show that the effect of varying ν from 0.4 to 1.0 leads to small differences in the SFH, especially on longer time-scales. In the middle panel we show that the spread caused by the wind parameter is also very small and it appears important only at late epochs, when the galactic wind is active. In the bottom panel of Fig. 3.1, one can see that the variation of the SFR is negligible when the time of the infall is larger than 5.0 Gyr. We obtain different results only when the time-scale of the infall is lower (i.e. 1.0 Gyr): the SFR reaches higher values at early epochs, because of the high amount of gas available to form stars, whereas at the end of the simulation is lower, because all the gas has been already consumed. The spread shown in Fig. 3.1 is in agreement with the typical behavior of irregulars, which, on average, are characterized by a smooth SFR with typical variations of factors 2-3 (Grebel, 2004) and present time values between 0.001 and 0.36 $M_{\odot}yr^{-1}$ according to their stellar mass (Kennicutt et al., 2011). Model I3 will be regarded as the fiducial one, as it accounts for the star formation rate values measured in DLAs as well as for their observed abundance pattern.

In Fig. 3.2 we show the evolution of some physical quantities independent of the dust prescriptions adopted in model I3. In the top panel we show the behavior of the SFR in comparison with the values measured in irregulars and DLA systems. We find a good agreement with the typical variation observed at the present time, between 0.001 and 0.36 $M_{\odot}yr^{-1}$ (Grebel, 2004; Dessauges-Zavadsky et al., 2007; Kennicutt et al., 2011). In the middle panel of Fig. 3.2, we show the time evolution of the mass of stars, ISM and the mass lost by galactic wind: at the beginning, the mass of the ISM represents the major

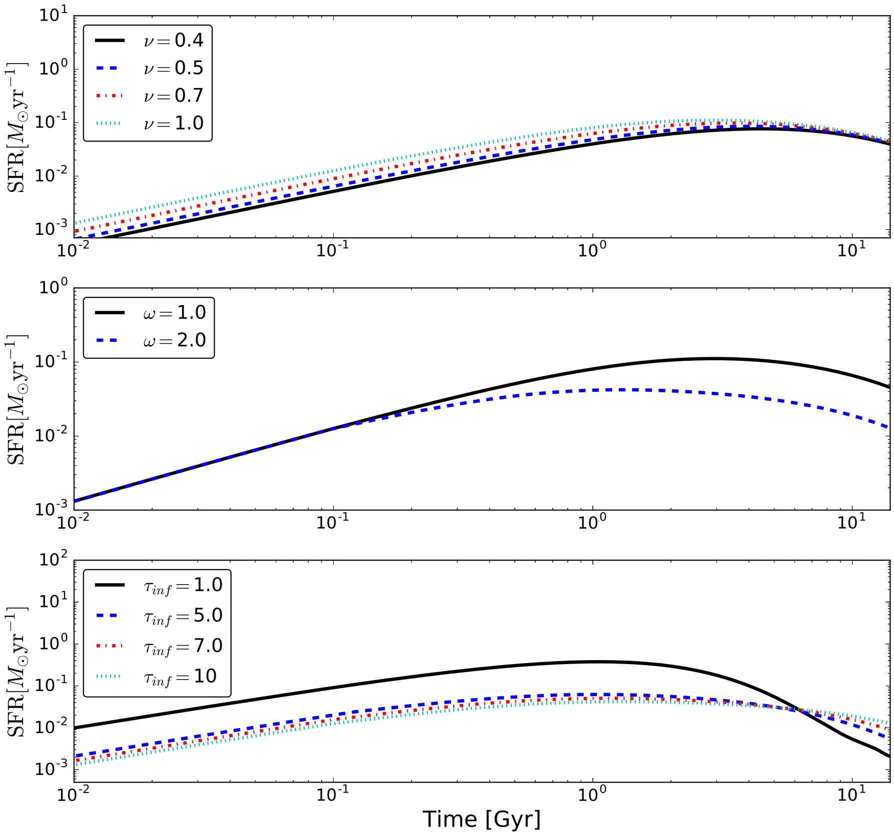

Figure 3.1: Time evolution of the star formation rate for different values of some key parameters: in the top panel we varied ν from 0.4 to 1.0 Gyr^{-1}, in the middle panel ω from 1.0 to 2.0 and in the lower panel the τ_{infall} from 1.0 to 10 Gyr^{-1}.

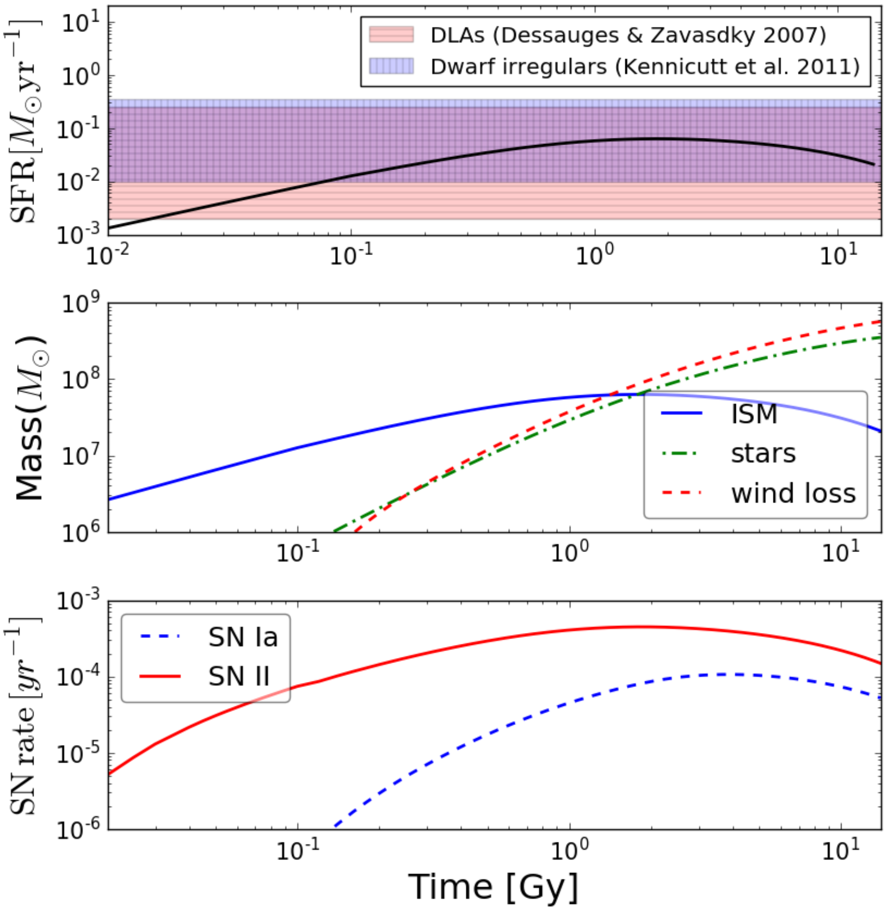

Figure 3.2: Top panel: time evolution of the SFR in $M_\odot yr^{-1}$ of our reference model for a dwarf irregular galaxy. The red shaded area represents the SFR range estimated by Dessauges-Zavadsky et al. (2007), computed assuming a scale radius of 1 kpc as a typical size for DLAs. The cyan area represents the SFR range measured in dwarf irregulars by Kennicutt et al. (2011). The dark area refers to the intersection between the SFR values in dwarf irregulars and DLA systems. Middle panel: time evolution of the mass (in solar masses) of the ISM (blue solid), stars (green dot-dashed) and the mass loss by galactic wind (red dashed). Bottom panel: galactic Type II and Type Ia SN rates (in number per year) in red solid and blue dashed, respectively.

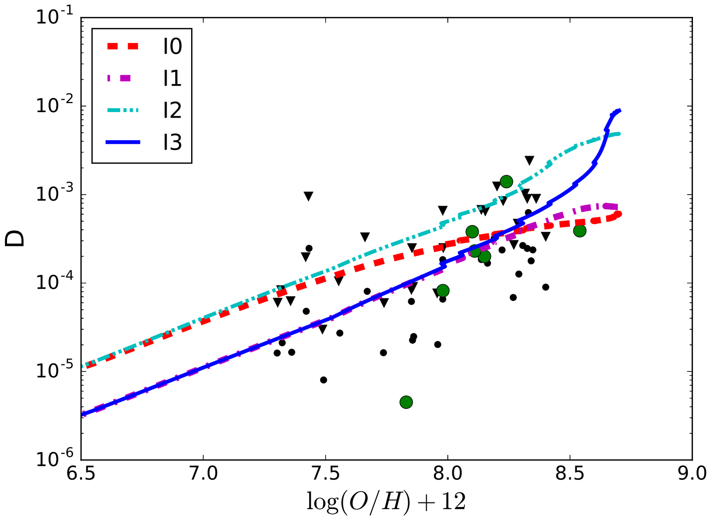

Figure 3.3: Dust-to-gas ratio versus metallicity. *Models*: Dashed red line refers to I0 model, magenta dot-dashed line to I1, cyan dot-dot-dashed line to I2 and blue solid line represents model I3. *Data*: black dots and triangles represent values and upper limits respectively for local dwarf irregulars by Lisenfeld & Ferrara (1998) and big green circles from Hirashita et al. (2008).

component of the galaxy and it increases as the pristine infalling gas accretes. As the SFR rises, also the stellar mass and the SN rate increase, as visible in the middle and bottom panel, respectively. Then, when the thermal energy exceeds the gravitational binding energy of the galaxy, a galactic wind starts and considerably reduces the mass of the ISM. In the bottom panel of Fig. 3.2, we show the predicted Type II and Type Ia supernova rates, which are important both for dust and gas components. The trend of Type II SN rate traces the SFR one, because of the very short typical time-scales involved (from 1 to 30 Myr). On the other hand, Type Ia SNe are characterized by longer time-scales (from 30 Myr up to the time of the Universe, e.g. Padovani & Matteucci 1993).

3.2.1 Dust-to-gas ratio

In Fig. 3.3 we show the ratio between the mass of dust and neutral hydrogen, $D = M_{dust}/M_{HI}$, versus the metallicity for different chemical evolution models compared to observations. We remind that the models differ only in dust prescriptions (dust condensation efficiencies, dust destruction and dust accretion), whereas the remaining parameters concerning the chemical evolution of the ISM are kept constant (ν, M_{infall}, τ_{infall}, IMF and ω_i). Data were taken from Lisenfeld & Ferrara (1998) (local dwarf irregulars), Hirashita et al. (2008) (blue compact dwarf spheroidals), which have been collected in Galametz et al. (2011). Those authors estimated the amount of dust mass from far-infrared measurements and compared them with the amount of neutral hydrogen and oxygen.

The models I0 and I1 (red dashed and solid lines, respectively), only consider dust production and destruction. The I0 model, which adopts D98 prescriptions, produces a higher amount of dust with respect to model I1, which adopts the updated ones. The two curves differ at the lowest metallicities: the offset between the two is caused by the major amount of dust ejected by Type II and Ia SNe when the condensation efficiencies δ_i, given by D98, are adopted (see section 3.2.2). For $\log(O/H)+12>8$, the two models converge and predict the same value for the dust-to-gas ratio.

Dwarf galaxies have very low star formation efficiency, which could reflect the paucity of molecular clouds present in these environments. In C08, dust accretion was not taken into account, as this process preferably occurs in such clouds. However, we tried to include dust accretion in other models because it plays a fundamental role during the entire evolution of a galaxy (Asano et al., 2013; Dwek & Cherchneff, 2011; Mancini et al., 2015). The I2 model contains the same prescriptions used in C08, with the addition of dust accretion: the total amount of dust in model I2 is higher than in I0 and the discrepancy increases at higher metallicities. The separation between the two models is evident since $\log(O/H)+12>7.0$, indicating that in I2 dust accretion becomes the dominant process since the early phases of dust evolution. Finally, model I3 adopts the condensation efficiencies δ_i by P11 and the new prescriptions for the swept up mass and for the accretion time-scale, as described in Eqs. (2.12) and (2.16), respectively. In this case, the discrepancy from I1 is negligible for lower metallicities, becoming larger when $\log(O/H)+12>8$. It means that in I3 model, dust accretion becomes important at higher metallicities or, in other words, at longer evolutionary time-scales with respect to I2.

I2 and I3 are the only models which can reproduce the observed high amount of dust at high metallicities. This indicates that dust accretion performs an important role in dust evolution and should be modeled in a proper way: the I3 model better reproduces the trend observed in the data, which seems to increase in a steep way with the metallicity. Therefore, we adopt this model as a reference for subsequent studies described in the rest of this chapter.

Effect of massive stars

For a long time, the scientific community has reserved great interest to the study of massive stars (above $10M_\odot$). In spite of this, nowadays it is not completely clear which stars do explode as core-collapse SNe and which ones instead collapse to a black hole. In fact, recent theoretical and observational studies suggest the possibility that massive stars may directly collapse to a black hole, with no explosion events and therefore no consequent enrichment of the ISM. From a theoretical point of view, it has been known for a long time that very high mass star explosions are more unlikely than those of lower masses (Fryer, 1999). O'Connor & Ott (2011) concluded that stars heavier than $20M_\odot$ have difficulty in exploding. Recently, simulations by Ugliano et al. (2012) have shown that core-collapse explosion and direct black hole formation are both possible outcomes for progenitor stars above $15M_\odot$. From the observational point of view, there is no evidence for SN progenitor mass above $\sim 20M_\odot$ (Smartt et al., 2009). Smartt (2015) explored the evolution of massive stars after the quiescent phase on the Main Sequence: the most probable scenario showed that stars above $18M_\odot$ fail SN explosion and directly collapse to a black hole. However, this is a strong assumption and many uncertainties are still present. An indication of

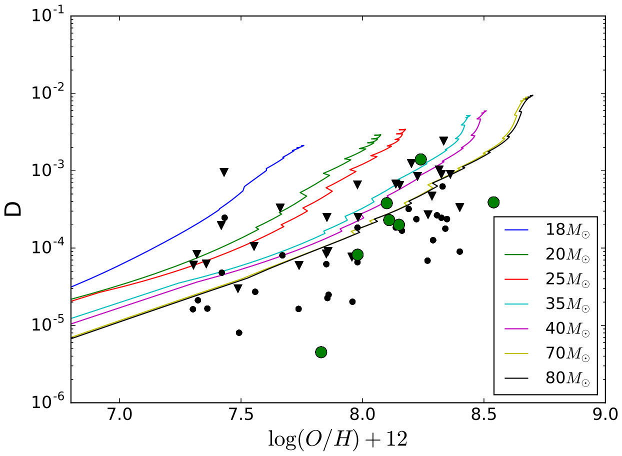

Figure 3.4: $D = M_{dust}/M_{HI}$ versus metallicity as in Fig. 3.3. The lines of various colors represent model I3 computed assuming different values for the cut-off mass fore core-collapse SNe (as reported in the legend).

the fact that this problem is not completely understood comes from Ugliano et al. (2012): their predictions do not take into account binary effects and, despite all black holes should swallow the progenitor star, they found an exception for a mass progenitor of 37 $M_\odot$. They also concluded that a direct comparison with observations requires caution.

Massive stars are very important actors in chemical evolution models as they are responsible for metal production. For this reason, model predictions can be affected if their chemical enrichment is not considered. In addition, even if massive stars do not explode as SNe, the mass loss via stellar wind integrated over the stellar life, contributes to the chemical enrichment of the ISM and cannot be neglected, especially for C and He. Brown & Woosley (2013) have already tested the effect of cutting chemical enrichment from massive stars in a chemical evolution study of the solar neighborhood. They could not reproduce the observed abundances without the chemical contribution of stars above $18M_\odot$. On the other hand, they almost reproduce the chemical pattern when the cut-off is moved to $25M_\odot$, and even better when a cut-off of $40M_\odot$ is adopted.

Here, we test for the first time the effect of the mass cut-off concerning high mass stars in the chemical evolution model which takes into account the presence of dust. In particular, we investigate the impact of this hypothesis on the dust-to-gas ratio, D. In Fig. 3.4 we show as the evolution of model I3 with different cut-off masses. We define the cut-off mass the maximum mass of stars able to contribute to the chemical enrichment of the ISM: for example, a mass cut-off of $18M_\odot$ means that the chemical contribution of the stars above this mass is not taken into account. We found disagreement between models and data when the cut-off mass is set below 25 $M_\odot$. On the other hand, our models well reproduce the data when a mass cut-off $\geq 35M_\odot$ is adopted. In fact, above this value, different cut-off masses lead to little differences and all of the models are able to reproduce the bulk of the data. Concerning the upper value of D for all different models we do not find big differences: this indicates that the total mass

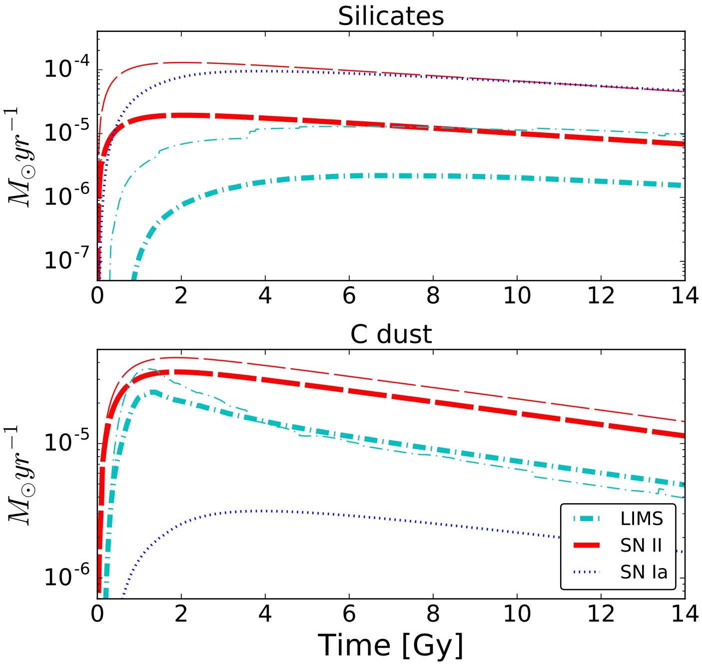

Figure 3.5: Production rate of carbon and silicate dust in a dwarf irregular galaxy. Red dashed and cyan dot-dashed lines correspond to Type II SNe and LIMS dust sources respectively. Thick lines are for the results using Piovan et al. (2011) dust condensation efficiencies (model I1), while thin lines correspond to Dwek (1998) ones (model I0). In blue dotted line we show the dust contribution of Type Ia SNe, as predicted in Dwek (1998).

of dust produced is not deeply affected by the cut-off mass. It is not possible to say the same for the metallicity: in fact, massive stars are very important metal producers, especially for alpha elements such as oxygen. It is impossible to reach $log(O/H) + 12 > 7.7$ when we cut the contribution of massive stars above $18M_\odot$, whereas a cut off of 25 $M_\odot$ leads to $log(O/H) + 12 > 8.0$ and is more acceptable. Finally, in order to reproduce the highest values of $log(O/H)$ showed by the data, exploding masses up to 35-40 $M_\odot$ are necessary.

In conclusion, from the point of view of the absolute metallicity, massive stars are fundamental and they must be included in our models in order to reach the observed log(O/H)+12. This is because the cut.off mass influences mostly the abundance of oxygen. On the other hand, they do not deeply affect the total dust production: in particular the dust-to-gas ratio at the end of the simulation is the same for different cut-off masses. In the rest of this work we will no further consider this cut-off, as we are most interested in the evolution of the dust and the effect that it produces on the observed chemical abundances of the ISM.

3.2.2 Dust composition

In this paragraph we focus on the composition of the dust: specifically, we study the total amount of dust mass produced by different types of stellar sources. For the sake of comparison between D98 and C08 we consider two species of dust, namely silicates and carbonaceous dust. Following the definitions of D98 and C08, silicates are dust particles formed by O, Mg, Si, S, Ca and Fe elements, while C dust consists of carbonaceous solids. The possible presence of an iron-rich dust different from silicates will be discussed in Section 3.3.4. The stoichiometry of different types of silicate dust grains will be investigated in Section 3.4.

In Fig. 3.5 we show the formation rate of silicates and carbonaceous dust predicted using the dust condensation efficiencies of D98 (thin lines) and P11 (thick lines). In the bottom panel one can see how the two dominant carbon dust sources are the Type II SNe and low and intermediate-mass stars (LIMS). As Type II SNe have shorter lifetimes with respect to LIMS (Padovani & Matteucci, 1993; Matteucci & Greggio, 1986), they dominate the dust production in the earliest epochs of the galactic evolution. AGB stars strongly pollute the ISM with carbonaceous dust and their contribution is comparable with Type II SNe at late epochs. Type Ia SNe do not influence the balance of carbonaceous grains.

The evolution of silicate dust production is presented in the top panel of Fig. 3.5: the bulk of this species is almost entirely produced by Type II SNe, whereas LIMS play a negligible role.

When D98 prescriptions are adopted, a higher dust production rate from Type II SNe and AGB stars is reached with respect to the model in which δ_i from P11 are considered. Furthermore, Type Ia SNe play a fundamental role, as they produce lots of iron that in this case is counted among silicates: actually, the iron from Type Ia SNe could be accreted in a separate, iron-rich dust species. We will deeply discuss this topic in Section 3.3.4, where we will compare our model with abundances in Damped Lyman Alpha Systems.

3.2.3 Dust processes and the critical metallicity

Depending on the star formation history (SFH) of a galaxy, the fraction of the dust and the contribution to its production by the different processes occurring in the ISM can vary during the galactic evolution. In our model we can study the different processes and their evolution during the galactic time.

In the top and middle panels of Fig. 3.6 we compare the rates of accretion, destruction, and production of dust versus time for the I2 and I3 models, respectively. In this figure we are able to compare the different evolution of the dust when C08 or updated recipes are adopted. For the I2 model, dust destruction and accretion trace each other, as they are both proportional to the characteristic time of the star formation (based on their time-scales definition of D98). Stars poorly contribute to the injection of dust in the ISM and the accretion process plays the major role during the whole galactic time. In the middle panel, we show the evolution of I3 model, and some differences emerge. In the initial phase, dust production by Type II SNe is the most important process: in fact, these massive stars ($8 - 40 M_\odot$) have short lifetimes and rapidly inject dust into the ISM. According to Eq. (2.14), the accretion rate increases because the dust amount in the ISM becomes larger and the infalling gas continues to accrete. In addition, Eq. (2.16) shows that the accretion time-scale becomes shorter as the metallicity increases, strengthening the rise of the accretion rate. At a certain point, the rate of dust production and accretion become equal and then, dust accretion dominates until the end of the simulation. This result is in agreement with predictions of Asano et al. (2013) who defined the so called *critical metallicity* as the metallicity at which the contribution of dust accretion overcomes the dust production from stars. In I3 model the critical metallicity assumes a value $Z_{crit,I3} = 0.442 Z_{\odot}$ ($Z_{\odot} = 0.0134$ from Asplund et al. 2009). As already mentioned, for I2 model the accretion rate becomes important at early epochs and we found a lower value for the critical metallicity, $Z_{crit,I2} = 0.172 Z_{\odot}$.

It is interesting that dust destruction plays a negligible role, while the most important process able to decrease the amount of dust is the galactic wind: in fact, it acts on two fronts as it directly removes the dust from the galaxy and regulates the efficiency of the accretion process. To better fix this concept, we report in the bottom panel of Fig. 3.6 the dust evolution for I4 model, characterized by a higher galactic wind parameter ($\omega = 5$). In this case, dust accretion always lies below dust production and the critical metallicity is not reached: the galactic wind removes gas from the ISM which cannot condensate onto pre-existing dust grains any more, causing a reduction in the accretion rate. As before, in the earliest epochs the dust production rate is dominated by Type II SNe, but it decreases as soon as the galactic wind starts. On the other hand, the galactic wind does not deeply influences the dust production rate by AGB stars and, in this scenario, their contribution is similar to the one of Type II SNe. Galactic wind also decreases the destruction process: in such a case the supernova rate decreases with the star formation (see Fig. 3.2), leading to higher values of destruction time-scales, according to Eq. (2.12).

3.3 Dust depletion patterns of Si and Fe

In the previous Section we have shown our results concerning the dust evolution in a typical dwarf irregular galaxy. In this Section, we compare our model to the chemical abundances observed in DLAs, in oder to study dust depletion of Si and Fe. We will adopt model I3 as the reference one to compare with DLA systems.

3.3.1 How to study depletion in DLAs

The abundances in DLA systems reflect the composition of the gas phase of the ISM, with no information on dust composition. This is because atoms incorporated into dust grains cannot be detected with absorption-line spectroscopy and, as a result, the measured elemental abundances are depleted with respect to the total interstellar abundance (gas plus dust). Calura et al. (2003) performed dust corrections on DLA data in order to directly compare them with the total abundances predicted by chemical evolution models. They used a scaling law from Vladilo (2002a,b) to take into account the interstellar depletion in DLAs, depending on the variation of the physical conditions.

Here we follow a different approach: with our model we predict the amount of dust in the ISM and, by tracking the dust production, destruction and accretion of the different elements, we calculate their fractions in the dust phase. By

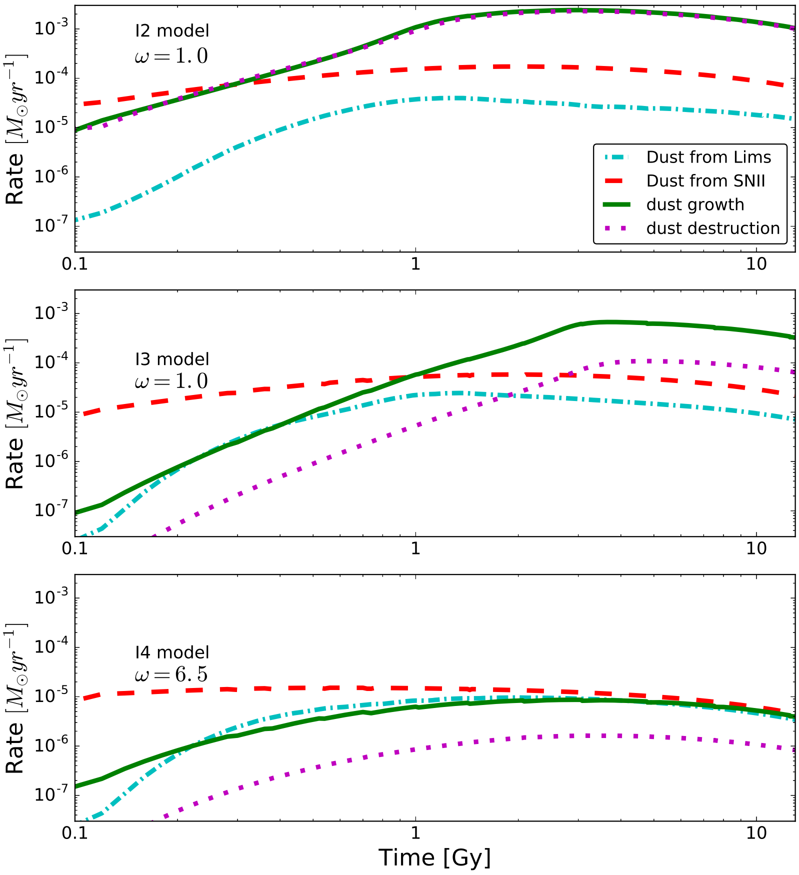

Figure 3.6: Rate in solar masses per year of the different processes governing the dust evolution. The dashed-dot cyan and dashed red lines show the production rate by AGB stars and Type II SNe, respectively; the solid green line indicates the rate of the accretion process while the magenta dotted line represents the destruction rate. Predictions for I2, I3 and I4 models are shown in the top, middle and bottom panel, respectively.

subtracting this fraction from the total, we predict the gas-phase abundances that can be directly compared with the DLA abundances. In this procedure, the condensation efficiencies of individual elements, δ_i, as well as the prescriptions for the accretion and destruction described in Section 2.2, are used to calculate the individual gas-phase abundances.

We focus on two refractory elements, iron and silicon, that are commonly measured in DLA systems and that are expected to be incorporated in dust form. On the other hand, we do not consider carbon depletion, which could be useful to test the presence of carbonaceous dust, because carbon abundance is extremely rare in DLA systems due to the saturation of the interstellar carbon lines.

In order to tune the parameters of the DLA model we use volatile elements (zinc and sulfur) which are not expected to be incorporated into the dust, even though it is not completely clear if sulfur can be treated as a perfect volatile (Calura et al., 2008; Jenkins, 2009). De Cia et al. (2016) showed that S depletion seems to rapidly increase with metallicity and in low-metallicity objects, like DLAs, can be negligible. In high-density molecular gas a fraction of zinc and sulfur might be incorporated in dust, but, unfortunately, we are far from this situation since the molecular fraction is generally very low in DLA systems (Ledoux et al., 2003).

Following the procedure of Vladilo et al. (2011) (hereafter V11) we first tune the parameters of galactic chemical evolution using the S/Zn ratio, which is unaffected by dust depletion processes both in the model predictions and in the data. We then use S and Zn as a reference to measure the relative abundances of the refractory elements Si and Fe, i.e. we study the ratios Si/S, Si/Zn, Fe/S, and Fe/Zn. The model predictions for these element-to-element ratios are more robust than the predictions for absolute abundances (relative to hydrogen), because they little depend on the uncertainties of stellar nucleosynthesis. At the same time, these ratios are strong indicators of the possible presence of dust, since in each case they represent a ratio between a refractory element, affected by dust processes, and a volatile element, independent from dust.

We assume that the elemental abundances in the galactic ISM are determined by two processes: 1) chemical enrichment of the gas by stellar ejecta and 2) elemental depletion caused by the condensation of the gas onto dust particles. In principle, one should also take into account the ionization state of the gas for a precise conversion of the column densities into abundances, but ionization corrections for DLA measurements are generally smaller than the column density errors (Vladilo et al., 2001).

3.3.2 DLA data

The dataset used in this work is based on the best measurements of DLA metal column densities, obtained with high resolution spectroscopy performed with 10-m class telescopes (mostly HIRES at KECK and UVES at ESO-VLT). Starting from the database of V11, we have added 34 DLA systems with associated measurements collected in the last years. We report the entire dataset used in this work in Table 3.2: in this Table, we report the name of the QSO in column one and the absorption redshift in column two, while in the third, fourth, fifth and sixth columns are presented the column density measurements of zinc, sulfur, iron and silicon, respectively. In the last column, are reported the codes for each column density which are associated to the literature references listed in Table 3.5. Before comparing the data with the model predictions we have lowered and increased the ZnII and SII column densities, respectively by 0.1 and 0.04 dex to take into account the recent redetermination of the relative oscillator strengths provided by Kisielius et al. (2014, 2015). The linear scaling of column density with the oscillator strength is justified by the fact that ZnII and SII absorption lines are unsaturated in most cases. The database of DLA ZnII and SII column densities found in the literature is instead based on the oscillator strengths of Morton (2003). In Table 3.2 we give the original column densities, before the application of this correction.

3.3.3 Results

As a first step of our procedure, we tailored our model to match the observed S/Zn ratio, which is not affected by dust parameters. We performed some tests on the input parameters of chemical evolution models: we changed the wind parameter, star formation efficiency, infall mass and IMF, as already explained in Section 3.2. In Fig. 3.7 we show the comparison between the model results of the dwarf irregular (model I3, Table 3.1) and the observed abundances of volatile elements in DLA systems. We refer to V11 for a study of the impact of parameter variations on the spread of the predicted S/Zn abundance ratios. To reproduce the full span of S/Zn values of DLAs as a function of metallicity, the use of an inhomogeneous chemical evolution model would be required, similar to the one presented in Cescutti (2008), and such a task is beyond the aim of the present work.

In Fig. 3.8 we show the relative abundance ratios between refractory (Si, Fe) and volatile (S, Zn) versus the absolute abundance of the corresponding volatile. We study each possible combination of these elements: Si/S and Fe/S versus S/H (in the top panels), and Si/Zn and Fe/Zn versus Zn/H (bottom panels). For a direct comparison with data, we remove the dust contribution from the chemical predictions of the ISM (red line), obtaining the *gas model* (black solid lines).

Assuming that volatile elements totally stay in the gas phase while a certain fraction of refractories is incorporated into dust grains, refractory gas abundances should show smaller values with respect to the total ISM (gas plus dust). For this reason we expect the refractory to volatile abundance ratios in the gas to lie below the total ISM abundances. In Fig. 3.8 we see that the ISM model lies above the majority of the data, in agreement with this expectation. On the other hand, the cases where measurements lie above the model could be due either to the natural dispersion present in DLA data or to the uncertainties related to the stellar yields for zinc, sulfur and silicon, which are especially critical at low metallicities (Romano et al., 2010).

We obtain interesting results for silicon and iron. In the left panels of Fig. 3.8 we show the case of silicon. The measured gas-phase DLA data shows a moderate decrease with increasing metallicity. This suggests that the amount of silicon in dust has a moderate tendency to increase in the course of galactic chemical evolution. Concerning the models, the difference of the predictions before and after the removal of the dust is evident (red and black solid lines, respectively). We obtain a reasonable agreement between the model and the data for both Si/Zn and Si/S ratios. This suggests that the dust contribution of accretion

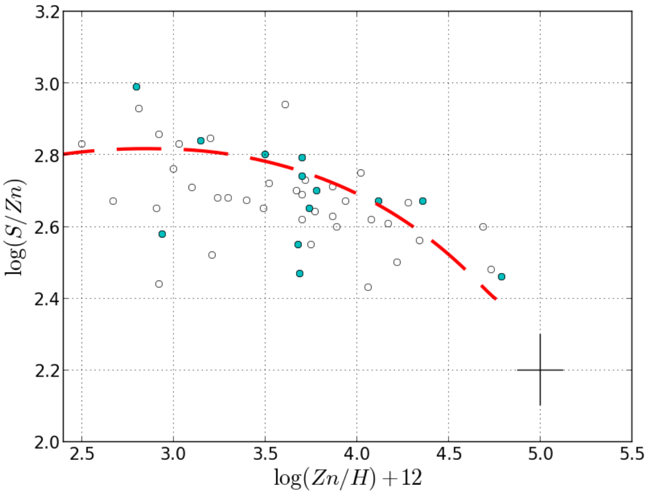

Figure 3.7: Volatile S/Zn abundance ratios versus Zn/H in DLA systems. The long dashed red line represents the chemical evolution calculated from model I3, whose parameters are reported in Table 3.1. Data: open circles are the measurements which were already present in Vladilo et al. (2011) work, while cyan circles represent the values of the sample presented in Table 3.2. In the figure, zinc and sulfur column densities are corrected as suggested by Kisielius et al. (2014, 2015) (see text).

together with dust production by Type II SNe and AGB stars is able to explain the depletion pattern of silicon observed in DLA systems. We notice that silicon observations are depleted even at the lowest metallicities of the sample, in agreement with a scenario in which Type II SNe give a fast contribution to silicon dust production.

In the right panels of Fig. 3.8, we show the pattern of iron abundance versus volatile elements. The abundance ratios show a marked decrease with metallicity as found in V11. In this case, the observed iron depletion tends to vanish at the lowest metallicities, suggesting that the mechanisms of production of iron-rich dust takes place on longer time-scales than those typical of Type II SNe. The gap between the total ISM model and the gas-phase data increases with metallicity, indicating that the mechanisms of production of iron-rich dust must be metallicity-dependent. However, at variance with the case of silicon, the gas-phase model (black solid line) does not fit at all the gas-phase Fe/S and Fe/Zn data. In fact, the model lies much higher than the data, suggesting that the adopted model predicts too little iron in dust. In this model, only the accretion process plays a significant contribution, whereas the dust production by Type II SNe and AGB stars leads to a negligible fraction with respect to the total iron abundance in the ISM. Even if we invoke a major contribution by either Type II SNe or AGB stars, the total iron in dust would be still negligible with respect to the iron amount ejected by Type Ia SNe in the gas phase. For this reason, the model cannot predict any appreciable iron depletion until the metallicity becomes high enough to make the accretion process important.

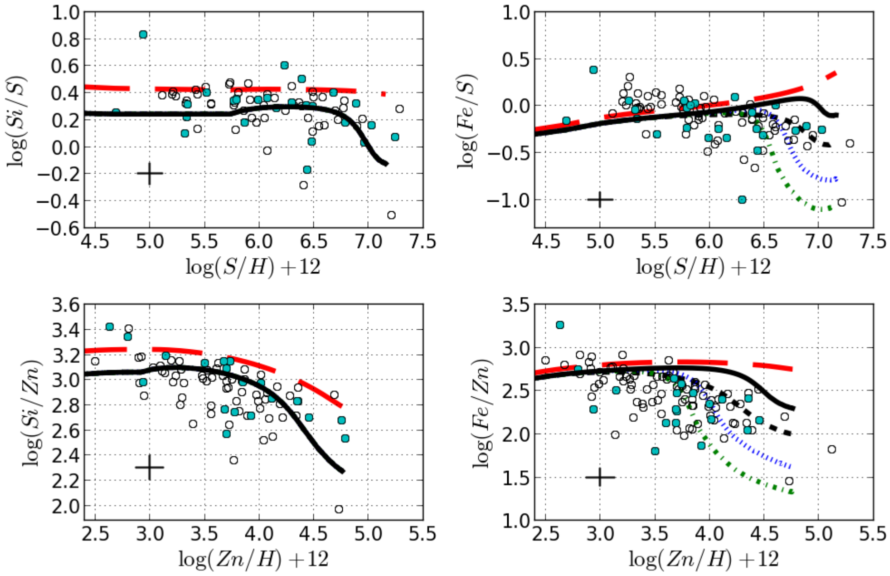

Figure 3.8: Abundance ratio of refractory elements Si and Fe over volatile elements S (top panels) and Zn (bottom panels), against the absolute abundances of the volatile element. The red long-dashed lines represent the cosmic ISM abundance ratios of model I3, whereas the black solid lines represent the same model after the removal of the dust, i.e. the gas model. The black short-dashed lines represent a model including iron dust production from Type Ia SNe. Blue dotted and green dashed-dotted lines show the predictions computed assuming a 5 and 10 times more efficient iron accretion, respectively. Data: same as Figure 3.7

It is evident that an extra source of iron-dust must be added to the model to reduce the discrepancy with the data. We considered two possibilities. First, we tested the contribution of Type Ia SNe to iron dust using the D98 prescription, even if we know that there is no observational support for this hypothesis. The results are shown as black short dashed lines in Fig. 3.8. One can see that this model can better follow the trend of the measured Fe abundance, but the agreement is still poor. As a second possibility, we assumed that the bulk of iron is incorporated in a solid component, different from silicates, characterized by a high accretion efficiency. The existence of this dust population is suggested by other works, e.g. in the form of iron-rich metallic nano-particles (Draine & Hensley, 2012, 2013). Such particles might have sizes one order of magnitude smaller than the standard size of silicates ($1-0.1\mu m$), and 2.16 predicts that the accretion time-scale should be correspondingly smaller. Therefore, to increase the efficiency of iron accretion we reduced the accretion time-scale by a factor 5 and 10. With such prescriptions we obtain a better match with data (green short dotted lines and blue dashed-dotted lines in Fig. 3.8). All the models that we have considered trace each other in the low metallicity range (early epochs), while they evolve in a substantially different way at metallicities above $\log(S/H)+12 \simeq 6.5$ and $\log(Zn/H)+12 \simeq 3.5$ for sulfur and zinc, respectively. This is consistent with Eq. (2.16) and what we explained in section 3.2.3: the dust accretion becomes important as the metallicity increases and, in particular, when it reaches a critical value.

3.3.4 Discussion

In the last sub-Section we have reproduced the depletion pattern of silicon and iron in the ISM of DLA systems: we showed that when we consider dust accretion and formation from Type II SNe and AGB stars (AGBs can produce Si and Fe dust originating inly from the original gas), a good agreement is obtained for silicon, but not for iron. The results we have found support a scenario in which iron and silicon undergo a different history of dust formation and evolution. Iron and silicon are believed to be coupled in silicate species, mostly in olivine ($Mg_{2y}Fe_{2(1-y)}SiO_4$) and pyroxene ($Mg_xFe_{(1-x)}SiO_3$) compounds. The absorption of silicate features at 9.7 and 20 μm has been observed in a variety of environments, such as the diffuse ISM, cold and dark interstellar clouds, planetary nebulae and also in DLA systems (Nuth & Hecht, 1990; Swamy, 2005; Kulkarni et al., 2007).

Observations in the local interstellar clouds by Kimura et al. (2003) suggested an iron enrichment in the cores of silicate grains composed by triolite (FeS), kamacite (FeNi) or oxides (FeO). Additional interstellar observations suggest the existence of a dust species decoupled from silicates: Fe and Si depletion in the Small Magellanic Cloud often diverges (Sofia et al., 2006), indicating that iron is not tied to the same grains as silicon. Voshchinnikov & Henning (2010) studied dust depletion in 196 different sight lines of the Milky Way, arguing that silicates grains cannot be a composition of olivines and pyroxenes only, but some amount of iron should reside in another dust population. Iron needles could represent an important additional dust species, having an appreciable contribution in the total amount of iron dust. Dwek (2004a) argued that iron needles contribute to the unexpected extinction law in the mid-infrared observation ($3-8\mu m$) of the Galactic center. In addition, theoretical prescriptions

(Hoyle & Wickramasinghe, 1999), different abundance ratio in various physical conditions (Voshchinnikov & Henning, 2010) and possible contribution of iron needles in Cas A (Dwek, 2004b) and SN 1987A (Wickramasinghe & Wickramasinghe, 1993) may suggest that: 1) those needles can be readily created in SNe environments and, 2) the destruction of silicates grains in the warm medium is more effective than for Fe-rich grains or, in other words, that iron particles are more resistant in the harshest ISM conditions.

Whilst the existence of a form of iron dust decoupled from silicates is suggested by many authors, its origin and nature are still under debate (Vladilo, 2004), the iron dust problem arises from the fact the bulk of this element is produced by Type Ia SNe, but at the same time there is no evidence of iron dust particles in their remnants. In our work we suggest that this iron species may originate directly in the ISM. Further evidence of iron dust accreting in the ISM is provided by Dwek (2016). Here, we demonstrate this possibility in a chemical evolution context. Draine & Hensley (2012, 2013) also investigated the same possibility: they showed that the sub millimeter and millimeter excess observed in low-metallicity galaxies might be explained by the presence of magnetic nano-particles, with radius $a < 0.1\mu m$, which include a large fraction of interstellar Fe.

If future observations will prove the existence of metallic nano-particles, the possibility that such solid component is partly produced by Type Ia SNe could be addressed with specific observational tests. As far as models are concerned, new algorithms for the production of metallic nano-particles by Type Ia SNe may be added to the efficient accretion in the ISM in order to improve the fit to the observed gas phase abundances in DLA systems.

QSO	zab	$\log\left(\frac{N(Zn_{II})}{cm^{-2}}\right)$	$\log\left(\frac{N(S_{II})}{cm^{-2}}\right)$	$\log\left(\frac{N(Fe_{II})}{cm^{-2}}\right)$	$\log\left(\frac{N(Si_{II})}{cm^{-2}}\right)$	Zn ref	S ref	Si ref	Fe ref
0008-0958	1.7675	13.31 ± 0.05	15.84 ± 0.05	15.62 ± 0.05	16.04 ± 0.05	35B	35B	35B	35B
0142-100	1.6265	11.43 ± 0.15	14.53 ± 0.10	14.59 ± 0.03	14.75 ± 0.03	30a	30a	30a	30a
0927+1543	1.7311	13.38 ± 0.05	–	15.14 ± 0.24	15.99 ± 0.05	35B	-	35B	35B
0927+5823	1.6352	13.29 ± 0.05	15.61 ± 0.05	–	15.72 ± 0.05	35B	35B	-	35B
1013+5615	2.2831	13.56 ± 0.05	–	–	16.14 ± 0.05	35B	-	-	35B
1049-0110	1.6577	13.14 ± 0.05	15.47 ± 0.05	15.17 ± 0.05	15.80 ± 0.05	35B	35B	35B	35B
1111-152	3.266	12.32 ± 0.10	14.62 ± 0.04	14.65 ± 0.03	15.10 ± 0.07	26e	34Z	34Z	34Z
1155+0530	3.326	12.89 ± 0.07	15.40 ± 0.05	15.37 ± 0.05	15.94 ± 0.05	35B	35B	35B	35B
1240+1455	3.1078	12.90 ± 0.07	15.56 ± 0.02	14.60 ± 0.03	15.93 ± 0.03	30d	30d	30d	30d
1310+5424	1.8006	13.57 ± 0.05	–	15.64 ± 0.05	16.44 ± 0.05	35B	-	35B	35B
1337+3152	3.1745	12.26 ± 0.26	15.11 ± 0.2	14.91 ± 0.08	15.50 ± 0.15	30c	30c	30c	30c
1454+0941	1.7884	12.72 ± 0.05	15.25 ± 0.06	15.02 ± 0.12	15.47 ± 0.05	35B	35B	35B	35B
1552+4910	1.9599	12.93 ± 0.05	15.34 ± 0.05	15.47 ± 0.05	15.98 ± 0.05	35B	35B	35B	35B
1604+3951	3.1633	13.00 ± 0.10	15.70 ± 0.02	15.40 ± 0.15	16.09 ± 0.02	30d	30d	30d	30d
1610+4724	2.5066	13.56 ± 0.05	–	15.62 ± 0.05	16.16 ± 0.05	35B	-	35B	35B
1629+0913	1.9023	12.68 ± 0.08	15.24 ± 0.05	–	15.32 ± 0.06	35B	35B	-	35B
1755+578	1.9692	13.85 ± 0.05	–	15.79 ± 0.05	16.58 ± 0.05	35B	-	35B	35B
1759+7539	2.625	12.56 ± 0.10	15.21 ± 0.02	14.94 ± 0.02	15.55 ± 0.06	22k	19c	19c	22k
2132-4321	1.916	12.69 ± 0.02	–	15.06 ± 0.04	15.57 ± 0.02	35A	-	35A	35A
1142+0701	1.8407	13.29 ± 0.05	–	15.47 ± 0.05	–	35B	-	35B	-
1313+1441	1.7947	13.30 ± 0.05	–	15.55 ± 0.05	–	35B	-	35B	-
1417+4132	1.9509	13.55 ± 0.05	–	15.58 ± 0.05	–	35B	-	35B	-
0027-1836	2.402	12.79 ± 0.02	15.23 ± 0.02	14.97 ± 0.04	15.67 ±0.08	27f	27f	28b	28b
0642-5038	2.659	12.75 ± 0.05	15.35 ± 0.05	14.91 ± 0.03	15.22 ±0.06	34a	34a	34Z	34Z
1209+0919	2.5841	12.98 ± 0.05	–	15.25 ± 0.03	15.91 ±0.02	27h	-	27h	27h
0035-0918	2.3401	–	13.08 ± 0.1	12.96 ± 0.05	13.37 ±0.05	-	34B	34B	34B
0044+0018	1.725	–	15.27 ± 0.05	–	15.34 ±0.05	-	35B	-	35B
0142+0023	3.3477	–	13.28 ± 0.06	13.70 ± 0.10	14.15 ±0.03	-	30d	30d	30d
0234-0751	2.3182	–	14.18 ± 0.03	14.18 ± 0.03	14.32 ±0.09	-	34A	34A	34A
0450-13	2.067	–	14.28 ± 0.12	14.30 ± 0.07	14.68 ±0.10	-	26a	26a	26a
0958+0145	1.9275	–	14.44 ± 0.05	14.23 ± 0.05	14.84 ±0.06	-	35B	35B	35B
1024+0600	1.895	–	15.45 ± 0.05	15.27 ± 0.08	15.81 ±0.05	-	35B	35B	35B
1112+1333	2.2709	–	13.69 ± 0.09	13.59 ± 0.02	13.95 ±0.02	-	34B	34B	34B
1211+0422	2.3766	–	14.53 ± 0.04	14.62 ± 0.03	14.91 ±0.04	-	28k	28k	28k
1335+0824	1.856	–	15.29 ± 0.05	–	15.73 ±0.05	-	35B	-	35B
1340+1106	2.7958	–	14.22 ± 0.02	14.32 ± 0.02	14.58 ±0.02	-	31a	31a	31a
1509+1113	2.0283	–	15.69 ± 0.05	15.48 ± 0.07	16.04 ±0.05	-	35B	35B	35B
1004+0018	2.5397	–	15.09 ± 0.02	15.13 ± 0.02	–	-	34A	34A	-
1009+0713	0.114	–	15.25 ± 0.12	15.29 ± 0.17	–	-	31b	31b	-
1451+1223	2.255	11.85 ± 0.11	–	14.33 ± 0.07	–	23b	-	-	23b
0112+029	2.423	–	14.83 ± 0.08	14.86 ± 0.05	–	-	23d	-	23d
1036-2257	2.777	–	14.79 ± 0.02	14.68 ± 0.02	–	-	23g	-	23g
0000-263	3.3901	12.01 ± 0.05	14.70 ± 0.03	14.76 ± 0.03	15.06 ± 0.02	20c	16d	20c	20c
0010-0012	2.0250	12.25 ± 0.05	14.96 ± 0.05	15.06 ± 0.05	15.31 ± 0.05	23d	25d	25d	23d
0058-2914	2.6711	12.23 ± 0.05	14.92 ± 0.03	14.75 ± 0.05	15.23 ± 0.07	23d	25d	25d	23d
0100+130	2.3090	12.47 ± 0.10	15.09 ± 0.06	13.37 ± 0.01	-	24a	24a	-	24a
0102-1902	2.3693	11.77 ± 0.11	14.30 ± 0.04	14.47 ± 0.10		23d	25d	-	23d
0201+365	2.4620	12.76 ± 0.30	15.29 ± 0.02	15.01 ± 0.01	15.53 ± 0.01	16e	22j	22j	22j
0216+080	2.2931	12.47 ± 0.05	15.04 ± 0.02	14.88 ± 0.02	15.45 ± 0.04	26e	31P	16d	31P
0347-383	3.0250	12.23 ± 0.12	14.76 ± 0.05	14.43 ± 0.01	14.77 ± 0.04	23d	25d	23d	22e
0405-443	2.5505	12.44 ± 0.05	14.82 ± 0.06	14.95 ± 0.06	15.32 ± 0.04	23e	23e	23e	23e
0528-2505	2.1410	12.29 ± 0.03	14.83 ± 0.04	14.85 ± 0.09	15.22 ± 0.05	26e	23a	23a	23a
0812+32	2.6260	13.15 ± 0.02	15.63 ± 0.08	15.98 ± 0.05	15.09 ± 0.01	27h	27h	27h	27h
0841+129	2.3745	12.20 ± 0.05	14.77 ± 0.03	14.87 ± 0.04	15.21 ± 0.04	23a	23a	27b	23a
0841+129	2.4764	11.69 ± 0.10	14.48 ± 0.10	14.50 ± 0.05	14.99 ± 0.03	26a	26a	26a	26a
0953+5230	1.7680	12.89 ± 0.05	15.35 ± 0.05	14.99 ± 0.05	15.67 ± 0.05	26k	26k	26k	26k

Table 3.2: The DLA sample used in this work. In the first column the QSO name, in the second the absorption redshift of the DLA system. Column density measurements of ZnII, SII, FeII and SiII are reported in column 3,4,5 and 6, respectively. Reference codes for the column densities are reported in columns 7,8,9 and 10: we report the corresponding literature references in Table 3.5

QSO	zab	$\log\left(\frac{N(Zn_{II})}{cm^{-2}}\right)$	$\log\left(\frac{N(S_{II})}{cm^{-2}}\right)$	$\log\left(\frac{N(Fe_{II})}{cm^{-2}}\right)$	$\log\left(\frac{N(Si_{II})}{cm^{-2}}\right)$	Zn ref	S ref	Si ref	Fe ref
1116+4118	2.9422	12.40 ± 0.33	15.01 ± 0.10	14.69 ± 0.04	15.34 ± 0.08	27j	27j	27j	27j
1210+1731	1.8918	12.40 ± 0.05	14.96 ± 0.03	15.01 ± 0.03	15.33 ± 0.03	27b	27b	27b	27b
1223+178	2.4661	12.42 ± 0.05	15.14 ± 0.04	15.21 ± 0.05	15.50 ± 0.03	25d	23d	25d	23d
1331+170	1.7764	12.54 ± 0.02	15.08 ± 0.11	14.63 ± 0.03	15.30 ± 0.01	24a	24a	24a	24a
2138-4427	2.8510	11.99 ± 0.05	14.50 ± 0.02	14.65 ± 0.05	14.86 ± 0.02	23d	25d	25d	23d
2206-199	1.9200	12.95 ± 0.02	15.42 ± 0.02	15.31 ± 0.01	15.80 ± 0.01	21i	31P	ww1	31P
2222-0946	2.3540	12.83 ± 0.01	15.31 ± 0.01	15.13 ± 0.01	15.62 ± 0.01	33a	33a	33a	33a
2230+025	1.8642	12.80 ± 0.11	15.29 ± 0.10	15.25 ± 0.05	15.70 ± 0.05	26a	26a	26a	26a
2231-0015	2.0662	12.30 ± 0.05	15.10 ± 0.15	14.83 ± 0.03	15.29 ± 0.04	24a	24a	24a	24a
2243-6031	2.3300	12.47 ± 0.02	15.02 ± 0.03	14.92 ± 0.03	15.36 ± 0.02	26f	22f	22f	22f
2314-409	1.8573	12.52 ± 0.10	15.10 ± 0.15	15.08 ± 0.10	15.41 ± 0.10	21c	21c	21c	21c
2318-1107	1.9890	12.50 ± 0.06	15.09 ± 0.04	14.91 ± 0.04	15.34 ± 0.04	27f	27f	27f	27f
2343+1232	2.4313	12.25 ± 0.10	14.66 ± 0.05	14.52 ± 0.05	15.15 ± 0.06	27f	27f	27f	27f
0013-004	1.9731	12.82 ± 0.04	15.28 ± 0.02	14.84 ± 0.03	15.43 ± 0.03	22h	22h	22h	22h
0551-3637	1.9615	13.02 ± 0.05	15.38 ± 0.11	15.05 ± 0.05	15.62 ± 0.06	22d	22d	22d	22d
0918+1636	2.5832	13.40 ± 0.02	15.82 ± 0.02	15.43 ± 0.01	16.01 ± 0.01	31C	31C	31C	31C
1439+1117	2.4184	12.93 ± 0.04	15.27 ± 0.06	14.28 ± 0.05	14.80 ± 0.04	28d	28d	28d	28d
1443+2724	4.2240	12.99 ± 0.03	15.52 ± 0.02	15.33 ± 0.03	–	28c	26f	-	26f
1444+014	2.0870	12.12 ± 0.15	14.62 ± 0.08	14.00 ± 0.06	14.38 ± 0.06	23d	23d	23d	23d
0149+33	2.1410	11.50 ± 0.10	–	14.23 ± 0.02	14.57 ± 0.05	ww1	-	ww1	ww1
0203-0910	1.0280	13.15 ± 0.15	–	15.65 ± 0.03	–	29d	-	-	29d
0225+0054	2.7140	12.89 ± 0.10	–	15.30 ± 0.10	15.62 ± 0.10	26c	-	26c	26c
0256+0110	0.7250	13.19 ± 0.04	–	15.13 ± 0.30	–	26j	-	-	26j
0302-223	1.0095	12.45 ± 0.04	–	14.67 ± 0.043	15.18 ± 0.04	20e	-	20e	20e
0354-2724	1.4051	12.73 ± 0.03	–	15.15 ± 0.05	–	27e	-	-	27e
0454+039	0.8597	12.42 ± 0.06	–	15.17 ± 0.04	15.45 ± 0.09	28a	-	20e	20e
0458-02	2.0400	13.13 ± 0.02	–	15.40 ± 0.05	–	ww1	-	-	19e
0515-4414	1.1510	12.11 ± 0.04	–	14.24 ± 0.20	14.74 ± 0.18	20b	-	20b	20b
0933+733	1.4790	12.71 ± 0.02	–	15.19 ± 0.01	–	25e	-	-	25e
0935+417	1.3726	12.25 ± 0.10	–	14.82 ± 0.10	–	15b	-	-	15b
0948+433	1.2330	13.15 ± 0.02	–	15.56 ± 0.01	–	25e	-	-	25e
1010+0003	1.2651	13.01 ± 0.02	–	15.26 ± 0.05	–	28a	-	-	26g
1013+0035	3.1040	13.33 ± 0.02	–	15.18 ± 0.050	15.78 ± 0.020	27h	-	27h	27h
1104-1805	1.6616	12.48 ± 0.02	–	14.77 ± 0.020	15.45 ± 0.020	19b	-	19b	19b
1107+0048	0.7410	13.06 ± 0.15	–	15.53 ± 0.02	–	26j	-	-	26j
1116+4118	2.6617	12.40 ± 0.20	–	14.36 ± 0.10	15.05 ± 0.11	27j	-	27j	27j
1117-1329	3.3511	12.25 ± 0.06	–	14.82 ± 0.05	15.12 ± 0.04	22g	-	22g	22g
1137+3907	0.7190	13.43 ± 0.05	–	15.45 ± 0.05	–	26g	-	-	26g
1157+0128	1.9436	12.99 ± 0.05	–	15.46 ± 0.02	15.97 ± 0.02	27b	-	27b	27b
1215+33	1.9990	12.33 ± 0.05	–	14.75 ± 0.05	15.03 ± 0.02	ww1	-	19e	ww1
1225+0035	0.7731	13.23 ± 0.07	–	15.69 ± 0.03	–	28a	-	-	26g
1230-101	1.9314	12.94 ± 0.05	–	15.32 ± 0.10	15.77 ± 0.10	25a	-	25a	25a
1249-0233	1.7810	13.11 ± 0.10	–	15.47 ± 0.10	15.80 ± 0.10	26c	-	26c	26c
1253-0228	2.7830	12.77 ± 0.07	–	15.36 ± 0.04	–	23g	-	-	23g
1323-0021	0.7160	13.43 ± 0.05	–	15.15 ± 0.03	–	26i	-	-	26i
1328+307	0.6922	12.53 ± 0.03	–	15.09 ± 0.01	–	28j	-	-	28j
1351+318	1.1491	12.52 ± 0.13	–	14.74 ± 0.09	15.23 ± 0.13	19d	-	19d	19d
1354+258	1.4200	12.59 ± 0.13	–	15.03 ± 0.09	15.36 ± 0.13	19d	-	19d	19d
1426+6039	2.8268	12.18 ± 0.04	–	14.48 ± 0.01	–	27h	-	-	27h
1501+0019	1.4832	12.93 ± 0.06	–	–	15.71 ± 0.02	26g	-	26g	-
1727+5302	0.9449	13.27 ± 0.05	–	15.38 ± 0.140	15.94 ± 0.02	24c	-	24c	24c
1727+5302	1.0311	12.65 ± 0.05	–	14.54 ± 0.100	15.60 ± 0.03	24c	-	24c	24c
1733+5533	0.9984	12.89 ± 0.06	–	–	15.48 ± 0.06	28a	-	26g	-
1850+40	1.9900	13.35 ± 0.10	–	15.58 ± 0.10	–	18g	-	-	18g
2059-0528	2.2100	12.94 ± 0.10	–	15.00 ± 0.10	15.36 ± 0.10	26c	-	26c	26c
2228-3954	2.0950	12.51 ± 0.05	–	15.17 ± 0.05	–	28c	-	-	28c
2340-00	2.0545	12.63 ± 0.08	–	–	15.17 ± 0.04	27h	-	27h	-
2359-0216	2.0950	12.60 ± 0.03	–	14.55 ± 0.03	15.40 ± 0.02	19e	-	ww1	ww1
0135-273	2.8000	–	14.78 ± 0.14	14.77 ± 0.11	–	-	23d	-	23d

Table 3.3: Continues from Table 3.2

QSO	zab	$\log\left(\frac{N(Zn_{II})}{cm^{-2}}\right)$	$\log\left(\frac{N(S_{II})}{cm^{-2}}\right)$	$\log\left(\frac{N(Fe_{II})}{cm^{-2}}\right)$	$\log\left(\frac{N(Si_{II})}{cm^{-2}}\right)$	Zn ref	S ref	Si ref	Fe ref
0201+1120	3.3848	–	15.21 ± 0.11	15.35 ± 0.05	–	-	ww1	-	ww1
0242-2917	2.5600	–	14.11 ± 0.04	14.36 ± 0.04	–	-	28c	-	28c
0254-4025	2.0460	–	14.10 ± 0.04	14.17 ± 0.04	–	-	28c	-	28c
0255+00	3.9146	–	14.72 ± 0.02	14.75 ± 0.15	–	-	ww1	-	ww1
0300-3152	2.1790	–	14.20 ± 0.04	14.21 ± 0.04	–	-	28c	-	28c
0336-0142	3.0621	–	14.99 ± 0.02	14.91 ± 0.03	15.25 ± 0.03	-	22j	26e	22j
0425-5214	2.2240	–	14.07 ± 0.04	13.96 ± 0.04	–	-	28c	-	28c
0741+4741	3.0174	–	14.00 ± 0.02	14.05 ± 0.01	14.35 ± 0.01	-	ww1	22j	22j
0900+4215	3.2458	–	14.65 ± 0.02	14.54 ± 0.02	–	-	27h	-	27h
0957+33	4.1798	–	14.39 ± 0.06	14.13 ± 0.05	14.56 ± 0.01	-	ww1	ww1	ww1
1021+3001	2.9490	–	13.87 ± 0.07	14.04 ± 0.01	14.32 ± 0.02	-	27h	27h	27h
1132+2243	2.7830	–	14.07 ± 0.06	14.02 ± 0.02	14.49 ± 0.12	-	23g	23g	23g
1220-1800	2.1130	–	14.39 ± 0.03	14.35 ± 0.03	–	-	28c	-	28c
1337+1121	2.7957	–	14.33 ± 0.02	14.07 ± 0.02	14.79 ± 0.07	-	27h	27h	27h
1354-1046	2.5010	–	14.13 ± 0.10	14.35 ± 0.10	–	-	28c	-	28c
1435+5359	2.3427	–	14.78 ± 0.05	–	15.13 ± 0.02	-	27c	27c	-
1558-0031	2.7026	–	14.07 ± 0.02	–	14.24 ± 0.02	-	27c	27c	-
2059-360	2.5073	–	13.49 ± 0.23	13.53 ± 0.05	13.91 ± 0.03	-	25d	25d	23d
2059-360	3.0830	–	14.38 ± 0.05	14.52 ± 0.07	14.80 ± 0.05	-	25d	25d	20d
2222-3939	2.1540	–	14.08 ± 0.03	14.42 ± 0.03	–	-	28c	-	28c
2241+1352	4.2820	–	14.58 ± 0.03	14.76 ± 0.11	15.06 ± 0.05	-	23g	23g	23g
2332-0924	3.0572	–	14.13 ± 0.04	14.06 ± 0.03	14.64 ± 0.03	-	34Z	34Z	34Z
2342+3417	2.9082	–	15.19 ± 0.02	15.02 ± 0.06	15.62 ± 0.02	-	27h	27h	27h
2348-147	2.2790	–	13.75 ± 0.06	13.84 ± 0.05	14.18 ± 0.05	-	26a	26a	26a
1232+0815	2.3377	–	14.81 ± 0.09	14.44 ± 0.08	15.06 ± 0.05	-	31c	31c	31c
2348-0108	2.4272	–	15.06 ± 0.04	14.83 ± 0.03	15.26 ± 0.09	-	27g	27g	27g

Table 3.4: Continues from Table 3.2

Code	Reference	Code	Reference
16d	Lu, L., Sargent, W.L.W., Barlow, T.A., et al. 1996, ApJS, 107, 475	26f	Ledoux, C., Petitjean, P., Srianand, R. 2006, ApJ, 640, L25
16e	Prochaska, J.X., Wolfe, A.M. 1996, ApJ, 470, 403	26g	Meiring, J.D., Kulkarni, V.P., Khare, P., et al. 2006, MNRAS, 370, 43
18g	Prochaska, J.X., Wolfe, A.M. 1998, ApJ, 507, 113	26i	Peroux, C., Kulkarni, V.P., Meiring, J., et al. 2006, A&A, 450, 53
19b	Lopez, S., Reimers, D., Rauch, et al. 1999, ApJ, 513, 598	26j	Peroux, C., Meiring, J.D., Kulkarni, V.P., et al. 2006, MNRAS, 372, 369
19c	Outram, P.J., Chaffee, F.H., Carswell, R.F. 1999, MNRAS, 310, 289	26k	Prochaska, J.X., O'Meara, J.M., Herbert-Fort, S., et al. 2006, ApJ, 648, L97
19e	Prochaska, J.X., Wolfe, A.M. 1999, ApJS, 121, 369	27b	Dessauges-Zavadsky, M., Calura, F., Prochaska, et al. 2007, A&A, 470, 431
19d	Pettini, M., Ellison, S.L., et al. 1999, ApJ, 510, 576	27e	Meiring, J.D., Lauroesch, J.T., Kulkarni, V.P., et al. 2007, MNRAS, 376, 557
20b	de la Varga, A., Reimers, D., Tytler, D., et al. 2000, A&A, 363, 69	27f	Noterdaeme, P., Ledoux, C., Petitjean, P., et al. 2007, A&A, 474, 393
20c	Molaro, P., Bonifacio, P., Centurion, M., et al. 2000, ApJ, 541, 54	27g	Noterdaeme, P., Petitjean, P., Srianand, R., et al. 2007, A&A, 469, 425
20e	Pettini, M., Ellison, S., Steidel, C.C., et al. 2000, ApJ, 532, 65	27h	Prochaska, J.X., Wolfe, A.M., Howk, J.C., et al. 2007, ApJS, 171, 29
21i	Ellison, S.L., Ryan, S.G., Prochaska, J.X. 2001, MNRAS, 326, 628	27j	Ellison, S.L., Hennawi, J.F., et al. 2007, MNRAS, 378, 801
22d	Ledoux, C., Srianand, R., Petitjean, P. 2002, A&A, 392, 781	28a	Nestor,D.B., Pettini, M., et al. 2008, MNRAS, 390, 1670
22e	Levshakov, S.A., Dessauges-Zavadsky, M., et al. 2002, ApJ, 565, 696	28b	Noterdaeme, P., Ledoux, C., et al. 2008, A&A, 481, 327
22f	Lopez, S., Reimers, D., et al. 2002, A&A, 385, 778	28c	Noterdaeme, P., Ledoux, C., et al. 2008, A&A, 481, 327
22g	Peroux, C., Petitjean, P., et al. 2002, NewA, 7, 577	28d	Noterdaeme, P., Petitjean, P., et al. 2008, A&A, 491, 397
22h	Petitjean, P., Srianand, R., Ledoux, C. 2002, MNRAS, 332, 383	28j	Wolfe, A.M., Jorgenson, R.A., Robishaw, T., et al. 2008, Nature, 455, 638
22j	Prochaska, J.X., Henry, R.B.C., O'Meara, J.M., et al. 2002, PASP, 114, 933	28k	Lehner, N., Howk, J.C., et al. 2008, MNRAS, 390, 2
22k	Prochaska, J.X., Howk, J.C., O'Meara, J.M., et al. N. 2002, ApJ, 571, 693	29d	Monier, E.M., Turnshek, et al. 2009, AJ, 138, 1609
23a	Centurion, M., Molaro, P., Vladilo, G., et al. 2003, A&A, 403, 55	30a	Cooke, R., Pettini, M., Steidel, C.C., et al. 2010, MNRAS, 409, 679
23b	Dessauges-Zavadsky, M., Peroux, C., Kim, T.-S., et al. 2003, MNRAS, 35, 447	30c	Srianand, R., Gupta, N., Petitjean, P., et al. 2010, MNRAS, 405, 1888
23d	Ledoux, C., Petitjean, P., Srianand, R. 2003, MNRAS, 346, 209	30d	Ellison, S.L., Prochaska, J.X., Hennawi, J., et al. 2010, MNRAS, 406, 1435
23e	Lopez, S., Ellison, S.L. 2003, A&A, 403, 573	31a	Cooke, R.,Pettini,M.,Steidel,C., et al. 2011, MNRAS,417,1534
23g	Prochaska, J.X., Gawiser, E., Wolfe, A.M., et al. 2003, ApJS, 147, 227	31b	Meiring, J.D., Tripp, T.M., Prochaska, J.X., et al. 2011, ApJ, 732, 35
24a	Dessauges-Zavadsky, M., Calura, F., Prochaska, J.X., et al. 2004, A&A, 416, 79	31c	Balashev, S.A., Petitjean, P., Ivanchik, A.V., et al. 2011, MNRAS, 418, 357
24c	Khare, P., Kulkarni, V.P., Lauroesch, J.T., et al. 2004, ApJ, 616, 86	31P	Vladilo, G., Abate, C., Yin, J., et al. 2011, A&A, 530, A33
25a	Akerman, C.L., Ellison, et al. 2005, A&A, 440, 499	33a	Krogager, J.K., Fynbo, J.P.U., Ledoux, C., et al. 2013, MNRAS, 433, 3091
25d	Srianand, R., Petitjean, P., Ledoux, C., et al. 2005, MNRAS, 362, 549	34a	Vasquez, D.A., Rahamani, H., Noterdaeme, P., et al. 2014, A&A, 562, A88
26a	Dessauges-Zavadsky, M., Prochaska, J.X., D'Odorico, S., et al. 2006, A&A, 445, 93	34B	Cooke, R., Pettini, M., et al. 2015, ApJ, 800, 12
26c	Herbert-Fort, S., Prochaska, J.X., Dessauges-Zavadsky, M., et al. 2006, PASP, 118, 1077	34Z	Zafar, T., Centurión, M., Péroux, C., et al. 2014, MNRAS, 444, 744
26e	Ledoux, C., Petitjean, P., Fynbo, J.P.U., et al. 2006, A&A, 457, 71	35A	Quiret, S., Peroux, C., Zafar, T., et al. 2016, MNRAS
35B	Berg, T., Neeleman, M., Prochaska, X., et al. 2015, MNRAS, 452, 4326-4346		

Table 3.5: References relative to the codes of Table 3.2

3.4 Dust chemical composition

As we have already pointed out, spectroscopic measurements detect the composition of the gas phase of the ISM (optical/UV) leaving undetected the elemental particles present in the dust phase. For this reason, we do not have any direct measurements or evidences of the dust composition in DLA systems.

Here we present a new method to provide for the first time the element-to-element abundance ratios of the dust phase in the ISM of DLA systems. To this purpose, we will take advantage of the properties of refractory and volatile elements and the predictions of chemical evolution models. In what follows, we explain our method and present the obtained results in sub-Section 3.4.1. In sub-Section 3.4.2 we compare our results with our chemical evolution model, in order to understand how different dust processes affect the element-to-element abundance ratio during the galactic evolution: this comparison represents an independent test, as our chemical evolution model is based on theoretical prescriptions. In sub-Section 3.4.3, we interpret our results through a simple dust model which accounts for silicates (variable mixture of pyroxenes and olivines) and Fe in metallic particles: this approach is necessary to study the stoichiometry of dust grains, and therefore study how different dust species evolve as a function of the metallicity.

3.4.1 Abundance ratios in dust

To obtain the dust abundance ratios in the ISM of DLA systems, we compare observations with chemical evolution models which are able to trace the total abundance of an element in the ISM. Because of dust depletion, this comparison leads to a different interpretation when volatile or refractory elements are used. Here, we first describe step by step how we take advantage of the peculiarity of volatile and refractory elements, and we show the fundamental equations that are necessary to obtain the dust abundance ratios.

Method

Let us express N_i^{ISM} as the total column density of an element i in the ISM, namely, part of its abundance resides in the gas phase of the ISM whereas the rest is incorporated in the dust phase. Therefore, the total column density can be expressed as follows:

$$N_i^{ISM} = N_i^g + N_i^d, \tag{3.1}$$

where the first and the second terms on the right side of the equation express the column density in the gas and in the dust phase, respectively. Eq. (3.1) is appropriate for a refractory element, $i = R$, for which we can write:

$$N_R^{ISM} = N_R^g + N_R^d \tag{3.2}$$

On the other hand, for a volatile element $i = V$, no abundance in the dust phase is expected and therefore the total column density in the ISM is equal to the one measured in the gas phase:

$$N_V^{ISM} = N_V^g \equiv N_V \tag{3.3}$$

By dividing equation (3.2) by (3.3), and deriving N_R^d we obtain:

$$N_R^d = (N_R/N_V)^{ISM} \cdot N_V - N_R^g \tag{3.4}$$

where $(N_R/N_V)^{ISM}$ is the total abundance ratio in the ISM between a refractory and a volatile element.

If we consider two refractory elements R_1 and R_2, we can simply derive their average abundance ratio in the dust along the DLA sight line $(N_{R_1}/N_{R_2})^d$ from eq. (3.4), namely:

$$\left(\frac{N_{R_1}}{N_{R_2}}\right)^d = \frac{N_V(N_{R_1}/N_V)^{ISM} - N_{R_1}^g}{N_V(N_{R_2}/N_V)^{ISM} - N_{R_2}^g} \tag{3.5}$$

High resolution spectroscopy in the optical and UV wavebands can measure only the gas phase column density of a single element, but it cannot give information on the dust phase. The column densities in the gas phase of refractories and volatile (N_{R_1}, N_{R_2}, N_V) can be directly measured from spectroscopy, while the total abundance ratios in the ISM, $(N_{R_1}/N_V)^{ISM}$ and $(N_{R_2}/N_V)^{ISM}$, can be constrained by a model of galactic chemical evolution.

We see from eq. (3.5) that the dust abundance ratio of two given chemical elements depends on the abundance of one volatile element. As a consequence of this, in DLAs we can use only one measured abundance of a volatile element to derive such a ratio. In particular, we can use the measurements of Zn and S and then select the abundance ratio with the smallest error.

Error on the dust abundance ratio

In order to estimate an error of the measured abundance dust ratio $(N_{R_1}/N_{R_2})^d$ we rewrite eq.(3.5) as:

$$\rho = \frac{ax - y}{bx - z}, \tag{3.6}$$

where $\rho \equiv (N_{R_1}/N_{R_2})^d$; x, y and z indicate the observed quantities N_V, N_{R_1}, N_{R_2}, respectively, and are considered as independent variables; a and b refer to the model predictions $(N_{R_1}/N_V)^{ISM}$ and $(N_{R_2}/N_V)^{ISM}$ respectively, which are assumed as reference values, without error. To estimate the error propagation on the variable ρ, we define the variables $u \equiv ax - y$ and $v \equiv bx - z$, obtaining:

$$\sigma_\rho = \frac{1}{v^2}\sqrt{(av - bu)^2\sigma_x^2 + v^2\sigma_y^2 + u^2\sigma_z^2} \tag{3.7}$$

With the above expression, we can put a selection criteria on our results: when σ_ρ is grater than 0.5 dex (arbitrary value), we reject the measurement of the dust abundance calculated by eq. (3.5).

Beside the estimate of the error, our results may be also affected by the assumption that a volatile element totally resides in the gas phase of the ISM. In fact, if a small fraction of a volatile element $f_V = N_V^d/(N_V^g + N_V^d)$ has been locked into dust grains, the total column density in the medium will be different from expressed in eq.(3.3), in particular:

$$N_V^{ISM} = N_V^g(1 + \epsilon_V), \tag{3.8}$$

where $\epsilon_V = f_V/(1-f_V)$. If we account for this possible small depletion of the volatile element, the dust column density expressed in eq.(3.5) becomes:

$$\left(\frac{N_{R_1}}{N_{R_2}}\right)^d = \frac{N_V(1+\epsilon_V)(N_{R_1}/N_V)^{ISM} - N^g_{R_1}}{N_V(1+\epsilon_V)(N_{R_2}/N_V)^{ISM} - N^g_{R_2}} \tag{3.9}$$

In this way, we face the possibility that we may introduce an error in the estimate of the dust abundance ratio. For ϵ_{Zn} and ϵ_S we explore a range of values from 0.1 to 0.25 dex, based on the depletions provided by De Cia et al. (2016) for those elements residing in low-metallicity environments. As we did not find substantial differences in this range, we adopt a final 0.1 dex depletion for both Zn and S. To quantify the uncertainties related to volatile depletions, we compare the results obtained from equations (3.5) and (3.9) and discard cases with an absolute deviation larger than 0.15 dex of the computed error of eq. (3.7), are rejected.

The galactic chemical evolution model

As in the Section 3.3, here we compare the chemical abundances predicted by the model with the ones observed in DLAs. Also in this case, we aim at a model which can reproduce the observed features in DLAs, namely the ones of a typical low-mass and -luminosity galaxy (Matteucci et al., 1997; Møller & Warren, 1998; Calura et al., 2003; Christensen et al., 2014; Gioannini et al., 2017a).

The model parameters are specifically fixed similarly to the ones of Vladilo et al. (2011): they did not use a chemical evolution model which accounts for the presence of dust, and their constraints were based on the comparison between model predictions and observations of volatile chemical abundances (i.e., the S/Zn abundance ratio). This comparison is indeed independent from the presence of dust. Using the S/Zn ratio in DLA systems, they performed a fine tuning by producing a grid of chemical evolution models, where the total mass M_{infall}, ν and ω were let to vary, and selected the best model by the comparison with the observed S/Zn ratios, on the basis of a least square method. At variance with Vladilo et al. (2011), we performed also some tests on the variation of the IMF and the time-scale of the infall τ, but we did not find substantial differences with the previous work. After performing these tests, we have adopted the parameter values shown in Table 3.6, which agree with the ones of a typical dwarf irregular galaxy (Bradamante et al., 1998; Recchi et al., 2002; Calura et al., 2008).

Results: the observational trend

In Fig. 3.9, we present the dust abundance ratios for Si and Mg over Fe computed with our method. The data are plotted as a function of metallicity, expressed as [Zn/H] or [S/H] (Eq. 3.5), depending on which element (Zn and S) has been used as the volatile to compute the dust abundance ratio. The solar reference value has been taken from Asplund et al. (2009).

In the top panel of Fig. 3.9 it is clear that the Si/Fe abundance ratio in the dust is not constant and decreases with the metallicity. This trend is very important in terms of dust evolution and suggests that the dust chemical composition varies with metallicity and therefore with time. The same trend is observed for the $(N_{Mg}/N_{Fe})^d$ dust abundance ratio, even if in this case there

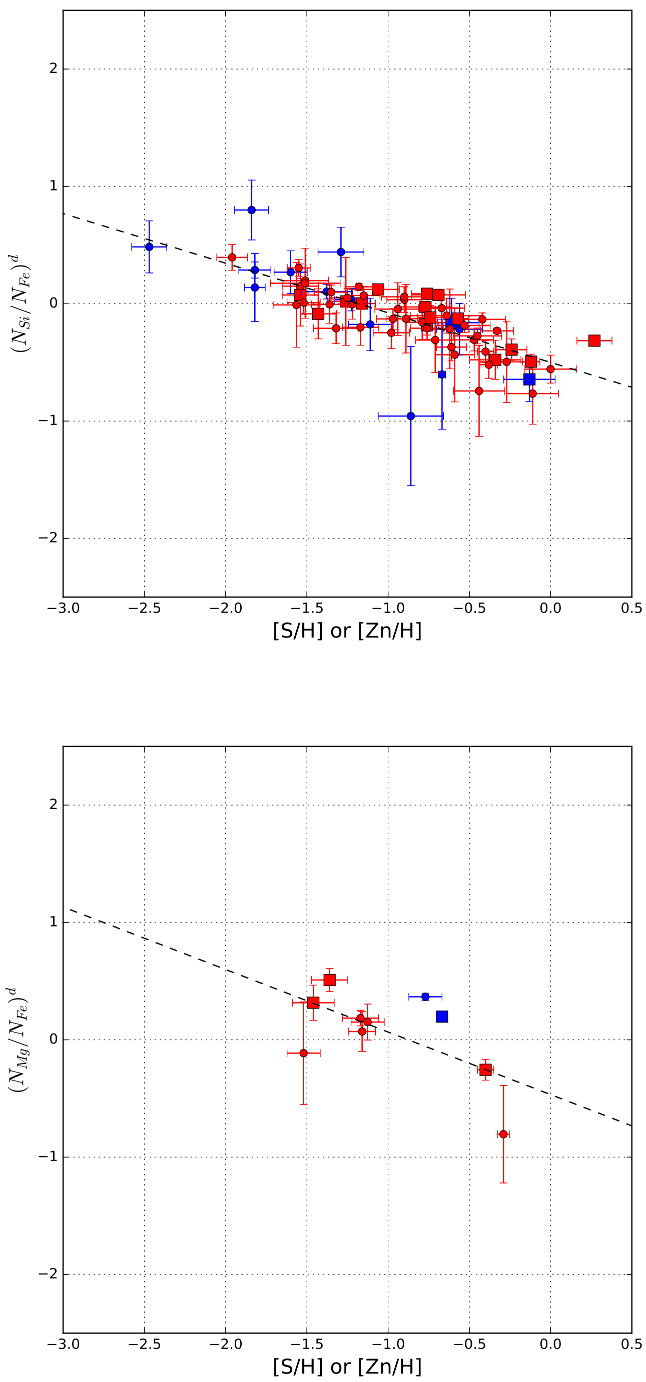

Figure 3.9: Dust abundance ratio of Si and Fe (top panel) and Mg and Fe (bottom panel) as a function of the measured abundance of Zn or S column density. Red and blue dots represent data for which only DLA measurement of Zn or S was available, respectively. Red and blue squares represent data for which both volatiles measurements were available but the propagated error was lower in the case of Zn or S, respectively. The error bar of each point has been computed through eq. (3.7). Black dotted line represents the linear regression of dust column density versus [Zn/H] data.

Parameter	Value
T_{infall}	$0.1\,Gyr$
M	$5 \times 10^9\,M_\odot$
ν	$0.050\,Gyr^{-1}$
ω	3.5
IMF	Salpeter

Table 3.6: Resume of the adopted parameters of the chemical evolution model to reproduce the abundances of DLA systems. From the first raw to the last we report the adopted time of the infall, mass of the galaxy, star formation efficiency, wind parameter and the initial mass function.

is a lower amount of data with respect to the previous case. In Fig. 3.9 we also present a linear fit to the dust abundances, which significance level strengthens our interpretation of the trend (black dashed line). The parameters of the fit are:

$$\left(\frac{N_{Si}}{N_{Fe}}\right)^d = -0.537_{\pm 0.05} \cdot [Zn/H] - 0.422_{\pm 0.04}$$
$$\left(\frac{N_{Mg}}{N_{Fe}}\right)^d = -0.466_{\pm 0.26} \cdot [Zn/H] - 0.533_{\pm 0.24}$$

with a Pearson correlation coefficients of -0.78 and -0.62 for $(N_{Si}/N_{Fe})^d$ and $(N_{Mg}/N_{Fe})^d$, respectively.

The flat trend of the $[(Si, Mg)/Fe]$ ratios in the ISM of low metallicity systems is a known feature confirmed by both observations (e.g. Lu et al., 1996; Cooke et al., 2011; Rafelski et al., 2012; Cooke et al., 2015) and chemical evolution models (e.g. Kunth et al., 1995; Matteucci et al., 1997; Calura et al., 2003; Spitoni et al., 2009), and it is attributed to the delayed pollution in the ISM of iron with respect to α-elements[1]. It is interesting that also the abundance ratio we found in the dust phase qualitatively follows the same evolution: this may suggest that the evolution of the abundance ratios in the dust phase is strictly connected to the evolution of the same elements in the ISM.

However, the decrease of dust abundance ratios is steeper than the one observed in the chemical evolution predictions which show a decrease of [Si, Mg]/Fe of only ≈ 0.2 dex in the metallicity range [-2.0,0.0]. Clearly, the interpretation of the element-to-element ratios in the dust is more complex. In fact, the dust abundance ratios may depend on the type of dust species present in the ISM and on the relative contributions of different dust sources (AGB stars, Type II SNe and dust growth). A very simple interpretation of this trend would suggest that iron-rich dust might be important at higher metallicities.

In order to better understand this evolution, in what follows we are going to present two distinct studies.

In the first one we compare the obtained abundance ratios in the dust with the theoretical predictions provided by the chemical evolution model. In this way, we are able to study how different dust processes (dust formation by stars, accretion and destruction) influence the abundance ratios of the elements in

---

[1] α-elements are those elements formed in massive stars ($M_* > 10M_\odot$) by subsequent addition of α-particles, such as O, Mg, Si, S, Ca

dust grains. Unfortunately, this study does not allow us to study the accurate species that compose dust grains (pyroxenes, olivines and iron particles). For this reason, we also present a different approach, based on a simplified model of dust grain composition (hereafter *dust grain model*). By means of this approach, we can directly investigate the real stoichiometry of silicates and the fraction of Fe-rich dust included in the *metallic* component.

3.4.2 Comparison with galactic evolution models with dust production

In this paragraph we present the comparison between the obtained dust abundance ratios calculated with Eq.(3.5) and the prediction of the galactic evolution model which accounts for the production of dust by different sources (Type II SNe, AGB stars and dust growth/accretion in the ISM). In this way, we are performing an independent test on the observed trend in the chemical abundances of the dust phase: in fact, the dust abundance ratios performed in paragraph 3.4.1 have been obtained starting from the observed abundances in DLA systems, whereas in the case of chemical evolution model we provide the same quantities based on a theoretical calculation.

In this context, we adopt the same galactic chemical evolution model used in Section 3.3 and we call it the *reference model*. In the previous Section we compared the abundance ratios of refractories and volatiles, whereas here we aim at comparing the element-to-element ratios in the dust grains. In Fig. 3.10, we present the predictions for the dust chemical abundance ratios of our chemical evolution model. The yellow thick line represents the reference model for $(Si/Fe)_d$ and $(Mg/Fe)_d$ in the top and bottom panels, respectively. In both cases, the model confirms that the evolution of Fe in dust is not correlated with the ones of Si and Mg. We can approximatively divide the trend in two distinct regions: a moderate decrease at low metallicities ($[Fe/H] < -0.7$) which becomes steeper at higher metallicities ($-0.7 < [Fe/H] < 0.5$). The two slopes are caused by roles of different dust processes during the galactic evolution. At low metallicities dust production from Type II SNe is the most important process of dust formation. These kind of stars produce mainly α-elements and only a small fraction of Fe. This characteristic, together with the typical short timescale involved in those massive stars (shorter than 30 Myr for stars with masses $M_* > 8M_\odot$, e.g. Padovani & Matteucci 1993), leads to the typical high values of $[\alpha/Fe]$ ratios observed in low metallicities environments (e.g., Matteucci et al., 1997; Calura et al., 2003; Spitoni et al., 2016). As already pointed out in Sec. 3.4.1, here we find that this behavior is also reproduced in the chemical abundances of the dust phase.

$(Si/Fe)_d$ and $(Mg/Fe)_d$ strongly depend on the adopted dust condensation efficiencies, namely on the dust stellar yields: we show in Fig. 3.10 the case in which the iron dust condensation efficiency from Type II SNe (δ^{II}_{Fe}) are increased by a factor 1.5 and 3.0 in cyan and blue lines, respectively (the increased values of δ^{II}_{Fe} remain strictly ≤ 1.0, in agreement with the definition of condensation efficiency). As we expected, as the δ^{II}_{Fe} increases, both ratios of $(Si/Fe)_d$ and $(Mg/Fe)_d$ decrease, proving that the variation of the dust abundance ratios at low metallicities is strictly connected to dust production from Type II SNe. The variation of δ^{II}_{Fe} provokes a visible scatter at low metallicity, whereas the three models (the reference model and the ones with increased δ_{Fe}) almost trace each

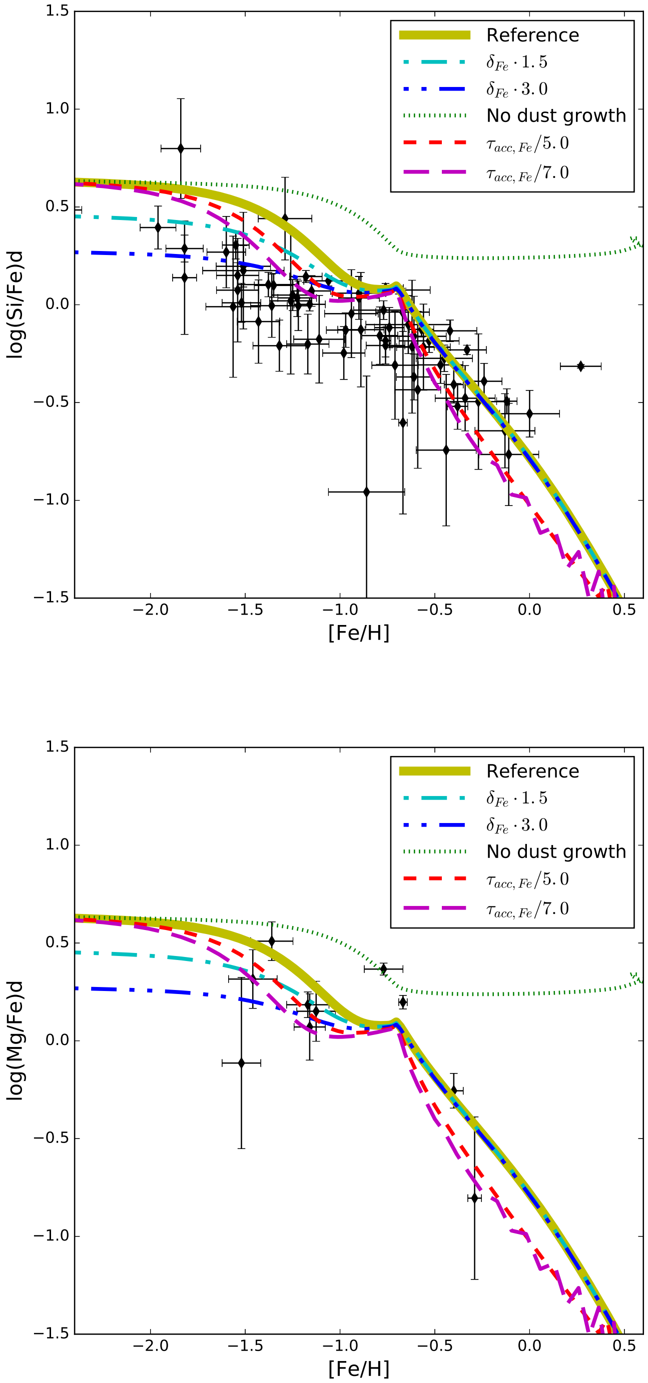

Figure 3.10: Chemical abundance ratios in the dust phase of $(Si/Fe)_d$ and $(Mg/Fe)_d$ versus metallicity in the top and bottom panels, respectively. The thick yellow line represents the variation of the chemical abundances in the dust phase as predicted by our chemical evolution model with dust. Other models vary from the reference one as showed in the box. Cyan dash-dotted and blue dash-dot-dotted line dust production of Fe by Type II SNe is increased by a factor 1.5 and 3.0, respectively. The dotted green model assumes that no dust accretion is occurring during the whole galactic time. Red dashed and magenta long-dashed lines have a more efficient Fe accretion of a factor 5 and 7, with respect to the reference model.

other at higher metallicities. The reason is that at those metallicities Type II SNe are not any more the most important channel for dust production: in fact, as the critical metallicity is reached (see Section 3.2.3), dust accretion becomes the dominant process and the abundance ratios $(Si, Mg/Fe)_d$ become almost independent of the condensation efficiencies of Type II SNe.

Dust accretion is indeed a fundamental process, which influences dust evolution in galaxies, especially at high metallicity. In Fig. 3.10 we show that the chemical evolution model without considering dust accretion (green-dotted line) anti-correlates with data. In fact, the model starts decreasing at low metallicity but at a certain point it predicts a constant value of $(Si/Fe)_d$ and $(Mg/Fe)_d$. The way the dust abundance ratios Si/Fe and Mg/Fe vary at higher metallicities depends on how different elements contribute to dust growth. The red and magenta lines represent models with more efficient Fe-rich dust accretion as described in the legend. Here, we find that models with shorter time-scales for Fe-rich dust accretion provide a better agreement with observations, even if the difference between the reference model is not so large. Finally, we remind that assuming a shorter timescale for Fe means that we are assuming the presence in the ISM of iron-rich dust grains with sizes smaller than 0.1 μm, as eq.(2.16) shows.

3.4.3 Interpretation: the composition of dust

To interpret the dust abundance ratios of Si, Mg and Fe we adopt a model of dust grains. In our idealized dust model, we consider interstellar dust grains made of silicates plus an iron-rich dust species (possibly metals, as suggested in Section 3.3). Carbon is not considered for two reasons. First, carbon abundances are not observable in DLA systems, either because the absorption lines are totally saturated or because they are too faint. Second, carbon is usually incorporated in organic compounds which are probably missing in the harsh interstellar conditions typical of DLA systems.

To describe our dust model we adopt a similar notation as proposed by Ueda et al. (2005). In our method we assume that all the Si and Mg abundance in the dust phase is bound in the form of silicates. In particular, we assume silicates composed by a mixture of pyroxenes, $Mg_xFe_{(1-x)}SiO_3$ ($x = 0, 1$ corresponds to ferrosilite and enstatite, respectively), and olivines, $Mg_{2y}Fe_{2(1-y)}SiO_4$ ($y = 0, 1$ corresponds to fayalite and forsterite, respectively). These classes of silicates are thought to be the dominant classes of interstellar silicates (e.g. Savage & Sembach, 1996). Each component can be Mg-rich or Fe-rich, depending on the values of the parameters x and y for pyroxenes and olivines, respectively:

$$x = \left(\frac{N_{Mg}}{N_{Mg} + N_{Fe}} \right)^{d}_{prx} \tag{3.10}$$

and

$$y = \left(\frac{N_{Mg}}{N_{Mg} + N_{Fe}} \right)^{d}_{olv}. \tag{3.11}$$

We fix the proportion of pyroxenes and olivines in the mixture with the parameter α:

$$\alpha = \frac{N_{prx}}{N_{prx} + N_{olv}}, \tag{3.12}$$

where $N_{prx} = N[Mg_xFe_{(1-x)}SiO_3]$ and $N_{olv} = N[Mg_{2y}Fe_{2(1-y)}SiO_4]$ represent the number density of pyroxenes and olivine molecules, respectively. Then, the number density of a refractory element in the silicate form can be expressed as:

$$N^d_{Si} = N_{prx} + N_{olv} \tag{3.13}$$

in the case of Si,

$$N^d_{Mg} = x \cdot N_{prx} + 2y \cdot N_{olv} \tag{3.14}$$

in the case of Mg, and:

$$N^d_{Fe_{(silicates)}} = (1-x) \cdot N_{prx} + 2(1-y) \cdot N_{olv} \tag{3.15}$$

in the case of Fe.

In the case of Fe, we assume that a fraction of its dust abundance (μ) is incorporated in another *"metallic"* dust component, beyond silicates:

$$\mu = \frac{N^d_{Fe_{(met)}}}{N^d_{Fe_{(met)}} + N^d_{Fe_{(sillicates)}}}, \tag{3.16}$$

where we defined $N_{Fe_{(met)}}$ as this additional iron-rich metallic component, with no assumption on its nature. Therefore, the total abundance of Fe in the dust phase will result from the sum of the Fe density in the two species, $N^d_{Fe} = N^d_{Fe_{(met)}} + N^d_{Fe_{(silicates)}}$:

$$N^d_{Fe} = \frac{(1-x) \cdot N_{prx} + 2(1-y) \cdot N_{olv}}{(1-\mu)}. \tag{3.17}$$

By the definitions given above of the parameters α, x, y and μ we can now introduce the equations that express in parametric form the number densities of (Si/Fe) and (Mg/Fe) in the dust phase:

$$\left(\frac{Si}{Fe}\right)_d = \frac{(1-\mu)}{(1-x)\alpha + 2(1-y)(1-\alpha)} \tag{3.18}$$

$$\left(\frac{Mg}{Fe}\right)_d = \frac{(1-\mu)[x\alpha + 2y(1-\alpha)]}{(1-x)\alpha + 2(1-y)(1-\alpha)}. \tag{3.19}$$

Equations (3.18) and (3.19) can be used to infer which type of dust grains is more abundant. Moreover, it can be used to track the evolution of the dust chemical composition, as we explain in the next paragraph.

Fixed parameters

The “graphite and silicate” model (Hoyle & Wickramasinghe, 1969), represents the basis of almost all subsequent dust grain composition models (Mathis et al., 1977; Draine & Lee, 1984; Desert et al., 1990; Li & Draine, 2001). In our work we focus on the study of the silicate grain composition, since we are analyzing the abundance ratios of Mg, Si and Fe, which represent the building blocks of silicate dust. Some observational studies of the parameters α, x, y and μ have been performed on several interstellar lines of sight, by using IR (Kemper et al., 2004; Min et al., 2007; Fogerty et al., 2016) and X-rays measurements

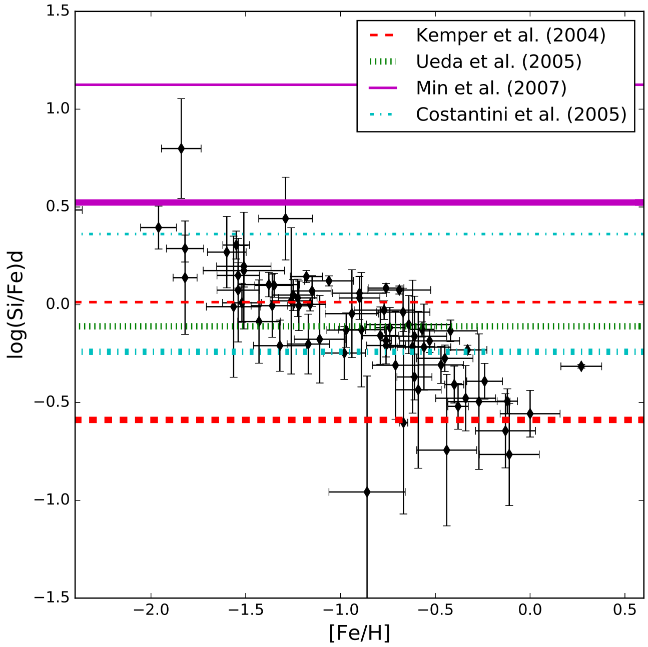

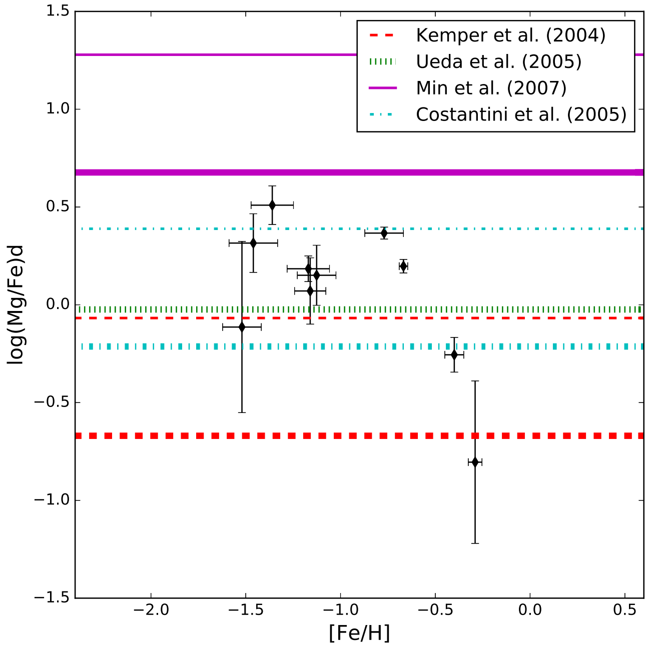

Figure 3.11: $(Si/Fe)_d$ and $(Mg/Fe)_d$ abundance ratios in the dust of DLA systems as a function of the metallicity. Abundances and error bars (black dots) are taken from equations (3.18), (3.19) and (3.7). Lines represent dust models without evolution as shown in the top right box: normal and thick lines represent values of $\mu = 0.0$ and 0.75, respectively. The fixed model parameters are given in Table 3.7.

α	x	y	μ	Reference	Observation	Interstellar Region
0.2	0.55	0.45	0.00	Kemper et al. (2004)	IR abs.	Galactic center
0.2	0.55	0.45	0.75	Kemper et al. (2004)	IR abs.	Galactic center
0.2	0.50	0.70	0.55	Ueda et al. (2005)	X-Ray abs.	Galactic center
0.5	0.71	0.71	0.00	Costantini et al. (2005)	X-Ray abs.	Cyg X-2
0.5	0.71	0.71	0.75	Costantini et al. (2005)	X-Ray abs.	Cyg X-2
0.5	0.95	0.95	0.00	Min et al. (2007)	IR abs.	Galactic center
0.5	0.95	0.95	0.75	Min et al. (2007)	IR abs.	Galactic center

Table 3.7: Assumed values of the parameters for the simple dust model obtained from different literature works. In the first, second, third and fourth columns are presented the values of α, x, y and μ, respectively. Then we report the bibliographic reference (column five), the adopted technique used (column six) as well as the related Galactic region (column seven).

(Ueda et al., 2005; Costantini et al., 2005; Lee & Ravel, 2005; Lee, 2010). Based on the IR measurements, Kemper et al. (2004) investigated the 10 μm silicate feature in the line of sight of the Galactic center, obtaining a best agreement with observations when a mixture of 15% for pyroxenes and 85% for olivines was adopted in their model. Similar results were confirmed by Fogerty et al. (2016), which suggest a fifty-fifty abundance of the two species. Ueda et al. (2005), by means of high resolution X-Ray spectroscopy constrained the parameters as $\alpha = 0.2$, $x = 0.5$ and $y = 0.7$. The parameter μ is generally unconstrained, except in the work of Ueda et al. (2005), who estimated a value of 0.45 for the fraction of Fe in silicates, and therefore $\mu = 0.55$. Based on these empirical results, we have considered a series of grain compositions with constant values of α , x, y and μ, listed in Table 3.7. In these grain models, when μ is not given, we adopt two representative values, namely $\mu = 0.75$ and $\mu = 0.0$ (all Fe is assumed in silicate form).

In Fig. 3.11, we compare the predictions of the grain models with fixed parameters with the computed dust abundance ratios. The parameter μ deeply affects the dust chemical composition: grain models with $\mu = 0$ lead to higher values of $(Si, Mg/Fe)_d$ than the corresponding models with $\mu = 0.75$, and cover different regions of the plot. The model of Kemper et al. (2004) better explains the abundance ratio at high metallicities ([Fe/H]> -1), whereas the one of Min et al. (2007) predicts too high values of $(Si/Fe)_d$ and $(Mg/Fe)_d$ at all metallicities. A good agreement is obtained with the grain model of Costantini et al. (2005), for which the majority of data are contained between the upper ($\mu = 0$) and lower limit ($\mu = 0.75$). Finally, the Ueda et al. (2005) model is qualitatively in agreement with the average of the DLA dust abundance ratios.

In conclusion, we have shown that the range of values of Si/Fe and Mg/Fe dust abundance ratios in DLA systems is consistent with empirical measurements of the same dust ratios in the ISM of our Galaxy. The comparison with the data suggests that the iron fraction in a non-silicate component, μ, increases with increasing metallicity. Obviously, the dust grain model with fixed parameters cannot explain the evolution of the dust abundance ratios with the metallicity (Fig. 3.9). In the next paragraph we will let evolve the grain model parameters, trying to reproduce the observed evolutionary trend.

Metal dependent parameters

In this paragraph we explain how we can vary the parameters of our grain composition model, on the basis of simple assumptions. To simplify our model we assume that the ratio of $N_{Mg}/(N_{Mg}+N_{Fe})^d$ in olivines and pyroxenes is the same. In other words, we are setting the parameters of our model as $x = y$.

Then, we assume that the Mg/Fe ratios in the dust phase scales with the total Mg/Fe ratios of the ISM. In this way, x and y vary as a function of the abundances predicted by the chemical evolution model (CEM):

$$x = y = \left(\frac{Mg}{Mg + Fe}\right)_{CEM} \tag{3.20}$$

In other words we assume that in galactic magnesium-rich environments x and y will be higher than in magnesium-poor ones.

To model μ, we assume that the fraction of iron-rich, non-silicate grains, grows with the fraction of the total Si/Fe ratio in the ISM. In this way, the lower is the $[Si/Fe]$ ratio, the higher will be the fraction of iron which can be included in a non-silicate dust component. Specifically, we adopt the functional form:

$$\mu = \frac{\mu_{max}}{1 + (Si/Fe)_{CEM}} \tag{3.21}$$

where we fixed $\mu_{max} = 1$. In this way, when Si is absent, we assume that silicates are not produced and all iron is in a non-silicate form and $\mu \to \mu_{max}$. Vice versa, when Fe is absent, all Fe in form of dust is incorporated in silicates and $\mu \to 0$.

Concerning the parameter α of eq. (3.12), we consider two distinct cases for $(Si/Fe)_d$ and $(Mg/Fe)_d$. For $(Si/Fe)_d$, since our chemical evolution model does not predict the ratio of the pyroxenes/olivines mixture, we consider different cases for fixed α. For $(Mg/Fe)_d$ case, α is not important because this ratio is independent from α when $x = y$. In fact assuming $x = y$ Eq. 3.19 becomes:

$$\left(\frac{Mg}{Fe}\right)_d = \frac{(1-\mu)\cdot x}{(1-x)} \tag{3.22}$$

With the above equations (3.20 and 3.21) we are able to estimate the parameters x, y and μ by means of our chemical evolution model, and to calculate the ratios of $(Si/Fe)_d$ and $(Mg/Fe)_d$ as functions of metallicity for comparison with the results obtained in Section 3.4.1. The different curves in the top panel of Fig. 3.12 show the predicted evolution of $(Si/Fe)_d$ versus metallicity, for different α values (as shown in the legend). The idealized dust grain model is in agreement with the observed trend in metalllicity: as the metallicity increases the $(Si/Fe)_d$ decreases indicating that the iron to dust abundance increases in a different way with respect to silicon. As α decreases, the curve shifts to lower values and we obtain the best agreement for $\alpha = 0.0$, i.e. for a silicate composition of only olivines. The predominance of olivines is in line with previous

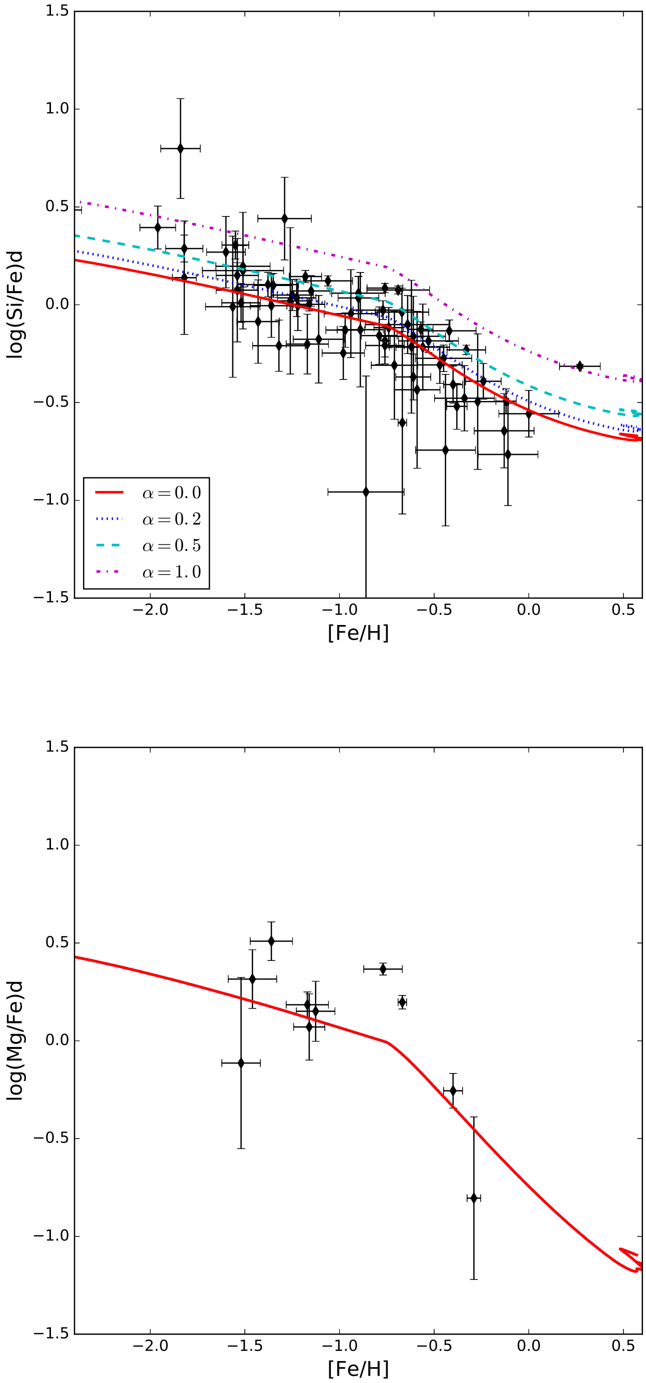

Figure 3.12: Chemical abundance ratios in the dust phase of $(Si/Fe)_d$ and $(Mg/Fe)_d$ versus metallicity in the top and bottom panels, respectively. Different lines represent dust models with different constant values of α (as shown in the legend) and when parameters x, y and μ depend on the chemical evolution model, according to equations (3.20) and (3.21), respectively. Abundances and error bars (black dots) are taken from equations (3.7), (3.18) and (3.18). The curve $(Mg/Fe)_d$ is independent of α.

studies on the composition of silicate grains made in many different environments. Zeegers et al. (2017) have performed new laboratory measurements of silicate compounds and made the comparison with the observed absorption feature in the line of sight of a X-Ray binary. Their best fit to the data is obtained when interstellar dust mainly consists of olivine. Xie et al. (2017) analyzed the silicate composition in a sample of 93 AGNs: for the majority of them they found a mixture of pyroxenes plus olivines or a olivine composition only, whereas only 2 out of the whole sample showed a pure pyroxene mixture. Other works have investigated the properties of the silicate feature at 13 μm (Aller et al., 2014a,b) and 9.7 μm (Kulkarni et al., 2007) in the spectra of QSO-absorbers, which represent a more similar environment to the one studied here. In particular, Aller et al. (2014a) found a general agreement between models and observations when an olivine-rich dust composition is adopted, even if they found variations in different absorbers which may indicate different silicate grain properties from one object to another.

In the bottom panel of Fig. 3.12, we show the evolution of $(Mg/Fe)_d$ versus metallicity: also in this case our model qualitatively follows the observational trend, even though the paucity of data makes the conclusion less robust. As already pointed out, in the case of $(Mg/Fe)_d$ we do not obtain different model predictions as it is independent from the parameter α, when $x = y$ is assumed. Given the fact that the predicted curve is obtained fixing all parameters, the agreement with the data is encouraging.

3.5 Conclusions

In this Chapter we have presented our results of our chemical evolution model which accounts for the presence of dust, for a typical dwarf irregular galaxy. We have studied the dust production rate and the processes occurring in the ISM during the galactic lifetime of a typical irregular galaxy. We have computed the evolution of dust by considering dust production (Type II SNe, AGB stars), destruction and accretion processes. It is worth noting that we excluded the Type Ia SNe as dust producers since there is no observational evidence for that.

Our predictions become even more important when we compare models with chemical abundances in Damped Lyman Alpha systems. We showed how is possible to observe the depletion patterns of the main refractory elements and how many information on dust properties are achievable.

Furthermore, we have presented an alternative method to constrain the element-to-element abundance ratios into dust grains. We have compared those measurements with 1) the prediction provided by our chemical evolution model and 2) with a model of dust grain with silicates and iron-rich dust. In the first case we have understood which dust processes are the main responsible for the observed trend as a function of the metallicity, whereas in the second case we have investigated which kind of dust grains should be more abundant.

Below, we summarize our main results:

- Our model reproduces the observed trend between the dust-to-gas ratios and the metallicity in irregular galaxies. We have found that dust accretion plays a fundamental role in dust evolution and in certain phases it becomes the dominant process, governing the evolution of the dust mass in the ISM, as predicted by Asano et al. (2013). In particular, this process is necessary to reproduce the highest values of the dust-to-gas ratio at high metallicity

- We have investigated the impact of the cut-off of high mass stars (from 18 to 80Mo) on the chemical evolution of a typical irregular galaxy. We fail in reproducing the metallicity values observed in dwarf irregulars when the cut-off mass is assumed to be in the range 18-25$M_{\odot}$. On the other hand, this effect does not deeply influence the predicted range of dust-to-gas ratio.

- We have compared the dust formation when both Piovan et al. (2011) and Dwek (1998) condensation efficiencies are adopted. We have found that the production rate of carbon is almost the same using different prescriptions, whereas a larger mass of silicates is produced by stars when Dwek (1998) are adopted.

- Dust destruction represents a negligible process in dwarf irregulars, whereas the galactic wind is an important mechanism which can affect dust evolution: we have showed that it can be the main responsible for stopping the accretion process in the ISM.

- We have compared our model for irregulars with the data of DLA systems and we have found that these objects can indeed be irregular galaxies, as already suggested in previous papers (e.g. Matteucci et al., 1997; Calura et al., 2003). We have found a particular combination of parameters which best fit the DLAs. In particular, our comparison shows that the depletion pattern of silicon in these objects is well reproduced by the dust contributions by Type II SNe, AGBs and by the accretion process.

- In the case of iron, at variance with the case of silicon, we have found a good agreement with the data only when an extra dust source is considered: in particular, we tested the case of adding dust production by Type Ia SNe and the case of a more efficient accretion in the ISM. The different behavior of iron and silicon brings new evidence that a significant fraction of iron has to be incorporated into a dust population different from silicates, as suggested by previous works (e.g. Sofia et al., 2006; Voshchinnikov & Henning, 2010; Dwek, 2004b; Draine & Hensley, 2012, 2013). Furthermore, since part of iron dust should be decoupled from silicates, it is possible that such species could originate in a different way: in particular, our results are consistent with a metallicity-dependent accretion of iron nano-particles.

- We have presented a new method to obtain the chemical abundances in the dust phase of the ISM. This method is based on DLA column density measurements and the ratio between volatile and refractory elements. The ratios of $(Si/Fe)_d$ and $(Mg/Fe)_d$ in the dust phase decrease with the metallicity: this suggests, that the chemical abundances inside dust grains approximately follow the variation of the abundances in the ISM.

- We compare the element-to-element abundance ratios in dust grains with the ones predicted by our chemical evolution model with dust. This comparison represents an independent test, since our model utilizes theoretical prescriptions. We find that the evolution in metallicity of $(Si/Fe)_d$ and $(Mg/Fe)_d$ can be divided in two regions, dominated by different dust processes. In the first low-metallicity region ($[Fe/H] < -0.6$), Type II SNe represent the most important source. In the metal-rich region ($[Fe/H] > -0.6$), dust accretion is the most important process and the relation between the dust abundance ratios and the metallicity becomes steeper. The existence of this transition strengthens that Fe-rich dust should preferably form by growth in the ISM than in the stellar ejecta.

- Finally, we have interpreted the obtained dust chemical composition on the basis of a simple dust model whose parameters are: α, that represents the fraction between pyroxenes and olivines, μ, that represents the fraction of Fe-rich dust out of silicates, x and y which indicate the Mg-rich composition of pyroxenes and olivines, respectively. When those parameters are kept constant, as in previous studies, it is impossible to reproduce the observed trend. On the other hand, we have obtained a good agreement when we let the parameters to vary according to our chemical evolution model.

- The best agreement is obtained for low values of α. Therefore, our study seems to prefer a silicate composition mainly made of olivine-type compounds, in agreement with other works and laboratory experiments (Xie et al., 2017; Zeegers et al., 2017).

Chapter 4

Dust in the Milky Way: the Galactic Habitable Zone

4.1 Introduction

The Galactic Habitable Zone (GHZ) is defined as the region with sufficiently high abundances of heavy elements to form planetary systems in which terrestrial planets could be found and might be capable of sustaining life, after surviving to supernova explosion events (Gonzalez et al., 2001). The degree of complexity to study in detail the habitable factors is very high, since it asks for the solution of non linear problems and involves many different fields such as astrophysics, geophysics, climatology and biology (Gonzalez, 2005). Because of that difficulty, the physical processes underlying the GHZ are hard to identify and even harder to quantify. For this reason the study of the GHZ has been also criticized, and maybe we are far away from drawing a significant conclusion about its extension (Prantzos, 2008).

Despite of this, the GHZ has generated a great deal of interest in the Astrophysics community, and its study has been extended even on other galaxies (e.g. Andromeda Galaxy, Carigi et al., 2013; Spitoni et al., 2014). Recently, the GHZ has also been studied in the cosmological context (ΛCDM) by Gobat & Hong (2016), Vukotić et al. (2016), Zackrisson et al. (2016) and Forgan et al. (2017). These studies showed which types of halos can give rise to galactic structures in which habitable planets can be formed.

In this Chapter we mainly focus on the study of the GHZ by mean of chemical evolution models, because of its affinity with this thesis. In the next paragraph we will show why chemical evolution models represent very useful tools in this context and the most important progresses reached in the last years.

4.1.1 Studying the GHZ with chemical evolution models

The GHZ concept was first introduced by Gonzalez et al. (2001) as an extension of the most common Circumstellar Habitable Zone (Huang, 1959; Sagan & Shklovskij, 1978; Hart, 1979). It was defined as that region in the Milky Way where an Earth-like planet can retain liquid water on its surface and provide a long-term habitat for animal-like aerobic life. One of the main important assumption is that a certain minimum abundance of heavy elements is needed to fully assemble Earth-sized planets, and therefore its location is variable inside the Galaxy due to the evolution of the chemical abundances in the Interstellar Medium. The GHZ is also sensible to destructive events for life, such as supernovae explosions. In this way chemical evolution models become a very useful tool to study the GHZ, as they aim at studying the evolution of both metallicity and SN rates. Gonzalez et al. (2001) used a Galactic chemical evolution model to find that at least half that of the metallicity of the Sun is required to build a habitable terrestrial planet. Since their pioneering work, several purely chemical evolution models have studied the habitable zones of our Galaxy as functions of the time and distance (Lineweaver, 2001; Lineweaver et al., 2004; Prantzos, 2008; Carigi et al., 2013; Spitoni et al., 2014).

The possible migration of gas giant planets in extrasolar systems may be another destructive factor for smaller planets, and therefore life (Lin et al., 1996; Lineweaver, 2001). The terms giant planets, gas giants, or simply Jupiters refer to large planets, typically $>10\ M_\oplus$, that are not composed primarily of rock or other solid matter. When orbiting close to the host star, they are referred to as hot Jupiters or very hot Jupiters. Gas giant planets are believed to form in a core-accretion scenario: a core of heavy elements is built by accretion of planetesimals and then, as the core grows, its ability to accrete gas from the surrounding disk increases. When the core is sufficiently massive, rapid gas accretion occurs onto the core and the gas giant is formed (Safronov & Zvjagina, 1969; Goldreich & Ward, 1973; Pollack et al., 1996; Matsuo et al., 2007).

This ”core accretion model” is the most widely accepted one in the literature for gas giant formation, and the next stochastic migration due to turbulent fluctuations in the disk could destroy the terrestrial planets. Rice & Armitage (2003) showed that the formation of Jupiter can be accelerated by almost an order of magnitude if the growing core executes a random walk with an amplitude of ≈ 0.5 AU. Today, about three thousand planets have been discovered, and the statistics is good enough to confirm that most planetary systems host planets that are not present in our solar system, such as hot Jupiters or super-Earths. Lineweaver (2001) studied, for the first time in the context of the GHZ, the metallicity relation of the destructive effect of gas giant planets on Earth-like ones. In fact, a well-established correlation between metallicity of the stars and the presence of giant implicates that more metallic stars preferably host giant planets (Gonzalez, 1997; Gonzalez et al., 2001; Santos et al., 2001, 2004; Fischer & Valenti, 2005; Udry et al., 2006, 2007; Mortier et al., 2012; Johnson et al., 2010). In particular, Fischer & Valenti (2005) and Sousa et al. (2011) presented the probabilities of the formation of giant planets as a function of [Fe/H] values observed in the host star. In Sozzetti et al. (2009); Mortier et al. (2013a,b) these probabilities are reported for different samples of stars.

Concerning Earth-sized planets, the relation between their occurrence and the metallicity of the host star is not totally clear. As we already stated, Gonzalez (1997) discussed for the first time the need for a minimum metallicity to form planets. On the other hand, simulations of numerical models of planetary formation tell us that the presence of small planets may be independent from metallicity, at variance from gas giants (Mordasini et al., 2006; Prantzos, 2008). In the study of the GHZ of Prantzos (2008) a constant probability of forming Earth-like planets was adopted for the first time.

In the following years, the observable confirmation of no dependence between metallicity and earth-like planet frequency has been provided by Buchhave et al. (2012). Analyzing the mission Kepler, they found that the frequencies of the planets with Earth-like sizes are almost independent of the metallicity, at least up to [Fe/H] values ~ 0.6 dex.

The work of Spitoni et al. (2014) comes as an updated study in the GHZ scenario: they took into account the possibility of planet destruction from gas giant migration and a constant probability of forming Earth-like planets in a chemical evolution model with radial gas flows. They confirmed previous results of Lineweaver et al. (2004) and found that the maximum number of stars that can host habitable terrestrial planets are located in the solar neighborhood, that is, in the region centered at 8 kpc and 2 kpc wide.

Nowadays, ongoing surveys are collecting more and more data, and therefore more and more information about host stars. These data are fundamental to understand possible correlations between the occurrence of exoplanets and stellar properties. Data from *Kepler* mission show that the occurrence rate for terrestrial planets ($R = 1 - 2R_{\oplus}$) with periods $P < 400$ days around FGK stars is about $\sim 20\%$ (Petigura et al., 2013). On the other hand, the same occurrence for small rocky planets of $R = 0.5 - 4R_{\oplus}$ orbiting M-dwarf stars is even higher, and can reach up to the 90 or 100%, depending on the selected periods and/or mass (Dressing & Charbonneau, 2013, 2015; Tuomi et al., 2014). Gaidos & Mann (2014) suggested that the power law for the occurrence of Hot Jupiters for low mass M-dwarf differs from the one of solar-type stars (Fischer & Valenti, 2005). Recently, Zackrisson et al. (2016) took advantage of the observed planetary occurrences to perform different probabilities of finding gas giant planets around FGK and M-dwarf stars. Therefore, in their study of the GHZ, they differentiated the probabilities by stellar type.

In this work we present the study of the galactic habitable zone in the Milky Way with a detailed chemical evolution model as in Spitoni et al. (2014), with at least two main improvements: 1) we use the most updated probabilities related to the formation of gas giant planets as functions of [Fe/H] as well as the stellar mass for FGK and M stars (Zackrisson et al., 2016), and 2) we connect our study with the evolution of dust in the Milky Way. In the next paragraph, we explain why is fundamental to include dust in a chemical evolution model, especially in the study of the GHZ.

4.1.2 Dust in the GHZ

As we already pointed out in this thesis, dust is very important because it is involved in almost all astrophysical processes which include light transmission, both in photometry and spectroscopy. Dust is also important in the field of planetary formation, as it represents the solid compounds of the matter forming rocky planetesimals, which are the necessary building blocks to form planets.

We know very little about the formation of planetary systems. In particular, the transition from a protoplanetary disk to a planetary system is poorly understood. In this transition, dust and gas rapidly evolve in very different ways as a result of many processes (Armitage, 2013) such as dust growth, gas photoevaporization (Alexander et al., 2014) and gas accretion onto the star (Gammie, 1996). The first fundamental step to understand and explain the origin of the observed diversity of exoplanetary systems is to measure the stellar disk properties, especially the disk mass. Dust grains of μm size are directly observed in protoplanetary disks and then, dust coagulation increases their size up to mm (Dullemond & Dominik, 2005). On the other hand, observations of the gas are almost forbidden because it is relatively cool and in molecular form. In most cases, the mass of the gas is fixed starting from the mass of the dust, by assuming a guess value for the dust-to-gas ratio (D/G) conversion factor. Unfortunately, this practice has several uncertainties (Williams & Best, 2014). Models of planetary formation commonly use an average value of 10^{-2} for the initial condition of the dust-to-gas ratio in a protoplanetary disk (Bohlin et al., 1978).

Moreover, even though Buchhave et al. (2012) showed that planets with radii smaller than 4 $R_\oplus$ do not present any metallicity correlation, the theoretical work of Johnson & Li (2012) predicted that first Earth-like planets likely formed from circumstellar disks with metallicities $Z \geq 0.1\ Z_\odot$.

Here, we present our chemical evolution model with dust specifically designed for the study of the Milky Way, and we study the dust mass evolution as a function of the galactic time and galactocentric distance. We discuss the connection between ISM metallicity and the D/G ratio (especially for the solar neighborhood). In this way, we can link the metallicity of stars, which is observationally related to the probability of the presence of hosted planets, with the initial D/G of the protoplanetary disks (the D/G of the ISM at the instant of the protoplanetary disk formation).

Below, we present in Section 4.2 the probabilities of finding terrestrial planets around M and FGK stars, in Section 4.3 we describe the Milky Way chemical evolution model including dust, and we present the main results in Section 4.4. Finally, our conclusions are summarized in Section 4.5.

4.2 Probabilities of finding planets around FGK and M stars

The probability of forming Earth-like planets (P_{FE}, where FE stands for ”forming earths”) depends on the metallicity, and this relation has varied during the past decades. Lineweaver (2001) assumed an exponential law in which Earth-like planets likely to form on relative high values of [Fe/H]. Years later, Prantzos (2008) fixed the probability of forming Earth-like planets at a value of 0.4 for [Fe/H] $\geq$ -1 dex. The minimum metallicity assumed for the formation of such a kind of planets was [Fe/H] $= -1$, dex: in other words, $P_{FE} = 0$ was assumed for [Fe/H]$<$ 1. Prantzos (2008) chose the value of P_{FE}= 0.4 to reproduce the metallicity-integrated probability of Lineweaver (2001). This assumption was also adopted by Carigi et al. (2013) and in Spitoni et al. (2014), reinforced by the observational confirmation of Buchhave et al. (2012). Buchhave et al. (2012) analyzed the *Kepler* mission and found that the frequencies of the planets with Earth-like sizes are almost independent of the metallicity of the host star down to [Fe/H] abundance values lower than 0.5 dex.

The probability of forming Earth-like planets may be not enough to properly study the GHZ. In fact, it is also important to consider the processes able to vary their orbital stability, and therefore destroy them. Armitage (2003) pointed out the potentially hazardous effects of the gas giant planet migration on the formation of Earth-like planets and suggested that these planets preferentially exist in systems where massive giants did not migrate significantly. Matsumura et al. (2013) studied the orbital evolution of terrestrial planets when gas giants become dynamically unstable. The authors showed that Earth-like planets far away from giants can also be removed. This possibility has been already adopted in previous works (e.g. Prantzos, 2008; Spitoni et al., 2014), even though various numerical simulations found that the formation of earths is not necessarily prevented by the gas giant planet migration, when eccentricity excitation timescales for (proto-)terrestrial planets are longer than the migration timescales of giant ones (e.g., Mandell & Sigurdsson 2003; Lufkin et al. 2006; Raymond et al. 2006.

The probability of the formation of a gaseous giant planet as a function of the iron abundance in the host star is given by Fischer & Valenti (2005):

$$P_{GGP}\left([\mathrm{Fe/H}]\right) = 0.03 \times 10^{2.0[\mathrm{Fe/H}]}. \tag{4.1}$$

A possible theoretical explanation of this relation is that the high metallicity observed in stars host giant planets represents the original composition in which the protostellar (and the protoplanetary molecular clouds) were formed. In this scenario, the higher the metallicity of the primordial cloud, the higher the proportion of D/G in the protoplanetary disk. This facilitates the condensation and accelerates the protoplanetary accretion before the disk gas is lost Pollack et al. (1996). Giant planets are subsequently formed by runaway accretion of gas onto such rocky cores with M $\approx 10 M_{\oplus}$ instead of by gravitational instabilities in a gaseous disk, which predicts a formation that is much less sensitive to metallicity Boss (2002).

The novelty of our work is that we consider the following new probabilities for gas giant planets formation reported by Zackrisson et al. (2016), which use observed relation of Fischer & Valenti (2005) for FGK and of Gaidos & Mann (2014) for M stars. These probabilities are also functions of the masses of the hosting stars:

$$P_{GGP/FGK}\left([\mathrm{Fe/H}], M_{\star}\right) = 0.07 \times 10^{1.8[\mathrm{Fe/H}]}\left(\frac{M_{\star}}{M_{\odot}}\right) \tag{4.2}$$

for FGK stars, and

$$P_{GGP/M}\left([\mathrm{Fe/H}], M_{\star}\right) = 0.07 \times 10^{1.06[\mathrm{Fe/H}]}\left(\frac{M_{\star}}{M_{\odot}}\right) \tag{4.3}$$

for M stars, where $M_{\star}$ is the mass of the host star in units of solar masses. We assume that the mass range spanned by M -type stars is $0.08 \leq \frac{M_{\star}}{M_{\odot}} \leq 0.45$, whereas for FGK stars, the range is $0.45 \leq \frac{M_{\star}}{M_{\odot}} \leq 1.40$.

The probability of forming terrestrial planets around FGK/M stars but not gaseous giant planets is given by

$$P_{E/FGK,M} = P_{FE} \times (1 - P_{GGP/FGK,M}). \tag{4.4}$$

Here, we adopt the conservative assumption of Prantzos (2008) and Spitoni et al. (2014) that the P_{FE} probability is constant at the value of 0.4 for all stellar types. On the other hand, Zackrisson et al. (2016) presented results where $P_{FE} = 0.4$ around FGK stars, and $P_{FE} = 1$ around M stars.

We define $P_{GHZ}(FGK/M, R, t)$ as the fraction of all FGK/M stars that host Earths (but no gas giant planets) that survived supernova (SN) explosions as a function of the Galactic radius and time:

$$P_{GHZ}(FGK/M, R, t) =$$

$$= \frac{\int_0^t SFR(R, t')P_{E/FGK,M}(R, t')P_{SN}(R, t')dt'}{\int_0^t SFR(R, t')dt'.} \tag{4.5}$$

This quantity must be interpreted as the relative probability to have complex life around one star at a given position. In Eq. (4.5), $SFR(R, t')$ is the star formation rate (SFR) at the time t' and Galactocentric distance R, and $P_{SN}(R, t')$ is the probability of surviving a SN explosion.

Hard radiation caused by close-by SN explosions may lead to the depletion of the ozone layer in a terrestrial atmosphere (Ruderman, 1974). At this point, the ultraviolet radiation from the host star can penetrate the atmosphere, altering and damaging the DNA and eventually causing the total sterilization of the planet Gehrels et al. (2003). The effect of sterilization of a habitable planet due to nearby supernovae explosion is hardly be quantifiable, because of our limits on the knowledge on how robust life really is (Prantzos, 2008). Carigi et al. (2013) explored different cases for the life annihilation on formed planets by SN explosions. Among those they assumed that the SN destruction is effective if the SN rate at any time and at any radius has been higher than $< RSN_{SV} >$, the average SN rate in the solar neighborhood during the last 4.5 Gyr of the Milky Way's life. Also Spitoni et al. (2014) tested different cases of SN rate thresholds in which life annihilation is effective.

Here, we adopt for this value $2\times < RSN_{SV} >$, which has been used in Spitoni et al. (2014), and it is almost the same as that used by Carigi et al. (2013) to describe their best models, motivated by the fact that life on Earth has proven to be highly resistant. Therefore, we impose that if the SN rate is higher than $2\times < RSN_{SV} >$, then $P_{SN}(R, t) = 0$, else $P_{SN}(R, t) = 1$. We also show results when SN effects are not taken into account: in this case, we simply impose $P_{SN}(R, t) = 1$ at any time and galactic radius. For $< RSN_{SV} >$ we adopt the value of 0.01356 Gyr^{-1} pc^{-2} using the results of the "S2IT" model of Spitoni & Matteucci (2011) and Spitoni et al. (2014).

Finally, we define the total number of stars formed at a certain time t and Galactocentric distance R that host an Earth-like planet with life as

$$N_{\star life}(FGK/M, R, t) = P_{GHZ} \times N_{\star tot}, \tag{4.6}$$

where $N_{\star tot}(FGK/M, R, t)$ is the total number of stars created up to a time t at the Galactocentric distance R.

4.3 Milky Way chemical evolution model that includes dust

In this Section we describe the adopted chemical evolution model to study the GHZ. We adopt the best "classical" chemical evolution of the Milky Way as already adopted in (Spitoni et al., 2014), and first presented by Spitoni & Matteucci (2011) as the "S2IT" (Two-infall model). In this work, we adopt an updated version of this model, in which we consider the dust evolution using the new prescriptions of explained in Gioannini et al. (2017a) and presented in Section 2.2 of this thesis.

4.3.1 Two-infall model

To follow the chemical evolution of the Milky Way, we adopt the S2IT model of Spitoni & Matteucci (2011) which is an updated version of the two infall model (Chiappini et al., 1997, 2001) model.

We define $G_i(t) = G(t)X_i(t)$ as the fractional mass of the element i at the time t in the ISM, where $X_i(t)$ represents the abundance of the element i in the ISM at the time t. The temporal evolution of $G_i(t)$ in the ISM is described by the following expression:

$$\dot{G}_i(t) = -\psi(t)X_i(t) + R_i(t) + \dot{G}_{i,inf}(t). \tag{4.7}$$

The first term on the right side of Eq. (4.7) represents the rate at which the fraction of the element i is subtracted by the ISM due to the SFR process. $R_i(t)$ is the returned mass fraction of the element i injected into the ISM from stars thanks to stellar winds and SN explosions. This term takes into account nucleosynthesis prescriptions concerning stellar yields and supernova progenitor models. The third term of Eq.(4.7) represents the rate of the infall of the element i. The infalling gas is not pre-enriched and has a pure primordial composition.

The two-infall model assumes that the halo-thick disk forms out of an infall episode independent of that which formed the disk. In this approach the law for the infall rate is given by:

$$\dot{G}_{i,inf}(t) = a(r)e^{-t/\tau_H} + b(r)e^{-(t-t_{max})/\tau_D(r)}, \tag{4.8}$$

where τ_H is the typical timescale for the formation of the halo and thick disk, and it is fixed to the value of 0.8 Gyr, while $t_{max} = 1$ Gyr is the time for the maximum infall onto the thin disk. The coefficients $a(r)$ and $b(r)$ are obtained by imposing a fit to the observed current total surface mass density in the thin disk as a function of Galactocentric distance given by

$$\Sigma(r) = \Sigma_0 e^{-R/R_D}, \tag{4.9}$$

where $\Sigma_0 = 531$ M$_\odot$ pc^{-2} is the central total surface mass density and $R_D = 3.5$ kpc is the scale length.

Moreover, the formation timescale of the thin disk $\tau_D(r)$ is assumed to be a function of the Galactocentric distance, leading to an inside-out scenario for the Galaxy disk build-up. In particular, we assume that

$$\tau_D(r) = 1.033\,R\,(\mathrm{kpc}) - 1.267\,\mathrm{Gyr}. \tag{4.10}$$

The Galactic thin disk is approximated by several independent rings, 2 kpc wide, without exchange of matter between them. A threshold gas density of 7 M$_\odot$ pc^{-2} in the SF process (Kennicutt, 1989, 1998; Martin & Kennicutt, 2001; Schaye, 2004) is also adopted for the disk. The halo has a constant surface mass density as a function of the Galactocentric distance at the present time equal to 17 M$_\odot$ pc^{-2} and a threshold for the star formation in the halo phase of 4 M$_\odot$ pc^{-2}, as assumed for model B of Chiappini et al. (2001).

Model S2IT		Units
Infall type	2 infall	Gyr
τ_d	1.033 R[kpc]-1.27	Gyr
τ_H	0.8	Gyr
ν	1	Gyr^{-1}
Threshold	7 (thin disc)	$\mathrm{M}_{\odot}\mathrm{pc}^{-2}$
Threshold	4 (halo-thick disk)	$\mathrm{M}_{\odot}\mathrm{pc}^{-2}$

Table 4.1: Chemical evolution model of the Milky Way: we report the main characteristics and the adopted parameter of the two-infall model. In the second raw the infall type is reported, in the third and forth ones the time-scale τ_d of the thin disk formation, and the time-scale τ_H of the halo formation are drawn. The adopted star formation efficiency is shown in raw 4 and the adopted threshold in the surface gas density for the star formation in the thin disc and in halo-thick disc are reported in raw 5 and 6, respectively

The assumed IMF is the one of Scalo (1986), which is assumed to be constant in time and space.

The adopted law for the SFR is a Schmidt (1959) like one:

$$\Psi = \nu \Sigma_{gas}^{k}(r,t), \tag{4.11}$$

where $\Sigma_{gas}(r,t)$ is the surface gas density with the exponent k equal to 1.5 (see Kennicutt 1998; Chiappini et al. 1997. The quantity ν is the efficiency of the star formation process, and it is fixed at the constant value of 1 Gyr $^{-1}$. Finally, we remind that the chemical abundances are normalized to the solar values of Asplund et al. (2009). In Table 4.3.1 we resume the principal characteristics of the S2IT model just now discussed.

Evolution of dust

We already gave a detailed explanation of our chemical evolution model which accounts for the presence of dust in Section 2.2. In this Chapter, the same dust model is applied to the Milky Way, where a specific chemical evolution model (the ”two-infall”) is adopted. In this paragraph we briefly remind the main ingredients and prescriptions of the dust model.

Defining $G_{i,dust}(t)$ as the mass fraction of the element i at the time t in the dust phase, we can write the equation for dust evolution as follows:

$$\begin{aligned}\dot{G}_{i,dust}(t) = -\psi(t)X_{i,dust}(t) + \delta_i R_i(t) + \left(\frac{G_{i,dust}(t)}{\tau_{accr}}\right) \\ - \left(\frac{G_{i,dust}(t)}{\tau_{destr}}\right).\end{aligned} \tag{4.12}$$

The right-hand side of this equation contains all the processes that govern the so-called ”dust cycle” : the first term represents the amount of dust removed from the ISM as a result of star formation, the second takes into account dust pollution by stars, while the third and fourth terms represent dust accretion and destruction in the ISM, respectively. Dust production is provided by taking into account the condensation efficiencies δ_i as provided by Piovan et al. (2011). The dust yields $\delta_i R_i(t)$ are not only metallicity dependent, but also depend on the mass of the progenitor star. In this work we consider as dust producers type II SNe ($M_\star > 8M_\odot$) and low- to intermediate-mass stars ($1.0M_\odot < M_\star < 8.0M_\odot$). For dust accretion and destruction, we calculated the respective metallicity-dependent time-scales (τ_{accr} and τ_{destr}) as described in Asano et al. (2013).

4.4 Results

In this section we first present the main results of our Milky Way chemical evolution model when dust is included. In particular, we focus on the study of the dust mass assembly in space and time, and on the relation between the dust-to-gas ratio and metallicity. Moreover, we show the $P_{E/FGK,M}$ probabilities of finding Earth-like planets, but no gas giants around FGK and M stars, computed with detailed chemical evolution model for the Galactic disk at different Galactocentric distances. We express these probabilities in terms of the dust-to-gas ratio $\left(\frac{D}{G}\right)$ obtained by our ISM chemical evolution models. Finally, we present the maps of habitability of our Galaxy as functions of Galactic time and Galactocentric distances in terms of the total number of FGK and M stars that could host habitable Earth-like planets and not gas giant planets.

4.4.1 Milky Way disk with dust

In Fig. 4.1 we show the time evolution of the SFR (panel A), the [Fe/H] abundances (panel B), the SN rates (panel C), and finally of the total dust (panel D) as functions of the Galactocentric distance. In panel A) we see the effect of the inside-out formation on the SFR in the thin-disk phase. During the halo and thick-disk phase (up to 1 Gyr since the beginning of the star formation), all the Galactocentric distances show the same star formation history (for all radii we assume the same surface gas density and same formation timescales in the halo and thick-disk phase, for details see Section 3). In the inner regions the SFR in the thin-disk phase is higher because the gas density is higher and the gas accretion timescale is longer than in the outer regions. In the outer regions the effect of the threshold on the gas density is more pronounced: the SFR reaches zero when the gas density is below the threshold. We also note that the same SFR history is obtained at all Galactocentric distances in the halo and thick-disk phase.

In panel B) we show the age-metallicity relation in terms of [Fe/H] ratio vs Galactic time. The effects of the inside-out formation are clear in this case as well: the inner regions exhibit a faster and more efficient chemical enrichment, with higher values of [Fe/H]. At early times, in correspondence to the beginning of the second infall of gas (thin-disk phase), the [Fe/H] abundance values decrease. This decrease is more evident in the inner regions of the Galactic disk. The reason is that the second infall of primordial gas related to the thin-disk phase is more massive in the inner regions and it occurs on shorter timescales, therefore the chemical abundances are more diluted at the beginning of the thin-disk phase in the inner Galactic regions than in the external regions.

In panel C) of Fig. 4.1 we present the total SN rates as functions of the Galactic time and Galactocentric distances. With the red line we show the limit we adopted here and in Paper I to take the destruction effects of SN explosions

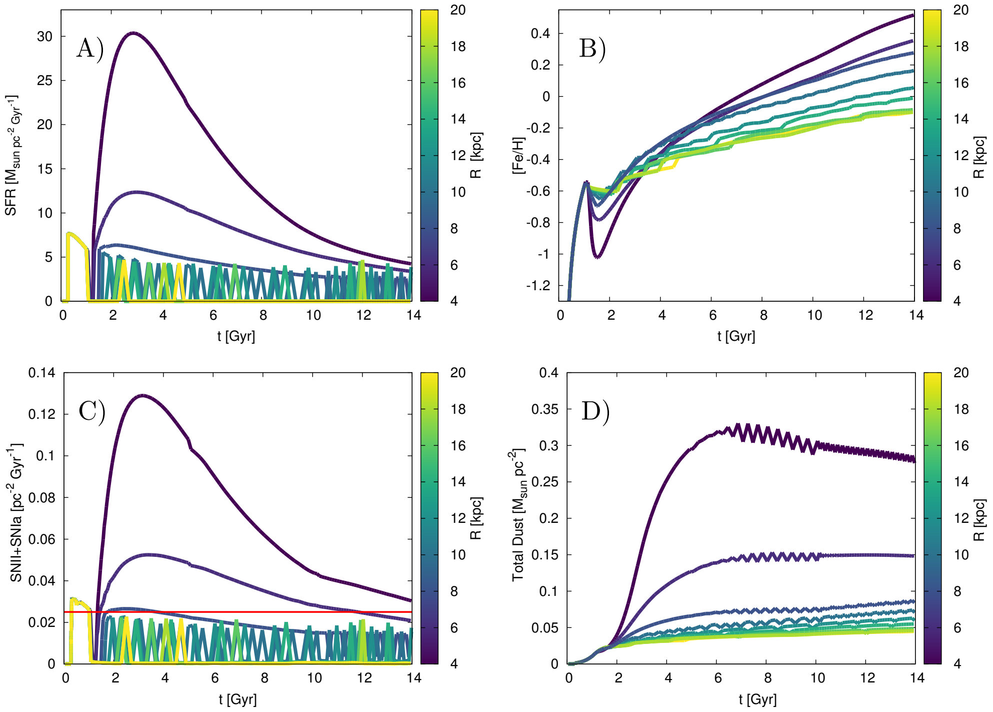

Figure 4.1: *Panel* A): SFR as the function of the Galactic time. *Panel* B): time evolution of the [Fe/H] abundances with the two-infall chemical evolution model for the Milky Way disk (the “age-metallicity” relation). *Panel* C): evolution in time of the type II SN rates plus the type Ia SN rates. With the red line we show the quantity $2\times < RSN_{SV} >$, which represents the minimum SN rate value (adopted in this work and in Paper I) for destruction effects from SN explosions. *Panel* D): time evolution of the total dust surface mass density. The color code in the four panels indicates the different Galactocentric distances.

on the Galactic habitable zone modeling into account ($2\times < RSN_{SV} >$). Above this SN rate limit, we assume that there is zero probability of life on a terrestrial planet.

Finally, in panel D) of Fig. 4.1 we show the time evolution of the total surface mass density of dust at different Galactocentric radii. Dust production by stars is the main source of dust in the early phases of the Milky Way evolution. For this reason, in the inner regions, the dust amount is higher because type II SNe during the initial burst of star formation produce more dust, as is visible in panel A). On the other hand, dust accretion becomes important at later epochs, and the dust mass tends to increase at all Galactocentric distances. The observed oscillation of the model occurs when the rates of dust accretion and dust destruction are similar. In this case, there is a gain of the total mass surface density of dust caused by the dust growth, rapidly followed by a decrease that is due to the dust destruction rate, which exceeds dust accretion. This turnover between these processes occurs especially in the quiescent phases of the Galactic evolution.

4.4.2 Evolution of the Dust-to-gas ratio

In this paragraph we provide a useful theoretical tool to set the proper initial conditions for the formation of protoplanetary disks. As underlined in Section 4.1.2, while dust grains of μm are directly observed in protoplanetary disks, the amount of gas mass is set starting from the dust mass and by assuming a value for the dust-to-gas ratio. Unfortunately, this practice has several uncertainties (Williams & Best, 2014). Here, we connect the evolution of the dust-to-gas ratios at different Galactocentric distances with the chemical enrichment expressed in terms of [Fe/H]. Because of the well-known age-metallicity relation reported in panel C) of Fig. 4.1, the relation between the dust-to-gas ratio (D/G) and [Fe/H] can be seen as the time evolution of the dust-to-gas ratio, (D/G)(t).

In the upper panel of Fig. 4.2 we present the evolution of the D/G ratio as a function of [Fe/H] at different Galactocentric distances. As expected, higher metallicities are reached in the inner radii, where the star formation is higher. The dust-to-gas ratio D/G increases in time for two reasons: the first is that dust production in star-forming regions is high, especially from type II SNe, while the second reason is related to dust accretion. Dust accretion is a very important process occurring in the ISM, and it becomes the most important process when the critical metallicity is reached[1]

As dust grains are formed by metals, dust accretion becomes more efficient as the metallicity in the ISM increases. For this reason, we found higher values of dust-to-gas ratio at high [Fe/H]. The relation between the [Fe/H] and the dust-to-gas ratio is important because it can provide the probability of planet formation depending on the amount of dust in the ISM, and on the other hand, it provides an estimate of the dust-to-gas ratio in the ISM during the formation of a protoplanetary disk.

The solar dust-to-gas ratio $\left(\frac{D}{G}\right)_{\odot}$ predicted by our model (value computed in the solar neighborhood at 9.5 Gyr) is 0.01066. In the lower panel of Fig. 4.2

---

[1] The critical metallicity is the metallicity at which the contribution of dust accretion exceeds the dust production from stars, see Chapter 3.2.3.

we show the D/G as a function of the [Fe/H] values only for the shell centered at 8 kpc and 2 kpc wide (the solar neighborhood). In the same plot, we present the sixth-degree polynomial fit that exactly follows the [Fe/H] vs (D/G) in the range of [Fe/H] between -1 dex and 0.5 dex. The expression of this fit is:

$$[\mathrm{Fe/H}] = \sum_{n=0}^{6} \alpha_n \left(\frac{D}{G}\right)^n . \tag{4.13}$$

All the coefficients α_n and n are reported in the footnote[2].

We found that for [Fe/H] values higher than -0.6 dex a linear fit is able to reproduce the computed [Fe/H] vs $\left(\frac{D}{G}\right)$ relation in the solar vicinity well. The equation of the linear fit reported in the lower panel of Fig. 4.2 is:

$$[\mathrm{Fe/H}] = 96.49 \left(\frac{D}{G}\right) - 0.92. \tag{4.14}$$

This relation is important to connect the dust-to-gas ratio with the [Fe/H] abundance. When we combine it with Eq. (4.4), we obtain the probability of having terrestrial planets, but no gas giants, depending on the amount of dust in the ISM.

Both the linear and polynomial fit are plotted in Fig. 4.2 in dotted red and solid green lines, respectively.

4.4.3 Terrestrial habitable planets around FGK and M stars

Computed probabilities $P_{GGP/FGK,M}$ with the two-infall chemical evolution model

To compute the probabilities $P_{GGP/FGK,M}$ presented in Eqs. (4.2) and (4.3) with our chemical evolution model, we considered the weighted values on the IMF using the following expressions:

$$< P_{GGP/FGK}(R,t) >_{IMF} =$$

$$0.07 \times 10^{1.8[\mathrm{Fe/H}](R,t)_{model}} \left(< \frac{M_{\star,FGK}}{M_\odot} >_{IMF} \right) \tag{4.15}$$

for the FGK stars, and

$$< P_{GGP/M}(R,t) >_{IMF} =$$

$$0.07 \times 10^{1.06[\mathrm{Fe/H}](R,t)_{model}} \left(< \frac{M_{\star,M}}{M_\odot} >_{IMF} \right) \tag{4.16}$$

for M stars.

The $[\mathrm{Fe/H}](R,t)_{model}$ quantity is the computed iron abundance with our chemical evolution model adopting the Scalo (1986) IMF at the Galactic time t and Galactocentric distance R.

---

[2] $[\mathrm{Fe/H}] = -1.48 + 1.05\,10^4 \left(\frac{D}{G}\right) - 4.91\,10^5 \left(\frac{D}{G}\right)^2 + 1.1410^8 \left(\frac{D}{G}\right)^3 - 1.32\,10^{10} \left(\frac{D}{G}\right)^4 + 7.57\,10^{11} \left(\frac{D}{G}\right)^5 - 1.69\,10^{13} \left(\frac{D}{G}\right)^6$

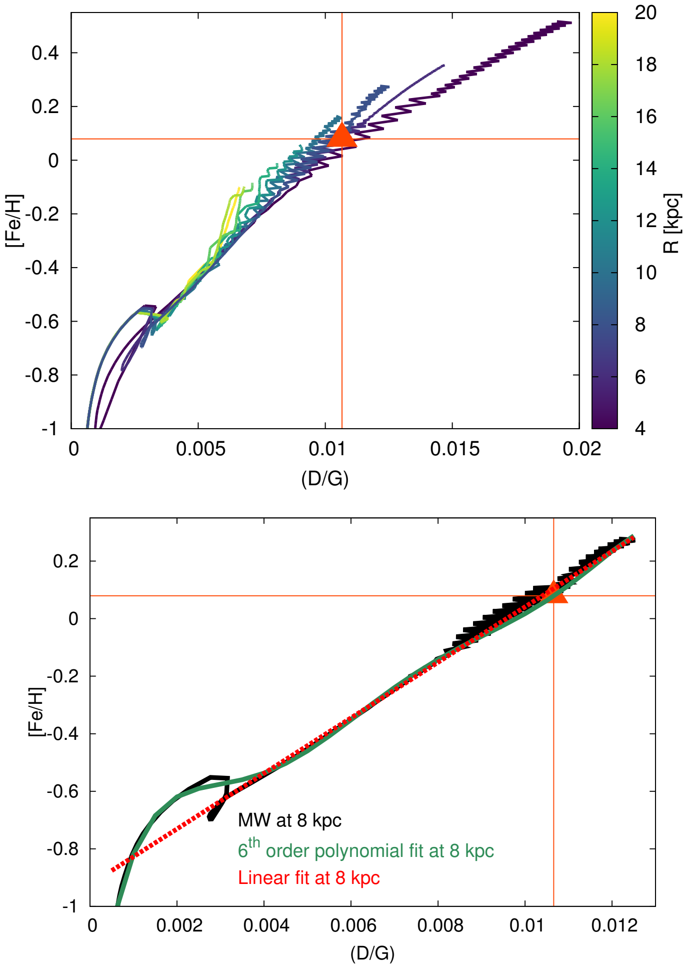

Figure 4.2: *Upper panel*: evolution of the abundance ratio [Fe/H] as a function of the dust-to-gas ratio D/G predicted by our chemical evolution model of the Milky Way disk. As in Fig. 4.1, the color code indicates different Galactocentric distances. *Lower panel:* with the black solid line we report the [Fe/H] ratio vs $\left(\frac{D}{G}\right)$ computed at 8 kpc (solar neighborhood) using the chemical evolution model of the Milky Way. With the green solid line we show the fit obtained by means of a sixth-order polynomial fit. With the red dashed line we report the linear fit at 8 kpc. In both panels with the orange triangle we label the value of the [Fe/H] as a function of the dust-to-gas ratio D/G for the model computed in the solar neighborhood at the Galactic time of 9.5 Gyr (i.e., model solar value).

To compute $< P_{GGP/M} >_{IMF}$ and $<P_{GGP/FGK}>_{IMF}$ quantities, we have only to know the weighted stellar mass on the IMF in the mass range of M and FGK stars, respectively. The weighted stellar masses on the Scalo (1986) IMF are:

$$< \frac{M_{\star,FGK}}{M_{\odot}} >_{IMF}= \frac{\int_{0.45\,M_{\odot}}^{1.4\,M_{\odot}} m^{-1.35}dm}{\int_{0.45\,M_{\odot}}^{1.4\,M_{\odot}} m^{-2.35}dm} = 0.72584 \tag{4.17}$$

and

$$< \frac{M_{\star,M}}{M_{\odot}} >_{IMF}= \frac{\int_{0.08\,M_{\odot}}^{0.45\,M_{\odot}} m^{-1.35}dm}{\int_{0.08\,M_{\odot}}^{0.45\,M_{\odot}} m^{-2.35}dm} = 0.15504. \tag{4.18}$$

In top panel of Fig. 4.3 we show the evolution of $< P_{GGP/FGK} >_{IMF}$ and $< P_{GGP/M} >_{IMF}$ probabilities as a function of the [Fe/H] abundance ratio computed at different Galactocentric distances using our chemical evolution model. Because of the inside-out formation, the inner regions exhibit a faster and more efficient chemical enrichment. The model computed at 4 kpc reaches at the present time a [Fe/H] of 0.55 dex; instead, at 20 kpc, the maximum [Fe/H] is equal to -0.1 dex. We see that the two probabilities are substantially different for super-solar values in the inner regions. For instance, at the present time, at the maximum values of the [Fe/H] abundance in panel C of Fig. 4.1, at 4 kpc, the probabilities $< P_{GGP/FGK} >_{IMF}$ and $< P_{GGP/M} >_{IMF}$ show values of 0.43 and 0.04, respectively.

In the bottom panel of Fig. 4.3 we show the evolution of $< P_{E/FGK} >_{IMF}$ and $< P_{E/M} >_{IMF}$ as a function of the metallicity, computed at different radius. These probabilities are computed following Eq. (4.4) and strongly depends on the probability $< P_{GGP/FGK} >_{IMF}$ and $< P_{GGP/M} >_{IMF}$, computed for giant planets.

P_{GHZ} probabilities around FGK and M stars

In the upper panels of Fig. 4.4 (A and B) we show the evolution in time of the P_{GHZ} values for FGK and M stars as functions of the Galactocentric distance when SN destruction effects are not taken into account.

We note that the $< P_{GHZ/M} >_{IMF}$ and $< P_{GHZ/FGK} >_{IMF}$ probabilities are identical at large Galactocentric distances. The reason is that the $< P_{E/FGK} >_{IMF}$ and $< P_{E/M} >_{IMF}$ probabilities are similar for sub-solar values of [Fe/H]. The chemical evolution in the outer parts of the Galaxy is slow and has longer time-scales because of the inside-out formation. The maximum values of [Fe/H] are lower than in the inner region and are sub-solar (see the age-metallicity relation reported in panel B of Fig. 4.1).

Moreover, in the inner regions, the $< P_{GHZ,M} >_{IMF}$ and $< P_{GHZ,FGK} >_{IMF}$ probabilities become different only for Galactic times longer than 8 Gyr. As expected, the higher probabilities are related to the M stars. Even when the $< P_{E/FGK} >_{IMF}$ and $< P_{E/M} >_{IMF}$ probabilities are substantially different for [Fe/H]$>$ 0.2 (see Fig. 4.3), the two associated P_{GHZ} probabilities are similar. The reason is the definition of $P_{GHZ}(t)$: at each Galactic time, the SFR $\times$ P_E quantity is integrated from 0 to t. In other words, we are weighting the P_E quantity on the SFR. From panel C) of Fig. 4.1 it is clear that the peak of the SFR in the inner regions (annular region between 3 and 7 kpc) is around 3 Gyr. From the age-metallicity relation reported in panel B) of Fig. 4.1, we

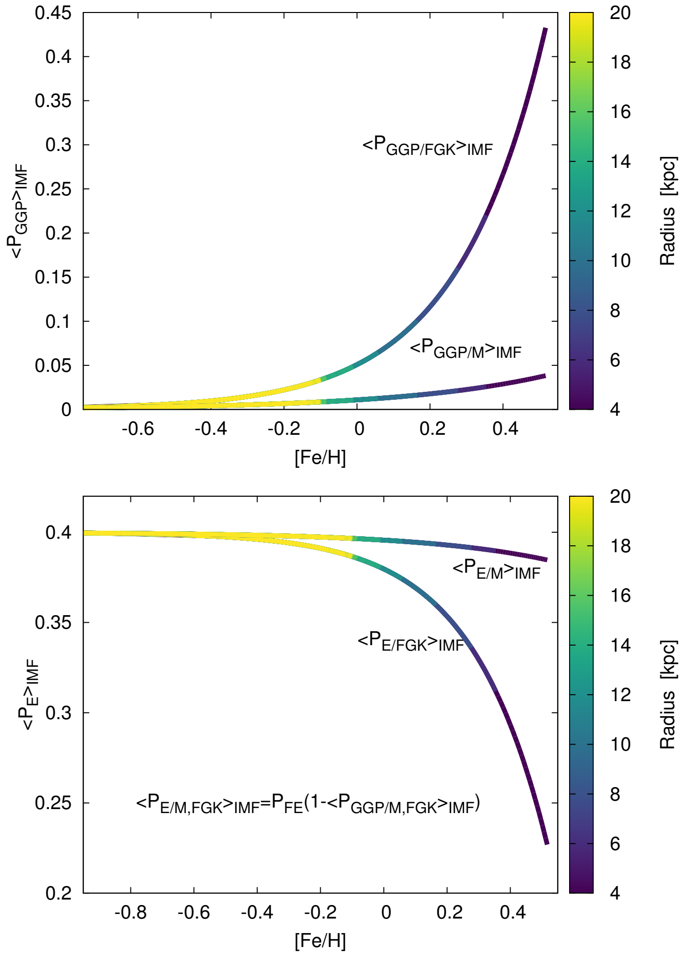

Figure 4.3: Top panel: probabilities $<P_{GGP/FGK}>_{IMF}$ and $<P_{GGP/M}>_{IMF}$ of finding gas giant planets around FGK and M stars, respectively, as functions of the abundance ratio [Fe/H] using our chemical evolution model for the Milky Way disk and adopting the prescriptions given by Gaidos & Mann (2014). Bottom panel: probabilities $< P_{E/FGK} >_{IMF}$ and $< P_{E/M} >_{IMF}$ of finding terrestrial planets but not gas giant planets around FGK and M stars, respectively. The color code indicates the Galactocentric distance.

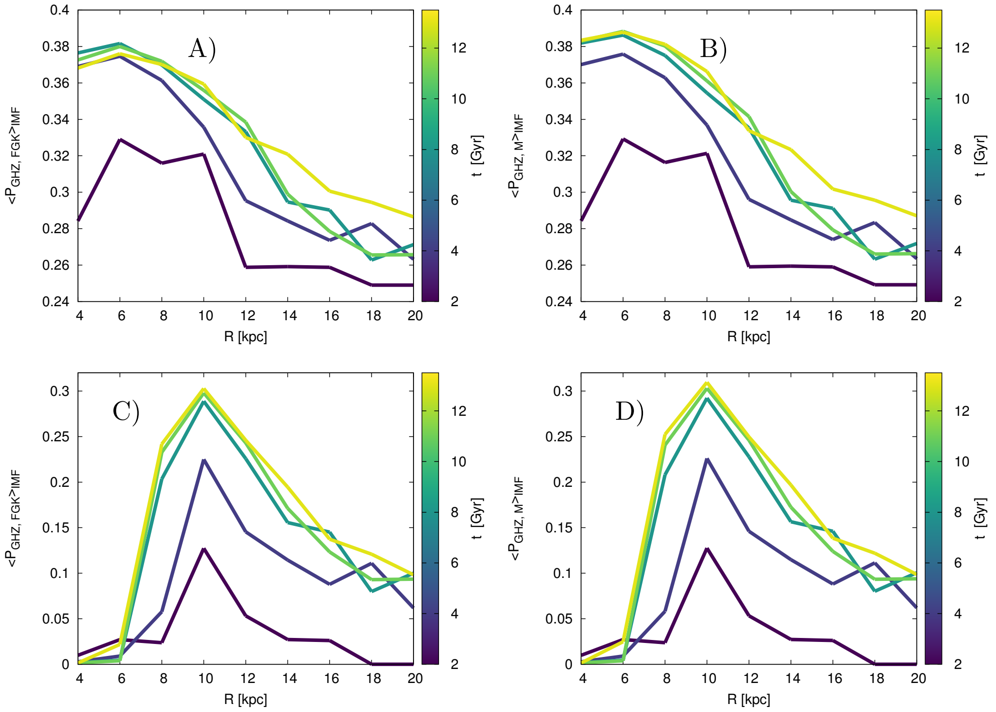

Figure 4.4: *Upper panels*: probability $<P_{GHZ}>_{IMF}$ of finding terrestrial habitable planets, but not gas giant around FGK stars (*panel* A) and M stars (*panel* B) as a function of the Galactocentric radius. In this case, we do not consider the destructive effects from nearby SN explosions. The color code indicates different Galactic times. *Lower panels*: probability P_{GHZ} of finding terrestrial habitable planets, but not gas giant around FGK stars (*panel* C) and M stars (*panel* D) as a function of the Galactocentric radius, taking (*panel* D) as a function of the Galactocentric radius, taking the destructive effects from nearby SN explosions into account. The color code indicates different Galactic times.

derive that at this age, the mean Galactic [Fe/H] is -0.5 dex. At this metallicity, as stated above, the $P_{E.FGK}$ and $P_{E.M}$ values are almost the same. This is the reason why the two P_{GHZ} probabilities are similar even at late time in the inner regions.

In the lower panels of Fig. 4.4 (C and D) we show that the P_{GHZ} probabilities for FGK and M stars as functions of the Galactocentric distances and time are almost identical when the SN destruction effects have been taken into account. As already found in Spitoni et al. (2014), the Galactocentric distance with the highest probability that a star (FGK or M type) hosts a terrestrial planet, but no gas giants, is 10 kpc.

4.4.4 GHZ maps for FGK and M stars

In order to recover the total number of stars at the Galactic time t and Galactocentric distance R that host habitable planets, the total number of stars created up to time t at the Galactocentric distance R ($N_{\star tot}$ quantity in Eq. 4.6) is required.

Our chemical evolution model reproduces very well the observed total local stellar surface mass density of 35 ± 5 $\mathrm{M}_\odot$ pc^{-2} (Gilmore et al., 1989; Spitoni et al., 2015). Our predicted value for the total surface mass density of stars is 35.039 $\mathrm{M}_\odot$ pc^{-2}. Moreover, we find that this value for M stars alone is 24.923 $\mathrm{M}_\odot$ pc^{-2} and the one for FGK stars is 9.579 $\mathrm{M}_\odot$ pc^{-2}.

In Fig. 4.5 we show the number of FGK stars (upper panel) and M stars (lower panel) that host habitable terrestrial planets, but no gas giant planets, as functions of the Galactic time and Galactocentric radius (quantity $N_{\star life}$ of Eq. 4.6).

We note that for both FGK and M stars, the GHZ maps, in terms of the total number of stars that host planets with life, peaks at 8 kpc. On the other hand, as we showed above, the maximum fraction of stars that can host habitable terrestrial planets peaks at 10 kpc (see panels C and D of Fig. 4.4). The reason why the GHZ peaks at galactocentric smaller distances than when it is expressed in terms of the fraction of stars is that in the external regions, the number of stars formed at any time is smaller than in the inner regions because the SFR is lower. This is in agreement with the results of Prantzos (2008) and Spitoni et al. (2014).

We see that at the present time, in the solar neighborhood the number $N_{\star,M,life}/N_{\star,FGK,life}$=10.60. This ratio is consistent with the IMF we adopted in our model. The ratio between the fraction of M stars over FGK stars (by number) in a newborn population adopting a Scalo IMF is:

$$\left(\frac{M_{number}}{FGK_{number}}\right)_{\text{Scalo IMF}} = \frac{\int_{0.08\,M_\odot}^{0.45\,M_\odot} m^{-2.35}dm}{\int_{0.45\,M_\odot}^{1.4\,M_\odot} m^{-2.35}dm} = 11.85. \qquad (4.19)$$

Finally, the predicted local surface mass density of M stars that host habitable planets predicted by our model is 5.446 $\mathrm{M}_\odot$ pc^{-2}, and the value for FGK stars is 2.40 $\mathrm{M}_\odot$ pc^{-2}.

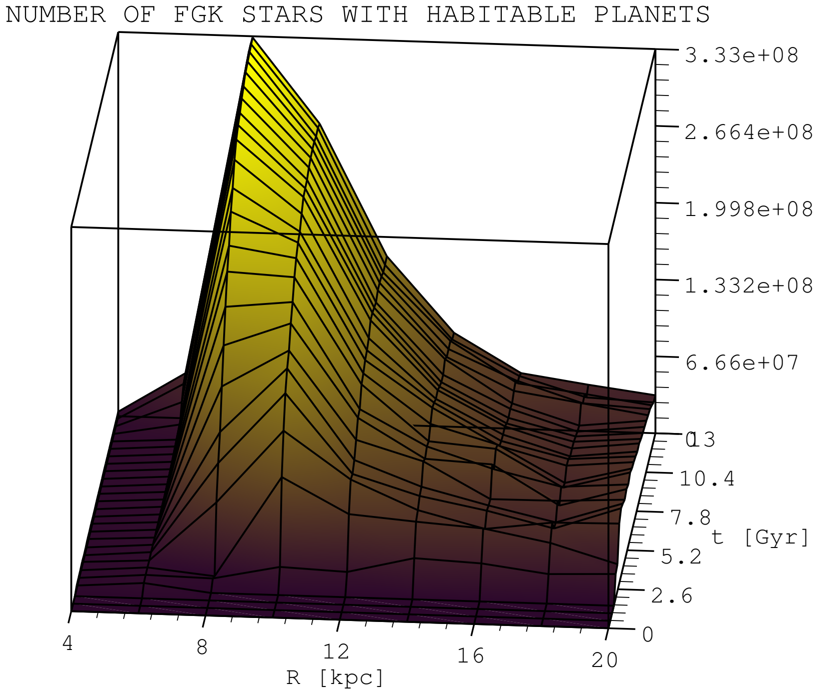

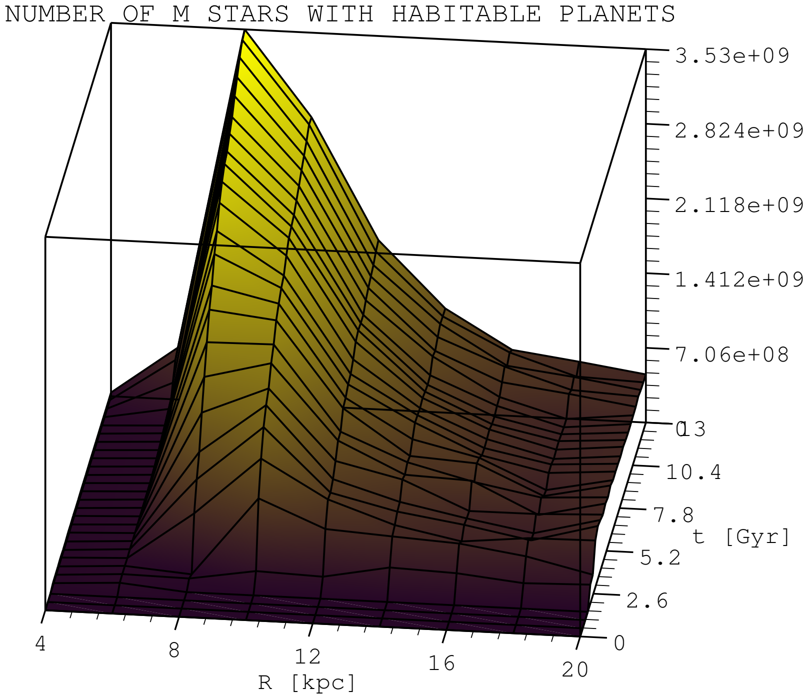

Figure 4.5: Total number of FGK stars (*upper panel*) and M stars (*lower panel*) with habitable terrestrial planets, but no gas giants, as functions of the Galactocentric distance and the Galactic time (the $N_{\star life}$ quantity in Eq. 4.6) where SN destructive effects are taken into account. The number of stars is computed within concentric rings that are 2 kpc wide.

4.5 Conclusions

In this Chapter we have studied the evolution of dust in the Milky Way by using a specific model of chemical evolution tuned to reproduce the main observables of the Galaxy. We have investigated the Galactic habitable zone of the Milky Way by adopting the most updated prescriptions for the probabilities of finding terrestrial planets and gas giant planets around FGK and M stars. Furthermore, we have studied the dust mass evolution in the Milky Way and we focused on the relation between the dust-to-gas ratio and the metallicity of the ISM. To do this, we adopted a chemical evolution model of the Milky Way that follows the evolution of the chemical abundances both in the gas and dust.

The main results can be summarized as follows:

- Thanks to the multi-zone model of the Milky Way, we find that the dust mass differs at varying the galactocentric distances. In particular, we find that it decreases as the distance from the Galactic center increases.
- As pointed out by several previous works, we find that the stellar production represents the main important source of dust during the initial phases of the star formation until a critical metallicity is reached. From this point the dust growth becomes the most important process. Here, we also find that the transition between the two processes (the critical metallicity) at different radii is reached at different times and metallicities, and it is caused by the different star formation history assumed at different galactocentric distances.
- The probabilities that an FGK or M star could host habitable planets are roughly identical. Slight differences arise only at Galactic times longer than 9 Gyr, where the probability of finding gas giant planets around FGK becomes substantially different from the probability associated to M stars.
- By adopting the same prescriptions for the destructive effects from close-by SN explosions of Spitoni et al. (2014), we find that the largest number of FGK and M stars with habitable planets are found in the solar neighborhood in the annular region between 7 and 9 kpc.
- At the present time, the total number of M stars with habitable terrestrial planets without gas giants are $\simeq$ 10 times the number of FGK stars. This result is consistent with the Scalo (1986) IMF adopted here.
- When we adopt the Scalo (1986) IMF, the probabilities of finding gas giant planets around FGK and M stars computed with the two-infall chemical evolution model start to differ from super-solar values of [Fe/H]. In particular, substantial differences are present in the annular region centered at 4 kpc from the Galactic center.
- We provide for the first time a sixth-order polynomial fit (and a linear fit, in the Solar neighborhood) for the relation found in the chemical evolution model between the [Fe/H] abundances and the D/G ratio. With this relation, it is possible to express the Gaidos & Mann (2014) probabilities of finding gaseous giant planets around FGK or M stars in terms of the D/G ratio.

- We provide a useful theoretical tool to set the proper initial condition for the formation of protoplanetary disks by connecting the evolution of the dust-to-gas ratios at different Galactocentric distances with the chemical enrichment expressed in terms of [Fe/H].

Chapter 5

Dust in elliptical galaxies

In this Chapter we focus on the study of the formation and evolution of dust in elliptical galaxies. The star formation history of a typical elliptical galaxy is completely different from the ones of irregulars or spirals we discussed in Chapters 3 and 4, respectively: their chemical composition is consistent with a strong and rapid episode of star formation (Larson, 1974; Matteucci, 1994; Pipino & Matteucci, 2004). During the initial starburst, an elliptical galaxy can reach a solar or super-solar metallicity due to stellar activity (Calura & Matteucci, 2004). Also dust seems to have a considerable mass in the initial phases, and it is extremely important to understand the responsible mechanisms of its formation.

During the past decade, large dust masses $> 10^7 M_\odot$ have been detected in the redshift range 5<z<9, thanks to observations in the millimeter (mm) and sub-millimeter (sub-mm) wavelengths (e.g. Bertoldi et al., 2003; Beelen et al., 2006; Michałowski et al., 2010; Carilli & Walter, 2013; Watson et al., 2015; Maiolino et al., 2015). Cooray et al. (2014) detected a huge amount of dust of $3 \times 10^8 M_\odot$ in a z=6.34 galaxy with an extreme ongoing star formation of $\sim 830 M_\odot yr^{-1}$. Observations at high redshift are biased to efficient starburst galaxies which are more luminous than less active ones, which instead are more numerous. Thanks to the Atacama Large Millimeter Array (ALMA), Maiolino et al. (2015) inferred dust upper limits on "normal" galaxies at redshift ~ 7, and during the last years, the gravitational lensing technique successfully solved the problem of dust detection in galaxies of moderate luminosity at very high redshift (Ota et al., 2014; Watson et al., 2015; Zavala et al., 2015). On the other hand, interferometric studies also reported no-detections of dust in galaxies between redshifts 6<z<8 (Walter et al., 2012; Ouchi et al., 2013; Berger et al., 2014; González-López et al., 2014; Schneider et al., 2015). In this context, it is not yet clear if the presence or absence of dust in high redshift systems is a common rule rather than an exception.

Laporte et al. (2017) measured a dust mass of $6 \times 10^6 M_\odot$ in a gravitational-lensed galaxy at the surprising redshift of 8.38, which corresponds to an age of the Universe of about 600 Myr. This short time-scale suggests that the responsible process for dust formation should be very rapid. In particular, massive stars exploding as Type II SNe have been advocated for the presence of dust at high redshift, because of their typical short lifetimes (Padovani & Matteucci, 1993). In particular, the formation of Pop III stars in primordial environments

$M_{infall}[M_\odot]$	$T_{infall}[Gyr]$	$\nu[Gyr^{-1}]$	ω_i	IMF	δ^{SNII}	Dust Accretion
Elliptical reference model						
10^{11}	0.3	15	10	Salpeter	δ^{SNII}_{MP}	yes
Parameter ranges						
$10^{11} \leq M_{infall} \leq 10^{12}$	0.3	15	10	Salpeter	$\delta^{SNII}_{LP} - \delta^{SNII}_{MP} - \delta^{SNII}_{HP}$	yes-no

Table 5.1: Parameters of the reference model for a typical elliptical galaxy. In the first column is presented the mass of the infall (in solar masses), in the second one the the infalling time-scale (in Gyr), in the third the star formation efficiency (in Gyr^{-1}), in the fourth the wind parameter, in the fifth the adopted IMF and in the sixth the efficiency of dust production by Type II SNe. In the last raw, we show the parameter ranges used in our work to study the dust formation in the starburst of elliptical galaxies.

may represent the first cosmic dust polluters (Marassi et al., 2014, 2015). Also AGB and super-AGB stars, which have slightly longer stellar lifetimes, can contribute to dust production in a non-negligible way (e.g. Valiante et al., 2009; Schneider et al., 2015), even if a minimum metallicity for the formation of low mass stars is needed (Schneider et al., 2003, 2012; Chiaki et al., 2015). However, a non-stellar source seems to be required, because the only contribution from stars can hardly account for the amount of dust observed in some high redshift systems (e.g. Mattsson, 2011; Pipino et al., 2011; Kuo & Hirashita, 2012; Calura et al., 2014). Such a "dust-budget crisis" can be solved by assuming a top-heavy IMF (Rowlands et al., 2014) or alternative channels for dust production. In Pipino et al. (2011) an "extra QSO-dust" source was introduced to explain the high amount of dust observed in QSOs, but they concluded that this contribution was negligible. Moreover, some authors claim that dust accretion may play a significant role even on short time-scales (e.g. Michałowski et al., 2010; Mancini et al., 2015, 2016). On the other hand, this process may be delayed or even stopped because of the high temperature of the ISM in the high redshift Universe (Ferrara et al., 2016).

In what follows, we are going to analyze the formation and the evolution of the dust mass during the initial burst of star formation in elliptical galaxies, to cast light on the role played by different processes. In fact, our chemical evolution model takes into account the stellar lifetimes, and therefore we can distinguish the contribution of different stellar sources at each time-step.

This Chapter is organized as follows: we describe the model of a typical elliptical galaxy in Section 5.1 and we present the comparison between our model and high redshift galaxies in Section 5.2, where we discuss in which way different processes (dust production, accretion, destruction) affect the dust mass in the early phases of galactic evolution. Then, in Section 5.3 we quantify the different dust contribution coming from stellar production, i.e. Type II SNe, AGB stars and Type Ia SNe. Finally, we summarize our conclusions in Section 5.4

5.1 The model of an elliptical galaxy

We consider elliptical galaxies to form by a monolithic collapse of a gas cloud, characterized by a short infalling time-scale (Matteucci & Tornambe, 1987; Matteucci, 1994). This assumption causes a rapid collapse, which triggers an intense and rapid star formation process. As soon as the thermal energy of the gas, heated by SN explosions, equates the binding energy of the system, an intensive galactic wind is produced. this wind stops the star formation and sweeps out all the residual ISM. After this moment, the galaxy is assumed to evolve passively.

Larson (1974) applied for the first time this methodology and he was able to reproduce two of the main common properties observed in elliptical galaxies: the mas-metallicity relation, i.e. the trend of increasing absorption metal lines strength with the velocity dispersion (Lequeux et al., 1979; Garnett & Shields, 1987; Pilyugin et al., 2004; Tremonti et al., 2004; Kewley & Ellison, 2008; Mannucci et al., 2010), and the color-magnitude relation, i.e. the increase of reddening in more massive galaxies (Bower et al., 1992). Larson (1974) assumed the star formation efficiency to be inversely proportional to the total mass of the galaxy, and therefore, more massive galaxies with deeper gravitational potentials develop galactic winds later. In this way, massive galaxies have a prolonged period of star formation which enhances the metallicity and the reddening.

On the other hand, observations of overabundances of $[\alpha/Fe]$ ratios and the increase of this ratio in more massive galaxies led to a different interpretation of the evolution of elliptical galaxies. In this context, chemical evolution models easily explain the mass-metallicity relation and $[\alpha/Fe]$ abundances thanks to the so called downsizing scenario, in which the star formation efficiency of a galaxy increases with the total mass (Matteucci, 1994; Pipino & Matteucci, 2004; Calura et al., 2009b).

These models have been extensively compared with low and high redshift massive galaxies (Calura et al., 2008; Pipino & Matteucci, 2004; Pipino et al., 2011; Pipino & Matteucci, 2011). Here, we present a chemical evolution model which represents a typical elliptical galaxy: we constrain the model parameters on the basis of previous works that were able to reproduce the main observational features of ellipticals, such as the chemical abundances, the mass-metallicity relation, the color-magnitude relation and the Type Ia SN rates (Matteucci & Tornambe, 1987; Matteucci, 1994; Pipino & Matteucci, 2004; Calura et al., 2007).

Concerning the dust phase of the ISM, we remind that we adopt stellar condensation efficiencies (δ_i) as provided by Piovan et al. (2011) (see Chapter 2). In particular, the condensation efficiencies of Type II SNe (δ_{SNII}) depend on the hydrogen density of the environment surrounding the explosion: in fact, the higher the density, the more resistance the shock will encounter, and therefore, more dust will be destroyed by the reverse shock. Generally, we adopt a median value of $n_H = 1\ cm^{-3}$ to describe the average density of the surrounding ISM of the SN. In this Chapter, we explore the consequences of adopting different values for this quantity: when we assume a density of $n_H = 0.1\ cm^{-3}$ we call the highest condensation efficiency as δ_{HP}^{SNII}, for $n_H = 10\ cm^{-3}$ we call the lowest value as δ_{LP}^{SNII} and for $n_H = 1\ cm^{-3}$ we call the medium value as δ_{MP}^{SNII}.

In Table 5.1 we report the main parameters characterizing our reference model, namely the mass of the infall, the infalling time-scale, the star formation efficiency, the wind efficiency, the adopted IMF and the adopted dust contribution from Type II SNe.

5.2 Dust mass at high redshift

With our model we are able to differentiate the contributions of different processes responsible for the dust formation in the initial evolutionary phases of a galaxy. For this purpose, we vary some key parameters of the reference model as shown in Table 5.1. In particular, the most interesting parameters that influence the dust mass growth in the initial phases are the mass of the infall, the Type II SN condensation efficiencies and the presence of dust accretion, whereas the variation of the time of the infall and the variation of the star formation and wind efficiencies produce negligible effects.

In order to compare our predictions with high redshift observations, we assume a galaxy to form at redshift=10 and let it evolve in a Λ-cold dark matter (ΛCDM) cosmology with $H_0 = 67.7 Km\, s^{-1}\, Mpc^{-1}$ (Planck Collaboration et al., 2016). Fig. 5.1 shows the evolution of the formed dust mass inside the galaxy for different models. The reference model (red-dashed line) lies below the upper limits fixed by observations and it reaches a total mass of dust $M_{dust} \geq 10^7 M_\odot$ at its maximum. When we adopt a more efficient dust production from Type II SNe (δ_{HP}^{SNII}, thin blue dashed), a large amount of dust is produced. This stresses the importance of massive stars in the firsts evolutionary phases: in fact, they are responsible for the rapid increase of M_{dust} during the first $\sim$ 100 Myr of galaxy evolution, when the bulk of dust is formed. To reach higher dust masses, our model needs the most efficient contribution from Type II SNe as well as a higher mass of the infall ($M_{infall} = 5 \times 10^{11} M_\odot$, thick blue long-dashed line): in this scenario a significant dust mass is produced even at $z \simeq 9.6$ (Zavala et al., 2015) and reaches values $M_{dust} > 10^8 M_\odot$ for $z \leq 6$ (Cooray et al., 2014). A similar result is obtained by the red thick dashed line, which represents the same prescriptions as the reference model, but with $M_{infall} = 5 \times 10^{11} M_\odot$.

We also tested the case in which dust accretion is avoided (magenta dash-dotted line): in this case, it is impossible to reproduce high values of M_{dust} at $z > 6$. However, if we consider the highest contribution by Type II SNe, the predicted M_{dust} is larger than in the reference model, even without considering dust accretion (magenta dash-dotted line). Dust growth acts on longer time-scales with respect to stellar dust production and it becomes particularly efficient in high metallicity environments. Even if this process has a fundamental importance in dust evolution, it does not affect the rapid increase of the initial phases (firsts 0.2 Gyr), which is mainly caused by stellar formation.

Our work also casts light on another important issue related to high redshift galaxies: the time-scale of dust formation. The simultaneous presence of both dust-rich (and metal-) and poor objects (e.g. Ouchi et al. 2013) at high redshift may indicate that the transition between these two populations has to be very rapid and may take place on a Myr time-scale (Mattsson, 2015). Fig. 5.1 is very useful to understand the typical time-scale of the the buildup of dust, as well as by which process it is driven. In the earliest phases, i.e. at times $\leq$ 0.1 Gyr, the fast increase of the dust mass is mainly driven by the production by Type II SNe. This is visible from, e.g., the lack of any difference in the behavior of

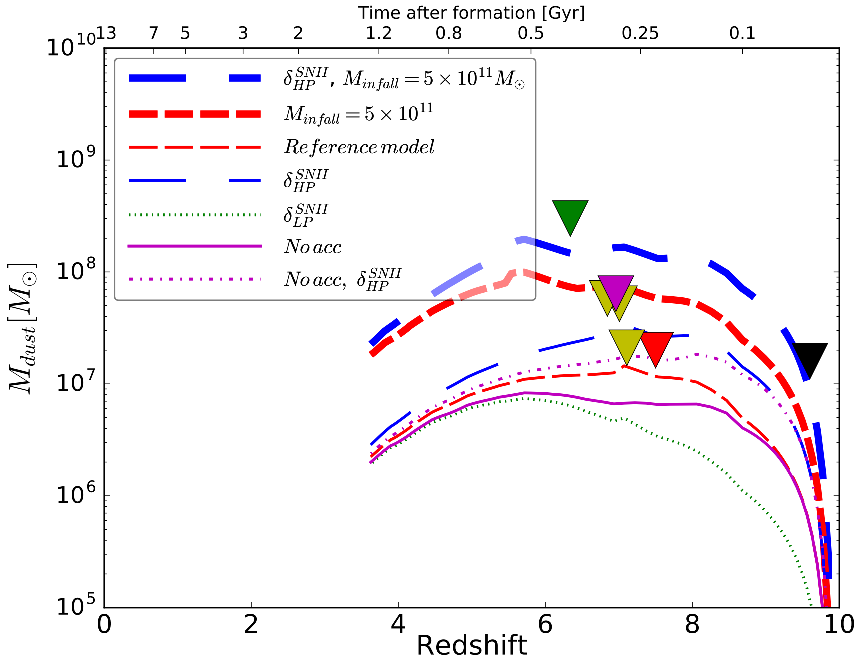

Figure 5.1: Dust mass in elliptical galaxies as a function of redshift (lower x-axis) and time (upper x-axis). The thin red long-dashed line is our reference model, whose parameters are shown in Table 5.1. In the models described by the blue long-dashed and green dotted lines, higher (δ_{HP}^{SNII}) and lower (δ_{LP}^{SNII}) dust production by Type II SNe are adopted, respectively. The magenta solid and dot-dashed lines represent models with no accretion: the former assumes a medium contribution from Type II SNe (δ_{MP}^{SNII}), whereas the latter assumes the highest one (δ_{HP}^{SNII}). The thick lines represent models with a higher infalling mass ($M_{infall} = 5 \times 11 M_\odot$). Data represent upper limits of the dust mass for high redshift galaxies by Watson et al. (2015) (red), Cooray et al. (2014) (green), Zavala et al. (2015) (black), Maiolino et al. (2015) (yellow) and Ota et al. (2014) (magenta).

the reference model and the "no accretion" model at these times.

Other works have already shown that in elliptical galaxies, the buildup of metals occurs on a rapid timescale, with a supersolar metallicity reached after only 0.1 Gyr from its formation (e.g., Pipino & Matteucci, 2004; Calura et al., 2014). As heavy elements are the main constituents of dust grains, dust accretion can start to be significant only after enough metals have been ejected into the ISM. Therefore, only in high metallicity environments (namely at later epochs), metals in the gas phase are able to condensate onto pre-existing dust grains. Moreover, the bulk of dust mass is settled already at $\sim$ 0.25 Gyr after the beginning of the star formation. Clearly, in proto-spheroids the rapid buildup of the dust is also helped by the rapid time-scale of the infall.

The fast increase of the dust mass in the initial phases reaches the maximum at the time in which the star formation stops ($z \sim 7$). Then, the dust mass starts to decrease as a consequence of many processes. First, due to the short lifetimes of massive stars, the Type II SN rate traces star formation rate. Therefore, when the star formation rate is zero, because almost all massive stars have already died in earlier phases, the dust production from Type II SNe stops. Second, from this moment the galactic wind starts and the majority of the ISM (gas and dust) is expelled outside the galaxy. Third, as we have already explained in Chapter 2.2, dust accretion mainly occurs in molecular clouds, namely in the regions of the ISM characterized by high densities and low temperatures, where new stars form. When the galactic wind is active, the thermal energy of the galaxy, heated by SN explosion events, is relatively high and molecular clouds (or cold ISM) are missing. For this reason, we stop the dust accretion process as soon as the star formation stops.

As a result of the previous points, at the moment of the onset of the galactic wind the only active dust processes are dust destruction and dust production from AGB stars (which have longer lifetimes than Type II SNe). However, dust production from low-intermediate mass stars, is negligible with respect to the contribution of massive ones (see Section 5.3.2), and therefore, the total dust mass decreases because dust destruction remains the only and the most important process in the ISM.

5.3 Stellar dust production

In the previous Section, we focused on the distinction between the role played by dust accretion and dust formation in stars. Here, we focus only on the stellar contribution because we want to distinguish different stellar sources. First, we quantify the dust contribution from Type Ia SNe, that in our case are not considered as dust factories, at variance with previous works. Second, we cast light on the dust formation time-scales when AGB stars or Type II SNe are considered: in particular, we show how their relative contribution changes by varying dust prescriptions during the initial burst of star formation.

5.3.1 The effect of Type Ia SNe

In previous works (e.g. Dwek, 1998; Calura et al., 2008, 2017) Type Ia SNe were considered as dust producers and therefore, a non-negligible mass of dust

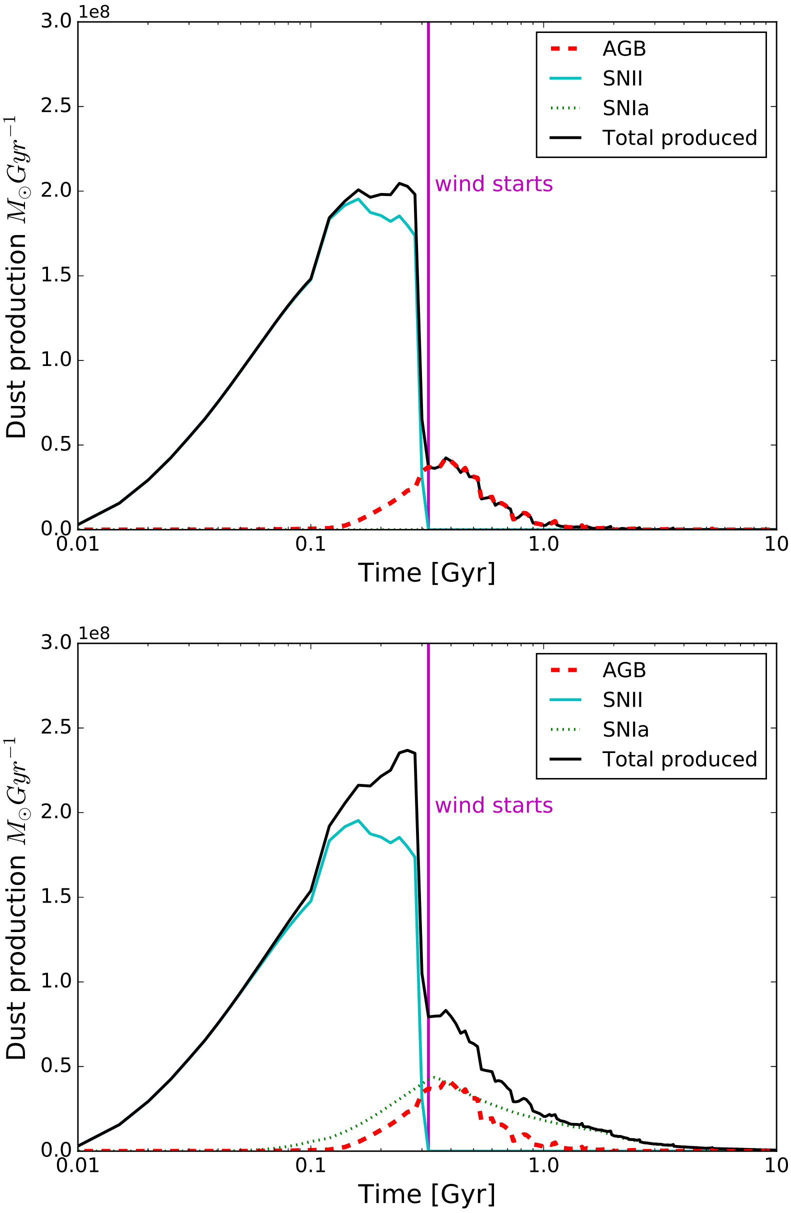

Figure 5.2: Dust production rate for AGB stars (dashed red line) Type II SNe (cyan solid line), Type Ia SNe (dotted green line) and the total contribution (black solid line). *Top panel:* model without the inclusion of Type Ia SNe as dust producers, as adopted in this thesis. *Bottom panel:* model with the inclusion of Type Ia SNe as dust producers as adopted in previous works (e.g. Dwek 1998; Calura et al. 2008, 2017)

was assumed to form after the burst of the star formation. These kind of stars originate from the explosion of a carbon-oxygen white dwarf, belonging to a binary system. The mechanism of such event involves low and intermediate mass stars ($0.8M_{\odot} < m < 8M_{\odot}$), and therefore SNe Ia explode over a large range of typical time-scales, from a minimum time delay of ∼30 Myr (the lifetime of an $8M_{\odot}$) to a maximum Hubble time. In our work, we do not consider Type Ia SNe as dust factories, because it is not supported by observational evidence (Blair et al., 2007; Williams et al., 2012; Gomez et al., 2012). Here we want to quantify the effect of considering or not dust formation by Type Ia SNe, in particular after the onset of the galactic wind, namely when the star formation stops. For the condensation efficiencies of Type Ia SNe we use the ones suggested by Dwek (1998).

We show in Fig. 5.2 the dust production rate from stellar sources before and after the onset of the galactic wind with the exclusion or the inclusion of Type Ia SNe as dust producers (bottom and top panel, respectively). In the first case, before the galactic wind starts (magenta vertical line), Type II SNe and AGB stars produce the bulk of dust. In fact, as soon as the star formation stops (when galactic wind is active), only AGB stars can contribute and produce a total mass of dust which is ∼3 times lower than the one produced during the burst of star formation. In the second case (bottom panel of Fig. 5.2), the situation is the opposite: Type Ia SNe, which continue to explode even after star formation stops, help the delayed dust production of AGB stars after the onset of the galactic wind, and the total dust production in the quiescent phase becomes almost similar or even higher than the one produced in the initial burst.

In this way, our results differ from previous work on the study of dust in elliptical galaxies (e.g. Calura et al., 2008; Pipino et al., 2011; Calura et al., 2017). However, we find big differences only after the burst of star formation, namely during the phase in which the galactic wind is active.

5.3.2 AGB stars versus Type II SNe

We have showed in the previous Section that the bulk of the dust forms during the initial burst of star formation. Dust production in Type II SN ejecta is often advocated to explain the origin of dust in the early Universe (e.g. Morgan & Edmunds, 2003). In fact, the typical time-scale of massive progenitors of $10-40\mathrm{M}_{\odot}$ is $\tau_{*} < 10$ Myr (Padovani & Matteucci, 1993), much shorter with respect to low-intermediate mass stars ($1-8\mathrm{M}_{\odot}$). Furthermore, Maiolino et al. (2004) showed that the extinction curve in a quasar at a redshift > 6 is in very good agreement with SN dust models.

However, observations show that the effective mass of dust in SN Remnants are still highly uncertain, varying from SN to SN (Galliano et al., 2011). On one hand, it seems that the reverse shock produced in the SN explosion can destroy up to 80% of the total dust produced (Todini & Ferrara, 2001; Dwek, 2005; Nozawa et al., 2006; Zhukovska et al., 2008; Bianchi & Schneider, 2007; Silvia et al., 2010), but on the other hand a very efficient production from those massive stars is expected to fit observations. For instance, Dwek et al. (2007) calculated that extreme conditions for SN-dust formation/evolution (100% dust condensation efficiencies, and therefore no destruction due to shocks) must be assumed to reproduce the observed $\sim 10^{8}\mathrm{M}_{\odot}$ in the hyperluminous quasar SDSS J1148+5251 at $z = 6.4$.

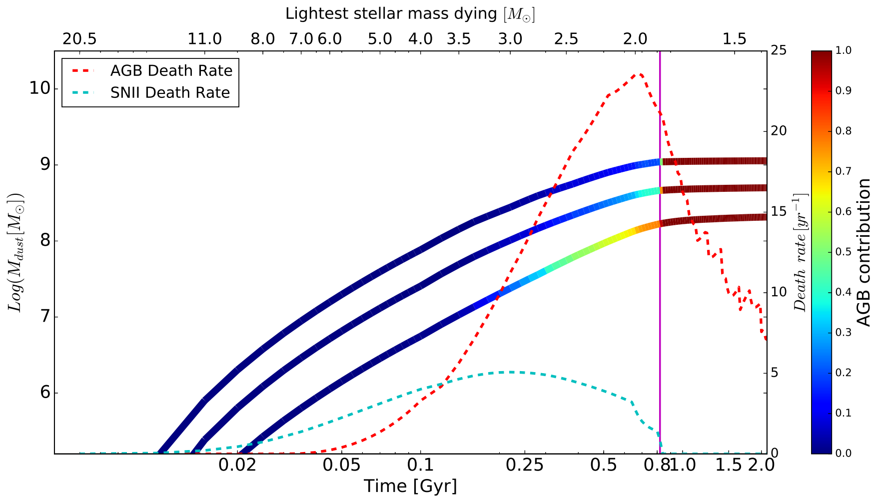

Figure 5.3: Evolution of the dust mass produced by Type II SNe and AGB stars in the initial phases of a typical elliptical galaxy. Different curves (solid lines) are obtained by varying δ_{SNII} from the highest value (upper curve) to the lowest one (lower curve). The color bar indicates the contribution of AGB stars among the total stellar dust production. Cyan and red dashed lines represent the death rate of AGB and Type II SNe, respectively. The vertical magenta line indicates the time-step of the onset of the galactic wind, namely when the star formation stops.

The (longer) stellar lifetime argument, does not necessarily implies that intermediate-mass stars cannot contribute to dust production at early cosmic epochs. Indeed, the contribution of AGB stars in high redshift galaxies may be as important as that of SNe (Valiante et al., 2009; Schneider et al., 2015).

Main sequence lifetimes of stars with masses lower than 3M$_\odot$ are shorter than 300Myr (Padovani & Matteucci, 1993), quite below 1 Gyr (about the age of the Universe $z \sim 6$). In addition, $1-8$M$_\odot$ stars are generally more numerous than $(10-100)$M$_\odot$ ones, even if their proportion depends on the adopted IMF. Assuming a certain IMF ϕ, the fraction of AGB stars and SNe with respect the total number of stars can be expressed as following:

$$f_{AGB} = \frac{\int_{1\,M_\odot}^{8\,M_\odot} \phi(m)dm}{\int_{0.1\,M_\odot}^{100\,M_\odot} \phi(m)dm} \tag{5.1}$$

$$f_{SN} = \frac{\int_{8\,M_\odot}^{100\,M_\odot} \phi(m)dm}{\int_{0.1\,M_\odot}^{100\,M_\odot} \phi(m)dm} \tag{5.2}$$

These fractions vary as a function of the adopted IMF and extremes of the integrals. With a Salpeter IMF (eq.(2.4)), $\sim 47\%$ of the stars will evolve through the AGB phase, whereas only $\sim 3\%$ will end their lives as core-collapse SNe. For a Scalo IMF (eq.(2.4)), we find a fraction of AGB and Type II SNe of $\sim 47\%$ and $\sim 1.5\%$, respectively. This difference is found also when we assume a top-heavy IMF (biased towards high mass stars): e.g. for a Chabrier IMF, (Chabrier, 2003), the fraction of AGB stars is $\sim 37\%$ and the one of SNe progenitors reaches $\sim 23\%$. In the previous calculations, we adopted for the mass ranges [1.0,8.0] and [8.0,100] for AGB stars and Type II SNe, respectively.

The contribution of AGB stars and SNe to the total dust budget in a galaxy depends on the SFH, stellar metallicity and on the stellar yields, more than the time-scales (Valiante et al., 2009, 2011). Here, we study how their contribution depends on the adopted stellar yields, in the framework of a typical high-redshift starburst galaxy. To investigate the role of SN dust yields in what follows we vary the SN dust condensation efficiency from the highest value δ_{HP}^{SNII} to the lowest one δ_{LP}^{SNII}.

Fig. 5.3 shows the total dust mass produced by stellar sources as a function of the time (solid curves) for a single burst of star formation. We compare three cases of δ^{SNII}, which reflect different dust destruction efficiencies caused by the reverse shock. The case of the highest δ_{HP}^{SNII} reproduces observations in historical SN remnants and produces the highest solid curve of Fig. 5.3, whereas the lowest case assumes that only $\sim$10% of dust survives after the reverse shock and leads to the lowest curve. Along the curves, different colors represent the fraction of dust from AGB relative to the total production (AGB + SNe), as shown by the color-bar on the right side of the Figure. AGB-driven dust production is $> 50\%$ already at early times for both the lowest and medium value of δ_{SNII}. On the other hand, the highest δ_{SNII} leads to a larger contribution from SNe ($\sim 80\%$).

In Fig. 5.3, we also show the death rate of SNe and AGB stars. The SN rate almost traces the one of the star formation because of their typical short time-scales: in fact, it reaches the peak at 0.2 Gyr, when the star formation is maximum, and then it decreases until 0.8 Gyr when it assumes a zero value as soon as the galactic wind starts (vertical violet line). On the other hand, AGB stars die on longer time-scales and their death rate is shifted to higher galactic times with respect to Type II SNe. Then, the AGB rate decreases but it remains larger than zero even after the onset of the galactic wind. In particular, is important to notice that the peak is reached before the galactic wind, and therefore they mostly contribute to dust formation in the initial phases. In other words, it means that AGB stars can potentially contribute in a significant way to the initial dust production, but the relative contribution with Type II SNe strongly depends on the adopted prescriptions (δ_{SNII} and δ_{AGB}).

To study the effects on the relative contribution of dust formation between low-intermediate and massive stars at varying different AGB condensation efficiencies, we also consider the new δ^{AGB} provided by Dell'Agli et al. (2017). We show in Fig. 5.4 the difference between the inclusion of δ^{AGB} from Dell'Agli et al. (2017) and Piovan et al. (2011) in a model with a SFH for a typical elliptical galaxy. Generally, Piovan et al. (2011) prescriptions lead to a major dust contribution from AGB stars, except for the first evolutionary phases. The reason of this trend, is that Dell'Agli et al. (2017) prescriptions of δ^{AGB} are larger than Piovan et al. (2011) ones only at very low metallicities.

However, the results we have presented in this paragraph are almost independent from the adopted δ^{AGB}. For this reason, we conclude that the relative dust contribution between Type II SNe and AGBs mainly depends on the adopted prescriptions for δ^{SNII}, which we remind are affected by large uncertainties.

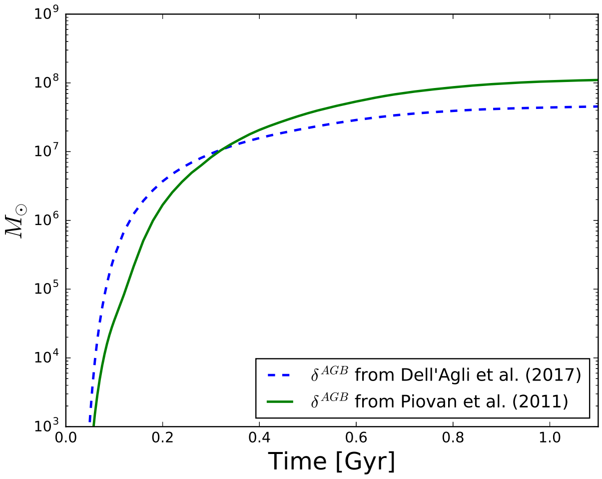

Figure 5.4: Dust mass produced by AGB stars versus the time in the initial phases of a typical elliptical galaxy, when AGB condensation efficiencies (δ^{AGB}) from Piovan et al. (2011) (solid green line) or from Dell'Agli et al. (2017) (blue dashed line) are adopted.

5.4 Conclusions

In this Chapter we have studied how different dust processes contribute to the dust mass assembly in the initial phases of a typical elliptical galaxy. We have investigated several aspects of dust-related issues on these objects and we can summarize our conclusions as follows:

- Our reference model provide a consistent amount of dust ($> 10^7 M_\odot$) at intermediate redshift (5<z<7), in agreement with current observations.
- The dust mass increases very fast in the initial burst of star formation. In particular, we found that the bulk of dust is already settled after 250 Myr.
- Type II SNe mainly contribute to the fast increase of the initial phases of the galactic evolution. The dust accretion indeed represents a fundamental process for dust evolution, but it becomes important on longer time-scales with respect the dust injection in the ISM from stellar sources.
- As soon as the star formation stops, the most important dust processes in the ISM become dust destruction and dust loss via galactic wind. For this reason, after the fast increase in the initial phases due to stellar production M_{dust} decreases.
- We quantified the effect of including in our model the dust production from Type Ia SNe. When we include them (using Dwek 1998 prescriptions), we find that they highly contribute to the total mass produced, and they also exceed the contribution of AGB stars. In particular, in the case of a typical elliptical galaxy, the contribution of such stars is extremely

important during the quiescent phases, after the onset of the galactic wind. In this thesis, we do not include Type Ia SNe as dust factories because of the lack of observational evidences. This choice influences the comparison between our predictions and previous models, in which Type Ia SNe were considered important dust contributors.

- We found that AGB stars contribute in a negligible way to the total stellar production in the initial burst with respect to Type II SNe. However, we have shown that the peak of the AGB death rate occurs before the onset of the galactic wind, and therefore, their small contribution is not due to the longer time-scales involved in such stars, but strongly depends on the adopted condensation efficiencies of Type II SNe δ^{SNII}.

Chapter 6

Dust rate across the Universe

6.1 Introduction

Interstellar dust mainly absorbs ultraviolet (UV) photons and re-emits in the infrared (IR) waveband (Calzetti, 2001): this dust property is particularly intriguing in the measure of the star formation rate (SFR) (Kennicutt, 1998; Madau & Dickinson, 2014). Observational tracers of star formation fundamentally measure the formation rate of massive stars, because these stars are responsible for most of the energy from a young stellar population. For example, the SFR can be constrained by Hα emissions, whose primary origin is from HII regions photoionized by O stars (Kennicutt, 1998; Hanish et al., 2006). Another way to infer star formation is to account for the UV continuum, which is dominated by the emission from massive stars, but with a broader mass range than Hα emissions (Hopkins, 2004; Madau & Dickinson, 2014). However, UV dust extinction can dramatically suppress or modify the emerging emission, producing an excess at IR wavelengths. The total IR luminosity represents a measurement of the energy that was absorbed by dust, namely an indirect measurement of the UV emission, and therefore another way to measure star formation (e.g. Bell et al., 2005). A good knowledge of dust is fundamental, because a dust emission model is needed to interpret the total IR luminosity.

In summary, the presence of dust is strictly correlated with the SFR measurements, and the best we know about dust the best we can constrain the cosmic SFR.

Chemical evolution models have been adopted to study the evolution of the SFR during the cosmic time. First, Calura & Matteucci (2003) studied the evolution of the luminosity density in U, B, V, J, K bands and the stellar mass density of galaxies of different morphological type. They compared models and observations to obtain the number density evolution of galaxies in the context of two reference scenarios of galaxy formation: the monolithic collapse, where ellipticals and bulges formed at high redshift, as the result of a violent burst of star formation (Larson, 1974; Matteucci, 1994), and the hierarchical clustering (HC) picture, developed mainly to study the behavior of the dark matter in which small dark matter halos are the first to collapse and then merge to form larger halos in a Λ-Cold dark Matter (ΛCDM)-dominated Universe (Press & Schechter, 1974). Then, they reconstructed the history of the cosmic star formation rate (CSFR), namely the rate of SF in a unitary volume of the Universe as a function of redshift.

The work of Calura & Matteucci (2003) has been the pioneering one for the study of the cosmic rates through chemical evolution models. Later, Calura & Matteucci (2004) studied the evolution of the cosmic metallicity and computed in detail the fraction of each element locked up in stars, interstellar gas and intergalactic medium. Vincoletto et al. (2012) utilized a more precise chemo-photometric model than the one of Calura & Matteucci (2004) and studied in detail the evolution of the luminosity function of galaxies. In that work, they studied the luminosity function, namely the distribution of galaxies per unit volume in the luminosity interval [L, L + dL] (Schechter, 1976), through α and β parameters to obtain the relative distribution of galaxies of different morphological type as a function of redshift:

$$\Phi(L)\frac{dL}{L^*} = \Phi_0(1+z)^\beta \left(\frac{L}{L^*}\right)^{-\alpha} e^{-L/L*} \frac{L}{L^*}, \tag{6.1}$$

where $\Phi_0 = \Phi^*(z=0)$ is the present-day number density of galaxies per unit volume, L^* is the characteristic luminosity which separates bright sources from faint ones. They fixed the parameters (α β) to obtain the best agreement between the model predictions and the photometric curves, and finally studied the CSFR by means of such a galactic evolutionary scenario. Grieco et al. (2014) applied the same method of Vincoletto et al. (2012) to study the evolution of the dust rates, e.g. how dust evolves during the cosmic time.

The main topic of this thesis is the study of dust across the Universe, and therefore our main goal is to study the cosmic dust rate (CDR). We also intend to study the cosmic star formation rate (CSFR) and the cosmic mean metallicity (CMM), because all these three rates are strictly connected. In fact, as we have already pointed out at the beginning of this Paragraph, dust deeply influences the UV photometric light, and therefore the CSFR measurements; on the other hand, the CSFR represents a crucial phenomenon for the evolution of the metallicity, because metals originate from the stellar evolution, after star formation episodes. Finally, dust is substantially made of metals, and thanks to our models we can study the fraction of metals present in the different component of the ISM (gas and dust phase). Moreover, the CSFR has been intensively studied, and despite of large uncertainties, several observational constraints have been fixed up to redshift 8 (Hopkins, 2007; Noeske et al., 2007; Madau & Dickinson, 2014). On the other side, for the CDR we do not have observational constraints, exception for the total amount of dust in the Universe (Ω_{dust}) which is only inferred at low redshift (e.g. Fukugita, 2011; Ménard & Fukugita, 2012). For this reason, before making any predictions on the CDR or the CMM, it is extremely important to compare our models with the observed CSFR and trying to reproduce its evolutionary trend as a function of the redshift.

In this Chapter, we present our study on the cosmic rates, with noticeable improvements with respect to previous works, especially concerning interstellar dust: first, we constrain our reference models of irregular, spiral and elliptical galaxies by the comparison with the observed dust and metals in each galaxy type; second, we use a chemical evolution model with updated and detailed dust prescriptions (see Chapter 2); third, we explore more evolutionary scenarios of galaxy formation than previously done: i) a pure luminosity scenario (PLE, as in Calura & Matteucci 2003), ii) a number density evolution scenario (DE, as in Vincoletto et al. 2012), representing the classical hierarchical clustering scenario and iii) an alternative scenario, in which both spirals and ellipticals are allowed to evolve in number on an observationally motivated basis.

In Section 6.2 of this Chapter we present and summarize the chemical evolution models we adopt to describe galaxies of different morphological type (ellipticals, spirals and irregulars). Our reference model for each galaxy Type is tuned through observational constraints: in particular, we constrained our models of irregular and spiral by reproducing the relation between the dust-to-gas ratio and the metallicity. In Section 6.3 we present the results of the evolution of the CDR, CSFR and the CMM evolution. Finally, we draw our conclusions in Section 6.4.

6.2 Evolution of galaxies of different morphological type

In this Section, we present the chemical evolution models we adopt to describe galaxies of different morphological type in order to study the cosmic rates. In particular, we consider three types of galaxies: irregulars, spirals and ellipticals. In Chapter 2, we gave a detailed description of the concepts, the parameters and the equations of our chemical evolution model. Depending on the parameters, we are able to reproduce the observable features of galaxies of different morphology.

Previous works have constrained the parameters of chemical evolution models for these galaxies. Many of those also showed the effects of varying the model parameters: Bradamante et al. (1998) varied the star formation efficiency, IMF and SFH, Romano et al. (2005) - Mollá et al. (2015) the IMF, Calura et al. (2009b) the star formation efficiency, Romano et al. (2010) the stellar yields. Recently Côté et al. (2016) studied the uncertainties in galactic chemical evolution models for the Milky Way, but without making a direct comparison with observational data. Our purpose is not focused on the precise characterization of a peculiar galaxy, rather we like to find models which represent the typical behavior of different galaxies, and study their contribution to the cosmic rates (see Section 6.3). We will call *reference model*, the model of a certain galaxy type with the best set of parameters able to fit the most important physical observables related to their type.

In our approach, the main difference between galaxies is the star formation history: in ellipticals it is assumed a very fast and intense star formation rate, and this rate decreases going towards spirals, irregulars and smaller galaxies. Our prescriptions lead to a galactic evolution in which more massive galaxies have higher star formation efficiency, namely stronger episodes of star formation. This technique has been already adopted in previous work: for instance, in this way Calura et al. (2009b) reproduced the mass-metallicity relation of different galaxies.

For a detailed description of the elliptical model we refer the reader to Chapter 5, where we deeply investigated dust evolution in high redshift galaxies.
Concerning spiral galaxies, we refer to the Milky Way as a typical object. Chi-

appini et al. (1997) described the formation of our Galaxy as a result of two main infalls which gave rise first to the galactic halo and thick disk on a time-scale of ~ 1 Gyr and later to the thin disk ~ 8 Gyr. More recently, Micali et al. (2013) computed a three-infall model, where the formation of the halo, the thick disk and the thin disk are originated in three different gas accretion episodes with time-scales of $\sim 0.2, \sim 1.25$ and ~ 6 Gyr, respectively. Here, we compare our predictions with observations of galactic disks, and therefore, we decide to use a chemical evolution model which consists of a single episode of infalling material on the typical time-scale for the formation of the thin disk in the Milky Way. For this model we adopt a Scalo IMF (Scalo 1986, eq. (2.4)). This choice is based on results of previous studies on chemical abundances: in fact, it is known that a Salpeter IMF reproduces the observed chemical pattern of local ellipticals and irregulars (Pipino & Matteucci, 2004; Recchi et al., 2002), whereas it overestimates the metal content of disk-like galaxies, for which a Scalo IMF is preferred (Romano et al., 2005; Calura et al., 2009b; Romano et al., 2010).
Finally, irregular galaxies are assumed to assemble with different star formation and infalling timescales with respect to spirals (Bradamante et al., 1998; Calura et al., 2008, 2009b; Grieco et al., 2014). In particular, irregulars have a lower mass with respect to spirals and ellipticals, and therefore we assume a smaller star formation efficiency.

In Fig. 6.1 we show the star formation history of the reference models we adopt for the irregular, spiral and elliptical galaxies. The spiral galaxy is characterized by a continuous SFR which is higher than the one of irregulars. The models are able to reproduce the present day SFR observed in irregulars (Chomiuk & Povich, 2011) and spirals (Harris & Zaritsky, 2009), respectively. The SFH of the elliptical model consists of an intense burst of star formation, which stops before 1 Gyr due to the onset of galactic winds. Elliptical galaxies in the Local Universe are characterized by a quiescent phase where they lack of star formation and therefore we cannot compare the SFR between model and observation at the present time.

In Table 6.1, we summarize the main parameters of our chemical evolution models for galaxies of different morphological type. We show in the second column the mass of the infall, in the third column the time-scale of the infall, in the fourth the star formation efficiency, in the fifth the efficiency of the wind and in the sixth the adopted IMF. In column seven, we report the adopted condensation efficiencies for Type II SNe, namely the efficiency of dust production in those stars. We remind here that, depending on the assumed density of the surrounding ISM of the SN explosion, the reverse shock can destroy little or almost all the produced dust. The real effect of the reverse shock is highly uncertain and, depending on the conditions, Type II SNe can produce dust with high efficiency (δ_{HP}^{SNII}), with low efficiency (δ_{LP}^{SNII}) or with a "medium" efficiency (δ_{MP}^{SNII}), as we already shown in Chapter 2.2.1.

6.2.1 The dust-to-gas ratio in the Local Universe

In this Section we focus on the study of the dust-to-gas ratio (G/D) versus metallicity in spiral and irregular galaxies. This study has been performed in order to test how dust evolves in these galaxies by varying the parameters of the chemical evolution models.

Type	$M_{infall}[M_\odot]$	$T_{infall}[Gyr]$	$\nu[Gyr^{-1}]$	ω_i	IMF	δ^{SNII}
Irregular	10^{10}	5.0	0.2	0.7	Salpeter	δ^{SNII}_{HP}
Spiral	5×10^{10}	7.0	2.0	0.3	Scalo	δ^{SNII}_{MP}
Elliptical	10^{11}	0.3	15	10	Salpeter	δ^{SNII}_{MP}

Table 6.1: Parameters of the reference models for galaxies of different morphological type. In the first column the morphological Type is shown, in the second one the mass of the infall (in solar masses), in the third the infalling time-scale (in Gyr), in the fourth the star formation efficiency (in Gyr^{-1}), in the fifth the wind parameter, in the sixth the adopted IMF and in the seventh the efficiency of dust production by Type II SNe.

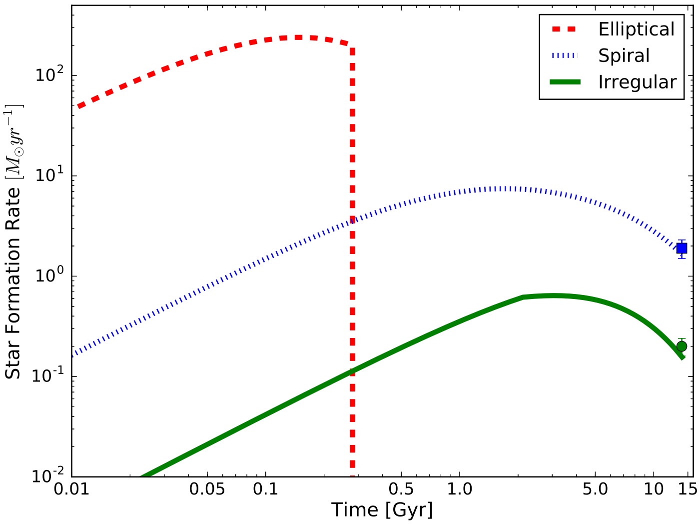

Figure 6.1: Star formation histories of the reference models for irregular (solid green), spiral (dotted blue) and elliptical (dashed red) galaxies. The SFR is expressed in unit of $M_\odot yr^{-1}$ and it is plotted as a function of the Time in Gyr. Present-time data of SFR are taken from Chomiuk & Povich (2011) (blue square) and Harris & Zaritsky (2009) (green circle) for our Galaxy and the Large Magellanic Cloud, respectively.

In fact, the dust-to-gas ratio is a very important diagnostic tools concerning dust evolution because it connects the amount of metals locked up into dust grains with the ones still present in the gas phase. The observed G/D of integrated galaxies as a function of metallicity has been intensively studied over the past decades (e.g. Issa et al., 1990; Lisenfeld & Ferrara, 1998; Hirashita et al., 2002; Draine & Li, 2007; Engelbracht et al., 2008; Galametz et al., 2011; Rémy-Ruyer et al., 2014). Generally, the dust-to-gas ratio increases as a function of metallicity, but we are still far from having a good interpretation of this relation.

Rémy-Ruyer et al. (2014) deeply investigated such a trend by providing more precise dust measurements of 160 galaxies, thanks to IRAS and Spitzer data. They used chemical evolution models to investigate the dispersion of this trend and concluded that the large observed spread results from the different histories and internal conditions of each single galaxy.

In our work, we separately consider the dust-to-gas ratio of irregular and spiral galaxies. We find that the two populations cover different regions in the dust-to-gas ratio versus metallicity space. In this way, we can separately compare the two sub-samples with detailed chemical evolution models of irregulars and spirals, in order to give a better explanation on this important relation.

Data sample

To study the observed spread in the dust-to-gas ratio, we use in our work a subsample of the Dwarf Galaxy Survey Madden et al. (2013, DGS) and the KINGFISH survey (Kennicutt et al., 2011). The information about gas and dust masses in these galaxies can be found in Rémy-Ruyer et al. (2014) and Rémy-Ruyer et al. (2015). The DGS sample consists of mostly dwarfs galaxies in the local Universe, including irregulars and blue compact dwarfs. The main physical parameters of these galaxies have been provided by Madden et al. (2013): the sample covers the low metallicity range, from $\log(O/H)+12 = 7.52$ up to 8.43. On the other hand, the KINGFISH sample contains more metal-rich galaxies, which are spirals. Contrary to previous studies, we build two subsamples, according to the different morphological type of these galaxies.

In the plots we are going to present we will refer to the metallicity of the gas based on the value of $\log(O/H) + 12$, as explained in Rémy-Ruyer et al. (2014), both in data and models. The dust masses provided by Rémy-Ruyer et al. (2015) are constrained on the basis of the spectral energy distribution of each galaxy. They provide two different values for the dust mass depending on the assumed dust species forming the carbonaceous grains: when carbon dust is assumed in form of amorphous carbonaceous grains, the dust mass is about 2.5 times lower than the one obtained by a graphite-grain model. Therefore, using different models for carbonaceous grains only modifies the absolute values of dust masses, leaving unchanged the observed trend in the dust-to-gas ratio versus metallicity. As we are mostly interested in this trend, we compare our models with the average value of the two measurements.

In the top panel of Fig. 6.2 we show the D/G data as a function of the metallicity for irregular and spiral galaxies in green pentagons and blue dots, respectively. The yellow and the green stars respectively represent the value $(D/G)_\odot$ for the solar neighborhood as predicted by Zubko et al. (2004) (BARE-GR-S model), and the one measured in the Small Magellanic Cloud by Spitzer ob-

Type	$M_{infall}[M_\odot]$	$T_{infall}[Gyr]$	$\nu[Gyr^{-1}]$	ω_i	δ_i^{SNII}
Irregular	$10^9 \leq M \leq 10^{10}$	$0.5 \leq T_{infall} \leq 10$	$0.01 \leq \nu \leq 0.2$	$0.1 \leq \omega_i \leq 1.5$	$\delta^{SNII}_{LP,\,MP,\,HP}$
Spiral	5×10^{10}	7.0	$1.0 \leq \nu \leq 3.0$	$0.1 \leq \omega_i \leq 1.0$	δ^{SNII}_{MP}

Table 6.2: Parameter ranges used in our work for the chemical evolution models of irregular and spiral galaxies. In the first column we report the morphological type of the galaxy, in the second, third, fourth and fifth columns the M_{infall}, T_{infall}, ν and ω_i, respectively. In columns six and seven we show the contribution of Type II SNe.

servations in the far-IR wavebands by Leroy et al. (2007), respectively. Finally, the black dashed line represents the reference scaling relation which assumes the D/G to increase proportionally to the inverse of the metallicity Z^{-1}, whereas the black dotted line represents the linear fit to the data as performed by Rémy-Ruyer et al. (2014). Both fits are constrained to reproduce the $(D/G)_\odot$ value of Zubko et al. (2004)

Interpretation through chemical evolution models

To study the observed spread of the dust-to-gas ratios in irregular and spiral galaxies, we vary the the parameters of our reference models shown in Table 6.2. We find that some of the studied parameters induce significant variations on the dust-to-gas ratio and metallicity.

In the top panel of Fig. 6.2 we show the model predictions in the gas-to-dust ratio versus metallicity space: the green and blue areas represent the regions occupied by models for various values of the parameters for irregulars and spirals, respectively. Irregulars mostly lie in a low metallicity range, with a median value of $[\log(O/H) + 12]_{irr} = 8.03$ and show a large spread of dust-to-gas ratio. This is mainly due to the efficiency of dust production from Type II SNe (δ^{SN}_{LP}, δ^{SN}_{MP}, or δ^{SN}_{HP}). On the other hand, the minor spread above $\log(O/H) + 12 \simeq 8.0$ is not due to dust prescriptions, but it can be attributed to the variation of the time-scale of the infall, the assumed mass of the infalling material or the efficiency of the galactic wind.

At variance with irregulars, spirals galaxies are more concentrated at higher metallicities, with a median value of $[\log(O/H) + 12]_{spi} = 8.37$. Furthermore, both models and data for spirals show a narrower dispersion of the dust-to-gas ratio with respect to irregulars. In this case, we find that the most important parameter responsible for the observed spread above $\log(O/H) + 12 = 8.4$ is the star formation efficiency. As a consequence, galaxies with the same value of dust-to-gas ratio, but different metallicities, can be interpreted as the result of the variation of the star formation rate.

In the bottom panel of Fig. 6.2 we show the models we have chosen as representative cases of each morphological type. These models represent our reference ones, and their parameters are those showed in Table 6.1. To have a better comparison between models and data, we have binned the data in metallicity: we obtained a good agreement for the irregular and the spiral models, in green dashed and blue lines, respectively, in the bottom panel of Fig. 6.2.

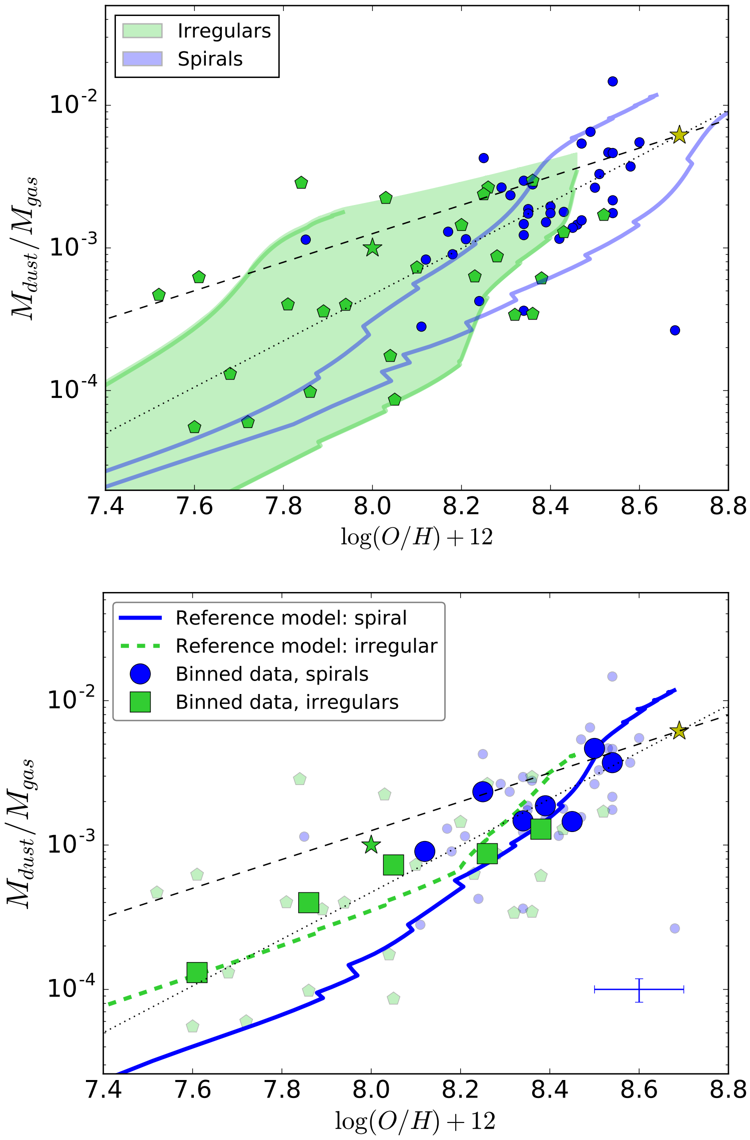

Figure 6.2: Dust-to-gas ratio versus $\log(O/H) + 12$. Data: Green pentagons correspond to irregular galaxies, whereas blue filled circles correspond to spirals. Yellow and green stars represent the dust-to-gas ratio observed in the solar neighborhood (Zubko et al., 2004) and in the Small Magellanic Cloud (Leroy et al., 2007), respectively. The dashed-black line expresses a linear relation between the dust-to-gas and the metallity, whereas the dotted straight line is the fit of the whole data sample as done in Rémy-Ruyer et al. (2014). Top panel: green and blue areas represent the possible values of dust-to-gas ratio and metallicity achievable by our models by varying the model parameters as shown in Table 6.2.1 for irregulars and spirals, respectively. Bottom panel: predictions by the reference models of a typical irregular (dashed green) and spiral (solid blue). Here, data for irregulars and spirals have been binned in metallicity, with a minimum dataset of 5 points in each bin (large green squares and blue circles, respectively). Typical errors in dust-to-gas and metallicity are expressed by the blue cross in the bottom-right corner.

6.3 Cosmic Rates

In this Section we present our study of the evolution of the cosmic star formation rate (CSFR), the CDR and the CMM rates. In general, a cosmic rate is defined as the rate in a comoving volume of the Universe: it is the result of the contribution of galaxies of different morphological type, which should be weighted according to their number density. Since now on, we will consider our models of irregular, spiral and elliptical of Table 6.1 as representative cases of each morphological type.

Our method is based on the evolution of the galaxy number density, as already adopted in previous studies involving the cosmic star formation rate (Calura & Matteucci, 2003; Vincoletto et al., 2012), the cosmic SN rates (Grieco et al., 2012; Bonaparte et al., 2013) and the cosmic dust production (Grieco et al., 2014). We assume that the maximum galaxy formation is at redshift z=10 in a Λ-cold dark matter (ΛCDM) cosmology with $H_0 = 67.7 Km\, s^{-1}\, Mpc^{-1}$ (Planck Collaboration et al., 2016), with their number density either constant or varying as a function of the redshift, according to different scenarios.

In Fig. 6.3 we present the redshift evolution of our reference models for the irregular, spiral and elliptical galaxies. The top left panel shows the SFR: the elliptical galaxy consists in an intense burst of SF, which stops before 1 Gyr of evolution due to the occurrence of galactic winds. The SFR in the initial phase is higher than the one of other types. The spiral galaxy is characterized by a continuous SFR which is higher than the one of irregulars. In the other panels of Figure 6.3, the evolution of various processes related to dust evolution (stellar production, accretion, and destruction) are shown. The stellar dust production rate (top-right panel of Fig. 6.3) shows a trend which is very similar to the SFR: this is because during the bursts, dust production from Type II SNe represent the dominant process and the rate of this kind of SNe traces the one of the star formation, because these massive stars ($M \geq 8M_{\odot}$) have short life-times ($\tau_* \leq 30 Myr$, Padovani & Matteucci 1993). The contribution of AGB stars ($M_* < 8M_{\odot}$) is mostly visible in the quiescent phases, i. e. at the end of the burst of star formation of the elliptical galaxy, because of their longer stellar life-times. In the lowest panels, the dust accretion and destruction rates are presented. In the cases of spirals and irregulars, dust production by stars has a dominant role at early epochs, while dust growth in the ISM becomes the most important process after the critical metallicity is reached[1]. In our models we found a critical metallicity of $Z_{crit,spi} = 0.31 Z_{\odot}$ and $Z_{crit,irr} = 0.19 Z_{\odot}$ for spirals and irregulars, respectively. Dust growth is strictly related to star formation, because it preferentially occurs in molecular clouds. Therefore, in the elliptical model, dust accretion stops as soon as the SF stops.

At variance with dust accretion, dust destruction never stops and it becomes the dominant process during the quiescent phases of the elliptical model, leading to a decrease of the dust mass in the galaxy, as shown in Chapter 5. In the case of irregular and spiral models, the dust destruction rate plays a marginal and negligible role with respect to other processes (accretion and stellar production).

The galaxy number density depends on the redshift and represents the rate at which galaxies have formed during the cosmic time and determines the growth

---

[1] The Critical metallicity is the metallicity at which the contribution of dust accretion overcomes the dust production by stars, see Chapter 2

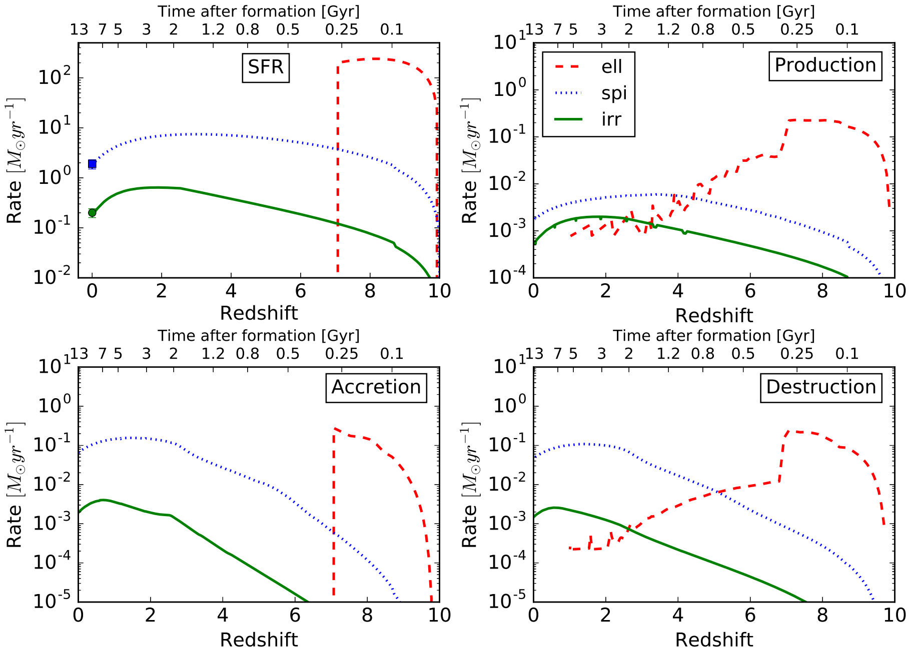

Figure 6.3: In the top left panel, the red dashed, blue dotted and green solid lines show the star formation rate as a function of time and redshift for our chemical evolution models of an elliptical, a spiral and an irregular galaxy, respectively. All galaxies are assumed to form at redshift 10. Present-time data on the SFR are taken from Chomiuk & Povich (2011) (blue square) and Harris & Zaritsky (2009) (green circle) for our Galaxy and the Large Magellanic Cloud, respectively. In clockwise sense, the other panels of the figure show the rate evolution of dust production, destruction and accretion in solar masses per year.

of baryonic structures in the Universe. The study of the cosmic rates can provide important constraints on galaxy formation mechanisms, such as the formation through the monolithic collapse (MC) or hierarchical clustering (HC). In the monolithic scenario, violent bursts of star formation originate spheroids and bulges at high redshift: massive galaxies form with higher star formation efficiencies with respect to lower ones, reproducing the "downsizing scenario" (Matteucci, 1994). On the contrary, in the HC scenario, spheroids and bulges mainly form at later epochs as a result of mergers of less massive galaxies such as spirals.

If we define n_k as the number density of galaxies of the k-th morphological type, its redshift evolution can be parametrized by the following equation:

$$n_k = n_{k,0} \cdot (1+z)^{\beta_k} \tag{6.2}$$

where $n_{k,0}$ is the number density at z=0 and β_k represents how the number density (or the luminosity function,) evolves. The parameters we adopted are shown in Table 6.3: these values have been taken from Vincoletto et al. (2012), who used a spectrophotometric code to reproduce galaxies of different morphological types and were able to constrain the slope of the luminosity function. Thanks to Eq. (6.2), we can study the cosmic rates in different scenarios: the "pure luminosity evolution" scenario (PLE), which consists in the case of no number density evolution ($\beta_k = 0$), and the "density evolution" one (DE), where the number density evolves with redshift ($\beta_k \neq 0$) as suggesting by the hierarchical clustering paradigm for galaxy formation. We also present an *alternative* scenario, based on the work of Pozzi et al. (2015) and able to best reproduce the CSFR (see next paragraph). In this scenario, the number density of spiral galaxies increases from z=0 up to z=2.3 in a similar way to the case of the DE model, but it decreases with an exponential law at higher redshifts:

$$n_S = n_0(1+z)e^{-(1+z)/2}. \tag{6.3}$$

In this context, at early cosmic times, the halo star formation phase is the dominant process in spiral galaxies, whereas the disk star formation becomes dominant at lower redshifts. In particular, in the alternative model, the disk formation is peaked at $z \sim 2$, in agreement with recent cosmological simulations (Murante et al., 2015). Concerning the number density evolution of ellipticals, Pozzi et al. (2015) used a "backward" approach to interpret of the evolution of the near-IR and the far-IR luminosity functions (LFs) across the redshift range $0 \leq z \leq 3$. The spectral evolution of spheroids were described by a single-mass model, corresponding to a present-day elliptical with a K-band luminosity comparable to the one of the break of the local early-type luminosity function. Pozzi et al. (2015) used the redshift distributions and the source counts in the near-IR and in the far-IR to constrain the main epoch of spheroid formation, finding that roughly half of them must have formed in the redshift range $2 \leq z \leq 5$ whereas the rest formed between $1 \leq z \leq 2$.

6.3.1 CSFR: Cosmic star formation rate

The cosmic star formation rate is defined as the comoving space density of the global SFR in a unitary volume of the Universe. The CSFR can be defined as:

$$CSFR = \sum_k \psi_k(t) \cdot n_k \tag{6.4}$$

Galaxy Type	$n_0\,[10^{-3}Mpc^{-3}]$	β_k
Irregular	0.6	0.0
Spiral	8.4	0.9
Elliptical	2.24	-2.5

Table 6.3: Parameters adopted for describing the evolution of the number density for galaxies of different morphological type.

where n_k and $\psi_k(t)$ are the number density (as defined in eq. 6.2) and the average star formation at the time t for galaxies of the $k-$th morphological type, respectively.

The CSFR is manly provided by the integrated light of galaxies in the rest-frame UV and IR wavebands (Kennicutt, 1998; Kennicutt & Evans, 2012). Measurements are affected by specific corrections related to the metal enrichment history or the choice of the IMF. In particular, they are deeply affected by the presence of dust, as it obscures UV region and produces IR emission (Calzetti, 2001): this correction presents several uncertainties, especially when CSFR is only inferred through UV light. At low redshifts (0<z<1), the CSFR is inferred from IR measurements, but for small comoving volumes over few independent sightlines (Madau & Dickinson, 2014, hereafter MD14). For higher redshifts, wider regions are covered, as the UV rest-frame light is visible using ground-based optical imaging (up to z$\simeq$ 4), but IR measurements are often unavailable (MD14). For these reasons, CSFR measurements should be used with caution.

Data collected in MD14 are shown in Fig. 6.4 together with the predictions of our models for the different scenarios: the data show a general increase of the CSFR from z=0 to $z \simeq 2.5$ and then a decrease until to z=8.

In the PLE model (dashed line), the CSFR shows two peaks: a first very broad one centered at $z \simeq 2-3$, and a second one centered at $z \simeq 9$ with a higher value. The latter peak is due to elliptical galaxies, which form at high redshift with strong star formation in a relatively short time-scale. As the burst of star formation ends, the CSFR decreases and spiral galaxies become the main drivers of the CSFR evolution until the present time.
On the other hand, the DE scenario presents a smoother evolution: it is in good agreement with data at $z < 3$, whereas it overestimates the observations at higher redshifts. In this case, the high redshift peak is absent because of the lower impact of elliptical galaxies, most of which form at lower redshifts by merging of spirals.
Despite of this, the CSFR still appears much higher than observations. In Fig. 6.4, we also show the CSFR as predicted in the alternative scenario in which the formation of ellipticals occurs as suggested by Pozzi et al. (2015) (dash-dotted line). Assuming this scenario for the formation of elliptical galaxies, the CSFR at high redshift ($z > 5$) is clearly dominated by spirals and a good agreement with data is obtained. At lower redshift, the combination between the formation of spirals and ellipticals leads the CSFR to peak at $z \simeq 3$, and then to decrease until $z = 0$.

We suggest the alternative model as the best scenario. In fact, the DE scenario provides a good fit to the CSFR at $z < 2$ but it predicts a too small density of ellipticals ($5.866 \times 10^5 M_\odot Mpc^{-3}$) in the Local Universe with respect to the observational estimate of Fukugita & Peebles (2004) ($1.84 \times 10^8 M_\odot Mpc^{-3}$). On the other hand, the alternative scenario provides a local stellar mass density in spheroids of $\sim 2 \times 10^8 M_\odot Mpc^{-3}$, in better agreement with observations.

As we have already pointed out, both observational and theoretical estimates of the CSFR are highly uncertain, mainly because of the complexity in performing the dust extinction correction at high redshift. However, the large discrepancy between the observed CSFR at $z > 6$ and the one predicted in the PLE can hardly be explained by these uncertainties only; it is possible that the observational data at high redshift could represent underestimates of the real values.

Some examples of CSFR measurements which substantially differ from the trend shown by the data presented here can be found in, e.g., Faucher-Giguère et al. (2008) and Kistler et al. (2009). Faucher-Giguère et al. (2008) found a nearly constant value for both the intergalactic hydrogen photo-ionization rate and the cosmic star formation density across the redshift range $2 \leq z \leq 4.2$, by analyzing the evolution of the Lyman α effective optical depth. Therefore, they found a roughly constant value of $\sim 0.2 M_\odot \ yr^{-1} \ Mpc^{-3}$ for the CSFR in this redshift range, in contrast with the most accepted decrease of MD14.
In addition, Kistler et al. (2009) measured relative higher values for the CSFR in the redshift range $6 \leq z \leq 8$ with respect to MD14. They used a sample of more than 100 Gamma Ray Bursts (GRBs) detected by *Swift* (Gehrels et al., 2004) and correlated the GRB rate with the CSFR. At such high redshift direct measurements of the star formation are quite challenging. However, GRBs offer a great opportunity to investigate the "faint" Universe and represent ideal tracers to the faint end of the galaxy luminosity function. As visible in Fig 6.4, the data of Kistler et al. (2009) (magenta dots) have systematic higher values and the decreasing trend towards higher redshifts is less steep than the one predicted by other surveys. Moreover, such data are more in agreement with both the alternative scenario and the DE one.

In conclusion, the best agreement with the observed trend of the CSFR is given by the alternative scenario based on observations. However, due to the uncertainties in the inferred CSFRs, there is still the possibility of a high-redshift evolution different than that depicted by the UV surveys. A clearer picture will hopefully be achievable in the future thanks to next generation telescopes, such as the James Webb Space Telescope, which will allow us to detect weak H transitions insensitive to dust extinction up to very high redshift (MD14).

6.3.2 Cosmic dust budget and cosmic dust rate

In this Section we present our results concerning the evolution of the global cosmic dust budget. From a theoretical perspective, an accurate assessment of the total amount of dust in the Universe is not an easy task, owing to several uncertainties related to dust formation and destruction in different environments, such as the ISM, galactic halos, the intergalactic medium and high redshift quasars (Ménard & Fukugita, 2012). An attempt to asses the global amount of dust in the Universe on a phenomenological basis was performed by Fukugita & Peebles (2004). They presented the cosmic mean density of several quantities and estimated the total amount of dust in galactic disks $\Omega_{dust} \sim 3 \times 10^{-6}$, in units of the critical density of the Universe. Similar results were obtained by

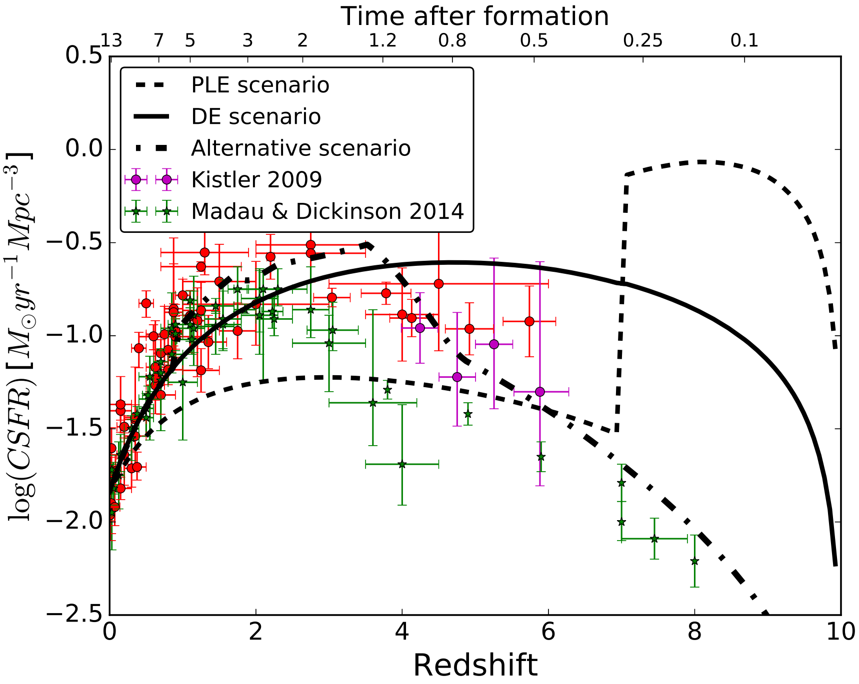

Figure 6.4: Cosmic star formation rate expressed in $[M_\odot yr^{-1} Mpc^{-3}]$ as a function of the redshift, for PLE (black dashed), DE (black solid) and for the alternative (black dash-dotted) scenarios. Green stars, red squares and magenta points data are taken from the compilation of Madau & Dickinson (2014), Hopkins (2007) and Kistler et al. (2009), respectively.

Driver et al. (2007), which analyzed the B-band attenuation of the galactic bulge and disk light of more than 10000 galaxies. Fukugita (2011) calculated the total dust mass produced by stellar sources by integrating the star formation rate as a function of the cosmic time, and found that the mass produced was higher than the total mass observed in galactic disks. Ménard & Fukugita (2012) attributed this mismatch to a missing component of dust in galactic halos. They calculated this contribution by analyzing the dust contribution present in Mg II absorbers on background quasars: these absorbers indeed provoke a significant reddening to foreground galaxies as a function of the relative angular dispersion (Ménard et al., 2010).

Another efficient method to derive constraints on the dust budget and its evolution is by studying the cosmic far infrared background (CFIRB), powered by the UV and optical emission of young stars, absorbed by the dust in galaxies and then re-emitted in the infrared (IR) wavelengths, as done by De Bernardis & Cooray (2012).

An accurate estimate of the evolution of the comoving dust mass density is the one performed by Dunne et al. (2011) by means a wide galaxy sample from the Herschel-Astrophysical Tera-hertz Large Area Survey (H-ATLAS; Eales et al. 2010). The sample, consisting of 1867 sources, includes galaxies selected at 250 μm presenting reliable counterparts in the Sloan Digital Sky Survey (SDSS) at $z < 0.5$. In the work by Dunne et al. (2011) dust masses were calculated using both a single-temperature gray-body model for the spectral energy distribution and a model with multiple temperature components, obtaining no significant differences in terms of dust temperature evolution between the two methods. Dunne et al. (2011) found a strong evolution of the dust mass density at redshifts $z \leq 0.5$.

To perform our study on the evolution of the global dust budget, in analogy with eq. (6.4) we can define the cosmic dust rate as:

$$CDR = \sum_k \{\dot{G}^{prod}_{i,dust} + \dot{G}^{acc}_{i,dust} - \dot{G}^{SFR}_{i,dust} - \dot{G}^{des}_{i,dust} - \dot{G}^{wind}_{i,dust}\} \cdot n_k \tag{6.5}$$

where the sum of the dust rates include the rate of dust production, accretion, astration by star formation, destruction and the dust loss via galactic wind.

In Fig. 6.5, we show the evolution of the comoving cosmic dust production, accretion and destruction rates in the three different scenarios.

In the PLE scenario, we obtain two distinct peaks of dust formation, as already found in the evolution of the CSFR. Either in the case of the CSFR or the CDR, the peak at high redshift ($z \sim 8$) is due to the presence of high mass elliptical galaxies, characterized by an intense star formation which is responsible for the considerable dust mass produced by stars. On the other hand, the peak at lower redshift ($z \sim 2$) is due to the efficient dust accretion rate in disk galaxies.

In the DE scenario, the peak related to the initial bursts of massive galaxies completely disappears as these objects form via merging of lower mass galaxies, for which the dust production rates are very low at high redshift. In this case, we obtain a peak at redshift $2 \leq z \leq 3$ which is higher with respect to the one of the PLE scenario. The peak visible in the DE scenario reaches approximately the value obtained by the sum of the two peaks of the PLE scenario. For this reason, the total amount of dust produced at $z \sim 0$ (see Fig. 6.6) is similar in

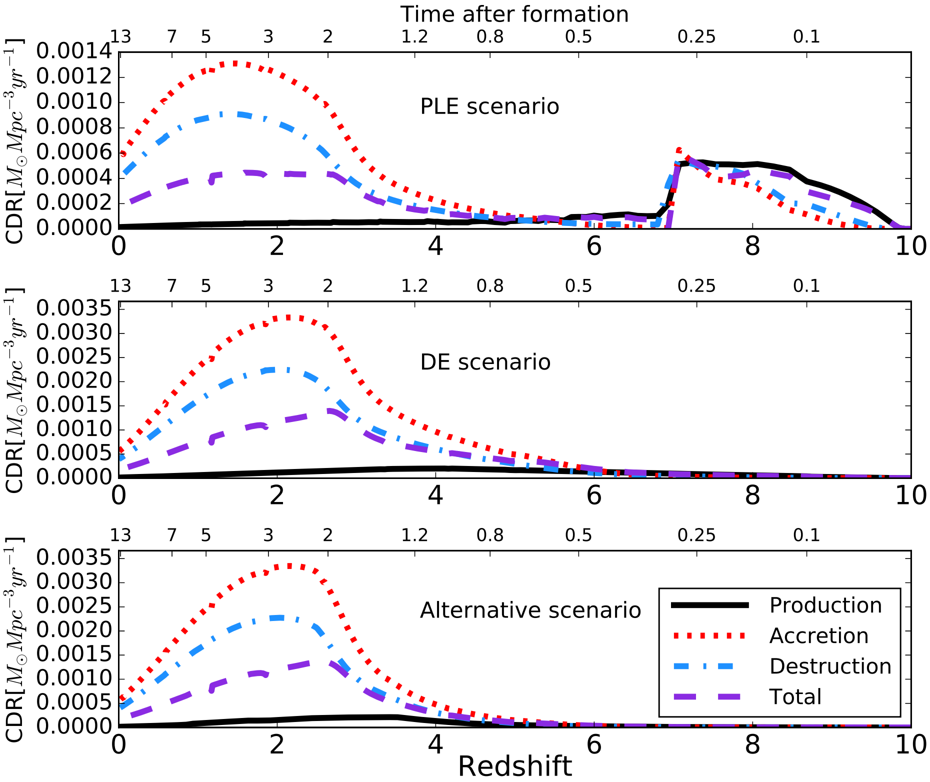

Figure 6.5: Cosmic dust rates versus redshift in the PLE (top panel), DE (middle panel) and alternative (bottom panel) scenarios. The black solid line refers to the dust production rate, the red dotted line the dust growth rate and the blue dash-dotted line is the dust destruction rate. The dashed violet line represents the total dust rate.

the two cases, although their redshift evolution is different.
On the bottom panel of Fig. 6.5, we show the results for the alternative scenario. In this case, the evolution of the total dust rate is very similar to that obtained in DE model.

The cosmic rates presented in Fig. 6.5 correspond to real predictions, because there are no available observations for these quantities. To compare our model with observations we need to estimate the total amount of dust in the Universe, which was computed in previous work on theoretical or observational approaches (Fukugita & Peebles, 2004; Fukugita, 2011; Ménard & Fukugita, 2012; Dunne et al., 2011; Popping et al., 2016; McKinnon et al., 2016). For this purpose, we calculate the comoving dust mass density as:

$$\rho_{dust} = \sum_k M_{dust,k} \cdot n_k, \tag{6.6}$$

where $M_{dust,k}$ is the average dust mass in galaxies of the k-th morphological type at a given redshift. The dust mass density parameter Ω_{dust} can then be derived by dividing ρ_{dust} by the critical density of the Universe $\rho_{cri} = 1.3 \times 10^{11}\ M_{\odot} Mpc^{-3}$ (Planck Collaboration et al., 2016).

In Fig. 6.6 we show the evolution of Ω_{dust} as a function of the redshift as calculated by means of our models, in comparison to other estimates.

In both DE and alternative scenarios, Ω_{dust} increases from $z < 6$ to $z \sim 2$, where it peaks at a value of $\sim\ 4 \times 10^{-6}$, and then it starts decreasing to a final value of $\sim 7 \times 10^{-7}$. The only difference between the DE and the alternative scenario concerns the evolution of Ω_{dust} at $z > 3$, which is slightly steeper in the latter case. This difference reflects the behavior of the CSFR, which in the redshift interval $3 \leq z \leq 8$ appears to grow more steeply in the alternative scenario than in the DE one (see Fig. 6.4).

In the PLE scenarios, the two peaks seen in the evolution of the cosmic dust rate are reflected into the Ω_{dust} vs z plot as variations in the slope. The fast increase of Ω_{dust} at redshift ~ 8 reflects the formation of elliptical galaxies, which is followed by a nearly constant evolution between $4 \leq z \leq 8$. Then a considerable growth is found at $2 \leq z \leq 4$, similarly to DE and alternative scenarios, but with lower values of Ω_{dust}. Finally, it decreases until redshift zero.

All scenarios predict present-day values of Ω_{dust} in very good agreement with the estimate obtained by Dunne et al. (2011) in local galaxies. On the other hand, the evolution of Ω_{dust} obtained in both DE and alternative scenarios are in reasonable agreement with the evolution of the dust content in H-ATLAS galaxies, whereas the PLE scenario predicts a weaker Ω_{dust} evolution than indicated by observations. It is worth to stress that the overall satisfactory agreement between predictions and observations is achieved without any further fine-tuning of the parameters of our models. One remarkable achievement is the coherency of the results obtained in the framework of the alternative and DE scenarios developed here, which allows us to simultaneously account for the evolution of the cosmic SFR and the cosmic dust budget in galaxies, even though the latter claim is valid only at redshift $z < 0.5$. The PLE scenario predicts a much weaker evolution of the dust mass density in galaxies, and this is again coherent with the results discussed in Sect. 6.3.1. This also confirms that the behavior of galaxies, as traced by multi-wavelength observations at $z < 0.5$, can only be explained with the assumption of an evolution of their number density across the same redshift range.

In Fig. 6.6, the Ω_{dust} estimates, except those of Dunne et al. (2011), are generally higher than our predictions. This is mostly because these values also account for the amount of dust present outside galaxies, i.e. in the intergalactic medium (IGM) or in galactic halos, hence they cannot be compared to our results, which pertain to the galactic dust content only. Our models do not include prescriptions about dust processing outside the galaxy. An assessment of the dust budget outside galaxies will have to account for the amount of dust and heavy elements ejected into the IGM throughout the cosmic history, as well as for the additional creation and destruction processes which may occur in the intergalactic and intra-cluster media. We also tested the case in which dust loss is taken into account, and we found that the dust fraction lost by galactic wind represents a negligible fraction with respect to the total amount inside the galaxies.

One of the most extended and comprehensive far-IR observational datasets of galaxies is the Herschel Guaranteed Time Observation (GTO) PACS Evolutionary Probe (PEP) Survey (Gruppioni et al., 2013). By means of such a dataset,

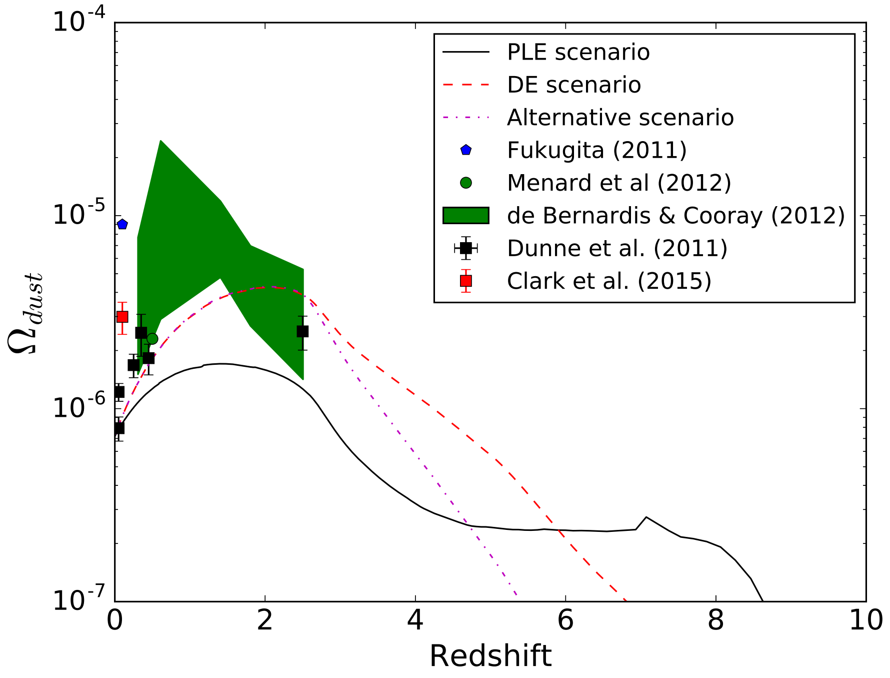

Figure 6.6: Evolution of Ω_{dust} as a function of the redshift in the PLE (black solid), DE (red dashed) and alternative scenarios. The references to the data are indicated in the box.

Gruppioni et al. (2013) studied the evolution of the far-IR galactic luminosity function up to redshift ~ 4. In such a work, a galactic counterpart was found for most of the sources (>87%), possibly leaving little room to extra-galactic emission in the far-IR and consequently to large reservoirs of dust outside galaxies.

6.3.3 Evolution of the cosmic mean metallicity

In this Section we aim at studying how the cosmic mean metallicity of the Universe evolves, in galaxies of different morphological type. This problem has been studied first by Calura & Matteucci (2003) by means of chemical and photometric models to derive the evolution of the total metal content in the Universe. Furthermore, Calura & Matteucci (2004) studied the evolution of single elements in order to compute in detail the fraction of each element locked up in stars, interstellar gas and intergalactic medium.

In this thesis, we study the metallicity evolution in connection with the evolution of the cosmic dust rate. Dust is indeed composed by metals, and we want to quantify the fraction of such metals in the gas phase and in the dust phase of the ISM. We define the cosmic mean metallicity, weighted by the galaxy number density, as in Edmunds & Phillips (1997) and Calura & Matteucci (2004):

$$CMM = \frac{\sum_k Z_k \cdot n_k}{\sum_k n_k}, \tag{6.7}$$

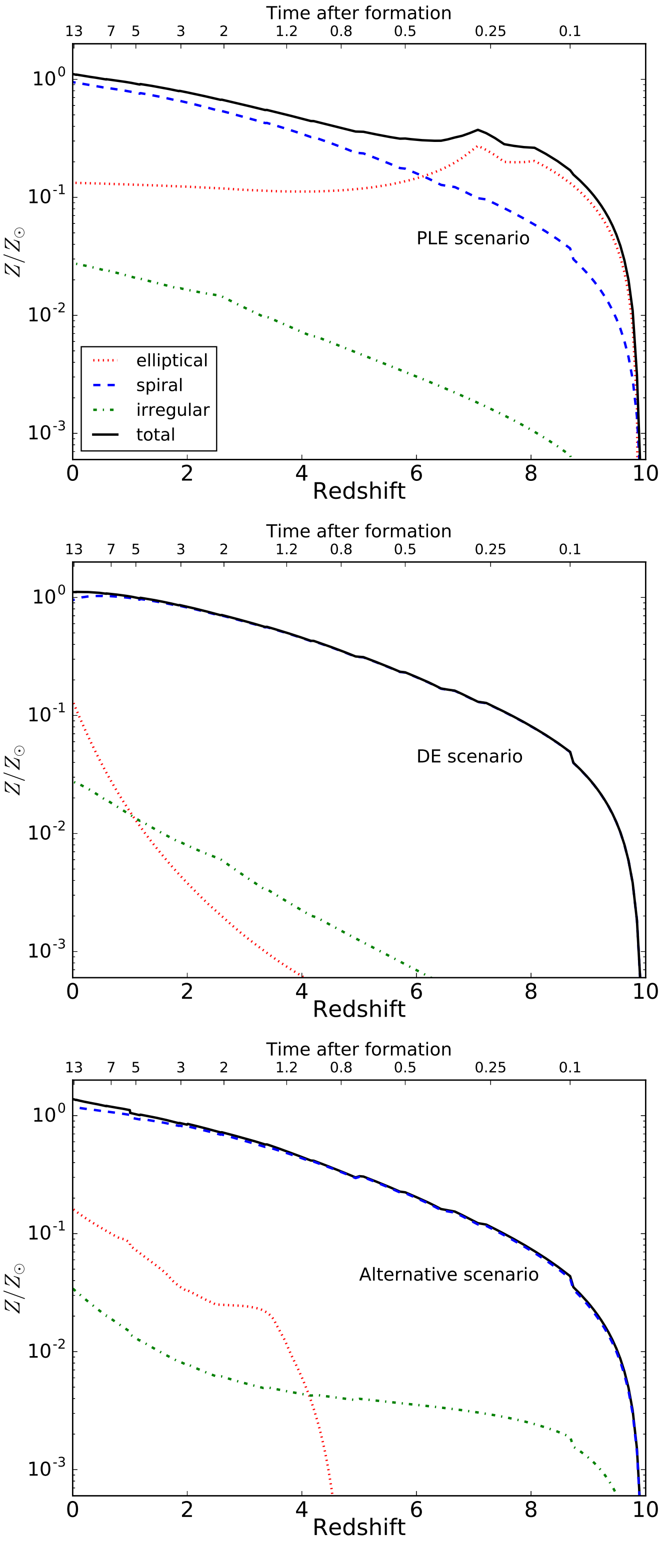

Figure 6.7: Metallicity evolution versus redshift for PLE (top panel), DE (middle panel) and the alternative (bottom panel) scenarios. Red dotted, blue dashed and green dash-dotted lines refer to the metallicity contribution of irregulars, spirals and ellipticals, respectively. Black solid line represents the total amount of metallicity as the sum of the different morphological types.

where Z_k is the average interstellar metallicity in galaxies of the $k-$th morphological type.

In Figure 6.7 we show the evolution of the cosmic mean metallicity, predicted by means of our models in the three scenarios considered in this work. In each panel of Fig. 6.7 we show also the contributions of each morphological type, defined as $\frac{n_k Z_k}{n_{tot}}$, where $n_{tot} = \sum_k n_k$. Clearly, irrespective of the chosen scenario, the CMM increases as the redshift decreases. The global increase is only marginally dependent on the galaxy evolution scenario.

In the PLE scenario, the cosmic metallicity is dominated by the contribution of elliptical galaxies at very high redshift ($z > 6$) and by the contribution of spirals at $z < 6$, with a negligible contribution from irregulars galaxies. This is the scenario characterized by the the steepest increase of the CMM, and this is a consequence of the simultaneous, rapid formation of the entire population of elliptical galaxies, beginning at $z = 10$. We find the main metal production in spheroids (ellipticals and bulges) to occur at very early times (~ 0.25 Gyr), implying an early peak in the metal production and a subsequent decrease. On the other hand, the metal production in spirals and irregulars is always increasing with time.
In the DE scenario, the CMM is always completely dominated by the contribution of spirals. In this model, both irregulars and ellipticals give a negligible contribution to the cosmic mean metallicity at any redshift.
Once again, in the alternative scenario the evolution of the CMM is similar to the one of the DE scenario, with the only difference of a larger contribution from elliptical galaxies at redshift < 4.

Our results show that the increase of the CMM is relatively fast every scenario, and that on average, already 0.25 Gyr after the onset of star formation the interstellar matter has already been enriched to a value of $\sim$ 0.1 solar. At $z = 0$ all scenarios predict a solar CMM. This confirms previous results (Calura & Matteucci, 2004) obtained on the basis of an approach very similar to the one adopted here and based on galactic chemical evolution models, estimates based on an average of the metal abundances in various components (stars and interstellar matter) in various types of galaxies (Edmunds & Phillips 1997) and mass- and volume-averaged quantities computed from the integrated spectra of large databases, such as the Sloan Digital Sky Survey (Gallazzi et al. 2008).

Our estimate of the mean interstellar metallicity discussed above does not take into account the fraction of heavy elements subtracted from the gas phase and incorporated into dust grains. This fraction is commonly expressed by the dust-to-metals ratio, defined as the ratio between the total mass in dust M_{dust} and the total interstellar mass in metals M_Z, i.e.:

$$DTM = \frac{M_{dust}}{M_z} \tag{6.8}$$

Our models for spirals and irregulars produce present-day dust-to-metal ratios $DTM_{spi} = 0.68$ and $DTM_{irreg} = 0.60$. This implies that in the local Universe, the fraction of metals which will indeed be observable in the ISM represents $\sim$ 30 − 40% of the total, and therefore the cosmic mean "undepleted" metallicity amounts to $\sim$ 0.005 and $\sim$ 0.003 in spirals and irregulars, respectively. Our estimate of the DTM_{irreg} represents a typical value observed in low-metallicity systems as analyzed by De Cia et al. (2013). Concerning elliptical galaxies, our estimate is $DTM_{ell} = 0.039$, which is lower than in spirals and irregulars and in good agreement with Calura et al. (2008).

6.4 Conclusions

In this Chapter we have presented our study on cosmic evolution of dust, star formation and metallicity. In order to calibrate the reference models of galaxies of different morphological type, we have compared our results with the amount of dust observed in irregular, spiral and elliptical galaxies.

Once we have constrained the models, we have considered three different cosmological scenarios of galaxy evolution: (i) a PLE scenario, in which the number densities of spirals, ellipticals and irregulars are anchored to their present-day values and are not allowed to vary with redshift; (ii) a DE scenario, in which the number density is assumed to evolve strongly with redshift in order to mimic a hierarchical growth, as suggested by the ΛCDM scenario; (iii) an alternative scenario based on the work of Pozzi et al. (2015), where ellipticals and spirals evolve in an observationally-motivated way. The main results can be summarized as follows:

- From the study of the dust-to-gas ratios in different galaxies we found that dust production by stars is the most important process at low metallicity, whereas it plays a negligible role at high metallicity, in agreement with previous works (Zhukovska et al. 2008; Asano et al. 2013).

- The most important parameter which can explain the spread of the dust-to-gas ratio in irregular galaxies is the dust condensation of Type II SNe, which reflects the density of the ISM in which they explode. In general, the denser the medium, the more resistance will be encountered by the SN shock and the more efficient will be the dust destruction.

- Dust formation at high redshift, in each type of galaxy, is dominated by the contribution of massive stars and also by massive AGB stars. Then, as the metallicity increases, also dust accretion plays a significant role, especially in the case of irregulars and spirals. In the case of ellipticals, dust accretion becomes inefficient as soon as the star formation stops and the galactic wind starts: therefore, the bulk of dust originates from stellar sources.

- In our analysis of the evolution of cosmic star formation, the scenario which provides the best agreement between model results and data is the alternative one, which allows us to reproduce the most up-to-date observations up to $z \sim 5$. On the other hand, within the DE scenario the agreement between model results and data is satisfactory only at $z < 2$, whereas the PLE scenario appears completely ruled out by present data. However, the reader has to be aware of the uncertainties affecting the CSFR data, especially in the high redshift Universe where the UV light should be corrected for dust extinction, and such a correction is in general highly uncertain (Madau & Dickinson, 2014).

- We predict the behavior of the dust production rate as a function of redshift in the three assumed galaxy formation scenarios. In the DE and alternative scenario, we find a peak in the cosmic dust rate in the redshift range $2 < z < 3$, while in the PLE scenario is present an additional peak at $z \sim 8$, due to the high redshift formation of ellipticals.

- In the study of the evolution of the cosmic dust rates, depending on different scenarios we find peaks at different redshifts, according to the peaks predicted in the CSFR. We find a peak at high redshift ($z \sim 8$) and one at low redshift ($z \sim 2$) in the case of the PLE scenario, as obtained in the study of the CSFR. The high redshift peak is caused by the efficient dust production in the starburst of elliptical galaxies, whereas the latter is mainly due to dust accretion in spirals. In the DE and alternative scenarios, because the number density of ellipticals becomes important at lower redshift, we only find a single peak at low redshift ($z \sim 2$).

- We compute the evolution of the comoving interstellar dust density parameter Ω_{dust}, finding a good agreement between our predictions and available data at $z < 0.5$ within the DE and alternative scenarios. Generally, our estimates of Ω_{dust} are lower than other independent measurements. We found that the dust ejected by galactic winds is negligible with respect to the one formed inside galaxies. Therefore, the discrepancy between model predictions and observations could be attributed to a possible underestimation of our models of the dust lost in the intergalactic medium, or to a possible overestimation of the global amount of dust.

- The global increase of the cosmic mean metallicity in galaxies with decreasing redshift is only marginally dependent on the adopted galaxy evolution scenario. The PLE scenario predicts a cosmic metallicity dominated by the contribution of ellipticals at very high redshift ($z > 6$), whereas spirals dominate at $z < 6$. In the alternative scenario, the evolution of the CMM is dominated by spirals and it is similar to the one of the DE scenario, with the only difference of a larger contribution from elliptical galaxies at redshift $z < 4$ in the alternative scenario.

- The increase of the CMM is fast in every scenario: on average, already ~ 0.25 Gyr after the onset of star formation, the interstellar matter has already been enriched to a metallicity of $\sim$ 0.1 solar. At $z = 0$ all scenarios predict a roughly solar CMM, confirming previous results based on galactic chemical evolution models (Calura & Matteucci 2004), and averages of the metal abundances in various components (stars and interstellar matter) in various types of galaxies (Edmunds & Phillips 1997), as well as observationally based estimates (Gallazzi et al. 2008). We predict that in star-forming galaxies of the local Universe, a large fraction of heavy elements ($\sim 60 - 70\%$) is incorporated into solid grains, therefore not observable in the gas phase.

Chapter 7

Conclusions

In this thesis we have presented a study on dust evolution in different galactic environments. We have performed our study by means of a new galactic chemical evolution model which takes into account the presence of dust and which was developed in the course of this PhD. We have adopted the most updated prescriptions for dust production from supernovae and asymptotic giant branch stars as well as for dust accretion and destruction processes. Our model has proven to be very useful to study various dust properties such as the dust mass, the dust-to-gas ratio and the gas chemical composition in galaxies of different morphological type, i.e. dwarf irregulars, spirals and ellipticals. In our approach, the main difference between galaxies is the star formation history: in ellipticals it is assumed a very fast and intense star formation rate, and this rate decreases going towards spirals, irregulars and smaller galaxies.

During this thesis we have dealt with many issues related to interstellar dust and we have tried to cast light on several problems. The discussed issues range from the study of the dust processes during the galaxy evolution to the dust chemical composition, up to the estimate of the total amount of dust in the Universe.

Here, we summarize the main results we have reached in this thesis. We divide our conclusions on the basis of the main topics we have investigated in each Chapter, namely i) how dust rates evolve during the galactic time, ii) the comparison between our model and Damped Lyman Alpha systems, iii) the role of dust in the Milky Way in the context of the Galactic Habitable Zone, iv) the study of dust evolution in galaxies of different morphological type and v) the cosmic dust rate across the Universe.

i) The dust in galactic chemical evolution models

As a first step, we have applied our chemical evolution model to the case of low-mass and low-luminosity galaxies with ongoing star formation, i.e. dwarf irregular galaxies. In particular, we have focused on the study of the dust rates (stellar production, accretion and destruction) occurring in the ISM during the galactic time to identify the most important processes that govern dust evolution. Furthermore, we have tested how some key parameters of our model not related to dust such as star formation efficiency, stellar yields and IMF, influence dust evolution. Below, we highlight the most important considerations:

- Dust accretion plays a fundamental role in the evolution of dust and in certain phases it becomes the dominant process in the ISM, in agreement with previous works. We have calculated the critical metallicity in dwarf irregular galaxies, namely the metallicity at which dust production from stellar sources becomes negligible with respect to dust growth in the ISM.

- Dust destruction represents a negligible process in dwarf irregulars, whereas the galactic wind is an important mechanism which can affect dust evolution. In fact, the galactic wind can be the main responsible for stopping the accretion process in the ISM. In particular, we have found that if the galactic wind is strong enough, the dust growth in the ISM becomes a negligible process and therefore the critical metallicity is never reached.

- We have investigated the impact of the cut-off of high mass stars (from 18 to $80 M_{\odot}$) on the chemical evolution of a typical irregular galaxy. We have failed in reproducing the metallicity values observed in dwarf irregulars when the cut-off mass is assumed to be in the range 18-$25 M_{\odot}$. Therefore, stars up to $25 M_{\odot}$ should contribute to galactic enrichment. On the other hand, we have found that it does not deeply affect the predicted range of dust-to-gas ratio.

ii) The dust composition in Damped Lyman Alpha systems

To study the chemical composition of dust in the ISM, we have undertaken a study on DLA systems. In fact, we have shown that they are particularly interesting concerning the study of the chemical evolution of dust.

DLAs are quasar absorbers characterized by a large reservoir of neutral hydrogen and lie in the redshift range $1.6 < z < 5$. They are assumed to be the progenitors of present-day dwarf galaxies and represent the best observable we have in order to investigate the faint ISM at intermediate and high redshifts. By means of high resolution spectroscopy (optical/UV) it is possible to measure the column densities of various elements and therefore measure the chemical abundances in the ISM at different redshifts, namely at different evolutionary stages.

We have compared DLA abundances with the ones predicted by our chemical evolution model of a typical dwarf irregular galaxy. In particular, to understand the chemical composition of dust, we have studied the relative abundance between volatile and refractory elements. In our work we have considered Zn and S as volatiles (elements with low condensation temperatures that preferentially stay in the gas phase of the ISM), whereas we considered Si, Mg and Fe as refractories (elements with high condensation temperatures which are mainly incorporated into dust grains).

Here we summarize the main results we obtained by comparing DLA data with our chemical evolution model results:

- By studying the abundances of volatile elements we have found that DLA systems can indeed be associated to irregular galaxies, as already suggested in previous works (Matteucci et al., 1997; Vladilo et al., 2011). In fact, the abundance pattern of the volatile elements is typical of irregular galaxies.

- The depletion pattern of Si in DLAs is well reproduced by our model. The depletion of Si increases with the metallicity and we can explain this trend by means of dust production by stars and accretion in the ISM.

- In the case of Fe, the depletion increases very rapidly with metallicity and we found a good agreement with data only when an extra dust source is considered. We performed two different tests: 1) we included dust production by Type Ia SNe, and 2) we assumed a more efficient Fe accretion in the ISM. We suggest the second option as the best one, because we obtain a better agreement with observations with respect to the first case, and because dust production from Type Ia SNe is not supported by observational evidences.

- The different behavior of Fe and Si brings new evidence that a significant fraction of iron should be incorporated into a dust population different from silicates, as suggested by previous works. It is possible that such an iron-rich species could originate in a different way with respect to silicates: in particular, our results are consistent with a metallicity-dependent accretion of iron nano-particles, in agreement with other independent works (Draine & Hensley, 2012, 2013).

- In this thesis we have also developed and presented a new method to estimate the element-to-element abundance ratios inside dust grains. This technique is very important, because it provides the chemical composition of dust grains in the ISM of DLAs, which is an information impossible to obtain with standard optical/UV spectroscopy. We have studied the evolution of the abundance ratios of Si/Fe and Mg/Fe as functions of the metallicity and we interpreted the observed trends by means of a new model of grain composition and our chemical evolution model.

- We have found that the ratios of Si/Fe and Mg/Fe abundances in the dust phase decrease with increasing metallicity. This suggests, that the chemical abundances inside dust grains approximately follow the variation of the abundances in the ISM.

- We have found a good agreement between the dust abundance ratios we derived from observations and the ones predicted by our chemical evolution model with dust. We have shown that the evolution in metallicity of the dust abundance ratios of (Si/Fe) and (Mg/Fe) can be divided in two regions, dominated by different dust processes. In the low-metallicity region, Type II SNe represent the most important dust source. In the metal-rich region ($[Fe/H] > -0.6$), dust accretion is the most important process and the trend in metallicity becomes steeper. The reason of this transition strengthen the fact that Fe-rich dust preferably forms by growth in the ISM than in the stellar ejecta.

- We have interpreted the observed dust chemical composition on the basis of a simple model of grain composition whose parameters are: α, which represents the fraction between pyroxenes and olivines in silicates, μ, that represents the fraction of Fe-rich dust out of silicates, x and y which indicate the Mg-rich composition of pyroxenes and olivines, respectively. When those parameters are kept constant, on the basis of observational studies, it is impossible to reproduce the observed trend. On the other hand, we have obtained a good agreement when we have varied the parameters according to the elemental abundances predicted by our chemical evolution models.

- We have studied the relative fraction of pyroxenes and olivines in silicates. We obtained the best agreement with observations, when a dust composition made of olivines is adopted, with a negligible fraction of pyroxenes. Our result is in agreement with other studies, where astronomical observations are strengthened by laboratory experiments on silicates (Xie et al., 2017; Zeegers et al., 2017).

Dust in the context of the Galactic Habitable Zone

During this work, we have implemented the updated dust prescriptions in a chemical evolution model which has been specifically adopted to study the Milky Way (Chiappini et al., 2001; Spitoni & Matteucci, 2011). In this model, the Galaxy is assumed to have formed by means of two main infall episodes: the first formed the halo and the thick disk components, whereas the second the thin disk one.

In this thesis, we have used this Galactic model in the context of the Galactic Habitable Zone (GHZ), which is defined as the region in the Galaxy with highly enough metallicity to allow the formation of planetary systems capable of sustaining life (Gonzalez et al., 2001). In this study, we have adopted the most updated prescriptions for the probabilities of finding terrestrial planets and gas giants around FGK and M stars. These probabilities depend on the metallicity of the host stars, and originate from the statistical study of planetary frequencies around stars of different types and properties (Gaidos & Mann, 2014; Zackrisson et al., 2016).

Dust plays a very important role in the study of planetary formation: in fact, it represents the necessary building block to form more massive and extended objects (planetesimals) that eventually accrete to form planets. In particular, the dust-to-gas ratio is a fundamental parameter, adopted in models of planetary systems formation. By means of our model, we can connect the dust-to-gas ratio (a fundamental parameter used in models) to the metallicity [Fe/H] (an observable of the host stars).

Here, we summarize our main results concerning the study of the GHZ in the Milky Way:

- We have shown that the largest number of FGK and M stars with habitable planets are found in the solar neighborhood, i.e. in the annular region between 7 and 9 kpc from the Galactic center.

- At the present time, the total number of M stars with habitable terrestrial planets without gas giant planets are $\simeq 10$ times the number of FGK stars.

- Thanks to the multi-zone model of the Milky Way, we have found that the dust mass changes with the Galactocentric distance. In particular, it decreases as the distance from the Galactic center increases.

- The probabilities that a FGK or M star could host habitable planets are roughly identical. Slight differences arise only at Galactic times longer than 9 Gyr, when the probability of finding gas giant planets around FGK stars becomes substantially lower than the probability associated to M stars.

- We provide a useful theoretical tool to set the proper initial condition for the formation of protoplanetary disks by connecting the evolution of the dust-to-gas ratios at different Galactocentric distances with the chemical enrichment expressed in terms of [Fe/H]. In particular, we have computed a linear relation between the dust-to-gas ratio and the metallicity of the ISM, valid for the solar neighborhood.

iv) Dust evolution in galaxies of different morphology

We have studied dust properties in galaxies of different morphological type, i.e. irregular, spiral and elliptical galaxies. The key parameters of the chemical evolution models for each galaxy type have been fixed on the basis of previous works, able to reproduce the main observable features of these galaxies (e.g. Chiappini et al., 2001; Pipino & Matteucci, 2004; Calura et al., 2009b; Romano et al., 2010). In this work, we have constrained some of the parameters related to dust by means of observations in different environments. Concerning irregulars and spirals, we mainly studied the relation between the dust-to-gas ratio and their metallicity. This relation is very important for our models, because it connects the metallicity (a fundamental observable for chemical evolution models) to the fraction of embedded metals in the dust phase of the ISM. For what concern ellipticals, we have investigated how dust forms in the initial burst of star formation of these galaxies and we compared the total mass of dust produced with the one observed in high redshift systems.

Below, we highlight the most important considerations about the dust evolution in galaxies of different morphological type:

- Our models of irregulars and spirals can reproduce the observed dust-to-gas ratio: we found that irregular galaxies show a large spread of this quantity in the low metallicity range ($7.5<\log(O/H)+12<8.0$), whereas spirals have a narrower dispersion mainly concentrated at higher metallicities. The most important parameter which regulates the spread of the dust-to-gas ratio in irregular galaxies is the adopted dust condensation efficiency of Type II SNe, which reflects the density of the ISM in which they explode.

- Our model of a typical elliptical, which suffer a strong and short starburst of early times, provides a consistent amount of dust ($> 10^7 M_\odot$) at intermediate redshift ($5<z<7$), in agreement with current observations. In particular, the dust mass formation in ellipticals increases very fast in the initial burst of star formation, and the bulk of dust is already settled after 250 Myr. We have found that the main driver for this rapid increase is the dust production from Type II SNe, whereas the accretion process becomes important only on longer time-scales.

- We also tested the effect of including in our model the dust production from Type Ia SNe. In this case, using Dwek's (1998) prescriptions, we found that they strongly contribute to the total dust mass produced, and they also exceed the contribution of AGB stars. In particular, in the case of a typical elliptical galaxy, the contribution of such stars is extremely important in the quiescent phases, after the onset of the galactic wind.

- We found that AGB stars contribute to the total stellar production in the initial burst less than Type II SNe. However, we have shown that the peak of the AGB death rate occurs before the onset of the galactic wind Therefore, the lower dust contribution of AGB stars with respect to Type II SNe is not due to the involved stellar life-times, but strongly depends on the adopted condensation efficiencies.

v) The cosmic dust rate

We have studied the cosmic dust rate across the Universe by assuming that the cosmic dust abundance results from the contribution of galaxies of different morphological type averaged in a unitary volume of the Universe. We have assumed as maximum redshift of galaxy formation z=10 and we varied their number density across the cosmic time on the basis of three different scenarios of galaxy formation and evolution: 1) a pure luminosity scenario (PLE) in which the number densities of spirals, ellipticals and irregulars are constant, 2) a number density evolution scenario (DE), as suggested by the classical hierarchical clustering scenario in the framework of the ΛCDM paradigm, and 3) an alternative scenario, where the number densities of ellipticals and spirals evolve in an observationally-motivated way (Pozzi et al., 2015).

In our work, we have studied the cosmic rates of: star formation (CSFR), dust (CDR) and mean metallicity (CMM). These rates are strictly connected: in fact, the presence of dust deeply influences the measurements of the star formation rate, which determines the evolution of metals, which represent the primary constituents of the interstellar dust.

- On the study of the CSFR.
  The PLE model predicts a peak of the CSFR at high redshift ($z \sim 8$) due to the formation of elliptical galaxies and another one at lower redshift ($z \sim 2$). The PLE scenario fails in reproducing the observed CSFR because it over-estimates the CSFR at high redshifts and under-estimates it at lower redshifts. The DE scenario produces a smooth evolution for the CSFR which is in agreement with observations only in the redshift range between $0 < z < 4$. Finally, we have shown that the alternative scenario reproduces the CSFR from redshift 0 up to redshift 8 much better than the previous scenarios.

- On the study of the CDR.
  Depending on different scenarios we have found peaks at different redshifts, according to the peaks we mentioned in the case of the CSFR. In the case of the PLE scenario, we have found a peak at high redshift ($z \sim 8$), caused by dust production in ellipticals, and one at low redshift ($z \sim 2$), due to dust accretion in spirals. In the DE and alternative scenarios, because the number density of massive ellipticals at high redshift is negligible, we only find the single peak at redshift ($z = 2$).

- On the study of the CMM.
  The global increase of the CMM in galaxies with decreasing redshift is

only marginally dependent on the adopted galaxy number density scenario. The PLE scenario predicts a cosmic metallicity dominated by the contribution of ellipticals at very high redshift ($z > 6$), whereas spirals dominate at $z < 6$. In the DE scenario, the evolution of the CMM is almost always dominated by spiral galaxies. The alternative scenario is similar to the DE one and only differs by a larger contribution from elliptical galaxies at redshift $z < 4$.
We have found that in star-forming galaxies of the Local Universe a large fraction of heavy elements ($\sim 60-70\%$) should be incorporated into solid grains.

- We have computed the evolution of the comoving interstellar dust density parameter Ω_{dust}, finding a good agreement between our predictions and available data at $z < 0.5$ within the DE and alternative scenarios.

- Our study suggests the alternative scenario based on observations as the best one. In fact, with this scenario we have been able to reproduce simultaneously both the observed star formation rate and the total dust mass (Ω_{dust}) during the cosmic time.

List of publications

- Gioannini, L., Matteucci, F., Vladilo, G., & Calura, F. "*A new galactic chemical evolution model with dust: results for dwarf irregular galaxies and DLA systems*", 2017, MNRAS, 464, 985
- Spitoni, E., Gioannini, L., & Matteucci, F. "*Galactic habitable zone around M and FGK stars with chemical evolution models that include dust*", 2017, A&A, 605, A38
- Gioannini, L., Matteucci, F., & Calura, F. "*The cosmic dust rate across the Universe*", 2017, MNRAS, 471, 4615

Bibliography

Abbott, B. P., Abbott, R., Abbott, T. D., et al. 2016, Physical Review Letters, 116, 061102

Abel, T., Bryan, G. L., & Norman, M. L. 2002, Science, 295, 93

Agladze, N. I., Sievers, A. J., Jones, S. A., Burlitch, J. M., & Beckwith, S. V. W. 1996, ApJ, 462, 1026

Aguirre, A. 1999, ApJ, 525, 583

Alexander, R., Pascucci, I., Andrews, S., Armitage, P., & Cieza, L. 2014, Protostars and Planets VI, 475

Aller, M. C., Kulkarni, V. P., York, D. G., et al. 2014, arXiv:1405.0426

Aller, M. C., Kulkarni, V. P., York, D. G., et al. 2014, ApJ, 785, 36

Altobelli, N., Kempf, S., Krüger, H., et al. 2005, Journal of Geophysical Research (Space Physics), 110, A07102

Anders, E., & Grevesse, N. 1989, Geochimica Cosmochimica Acta, 53, 197

Aoyama, S., Hou, K.-C., Shimizu, I., et al. 2017, MNRAS, 466, 105

Armitage, P. J. 2003, ApJL, 582, L47

Armitage, P. J. 2013, Astrophysics of Planet Formation, by Philip J. Armitage, Cambridge, UK: Cambridge University Press, 2013,

Asano, R. S., Takeuchi, T. T., Hirashita, H., & Nozawa, T. 2013, MNRAS, 432, 637

Asplund, M., Grevesse, N., & Sauval, A. J. 2005, Cosmic Abundances as Records of Stellar Evolution and Nucleosynthesis, 336, 25

Asplund, M., Grevesse, N., Sauval, A. J., & Scott, P. 2009, ARA&A, 47, 481

Ballero, S. K., Matteucci, F., Origlia, L., & Rich, R. M. 2007, A&A, 467, 123

Baguhl, M., Grün, E., & Landgraf, M. 1996, Space Sci. Rev., 78, 165

Beelen, A., Cox, P., Benford, D. J., et al. 2006, ApJ, 642, 694

Bekki, K. 2013, MNRAS, 432, 2298

Bekki, K. 2015, ApJ, 799, 166

Bell, E. F., Papovich, C., Wolf, C., et al. 2005, ApJ, 625, 23

Berger, E., Zauderer, B. A., Chary, R.-R., et al. 2014, ApJ, 796, 96

Berné, O., Joblin, C., Deville, Y., et al. 2007, A&A, 469, 575

Bertoldi, F., Carilli, C. L., Cox, P., et al. 2003, A&A, 406, L55

Bianchi, S., & Schneider, R. 2007, MNRAS, 378, 973

Bianchi, S., Schneider, R., & Valiante, R. 2009, Cosmic Dust - Near and Far, 414, 65

Blair, W. P., Ghavamian, P., Long, K. S., et al. 2007, ApJ, 662, 998

Bocchio, M., Jones, A. P., & Slavin, J. D. 2014, A&A, 570, A32

Bocchio, M., Bianchi, S., Hunt, L. K., & Schneider, R. 2016, A&A, 586, A8

Bohlin, R. C., Savage, B. D., Drake, J. F. 1978, ApJ, 224, 132

Bonaparte, I., Matteucci, F., Recchi, S., et al. 2013, MNRAS, 435, 2460

Boss, A. P. 2002, ApJ, 567, L149

Boudet, N., Mutschke, H., Nayral, C., et al. 2005, ApJ, 633, 272

Bower, R. G., Lucey, J. R., & Ellis, R. S. 1992, MNRAS, 254, 589

Bradamante, F., Matteucci, F., & D'Ercole, A. 1998, A&A, 337, 338

Brown, L. M., Pais, A., & Pippard, B. 1995, Philadelphia, PA: Institute of Physics Pub., and New York: American Institute of Physics Press, |c1995, edited by Brown, Laurie M.; Pais, Abraham; Pippard, Brian,

Brown, J. M., & Woosley, S. E. 2013, ApJ, 769, 99

Buchhave, L. A., Latham, D. W., Johansen, A., et al. 2012, Nature, 486, 375

Calura, F., Matteucci, F., & Vladilo, G. 2003, MNRAS, 340, 59

Calura, F., & Matteucci, F. 2004, MNRAS, 350, 351

Calura, F., Matteucci, F., & Tozzi, P. 2007, MNRAS, 378, L11

Calura, F., Pipino, A., & Matteucci, F. 2008, A&A, 479, 669

Calura, F., Dessauges-Zavadski, M., Prochaska, J. X., & Matteucci, F. 2009a, ApJ, 693, 1236

Calura, F., Pipino, A., Chiappini, C., Matteucci, F., & Maiolino, R. 2009, A&A, 504, 373

Calura, F., Gilli, R., Vignali, C., et al. 2014, MNRAS, 438, 2765

Calura, F., Pozzi, F., Cresci, G., et al. 2017, MNRAS, 465, 54

Calura, F., Matteucci, F., 2003, ApJ, 596, 734

Calura, F., & Matteucci, F. 2006, MNRAS, 369, 465

Calzetti, D. 2001, PASP, 113, 1449

Carigi, L., García-Rojas, J., & Meneses-Goytia, S. 2013, Rev. Mex. Astron. Astrofis., 49, 253

Carilli, C. L., Bertoldi, F., Rupen, M. P., et al. 2001, ApJ, 555, 625

Carilli, C. L., & Walter, F. 2013, ARA&A, 51, 105

Casasola, V., Cassarà, L. P., Bianchi, S., et al. 2017, A&A, 605, A18

Centurión, M., Bonifacio, P., Molaro, P., & Vladilo, G. 2000, ApJ, 536, 540

Cescutti, G. 2008, A&A, 481, 691

Chabrier, G. 2003, ApJ, 586, L133

Chiaki, G., Marassi, S., Nozawa, T., et al. 2015, MNRAS, 446, 2659

Chiappini, C., Matteucci, F., & Gratton, R. 1997, ApJ, 477, 765

Chiappini, C., Matteucci, F., & Romano, D. 2001, ApJ, 554, 1044

Chomiuk, L., & Povich, M. S. 2011, AJ, 142, 197

Christensen, L., Møller, P., Fynbo, J. P. U., & Zafar, T. 2014, MNRAS, 445, 225

Clark, C. J. R., Dunne, L., Gomez, H. L., et al. 2015, MNRAS, 452, 397

Clayton, D. D., & Nittler, L. R. 2004, ARA&A, 42, 39

Cooke, R., Pettini, M., Steidel, C. C., Rudie, G. C., & Nissen, P. E. 2011, MNRAS, 417, 1534

Cooke, R. J., Pettini, M., & Jorgenson, R. A. 2015, ApJ, 800, 12

Cooke, R. J., Pettini, M., & Steidel, C. C. 2017, MNRAS, 467, 802

Cooray, A., Calanog, J., Wardlow, J. L., et al. 2014, ApJ, 790, 40

Costantini, E., Freyberg, M. J., & Predehl, P. 2005, A&A, 444, 187

Côté, B., Ritter, C., O'Shea, B. W., et al. 2016, ApJ, 824, 82

Coupeaud, A., Demyk, K., Meny, C., et al. 2011, A&A, 535, A124

Crinklaw, G., Federman, S. R., & Joseph, C. L. 1994, ApJ, 424, 748

Danziger, I. J., Bouchet, P., Gouiffes, C., & Lucy, L. B. 1991, The Magellanic Clouds, 148, 315

Davies, J. I., Baes, M., Bianchi, S., et al. 2017, PASP, 129, 044102

Dayal, P., Ferrara, A., & Saro, A. 2010, MNRAS, 402, 1449 de Bennassuti, M., Schneider, R., Valiante, R., & Salvadori, S. 2014, MNRAS, 445, 3039

De Bernardis, F., & Cooray, A. 2012, ApJ, 760, 14

De Cia, A., Ledoux, C., Savaglio, S., Schady, P., & Vreeswijk, P. M. 2013, A&A, 560, A88

De Cia, A., Ledoux, C., Mattsson, L., et al. 2016, A&A, 596, A97

Dell'Agli, F., García-Hernández, D. A., Ventura, P., et al. 2015, MNRAS, 454, 4235

Dell'Agli, F., García-Hernández, D. A., Schneider, R., et al. 2017, MNRAS, 467, 4431

Desert, F.-X., Boulanger, F., & Puget, J. L. 1990, A&A, 237, 215

Dessauges-Zavadsky, M., Péroux, C., Kim, T.-S., D'Odorico, S., & McMahon, R. G. 2003, MNRAS, 345, 447

Dessauges-Zavadsky, M., Calura, F., Prochaska, J. X., D'Odorico, S., & Matteucci, F. 2007, A&A, 470, 431

Draine, B. T. 2003, ARA&A, 41, 241

Draine, B. T., & Hensley, B. 2012, ApJ, 757, 103

Draine, B. T., & Hensley, B. 2013, ApJ, 765, 159

Draine, B. T., & Lee, H. M. 1984, ApJ, 285, 89

Draine, B. T., & Lee, H. M. 1984, ApJ, 285, 89

Draine, B. T., & Li, A. 2007, ApJ, 657, 810

Dressing, C. D., & Charbonneau, D. 2013, ApJ, 767, 95

Dressing, C. D., & Charbonneau, D. 2015, ApJ, 807, 45

Driver, S. P., Popescu, C. C., Tuffs, R. J., et al. 2007, MNRAS, 379, 1022

Dullemond, C. P., & Dominik, C. 2005, A&A, 434, 971

Dunne, L., Eales, S., Ivison, R., Morgan, H., & Edmunds, M. 2003, Nature, 424, 285

Dunne, L., et al., 2011, MNRAS, 417, 1510

Dwek, E. 1998, ApJ, 501, 643

Dwek, E. 2004, ApJ, 611, L109

Dwek, E. 2004, ApJ, 607, 848

Dwek, E. 2004, ApJ, 611, L109

Dwek, E. 2005, The Spectral Energy Distributions of Gas-Rich Galaxies: Confronting Models with Data, 761, 103

Dwek, E. 2016, ApJ, 825, 136

Dwek, E., & Cherchneff, I. 2011, ApJ, 727, 63

Dwek, E., Galliano, F., & Jones, A. P. 2007, ApJ, 662, 927

Dwek, E., & Scalo, J. M. 1980, ApJ, 239, 193

Eales S., at al., 2010, PASP, 122, 499

Edmunds, M. G., Phillips, S., 1997, MNRAS, 292, 733

Engelbracht, C. W., Rieke, G. H., Gordon, K. D., et al. 2008, ApJ, 678, 804-827

Fanciullo, L., Guillet, V., Jones, A., et al. 2013, Proceedings of The Life Cycle of Dust in the Universe: Observations, Theory, and Laboratory Experiments (LCDU2013). 18-22 November, 2013. Taipei, Taiwan.

Faucher-Giguère, C.-A., Prochaska, J. X., Lidz, A., Hernquist, L., & Zaldarriaga, M. 2008, ApJ, 681, 831-855

Ferrara, A., Viti, S., & Ceccarelli, C. 2016, MNRAS, 463, L112

Ferrarotti, A. S., & Gail, H.-P. 2006, A&A, 447, 553

Ferrière, K. M. 2001, Reviews of Modern Physics, 73, 1031

Field, G. B. 1974, ApJ, 187, 453

Fischer, D. A., Valenti J., 2005, ApJ, 622, 1102

Fogerty, S., Forrest, W., Watson, D. M., Sargent, B. A., & Koch, I. 2016, ApJ, 830, 71

Forgan, D., Dayal, P., Cockell, C., & Libeskind, N. 2017, International Journal of Astrobiology, 16, 60

François, P., Matteucci, F., Cayrel, R., et al. 2004, A&A, 421, 613

Fryer, C. L. 1999, ApJ, 522, 413

Fukugita, M. 2011, arXiv:1103.4191

Fukugita, M., & Peebles, P. J. E. 2004, ApJ, 616, 643

Fumagalli, M., O'Meara, J. M., & Prochaska, J. X. 2016, MNRAS, 455, 4100

Fynbo, J. P. U., Laursen, P., Ledoux, C., et al. 2010, MNRAS, 408, 2128

Gaidos, E., & Mann, A. W. 2014, ApJ, 791, 54

Gammie, C. F. 1996, ApJ, 457, 355

Gail, H.-P., Zhukovska, S. V., Hoppe, P., & Trieloff, M. 2009, ApJ, 698, 1136

Galametz, M., Madden, S. C., Galliano, F., et al. 2011, A&A, 532, A56

Gall, C., Andersen, A. C., & Hjorth, J. 2011, A&A, 528, A14

Gallazzi,A., Brinchmann, J., Charlot, S., White, S. D. M., 2008, MNRAS, 383, 1439

Gall, C., Hjorth, J., & Andersen, A. C. 2011, A&ARv, 19, 43

Galliano, F., Madden, S. C., Jones, A. P., Wilson, C. D., & Bernard, J.-P. 2005, A&A, 434, 867

Galliano, F., Hony, S., Bernard, J.-P., et al. 2011, A&A, 536, A88

Garnett, D. R., & Shields, G. A. 1987, ApJ, 317, 82

Gehrels, N., Laird, C. M., Jackman, C. H., et al., 2003, ApJ, 585, 1169

Gehrels, N., Chincarini, G., Giommi, P., et al. 2004, ApJ, 611, 1005

Gilmore, G., Wyse, R. F. G., Kuijken, K. 1989, ARA&A, 27, 555

Ginolfi, M., Graziani, L., Schneider, R., et al. 2017, arXiv:1707.05328

Gioannini, L., Matteucci, F., Vladilo, G., & Calura, F. 2017, MNRAS, 464, 985

Gioannini, L., Matteucci, F., & Calura, F. 2017, MNRAS, 471, 4615

Gobat, R., & Hong, S. E. 2016, A&A, 592, A96

Goldreich, P., & Ward, W. R. 1973, ApJ, 183, 1051

Gomez, H. 2013, Proceedings of The Life Cycle of Dust in the Universe: Observations, Theory, and

Gomez, H. L., Krause, O., Barlow, M. J., et al. 2012, ApJ, 760, 96

Gonzalez, G. 1997, MNRAS, 285, 403

Gonzalez, G., Brownlee, D., & Ward, P. 2001, Icarus, 152, 185

Gonzalez, G. 2005, Origins of Life and Evolution of the Biosphere, 35, 555

González-López, J., Riechers, D. A., Decarli, R., et al. 2014, ApJ, 784, 99

Gordon, K. D., Clayton, G. C., Misselt, K. A., Landolt, A. U., & Wolff, M. J. 2003, ApJ, 594, 279

Granato, G. L., Lacey, C. G., Silva, L., et al. 2000, ApJ, 542, 710

Grebel, E. K. 2004, Origin and Evolution of the Elements, 234

Grieco, V., Matteucci, F., Meynet, G., et al. 2012, MNRAS, 423, 3049

Grieco, V., Matteucci, F., Calura, F., et al. 2014, MNRAS, 444, 1054

Grun, E., Zook, H. A., Baguhl, M., et al. 1993, Nature, 362, 428

Gruppioni, C., Pozzi, F., Rodighiero, G., et al. 2013, MNRAS, 432, 23

Hallenbeck, S. L., Nuth, J. A., III, & Nelson, R. N. 2000, ApJ, 535, 247

Hanish, D. J., Meurer, G. R., Ferguson, H. C., et al. 2006, ApJ, 649, 150

Harris, J., & Zaritsky, D. 2009, AJ, 138, 1243

Hart, M. H. 1979, Icarus, 37, 351

Hirashita, H. 2000, PASJ, 52, 585

Hirashita, H., Hunt, L. K., & Ferrara, A. 2002, MNRAS, 330, L19

Hirashita, H., & Ferrara, A. 2002, MNRAS, 337, 921

Hirashita, H., Tajiri, Y. Y., & Kamaya, H. 2002, A&A, 388, 439

Hirashita, H., Kaneda, H., Onaka, T., & Suzuki, T. 2008, PASJ, 60, S477

Hirashita, H. 2013, Proceedings of The Life Cycle of Dust in the Universe: Observations, Theory, and Laboratory Experiments (LCDU2013),

Hirashita, H., Ferrara, A., Dayal, P., & Ouchi, M. 2014, MNRAS, 443, 1704

Hirashita, H. 2015, MNRAS, 447, 2937

Hirashita, H., Nozawa, T., Asano, R. S., & Lee, T. 2016, Planet. Space Sci., 133, 17

Hollenbach, D., & Salpeter, E. E. 1971, ApJ, 163, 155

Hopkins, A. M. 2004, ApJ, 615, 209

Hopkins, A. M. 2007, ApJ, 654, 1175

Huang, S.-S. 1959, American Scientist, 47, 397

Hoyle, F., & Wickramasinghe, N. C. 1962, MNRAS, 124, 417

Hoyle, F., & Wickramasinghe, N. C. 1969, Nature, 223, 459

Hoyle, F., & Wickramasinghe, N. C. 1999, Ap&SS, 268, 77

Inoue, A. K. 2011, Earth, Planets, and Space, 63, 1027

Issa, M. R., MacLaren, I., & Wolfendale, A. W. 1990, A&A, 236, 237

Iwamoto, K., Brachwitz, F., Nomoto, K., et al. 1999, ApJS, 125, 439

Jenkins, E. B. 2009, ApJ, 700, 1299

Jenkins, E. B. 2014, arXiv:1402.4765

Jones, A. P. 2000, J. Geophys. Res., 105, 10257

Jones, A. 2013, Proceedings of The Life Cycle of Dust in the Universe: Observations, Theory, and Laboratory Experiments (LCDU2013). 18-22 November, 2013. Taipei, Taiwan.

Jones, A. 2014, arXiv:1411.6666

Jones, A. P., Tielens, A. G. G. M., Hollenbach, D. J., & McKee, C. F. 1994, ApJ, 433, 797

Johnson, J. A., Aller, K. M., Howard, A. W., & Crepp, J. R. 2010, PASP, 122, 905

Johnson, J. L., Li H., 2012, ApJ, 751, 81

Junkkarinen, V. T., Cohen, R. D., Beaver, E. A., et al. 2004, ApJ, 614, 658

Kapteyn, J. C. 1909, ApJ, 30, 284

Karakas, A. I. 2010, MNRAS, 403, 1413

Kemper, F., Vriend, W. J., & Tielens, A. G. G. M. 2004, ApJ, 609, 826

Kennicutt R. C., Jr, 1989, ApJ, 344, 685

Kennicutt R. C., Jr, 1998, ApJ, 498, 541

Kennicutt, R. C., Jr. 1998, ARA&A, 36, 189

Kennicutt, R. C., Calzetti, D., Aniano, G., et al. 2011, PASP, 123, 1347

Kennicutt, R. C., & Evans, N. J. 2012, ARA&A, 50, 531

Kewley, L. J., & Ellison, S. L. 2008, ApJ, 681, 1183-1204

Kimm, T., & Cen, R. 2013, ApJ, 776, 35

Kimura, H., Mann, I., & Jessberger, E. K. 2003, ApJ, 583, 314

Kisielius, R., Kulkarni, V. P., Ferland, G. J., Bogdanovich, P., & Lykins, M. L. 2014, ApJ, 780, 76

Kisielius, R., Kulkarni, V. P., Ferland, G. J., et al. 2015, ApJ, 804, 76

Kissel, J., Brownlee, D. E., Buchler, K., et al. 1986, Nature, 321, 336

Kistler, M. D., Yüksel, H., Beacom, J. F., Hopkins, A. M., & Wyithe, J. S. B. 2009, ApJ, 705, L104

Kobayashi, C., Umeda, H., Nomoto, K., Tominaga, N., & Ohkubo, T. 2006, ApJ, 653, 1145

Krogager, J.-K., Fynbo, J. P. U., Ledoux, C., et al. 2013, MNRAS, 433, 3091

Kulkarni, V. P., York, D. G., Vladilo, G., & Welty, D. E. 2007, ApJ, 663, L81

Kunth, D., Matteucci, F., & Marconi, G. 1995, A&A, 297, 634

Kuo, T.-M., & Hirashita, H. 2012, MNRAS, 424, L34

Lanfranchi, G. A., & Matteucci, F. 2010, A&A, 512, A85

Landgraf, M., Müller, M., & Grün, E. 1999, Planet. Space Sci., 47, 1029

Lanzetta, K. M., Wolfe, A. M., Turnshek, D. A., et al. 1991, ApJS, 77, 1

Lanzetta, K. M., Wolfe, A. M., & Turnshek, D. A. 1995, ApJ, 440, 435

Laporte, N., Ellis, R. S., Boone, F., et al. 2017, ApJ, 837, L21

Larson, R. B. 1974, MNRAS, 166, 585

Ledoux, C., Petitjean, P., & Srianand, R. 2003, MNRAS, 346, 209

Lee, J. C. 2010, Space Sci. Rev., 157, 93

Lee, J. C., & Ravel, B. 2005, ApJ, 622, 970

Lequeux, J., Peimbert, M., Rayo, J. F., Serrano, A., & Torres-Peimbert, S. 1979, A&A, 80, 155

Leroy, A., Bolatto, A., Stanimirovic, S., et al. 2007, ApJ, 658, 1027

Li, A., & Draine, B. T. 2001, ApJ, 554, 778

Liffman, K., & Clayton, D. D. 1989, ApJ, 340, 853

Lin, D. N. C., Bodenheimer, P., & Richardson, D. C. 1996, Nature, 380, 606

Lineweaver, C. H., 2001, Icarus, 151, 307

Lineweaver, C. H., Fenner, Y., Gibson, B. K., 2004, Science, 303, 59

Lodders, K. 2003, ApJ, 591, 1220

Lu, L., Sargent, W. L. W., Womble, D. S., & Barlow, T. A. 1996, ApJ, 457, L1

Lufkin, G., Richardson, D. C., Mundy, L. G. 2006, ApJ, 653, 1464

Lisenfeld, U., & Ferrara, A. 1998, ApJ, 496, 145

Madau, P., & Dickinson, M. 2014, ARA&A, 52, 415

Madden, S. C., Galliano, F., Jones, A. P., & Sauvage, M. 2006, A&A, 446, 877

Madden, S. C., Rémy-Ruyer, A., Galametz, M., et al. 2013, PASP, 125, 600

Maiolino, R., Schneider, R., Oliva, E., et al. 2004, Nature, 431, 533

Maiolino, R., Nagao, T., Marconi, A., et al. 2006, Mem. Soc. Astron. Italiana, 77, 643

Maiolino, R., Carniani, S., Fontana, A., et al. 2015, MNRAS, 452, 54

Mancini, M., Schneider, R., Graziani, L., et al. 2015, MNRAS, 451, L70

Mancini, M., Schneider, R., Graziani, L., et al. 2016, MNRAS, 462, 3130

Mandell, A. M., Sigurdsson, S. 2003, ApJL, 599, L111

Mannucci, F., Cresci, G., Maiolino, R., Marconi, A., & Gnerucci, A. 2010, MNRAS, 408, 2115

Marassi, S., Chiaki, G., Schneider, R., et al. 2014, ApJ, 794, 100

Marassi, S., Schneider, R., Limongi, M., et al. 2015, MNRAS, 454, 4250

Martin C. L., Kennicutt R. C., Jr, 2001, ApJ, 555, 301

Martin, P. G., Roy, A., Bontemps, S., et al. 2012, ApJ, 751, 28

Mathis, J. S. 1990, ARA&A, 28, 37

Mathis, J. S., Rumpl, W., & Nordsieck, K. H. 1977, ApJ, 217, 425

Matsumura, S., Ida, S., Nagasawa, M., 2013, Apj, 767, 129

Matsuo, T., Shibai, H., Ootsubo, T., & Tamura, M. 2007, ApJ, 662, 1282

Matteucci, F., & Brocato, E. 1990, ApJ, 365, 539

Matteucci, F. 1994, A&A, 288, 57

Matteucci, F. 2001, Astrophysics and Space Science Library, Kluwer Academic Publishers

Matteucci, F. 2001, Astronomy and Astrophysics Library, Springer-Verlag Berlin Heidelberg

Matteucci, F., Molaro, P., & Vladilo, G. 1997, A&A, 321, 45

Matteucci, F., & Greggio, L. 1986, A&A, 154, 279

Matteucci, F., & Tornambe, A. 1987, A&A, 185, 51

Mattsson, L. 2011, MNRAS, 414, 781

Mattsson, L. 2015, arXiv:1505.04758

Matsuda, T., Satō, H., & Takeda, H. 1969, Progress of Theoretical Physics, 42, 219

McKee, C. 1989, Interstellar Dust, 135, 431

McKinnon, R., Torrey, P., & Vogelsberger, M. 2016, MNRAS, 457, 3775

Meixner, M., Gordon, K. D., Indebetouw, R., et al. 2006, AJ, 132, 2268

Meixner, M., Panuzzo, P., Roman-Duval, J., et al. 2013, AJ, 146, 62

Ménard, B., Scranton, R., Fukugita, M., & Richards, G. 2010, MNRAS, 405, 1025

Ménard, B., & Fukugita, M. 2012, ApJ, 754, 116

Mennella, V., Brucato, J. R., Colangeli, L., et al. 1998, ApJ, 496, 1058

Messenger, S., Keller, L. P., & Nguyen, A. N. 2013, Proceedings of The Life Cycle of Dust in the Universe: Observations, Theory, and Laboratory Experiments (LCDU2013). 18-22 November, 2013.

Micali, A., Matteucci, F., & Romano, D. 2013, MNRAS, 436, 1648

Michałowski, M. J., Murphy, E. J., Hjorth, J., et al. 2010, A&A, 522, A15

Min, M., Waters, L. B. F. M., de Koter, A., et al. 2007, A&A, 462, 667

Molaro, P., Bonifacio, P., Centurión, M., et al. 2000, ApJ, 541, 54

Mollá, M., Cavichia, O., Gavilán, M., & Gibson, B. K. 2015, MNRAS, 451, 3693

Møller, P., & Warren, S. J. 1998, MNRAS, 299, 661

Mordasini, C., Alibert, Y., Benz, W., & Naef, D. 2006, European Planetary Science Congress 2006, 672

Morgan, H. L., & Edmunds, M. G. 2003, MNRAS, 343, 427

Mortier, A., Santos, N. C., Sozzetti, A., et al., 2012, A&A, 543, A45

Mortier, A., Santos, N. C., Sousa, S. G., Fernandes, J. M., Adibekyan, V. Zh., Delgado Mena, E., Montalto, M., Israelian, G., 2013a, 558, A106

Mortier, A.; Santos, N. C.; Sousa, S.; Israelian, G.; Mayor, M.; Udry, S., 2013b, 557, A70

Mortlock, D. J., Warren, S. J., Venemans, B. P., et al. 2011, Nature, 474, 616

Morton, D. C. 2003, ApJS, 149, 205

Murante, G., Monaco, P., Borgani, S., et al. 2015, MNRAS, 447, 178

Nakamura, F., & Umemura, M. 2002, ApJ, 569, 549

Nanni, A., Bressan, A., Marigo, P., & Girardi, L. 2013, MNRAS, 434, 2390

Noeske, K. G., Weiner, B. J., Faber, S. M., et al. 2007, ApJ, 660, L43

Nomoto, K., Kobayashi, C., & Tominaga, N. 2013, ARA&A, 51, 457

Noterdaeme, P., Laursen, P., Petitjean, P., et al. 2012, A&A, 540, A63

Nozawa, T., Kozasa, T., & Habe, A. 2006, ApJ, 648, 435

Nozawa, T., Kozasa, T., Habe, A., et al. 2007, ApJ, 666, 955

Nozawa, T., Maeda, K., Kozasa, T., et al. 2011, ApJ, 736, 45

Nuth, J. A., III, & Hecht, J. H. 1990, Ap&SS, 163, 79

O'Connor, E., & Ott, C. D. 2011, ApJ, 730, 70

Oort, J. H., & van de Hulst, H. C. 1946, Bull. Astron. Inst. Netherlands, 10, 187

Ota, K., Walter, F., Ohta, K., et al. 2014, ApJ, 792, 34

Otsuka, M., Meixner, M., Panagia, N., et al. 2012, ApJ, 744, 26

Ouchi M., et al., 2013, ApJ, 778, 102

Overbeck, J. W. 1965, ApJ, 141, 864

Padovani, P., & Matteucci, F. 1993, ApJ, 416, 26

Padovani, P., & Matteucci, F. 1993, ApJ, 416, 26

Pagel B. E. J., 2009, Nucleosynthesis and Chemical Evolution of Galaxies, Cambridge, UK, Cambridge University Press, 2009

Parvathi, V. S., Sofia, U. J., Murthy, J., & Babu, B. R. S. 2012, ApJ, 760, 36

Pei, Y. C., Fall, S. M., & Bechtold, J. 1991, ApJ, 378, 6

Péroux, C., Dessauges-Zavadsky, M., D'Odorico, S., Kim, T.-S., & McMahon, R. G. 2003, MNRAS, 345, 480

Petigura, E. A., Howard, A. W., Marcy, G. W., 2013, PNAS, 110, 19175

Petitjean, P., Srianand, R., & Ledoux, C. 2000, A&A, 364, L26

Pettini, M., Smith, L. J., Hunstead, R. W., & King, D. L. 1994, ApJ, 426, 79

Pilbratt, G. L., Riedinger, J. R., Passvogel, T., et al. 2010, A&A, 518, L1

Pilyugin, L. S., Vílchez, J. M., & Contini, T. 2004, A&A, 425, 849

Piovan, L., Chiosi, C., Merlin, E., et al. 2011, arXiv:1107.4541

Pipino, A., Fan, X. L., Matteucci, F., et al. 2011, A&A, 525, A61

Pipino, A., & Matteucci, F. 2004, MNRAS, 347, 968

Pipino, A., & Matteucci, F. 2011, A&A, 530, A98

Planck Collaboration, Ade, P. A. R., Aghanim, N., et al. 2016, A&A, 594, A13

Pollack, J. B., Hubickyj, O., Bodenheimer, P., et al., 1996, Icarus, 124, 62

Poteet, C. A., Megeath, S. T., Watson, D. M., et al. 2011, ApJ, 733, L32

Popping, G., Somerville, R. S., & Galametz, M. 2016, arXiv:1609.08622

Pozzi, F., Calura, F., Gruppioni, C., et al. 2015, ApJ, 803, 35

Prantzos N., 2008, Space Sci. Rev., 135, 313

Press, W. H., & Schechter, P. 1974, ApJ, 187, 425

Prochaska, J. X., Gawiser, E., Wolfe, A. M., Castro, S., & Djorgovski, S. G. 2003, ApJ, 595, L9

Prochaska, J. X., O'Meara, J. M., & Worseck, G. 2010, ApJ, 718, 392

Rafelski, M., Wolfe, A. M., Prochaska, J. X., Neeleman, M., & Mendez, A. J. 2012, ApJ, 755, 89

Raymond, S. N., Mandell, A. M., Sigurdsson, S. 2006, Sci, 313, 1413

Recchi, S., Matteucci, F., & D'Ercole, A. 2002, Chemical Enrichment of Intracluster and Intergalactic Medium, 253, 397

Rémy-Ruyer, A., Madden, S. C., Galliano, F., et al. 2014, A&A, 563, A31

Rémy-Ruyer, A., Madden, S. C., Galliano, F., et al. 2015, A&A, 582, A121

Rice. W.K.M., Armitage P.J., 2003, ApJ, 598, L55

Romano, D., Chiappini, C., Matteucci, F., & Tosi, M. 2005, A&A, 430, 491

Romano, D., Karakas, A. I., Tosi, M., & Matteucci, F. 2010, A&A, 522, A32

Routly, P. M., & Spitzer, L., Jr. 1952, ApJ, 115, 227

Rowlands, K., Gomez, H. L., Dunne, L., et al. 2014, MNRAS, 441, 1040

Ruderman, M. A. 1974, Science, 184, 1079

Safronov, V. S., & Zvjagina, E. V. 1969, Icarus, 10, 109

Sagan, C., & Shklovskij, I. S. 1978, Intelligent life in the universe., by Sagan, C.; Shklovskij, I. S.. San Francisco, CA (USA): Holden-Day, 509 p.,

Salpeter, E. E. 1955, ApJ, 121, 161

Salvadori, S., & Ferrara, A. 2012, MNRAS, 421, L29

Sánchez-Ramírez, R., Ellison, S. L., Prochaska, J. X., et al. 2016, MNRAS, 456, 4488

Sandford, S. A. 1987, Fundamentals Cosmic Phys., 12, 1

Santini, P., Maiolino, R., Magnelli, B., et al. 2010, A&A, 518, L154

Santini, P., Maiolino, R., Magnelli, B., et al. 2014, A&A, 562, A30

Santos, N. C., Israelian, G., & Mayor, M. 2001, A&A, 373, 1019

Santos, N. C., Israelian, G., & Mayor, M. 2004, A&A, 415, 1153

Savage, B. D., & Sembach, K. R. 1996, ARA&A, 34, 279

Scalo, J. M. 1986, Fundamentals Cosmic Phys., 11, 1

Schaerer, D., Boone, F., Zamojski, M., et al. 2015, A&A, 574, A19

Schaye J., 2004, ApJ, 609, 667

Schechter, P. 1976, ApJ, 203, 297

Schmidt, M. 1959, ApJ, 129, 243

Schneider, R., Ferrara, A., Salvaterra, R., Omukai, K., & Bromm, V. 2003, Nature, 422, 869

Schneider, R., Omukai, K., Bianchi, S., & Valiante, R. 2012, MNRAS, 419, 1566

Schneider, R., Valiante, R., Ventura, P., et al. 2014, MNRAS, 442, 1440

Schneider, R., Valiante, R., Ventura, P., dell'Agli, F., & di Criscienzo, M. 2015, Why Galaxies Care about AGB Stars III: A Closer Look in Space and Time, 497, 369

Schoenberg, E., & Jung, B. 1934, Astronomische Nachrichten, 253, 261

Siebenmorgen, R., Voshchinnikov, N. V., & Bagnulo, S. 2014, A&A, 561, A82

Silva, L., Granato, G. L., Bressan, A., & Danese, L. 1998, ApJ, 509, 103

Silvia, D. W., Smith, B. D., & Shull, J. M. 2010, ApJ, 715, 1575

Smartt, S. J. 2015, Publ. Astron. Soc. Australia, 32, e016

Smartt, S. J., Eldridge, J. J., Crockett, R. M., & Maund, J. R. 2009, MNRAS, 395, 1409

Smith, R. K., Dame, T. M., Costantini, E., & Predehl, P. 2006, ApJ, 648, 452

Sozzetti, A., Torres, G., Latham, David W., Stefanik, R. P., Korzennik, S. G., Boss, A. P., Carney, B. W., Laird, J. B., 2009, ApJ, 697,544

Snow, T. P., Rachford, B. L., & Figoski, L. 2002, ApJ, 573, 662

Sofia, U. J., Gordon, K. D., Clayton, G. C., et al. 2006, ApJ, 636, 753

Songaila, A., & Cowie, L. L. 2010, ApJ, 721, 1448

Sousa, S. G., Santos, Israelian, G., Mayor, M., Udry, S., 2011, A&A, 533, A141

Spitoni, E., Matteucci, F., Recchi, S., Cescutti, G., & Pipino, A. 2009, A&A, 504, 87

Spitoni E., Matteucci F., 2011, A&A, 531, A72

Spitoni, E., Matteucci, F., Sozzetti, A., 2014, MNRAS, 440, 2588

Spitoni, E., Romano, D., Matteucci, F., Ciotti, L., 2015, ApJ, 802, 129

Spitoni, E., Vincenzo, F., Matteucci, F., & Romano, D. 2016, MNRAS, 458, 2541

Spitoni, E., Gioannini, L., & Matteucci, F. 2017, In press., arXiv:1705.01297

Spitoni E., Matteucci F., 2011, A&A, 531, A72

Stecher, T. P., & Donn, B. 1965, ApJ, 142, 1681

Stepnik, B., Abergel, A., Bernard, J.-P., et al. 2003, A&A, 398, 551

Storrie-Lombardi, L. J., & Wolfe, A. M. 2000, ApJ, 543, 552

Struve, F. G. W. 1847, St. Petersburg : Tip. Acad. Imper., 1847; IV, 165 p. ; in 8.; DCCC.4.211,

Swamy, K. S. K. 2005, Dust In The Universe. Series: World Scientific Series in Astronomy and

Talbot, R. J., Jr., & Arnett, W. D. 1971, ApJ, 170, 409

The LIGO Scientific Collaboration, the Virgo Collaboration, Abbott, R., et al. 2017, arXiv:1709.09660

The LIGO Scientific Collaboration, & The Virgo Collaboration 2017, arXiv:1710.05832

Tiengo, A., Vianello, G., Esposito, P., & Mereghetti, S. 2010, X-ray Astronomy 2009; Present Status, Multi-Wavelength Approach and Future Perspectives, 1248, 81

Todini, P., & Ferrara, A. 2001, MNRAS, 325, 726

Todini, P., & Ferrara, A. 2001, MNRAS, 325, 726

Tremonti, C. A., Heckman, T. M., Kauffmann, G., et al. 2004, ApJ, 613, 898

Trumpler, R. J. 1930, Lick Observatory Bulletin, 14, 154

Tuomi, M., Jones, H. R. A., Barnes, J. R., Anglada-Escudé, G., & Jenkins, J. S. 2014, MNRAS, 441, 1545

Tytler, D. 1982, Nature, 298, 427

Ueda, Y., Mitsuda, K., Murakami, H., & Matsushita, K. 2005, ApJ, 620, 274

Udry, S., Mayor, M., Benz, W., et al. 2006, A&A, 447, 361

Udry, S. & Santos, N. C. 2007, ARA&A, 45, 397

Ugliano, M., Janka, H.-T., Marek, A., & Arcones, A. 2012, ApJ, 757, 69

Valiante, R., Schneider, R., Bianchi, S., & Andersen, A. C. 2009, MNRAS, 397, 1661

Valiante, R., Schneider, R., Salvadori, S., & Bianchi, S. 2011, MNRAS, 416, 1916

Valiante, R., Schneider, R., Salvadori, S., & Gallerani, S. 2014, MNRAS, 444, 2442

van den Hoek, L. B., & Groenewegen, M. A. T. 1997, A&AS, 123,

Ventura, P., Criscienzo, M. D., Schneider, R., et al. 2012, MNRAS, 424, 2345

Vincenzo, F., Matteucci, F., Vattakunnel, S., & Lanfranchi, G. A. 2014, MNRAS, 441, 2815

Vincoletto, L., Matteucci, F., Calura, F., Silva, L., & Granato, G. 2012, MNRAS, 421, 3116

Vladilo, G. 2002, A&A, 391, 407

Vladilo, G. 2002, ApJ, 569, 295

Vladilo, G. 2004, A&A, 421, 479

Vladilo, G., Centurión, M., Bonifacio, P., & Howk, J. C. 2001, ApJ, 557, 1007

Vladilo, G., & Péroux, C. 2005, A&A, 444, 461

Vladilo, G., Centurión, M., Levshakov, S. A., et al. 2006, A&A, 454, 151

Vladilo, G., Abate, C., Yin, J., Cescutti, G., & Matteucci, F. 2011, A&A, 530, A33

Voshchinnikov, N. V., & Henning, T. 2010, A&A, 517, A45

Vukotić, B., Steinhauser, D., Martinez-Aviles, G., et al., 2016, MNRAS, 459, 3512

Walter, F., Decarli, R., Carilli, C., et al. 2012, ApJ, 752, 93

Watson, D., Christensen, L., Knudsen, K. K., et al. 2015, Nature, 519, 327

Weingartner, J. C., & Draine, B. T. 2001, ApJ, 548, 296

Welty, D. E., Lauroesch, J. T., Blades, J. C., Hobbs, L. M., & York, D. G. 2001, ApJ, 554, L75

Whelan, J., & Iben, I., Jr. 1973, ApJ, 186, 1007

Wickramasinghe, N. C. 1963, MNRAS, 126, 99

Wickramasinghe, N. C. 1970, Nature, 227, 51

Wickramasinghe, C. 2011, International Journal of Astrobiology, 10, 25

Wickramasinghe, N. C., & Wickramasinghe, A. N. 1993, Ap&SS, 200, 145

Williams, B. J., Borkowski, K. J., Reynolds, S. P., et al. 2012, ApJ, 755, 3

Williams, J. P., Best, W. M. J. 2014, ApJ, 788, 59

Witt, A. N., & Gordon, K. D. 2000, ApJ, 528, 799

Wolfe, A. M., Turnshek, D. A., Smith, H. E., & Cohen, R. D. 1986, ApJS, 61, 249

Wolfe, A. M., Gawiser, E., & Prochaska, J. X. 2005, ARA&A, 43, 861

Woosley, S. E., & Weaver, T. A. 1995, ApJS, 101, 181

Wright, E. L., Eisenhardt, P. R. M., Mainzer, A. K., et al. 2010, AJ, 140, 1868-1881

Xie, Y., Li, A., & Hao, L. 2017, ApJS, 228, 6

Yao, Y., Zhang, S. N., Zhang, X., & Feng, Y. 2003, ApJ, 594, L43

Ysard, N., Juvela, M., Demyk, K., et al. 2012, A&A, 542, A21

Zackrisson, E., Calissendorff, P., González, J., et al. 2016, ApJ, 833, 214

Zavala, J. A., Michałowski, M. J., Aretxaga, I., et al. 2015, MNRAS, 453, L88

Zeegers, S. T., Costantini, E., de Vries, C. P., et al. 2017, A&A, 599, A117

Zhukovska, S. 2008, Ph.D. Thesis,

Zhukovska, S., Gail, H.-P., & Trieloff, M. 2008, A&A, 479, 453

Zhukovska, S., & Henning, T. 2013, A&A, 555, A99

Zhukovska, S. 2014, A&A, 562, A76

Zhukovska, S., Dobbs, C., Jenkins, E. B., & Klessen, R. S. 2016, ApJ, 831, 147

Zhukovska, S., & Henning, T. 2013, A&A, 555, A99

Zu, Y., Weinberg, D. H., Davé, R., et al. 2011, MNRAS, 412, 1059

Zubko, V., Dwek, E., & Arendt, R. G. 2004, ApJS, 152, 211

Zwaan, M. A., van der Hulst, J. M., Briggs, F. H., Verheijen, M. A. W., & Ryan-Weber, E. V. 2005, MNRAS, 364, 1467

List of Figures

List of Tables

List of abbreviations

AGB Asymptotic Giant Branch

C08 Calura et al. (2008)

CDR Cosmic dust rate

CMM Cosmic mean metallicity

CSFR Cosmic star formation rate

D98 Dwek (1998)

DE number density evolution scenario

DLA Damped Lyman Alpha system

GHZ Galactic Habitable Zone

IGM Intergalactic medium

IR Infrared wavelengths

IRA Instantaneous recycling approximation

IMF Initial mass function

ISM Interstellar medium

LMC Large Magellanic Cloud

PAH Polycyclic Aromatic Hydrocarbon

PLE Pure luminosity evolution scenario

SFH Star formation history

SED Spectral energy distribution

SMC Small Magellanic Cloud

SN Supernova

SNR Supernova Remnant

UV Ultraviolet wavelengths

V11 Vladilo et al. (2011)